Sektion 5.2. Klimadynamik und Landschaftsentwicklung
Helmholtz-Zentrum Potsdam - Deutsches GeoForschungsZentrum GFZ

Varve and Event Layer Chronology of Lake Suigetsu (Japan) Back to 40 kyr BP and Contribution to the International Consensus Atmospheric Radiocarbon Calibration Curve

Dissertation zur Erlangung des akademischen Grades Doktor der Naturwissenschaften (Dr. rer. nat.) in der Wissenschaftsdisziplin Geologie

Eingereicht an der Mathematisch-Naturwissenschaftlichen Fakultät der Universität Potsdam

von
Gordon Schlolaut
Juni 2013

Betreuer:
apl. Prof. Dr. Achim Brauer
Universität Potsdam
Helmholtz-Zentrum Potsdam, Deutsches GeoForschungsZentrum GFZ

Published online at the
Institutional Repository of the University of Potsdam:
URL http://opus.kobv.de/ubp/volltexte/2013/6909/
URN urn:nbn:de:kobv:517-opus-69096
http://nbn-resolving.de/urn:nbn:de:kobv:517-opus-69096

Erklärung

Hiermit erkläre ich gemäß §9 Abs. 7 der Promotionsordnung der Mathematisch-Naturwissenschaftlichen Fakultät der Universität Potsdam, dass ich die von mir vorgelegte Dissertation mit dem Titel

Varve and Event Layer Chronology of Lake Suigetsu (Japan) Back to 40 kyr BP and Contribution to the International Consensus Atmospheric Radiocarbon Calibration Curve

selbstständig angefertigt, die benutzten Quellen und Hilfsmittel vollständig angegeben und wörtliche und sinngemäße Zitate als solche gekennzeichnet habe sowie Tabellen, Karten und Abbildungen, die anderen Werken in Wortlaut oder dem Sinn nach entnommen sind, in jedem Einzelfall als Entlehnung kenntlich gemacht habe. Ich erkläre außerdem, dass diese Dissertation noch keiner anderen Fakultät oder Hochschule zur Prüfung vorgelegen hat; dass sie, abgesehen von unten angegebenen Teilpublikationen, noch nicht veröffentlicht worden ist sowie, dass ich eine solche Veröffentlichung vor Abschluss des Promotionsverfahrens nicht vornehmen werde. Die Bestimmungen der Promotionsordnung sind mir bekannt.

Teilveröffentlichungen:

- Takeshi Nakagawa, Katsuya Gotanda, Tsuyoshi Haraguchi, Toru Danhara, Hitoshi Yonenobu, Achim Brauer, Yusuke Yokoyama, Ryuji Tada, Keiji Takemura, Richard A. Staff, Rebecca Payne, Christopher Bronk Ramsey, Charlotte Bryant, Fiona Brock, Gordon Schlolaut, Michael Marshall, Pavel Tarasov, Henry Lamb, Suigetsu 2006 Project Members, 2012, SG06, a fully continuous and varved sediment core from Lake Suigetsu, Japan: stratigraphy and potential for improving the radiocarbon calibration model and understanding of late Quaternary climate changes, Quaternary Science Reviews, Vol 36, p 164-174

- Gordon Schlolaut, Michael Marshall, Achim Brauer, Takeshi Nakagawa, Henry Lamb, Richard Staff, Christopher Bronk Ramsey, Charlotte Bryant, Fiona Brock, Annette Kossler, Pavel Tarasov, Yusuke Yokoyama, Ryuji Tada, Tsuyoshi Haraguchi, Suigetsu 2006 project members, 2012, An automated method for varve interpolation and its application to the Late Glacial chronology from Lake Suigetsu, Japan, Quaternary Geochronology, Vol. 13, p 52-69

- Michael Marshall, Gordon Schlolaut, Takeshi Nakagawa, Henry Lamb, Achim Brauer, Richard Staff, Christopher Bronk Ramsey, Pavel Tarasov, Katsuya Gotanda, Tsuyoshi Haraguchi, Yusuke Yokoyama, Hitoshi Yonenobu, Ryuji Tada & Suigetsu 2006 project members, 2012, A novel approach to varve counting using - XRF and X-radiography in combination with thin section microscopy, applied to the Late Glacial chronology from Lake Suigetsu, Japan, Quaternary Geochronology, Vol. 13, p 70-80

- Christopher Bronk Ramsey, Richard A. Staff, Charlotte L. Bryant, Fiona Brock, Hiroyuki Kitagawa, Johannes van der Plicht, Gordon Schlolaut, Michael H. Marshall, Achim Brauer, Henry F. Lamb, Rebecca L. Payne, Pavel E. Tarasov, Tsuyoshi Haraguchi, Katsuya Gotanda, Hitoshi Yonenobu, Yusuke Yokoyama, Ryuji Tada, Takeshi Nakagawa, 2012, A complete terrestrial radiocarbon record for 11.2-52.8 kyr BP, Science, Vol. 338 (6105), p 370-374

- Gordon Schlolaut, Achim Brauer, Michael H. Marshall, Takeshi Nakagawa, Richard A. Staff, Christopher Bronk Ramsey, Henry F. Lamb, Charlotte L. Bryant, Rudolf Naumann, Peter Dulski, Fiona Brock, Yusuke Yokoyama, Ryuji Tada, Tsuyoshi Haraguchi and Suigetsu 2006 project members, submitted, Event layers in the Japanese Lake Suigetsu 'SG06' sediment core: description, interpretation and climatic implications, Quaternary Science Reviews (submitted)

Ort, Datum, Unterschrift (Gordon Schlolaut)

Contents

Abstract i
Kurzfassung iii
Acknowledgements v

0. Preface **1**
0.1. Aims of the PhD project 1
0.2. Radiocarbon dating and calibration 2
0.3. Study site 4
0.4. The climate of Japan and flood risk 5
0.5. Materials and methods 6
0.6. Thesis structure 7

I. Introduction: The SG06 sediment core **11**
I.0. Definitions 11
I.1. Introduction 12
I.2. Site description 13
I.3. Coring, logging and storage methods 15
I.4. Stratigraphy of the SG06 core 16
I.4.1. General rule for coding and depth control 16
I.4.2. Construction of the composite section 19
I.4.3. Varved sediment 20
I.4.4. Event layers 23
I.4.5. Tephrostratigraphy and preliminary chronology 24
I.4.6. Plant macro remains 24
I.5. Potential contributions for INTIMATE perspectives - coming attractions - 26
I.5.1. Terrestrial radiocarbon calibration model 26
I.5.2. Climate changes 27
I.5.3. Correlation with other study sites 27

II. Dating the SG06 sediment core: Varve counting by thin-section microscopy and varve interpolation **29**
II.1. Introduction 29
II.1.1. Study site 30
II.2. Materials and methods 31
II.2.1. Varve description and counting 31
II.2.2. Interpolation 35
Generation of artificial varve count data and the Settings Matrix 39
Applying the Settings Matrix to a real count 41
Error estimation 41
Limitations and requirements for interpolation 42
Combining results from different counts from the same core 43
II.3. Results 43
II.3.1. Varve counting and first step interpolation results 45
II.3.2. Comparison of first step interpolation results and combined chronology . . 47
II.4. Discussion 50
II.4.1. Seasonal layer formation/preservation 50
II.4.2. Accuracy and precision of the interpolation result 50
II.4.3. Comparison with conventional varve interpolation 51
II.4.4. Outlook: Further improvements to the SG06 varve chronology 52
II.5. Conclusion 53

III. Dating the SG06 sediment core: Varve counting by μXRF and combination with the thin-section count **55**
III.1. Introduction . . . 55
III.2. Regional setting . . . 56
III.3. Material and methods . . . 57
III.3.1. Coring and logging . . . 57
III.3.2. High resolution μ-XRF and X-radiography . . . 57
Optimisation of scanner settings . . . 57
Counting . . . 60
III.4. Results . . . 61
III.4.1. Varve structure . . . 61
III.4.2. Varve structure in the μXRF signal . . . 62
III.4.3. μXRF count results . . . 63
III.4.4. Comparison with results from microscopic varve counting . . . 64
Comparison of raw counts . . . 64
Interpolation of μXRF counts . . . 65
Comparison of μXRF with microscopic interpolation results and combination to final SG06 floating varve chronology . . . 67
III.5. Discussion . . . 69
III.5.1. Differences in raw counts . . . 69
III.5.2. Combined count - ^{14}C comparison (to 12,550 cal yr BP) . . . 69
III.6. Conclusions . . . 70

IV. Dating the SG06 sediment core: A 40,000 year ^{14}C chronology and constraining the SG06 varve count **73**
IV.1. A complete terrestrial radiocarbon record for 11.2 to 52.8 kyr B.P. . . . 73

V. Palaeo-environmental information: Event layers and a 40,000 year flood record from Lake Suigetsu **81**
V.1. Introduction . . . 81
V.1.1. Study site . . . 82
V.2. Materials and methods . . . 83
V.2.1. Core photographs . . . 84
V.2.2. Thin section microscopy . . . 84
V.2.3. μXRF analysis of core material . . . 84
V.2.4. XRF analysis of catchment samples . . . 84
V.2.5. Age model . . . 85
V.3. Results . . . 85
V.3.1. Sediment characterisation and major facies changes . . . 85
V.3.2. Event layer types . . . 85
Event layer type I . . . 85
Event layer type II . . . 87
Event layer type III . . . 87
V.3.3. Event layer type I frequency . . . 88
V.3.4. XRF analysis of catchment samples . . . 90
V.4. Discussion . . . 90
V.4.1. Interpretation of event layers . . . 90
V.4.2. Facies change at EL-3107 (38,213 $SG06_{2012}$ yr BP) . . . 93
V.4.3. Comparison with earlier findings from Lake Suigetsu . . . 93
V.4.4. Flood layer frequency . . . 94
V.5. Conclusions . . . 96

VI. Synthesis **99**
VI.1. Summary . . . 99
VI.2. Conclusions and Outlook . . . 101
VI.2.1. Varve Counting and Varve Interpolation . . . 101
VI.2.2. Radiocarbon Calibration . . . 102
VI.2.3. Event Layer Analysis . . . 102
VI.2.4. Unpublished Methods and Preliminary Results . . . 103

Bibliography 105

Appendix 119

A. Main Matlab commands for VIP (Chapter II) 121

B. Supporting (online) material (SOM) to chapter IV 123
B.1. Materials and Methods . . . 123
B.1.1. Radiocarbon dating methodology . . . 123
B.1.2. Varve counting . . . 123
B.1.3. Compilation of the radiocarbon dataset . . . 123
B.1.4. Modeling of speleothem datasets onto the SG06 varve chronology . . . 124
B.1.5. Using the SG06 dataset in comparison to other records . . . 126
Terrestrial data (Soppensee) . . . 126
Marine data (Cariaco Basin and Iberian Margin) . . . 126
Coral data . . . 127
B.2. Figures . . . 127
B.3. Tables . . . 139

Abstract

The main intention of the PhD project was to create a varve chronology for the 'Suigetsu Varves 2006' (SG06) composite profile from Lake Suigetsu (Japan) by thin section microscopy. The chronology was not only to provide an age-scale for the various palaeo-environmental proxies analysed within the SG06 project, but also and foremost to contribute, in combination with the SG06 ^{14}C chronology, to the international atmospheric radiocarbon calibration curve (IntCal). The SG06 ^{14}C data are based on terrestrial leaf fossils and therefore record atmospheric ^{14}C values directly, avoiding the corrections necessary for the reservoir ages of the marine datasets, which are currently used beyond the tree-ring limit in the IntCal09 dataset (Reimer et al., 2009).

The SG06 project is a follow up of the SG93 project (Kitagawa and van der Plicht, 2000), which aimed to produce an atmospheric calibration dataset, too, but suffered from incomplete core recovery and varve count uncertainties. For the SG06 project the complete Lake Suigetsu sediment sequence was recovered continuously, leaving the task to produce an improved varve count.

Varve counting was carried out using a dual method approach utilizing thin section microscopy and micro X-Ray Fluorescence (μXRF). The latter was carried out by Dr. Michael Marshall in cooperation with the PhD candidate. The varve count covers 19 m of composite core, which corresponds to the time frame from ≈10 to ≈40 kyr BP.

The count result showed that seasonal layers did not form in every year. Hence, the varve counts from either method were incomplete. This rather common problem in varve counting is usually solved by manual varve interpolation. But manual interpolation often suffers from subjectivity. Furthermore, sedimentation rate estimates (which are the basis for interpolation) are generally derived from neighbouring, well varved intervals. This assumes that the sedimentation rates in neighbouring intervals are identical to those in the incompletely varved section, which is not necessarily true. To overcome these problems a novel interpolation method was devised. It is computer based and automated (i.e. avoids subjectivity and ensures reproducibility) and derives the sedimentation rate estimate directly from the incompletely varved interval by statistically analysing distances between successive seasonal layers. Therefore, the interpolation approach is also suitable for sediments which do not contain well varved intervals. Another benefit of the novel method is that it provides objective interpolation error estimates.

Interpolation results from the two counting methods were combined and the resulting chronology compared to the ^{14}C chronology from Lake Suigetsu, calibrated with the tree-ring derived section of IntCal09 (which is considered accurate). The varve and ^{14}C chronology showed a high degree of similarity, demonstrating that the novel interpolation method produces reliable results.

In order to constrain the uncertainties of the varve chronology, especially the cumulative error estimates, U-Th dated speleothem data were used by linking the low frequency ^{14}C signal of Lake Suigetsu and the speleothems, increasing the accuracy and precision of the Suigetsu calibration dataset. The resulting chronology also represents the age-scale for the various palaeo-environmental proxies analysed in the SG06 project.

One proxy analysed within the PhD project was the distribution of event layers, which are often representatives of past floods or earthquakes. A detailed microfacies analysis revealed three different types of event layers, two of which are described here for the first time for the Suigetsu sediment. The types are: matrix supported layers produced as result of subaqueous slope failures, turbidites produced as result of landslides and turbidites produced as result of flood events. The former two are likely to have been triggered by earthquakes. The vast majority of event layers was related to floods (362 out of 369), which allowed the construction of a respective chronology for the last 40 kyr. Flood frequencies were highly variable, reaching their greatest values during the global sea level low-stand of the Glacial, their lowest values during Heinrich Event 1. Typhoons affecting the region represent the most likely control on the flood frequency, especially during the Glacial. However, also local, non-climatic controls are suggested by the data.

In summary, the work presented here expands and revises knowledge on the Lake Suigetsu sediment and enabls the construction of a far more precise varve chronology. The ^{14}C calibration dataset is the first such derived from lacustrine sediments to be included into the (next) IntCal dataset.

Kurzfassung

Die Hauptzielsetzung der Doktorarbeit war die Erstellung einer Warvenchronologie für das Kompositprofil der "Suigetsu Varves 2006" (SG06) Sedimentbohrung vom Suigetsu See (Japan) durch Dünnschliffmikroskopie. Die Chronologie soll dabei nicht nur als Altersskala für die unterschiedlichen Proxies, die im Rahmen des SG06 Projekts bearbeitet werden, dienen, sondern in Kombination mit der SG06 ^{14}C Chronologie auch zur Verbesserung der internationalen Radiokarbon Kalibrationskurve (IntCal) beitragen. Da die SG06 ^{14}C Daten aus fossilen, in den See eingewehten Blättern gewonnen wurden, geben sie den ^{14}C Gehalt der Atmosphäre direkt wieder. Das heißt, dass Korrekturen entfallen, wie sie bei den derzeit im IntCal09 Datensatz (Reimer et al., 2009) genutzten marinen ^{14}C Daten notwendig sind.

Das SG06 Projekt ist ein Folgeprojekt des SG93 Projekts (Kitagawa and van der Plicht, 2000), welches ebenfalls die Erstellung eines Kalibrationsdatensatzes zur Zielsetzung hatte. Allerdings war das Sedimentprofil der SG93 Bohrung unvollständig und die Warvenchronologie unzureichend genau. Im Rahmen des SG06 Projekts wurde die komplette Sedimentabfolge des Sees erbohrt, so dass die Erstellung einer verbesserten Warvenchronologie als Aufgabe verblieb.

Für die Erstellung der Warvenchronologie kam neben Dünnschliffmikroskopie eine zweite, unabhängige Zähltechnik zum Einsatz, die Mikro-Röntgenfluoresenz (μXRF) Daten nutzt. Diese wurde von Dr. Michael Marshall in Zusammenarbeit mit dem Doktoranden erstellt. Insgesamt wurden in 19 m des SG06 Sedimentprofils Warven gezählt, was dem Zeitabschnitt zwischen ≈10 und ≈40 ka BP entspricht.

Die Warvenzählung zeigte, dass sich nicht jedes Jahr saisonale Lagen ausgebildet hatten und die Zählungen von beiden Techniken damit unvollständig waren. Dieses Problem tritt bei Warvenzählungen häufiger auf und wird in der Regel durch manuelle Interpolation der fehlenden Lagen gelöst. Allerdings hat der manuelle Ansatz Schwächen. Zum einen kann es zu subjektiven Ungenauigkeiten kommen, zum anderen wird die durchschnittliche Sedimentationsrate (welche die Grundlage der Interpolation ist) in der Regel aus benachbarten, gut warvierten Bereichen abgeleitet. Das setzt jedoch voraus, dass die Sedimentationsrate in den benachbarten Intervallen identisch mit der im zu interpolierenden Bereich ist, was nicht zwingend der Fall ist. Um diese Probleme zu umgehen wurde für die vorliegende Arbeit eine neuartige Interpolationsmethode entwickelt. Diese ist computergestützt und automatisiert und Ergebnisse daher objektiv und reproduzierbar. Weiterhin wird die Sedimentationsrate direkt aus dem zu interpolierenden Bereich bestimmt, indem die Abstände der auftretenden saisonalen Lagen statistisch ausgewertet werden. Daher kann die Methode auch für Profile ohne gut warvierte Bereiche eingesetzt werden. Ein weiterer Vorteil des neuen Interpolationsprogramms ist, dass ein objektiver Interpolationsfehlers berechnet wird.

Die interpolierten Ergebnisse der beiden Zähltechniken wurden kombiniert und um nachzuweisen, dass es sich bei der resultierenden Chronologie um ein verlässliches Ergebnis handelt, wurde diese mit der mit IntCal09 kalibrierten ^{14}C Chronologie vom Suigetsu See verglichen. Dabei wurde nur der Abschnitt berücksichtigt, in dem IntCal09 auf dendrologischen Daten beruht (bis 12,55 ka cal BP) da diese Daten als zuverlässig gelten. Der

Vergleich zeigte, dass die finale Warvenchronologie innerhalb des 68,2% Fehlerbereichs der ^{14}C Datierungen lag. Das heißt, dass die Interpolationsmethode hinreichend genaue und zuverlässige Ergebnisse erzielt.

Die Genauigkeit wurde weiter verbessert, indem die Chronologie mit U-Th Altern von Speläothemen modelliert wurde, wobei die tieffrequenten Signale der ^{14}C Daten als Verbindung zwischen Suigetsu und den Speläothemen verwendet wurde, was die Konstruktion eines verbesserten Kalibrationdatensatzes erlaubte. Die modellierte Chronologie stellt dabei auch die Altersskale für die im SG06 Projekt analysierten Proxies dar.

Ein Proxy der im Rahmen der Doktorarbeit untersucht wurde war die Verteilung von Ereignislagen. Diese sind in der Regel Anzeiger für Flutereignisse oder Erdbeben. Die mikrofazielle Untersuchung der Ereignislagen zeigte drei verschiedene Lagentypen auf, wobei zwei davon hier erstmals für den Suigetsu See beschrieben sind. Die Lagentypen sind: Matrix dominierte Lagen als Ergebnis von Seegrundrutschungen, Turbidite als Ergebnis von Hangrutschungen und Turbidite als Ergebnis von Flutereignissen. Die ersten beiden Lagentypen wurden vermutlich durch Erdbeben ausgelöst. Die große Mehrheit der Ereignislagen ist jedoch auf Flutereignisse zurückzuführen (362 von 369). Dies erlaubte die Rekonstruktion der Hochwasserhäufigkeit für die letzten 40 ka. Dabei zeigten sich starke Schwankungen über den analysierten Zeitraum. Die höchsten Werte wurden während des glazialen Meeresspiegelminimums erreicht während die niedrigsten Werte im Zusammenhang mit Heinrich Ereignis 1 auftraten, was vermutlich in erster Linie mit der Taifunhäufigkeit in der Region zusammenhängt. Allerdings zeigten die Daten auch Einflüsse von lokalen, nicht Klima getriebenen Prozessen.

Zusammenfassend kann gesagt werden, dass die hier vorliegende Arbeit die Kenntnisse über die Sedimente des Suigetsu Sees deutlich erweitert hat und die Revidierung einiger älterer Interpretationen nahe legt. Die verbesserte Warvenchronologie trug zu einem deutlich verbesserten Kalibrationsdatensatz bei. Dieser ist der erste aus lakustrinen Daten gewonnen Datensatz, der in den (kommenden) IntCal Datensatz eingearbeitet werden wird.

Acknowledgements

There are lots of people without whom I would not have been able to accomplish the mission "(submitting my) Phd Thesis". First of all I would like to thank my supervisor Achim Brauer for giving me the opportunity to work in the SG06 project and for finding a good balance between helping and challenging me and for lots of good advice. I owe a lot of thanks to the whole 'Suigetsu Varves 2006' working group for providing a fantastic, supportive, encouraging, challenging and friendly research environment. Special thanks goes to Mike Marshall for endless Skype discussions on how to deal with our varve count data and a generally great cooperation. Also a lot of thanks to Richard Staff for lots and lots and lots of suggestions on the grammar in my manuscripts, for helping me to understand the ^{14}C data and for happily being the target of my jokes. Special thanks also goes to Takeshi Nakagawa for enjoying long discussions on tiny details as much as I do (and sometimes a bit more ;)), a great sense of humour, a great job on organising the group and for a few free pints. I thank Christopher Bronk Ramsey and Charlotte Bryant for great expertise on chronology and statistics and helpful discussions on either. Thanks goes also to Annette Kossler and Pavel Tarasov for a productive and interesting collaboration on our 'YD-paper'.

Furthermore, a lot of thanks has to go to the people of GFZ section 5.2 (and beyond) for helping me wherever possible. Especially to Gaby Arnold and Dieter Berger for all the help producing hundreds of thin sections and having solutions for all kinds of small technical problems (if asked nicely). Also, a big thanks to Peter Dulski and Brigitte Richert for all the help producing μXRF measurements. I thank Birgit Plessen for accepting the challenge my stable isotope samples provided and Rudolf Naumann for the help with the XRF measurements on the catchment samples. Another thanks goes to Christine Gerschke who adeptly helped with everything bureaucratic. Special thanks goes to my office mates Stefan Lauterbach and Ina Neugebauer for the discussion of scientific problems, cigarette breaks and making sure that life in the office never got boring.

And of course I thank my friends outside my scientific world, who made sure that I don't forget that there is such a world. I thank my brothers for a roof and a motorcycle and my parents for virtually lifelong support.

0. Preface

0.1. Aims of the PhD project

The work presented here contributes to the 'Suigetsu Varves 2006' project (SG06) (Nakagawa et al., 2012) in which the sediment of Lake Suigetsu (Honshu Island, Japan) is analysed in order to i) establish a truly atmospheric radiocarbon (^{14}C) calibration dataset and ii) reconstruct palaeo-environmental conditions by multi-proxy analysis.

The potential to create a wholly atmospheric (i.e. not reservoir corrected) ^{14}C calibration dataset beyond the tree-ring limit based on Lake Suigetsu sediment data was first recognised and utilised by Kitagawa and van der Plicht (1998a,b, 2000), who analysed sediment cores retrieved in 1993 (SG93). They showed that the lake sediment is rich in terrestrial leaf fossils (enabling the construction of the atmospheric ^{14}C record) and that it contains annual laminations (enabling the construction of the calendar age scale). However, their data significantly diverged from alternative marine datasets. Staff et al. (2010) showed that the main reason for the inconsistency were gaps between successively drilled cores in the SG93 profile. Additionally there were problems with the varve count (van der Plicht et al., 2004). For instance, Nakagawa et al. (2003) argued, based on the SG93 varve age model, that the Late Glacial interstadial (i.e. climatic equivalent of the Bølling/Allerød biozone as defined in Europe (Mangerud et al., 1974; Jessen, 1935)) started earlier and ended later than in the North Atlantic region, leading to a duration difference of several centuries. Stalagmite data from Japan (Shen et al., 2010) (as well as the new SG06 data) revealed that the duration was overestimated, which in turn means that despite missing sediment in the SG93 profile, and hence missing varves, too many varves were counted in this section.

To overcome the problems of the SG93 project, new sediment cores were retrieved in 2006, which contain the complete Lake Suigetsu sediment sequence continuously (Nakagawa et al., 2012). For an improved varve count chronology two complementary, yet independent, counting methods were applied, utilising thin section microscopy and micro X-Ray Fluorescence/X-radiography.

The main aim within the PhD study was to create the microscopic varve count chronology. Alongside the thin section counting also a novel, automated varve interpolation program was devised. The final varve count chronology, incorporating the microscopic and the µXRF chronology, was to be constructed in cooperation with Dr. Michael Marshall from Aberystwyth University, who created the µXRF varve chronology.

Contributions were also to be made to the second aim of the project: palaeo-environmental reconstruction. Micro-facies information from thin section analysis can be used to deduce the climatic controls on sediment formation. Especially the analysis of event layers, usually the result of earthquakes or floods, can be used to improve our understanding of natural hazards risk under changing climate conditions.

0.2. Radiocarbon dating and calibration

Since the discovery of natural radiocarbon and its usability for dating (Libby, 1946; Anderson et al., 1947; Libby, 1949) the method has become the most important dating technique in palaeo-environmental and archaeological studies, which address the last ≈50 kyr (Olsson, 2009; Reimer, 2012). Radiocarbon (^{14}C) is produced in the upper atmosphere as result of neutron capture by ^{14}N, with the neutrons being set free by the interaction of cosmic rays with atomic nuclei. The produced ^{14}C is then oxidised to CO_2 and becomes part of the carbon cycle. For instance, by photosynthesis it enters the biosphere and becomes integrated into the living tissue of plants and animals. The ^{14}C content in the organisms is in equilibrium with that of the atmosphere as long as these live. When they die, ^{14}C is not taken up any longer and the remaining ^{14}C in the tissue keeps decaying with a constant half life of about 5730 yr (Godwin, 1962). By determining the ratio of the remaining ^{14}C and the stable isotope ^{12}C, the time of death can be calculated if the initial ratio is known. Similarly also inorganic carbon precipitates can be dated.

However, the method is not as straight forward in practise as many processes have an influence on the ^{14}C:^{12}C ratio. These can be divided into three major groups: i) fractionation effects ii) reservoir effects and iii) production effects. Fractionation occurs, for instance, on a cellular level (Craig, 1953; Olsson and Osadebe, 1974). Light carbon is assimilated preferentially leading to a relative depletion in ^{14}C. This effect can be corrected for by consideration of the stable isotope ^{13}C, with the relative depletion of ^{14}C being, in first order approximation, twice that of ^{13}C.

Reservoir effects play a role when comparing atmospheric ^{14}C values with those from other pools of radiocarbon, most prominently the oceans (Craig, 1957; Stuiver et al., 1976). The radiocarbon content in the oceans is controlled by exchange of CO_2 at the water-atmosphere interface and the mixing of the oceans. Deeper parts of the oceans have a considerably lower ^{14}C:^{12}C ratio, since the decay of ^{14}C outweighs the supply from the atmosphere. As a result ocean waters have much older ^{14}C ages (Fig. 0.1), with the age difference being called the 'radiocarbon reservoir age' (R). The oceans can also affect the ^{14}C content in the atmosphere as result of changes in the upwelling (Hughen et al., 1998), since an increased upwelling can lead to an release of 'old carbon' from formerly deep ocean water (Rose et al., 2010; Bryan et al., 2010).

The third major influence on ^{14}C is the variation of the production rate. On the one hand, production can be increased when the geomagnetic field of the earth weakens, as more cosmic radiation can reach the atmosphere (and vice versa). On the other hand, changes in the radiation itself have an impact. These can be the result of solar cycles or changes in the deep space radiation (Stuiver et al., 1991; McHargue et al., 1995).

So called 'conventional radiocarbon dates' assume a constant atmospheric ^{14}C:^{12}C ratio. But since variations in the ^{14}C:^{12}C ratio occurred in the past, due to the mentioned production changes or the release of old carbon, calibration is necessary to transfer ^{14}C ages to calendar ages. To construct a calibration dataset, an archive is required which provides carbon for dating and allows the implementation of an independent dating technique, which provides calendar ages against which the radiocarbon ages can be calibrated.

The best of such archives are trees. The atmospheric carbon is stored in the tissue and tree ring counting provides a reliable calendar age scale (Kaiser et al., 2012). Back to 12,550 yr BP the current international atmospheric radiocarbon calibration curve (IntCal09) is based upon tree data and is considered accurate (Reimer et al., 2009). Beyond this 'tree-ring limit' only floating tree ring chronologies are available, i.e. they lack a fixed calendar age scale. Alternative archives, which can be used beyond the tree-ring limit are marine archives (sediments, corals) (Hughen et al., 2004; Fairbanks et al., 2005), speleothems (Hoffmann et al., 2010; Southon et al., 2012) and lake sediments (Hajdas et al., 1993; Goslar et al., 1995; Schramm et al., 2000; Kitagawa and van der Plicht, 2000). All of which have weaknesses. Marine archives do not record the atmospheric

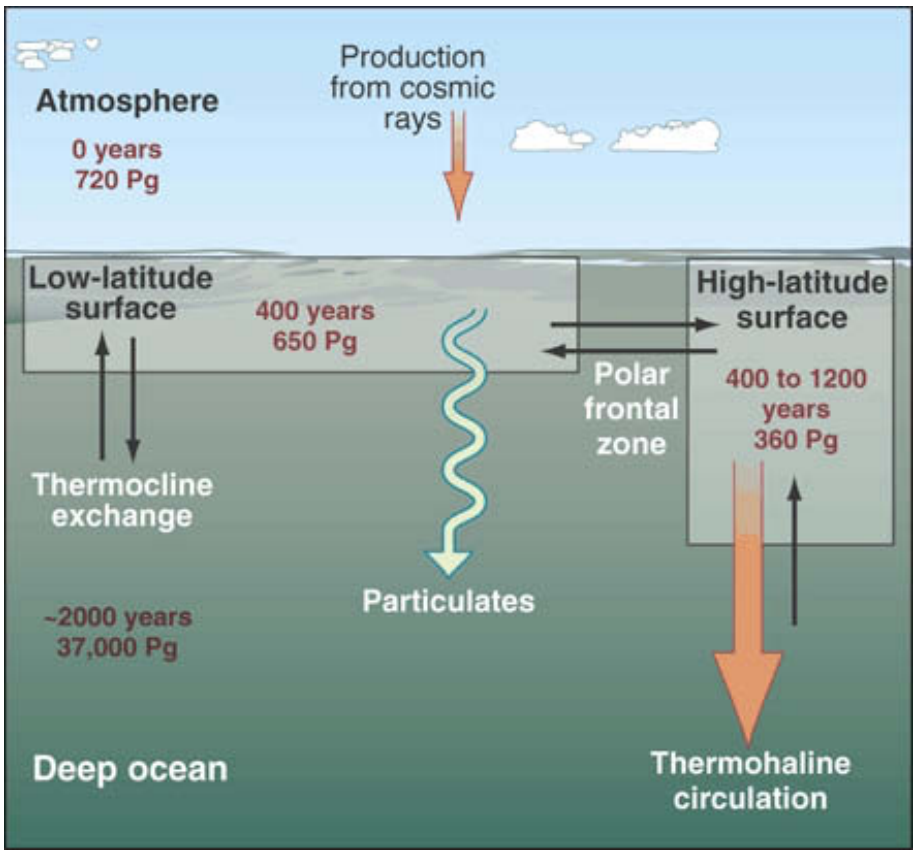

Figure 0.1.: Radiocarbon reservoir ages and amount of ^{14}C in different parts of the oceans and exchange processes (from Adkins (2001)).

radiocarbon directly and must be corrected for the reservoir effect. The calendar age scale can be derived by different means, including varve counting (for certain intervals), climate tuning (which leads to circularity when discussing leads and lags of the climate system) and U-Th dating if suitable material is available. Speleothems contain a dead carbon fraction (DCF), which derives from the surrounding limestone or from soils, and therefore require a correction of the ^{14}C values, too. The calendar age scale is derived by U-Th dating. In both cases (marine archives and speleothems) the corrections necessary for R and DCF are likely to be time dependent and therefore unknown for older samples. Lake sediments can be similarly problematic when the ^{14}C is determined from autochthonous components, due to the hardwater effect. The hardwater effect occurs when there are older sources of carbon in the lake or its catchment, mixing with the atmospheric ^{14}C signal and thus creating a reservoir age (Shotton, 1972). For instance, the Lake Lisan calibration dataset, which is based on U-Th and ^{14}C dated aragonite (Schramm et al., 2000) suffered from high frequency, temporal changes of the reservoir age (Prasad et al., 2009). Alternatively, terrestrial plant fossils in lake sediments record atmospheric ^{14}C directly, and when these sediments are varved they also provide the mean to create an independent calendar age scale. However, the attempts to create calibration datasets from varved lake sediments encountered problems with the varve chronology related to hiatuses, disturbances or incomplete varve formation (Wohlfarth, 2000; Goslar et al., 2000; Hajdas et al., 2000; van der Plicht et al., 2004). Hence, no data from lakes were included in the current atmospheric ^{14}C calibration curve IntCal09 and it relies exclusively on marine datasets beyond 12,550 yr cal BP (Reimer et al., 2009). But since marine data have weaknesses, too, improving the IntCal dataset is an ongoing effort, to which the SG06 project aims to contribute.

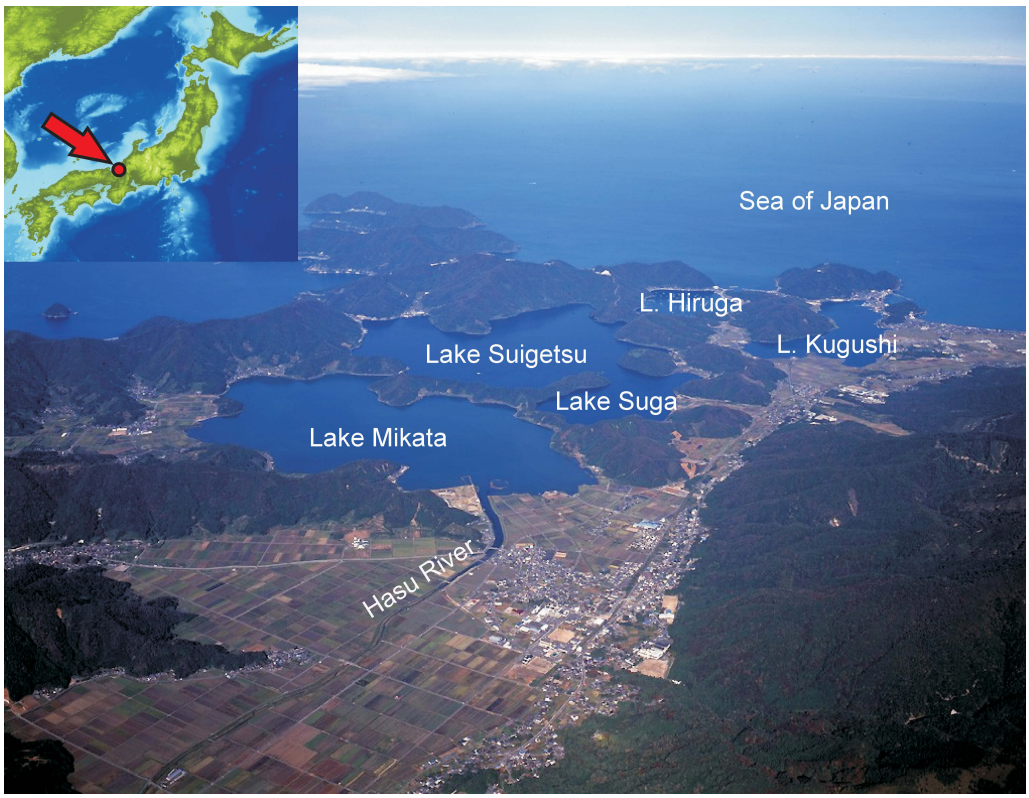

Figure 0.2.: Aerial photograph of the Mikata Five Lakes (Mikata-goko), view from SSE

0.3. Study site

Lake Suigetsu is situated in Fukui prefecture on the west coast of Honshu Island, central Japan at the Wakasa Bay (Sea of Japan). The Lake is part of the Mikata Five Lakes (Mikata-goko: Lake Suigetsu, Lake Mikata, Lake Suga, Lake Kukushi and Lake Hiruga; Fig. 0.2) and is tectonic in origin. It formed during the late Pleistocene when subsidence of crustal blocks occurred along faults of the Tsurugawa Tectonic Line and the Hanaore-Kongo Fault Line (Kawakami et al., 1996). Lake Suigetsu is approximately 2 km in diameter and has a maximum water depth of 34 m (Nakagawa et al., 2005). Originally a freshwater lake, Suigetsu became brackish when connections with Lake Kugushi (Urami River; AD 1664 (Kawakami et al., 1996)) and Lake Hiruga (Saga Tunnel; AD 1801 (Matsuyama and Saijo, 1971)) were built, as these lakes were already artificially connected to the Sea of Japan and thus allowed the inflow of salt water (Shigematsu et al., 2010). Freshwater is provided by the Hasu River via Lake Mikata. Hence, a chemocline formed in Lake Suigetsu, which separates the upper freshwater and the lower salt water body and occurs today between 3 m and 8 m water depth (Kondo et al., 2009).

The sediment column of Lake Suigetsu is about 75 m long and between 1991 and 1993 four piston cores ('SG1' (2m long), 'SG2' (11 m), 'SG3' and 'SG4' (both 16 m)) and a 75 m drilling core ('SG' (later called 'SG93')) were retrieved (Kitagawa et al., 1995). Research on these cores led to the release of various publications, which showed the high potential of the Lake Suigetsu sediment for ^{14}C calibration (Kitagawa et al., 1995; Kitagawa and van der Plicht, 1998a,b, 2000) and palaeo-environmental reconstruction (Yamada and Fukusawa, 1999; Yasuda et al., 2004; Nakagawa et al., 2003, 2005, 2006; Katsuta et al., 2006, 2007).

However, the piston cores covered only a limited section of the Suigestu sediment and ^{14}C age inversions suggest that they were stratigraphically not intact (*Nakagawa, personal communication*) and SG93, as mentioned before, suffered from missing sediment and varve count uncertainties, which led to the re-coring of the lake in the SG06 project.

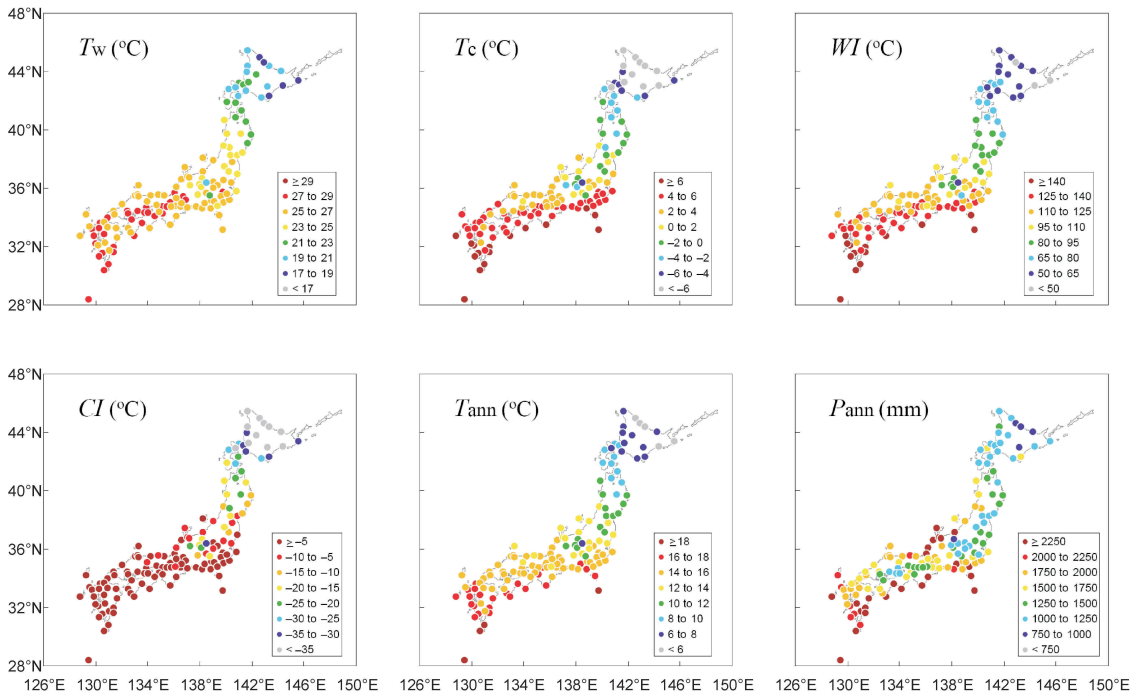

Figure 0.3.: Distribution of six climate variables averaged for the 30 years period of 1961-1990 at 147 meteorological observatories. Tw: temperature of the warmest month; Tc: temperature of the coldest month; WI: warm index (annual sum of the mean monthly temperature above 51°C); CI: cold index (annual sum of the mean monthly temperature below 51°C); Tann: mean annual temperature; Pann: annual precipitation. (from Nakagawa et al. (2002)).

0.4. The climate of Japan and flood risk

Japan is an archipelago consisting of 4 main and several 1000 small islands. The extension is on average less than 300 km in Northwest-Southeast direction but over 2,500 km in Northeast-Southwest direction. It therefore stretches over multiple climate zones, from subtropical in the South to cool temperate in the North. Mean temperatures (Fig. 0.3) range from ≈4°C (winter) to ≈29°C (summer) in the South and from < -6°C to ≈21°C in the North (Nakagawa et al., 2002). Annual precipitation is high throughout the archipelago, about 1500 to over 2250 mm/yr in the South and 750-1500 mm/yr in the North (Fig. 0.3). There are three main causes for heavy precipitation. Typhoons regularly affect Japan and can lead to severe flood damages. On average 2.8±1.4 typhoons make landfall on Japan (mean value and standard deviation 1951-2003), with the typhoon season lasting from June to October and August/September showing the highest number of landfalls (Kim et al., 2005). Many typhoons move initially into the Philippine and East China Sea and then recurve to the Northeast when they meet the mitlatitude westerlies, moving towards Korea and Japan (Kim et al., 2005).

The second cause is the Meiyu-Baiu front (the Chinese component West of 130°E is the Meiyu front, the Japanese component East of 130°E the Baiu front). The Baiu front marks the boundary between the polar air mass of the Okthosk High and the tropical air mass of the North Pacific Subtropical High (NSPH), while the Meiyu front is also strongly affected by the continental heat low. The precipitation of the Meiyu-Baiu front is maintained by the water vapour carried through the western edge of the NPSH (Yamaura and Tomita, 2011). The front develops around May and with the Pacific High gaining in strength moves northward, dissipating in August. The rainy season produced by this circulation patterns affects Japan is most pronounced in June and July.

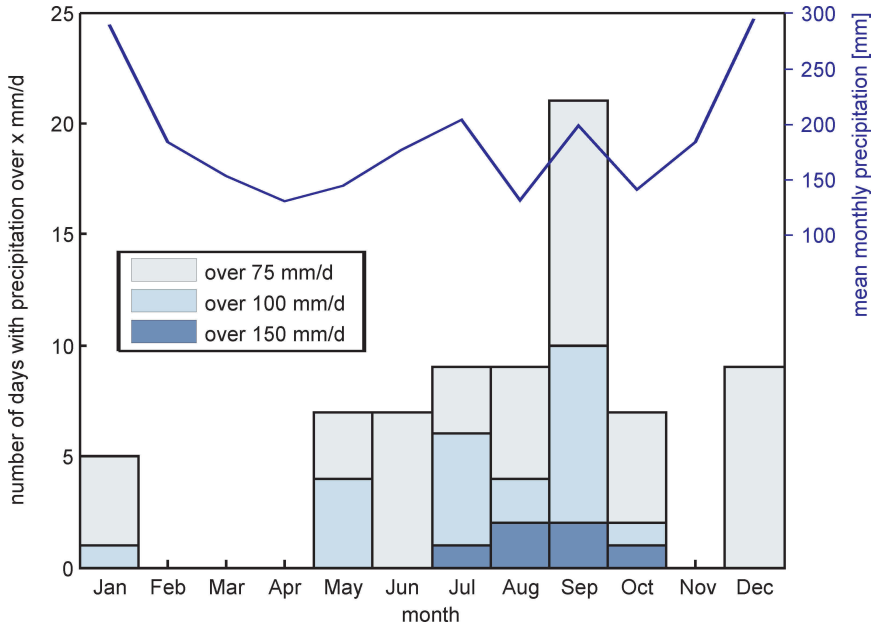

Figure 0.4.: Precipitation values from Tsuruga station (≈20 km East of Lake Suigetsu) for the period from 1/1/1960 to 12/31/2012 (24h data integrity 82%; data source: NOAA)

The third cause is the East Asian Winter Monsoon (EAWM) in combination with the warm Tsushima current in the Sea of Japan. The current is a branch of the warm Kuroshio western boundary current and enters the Sea of Japan through the Tsushima (Korea) strait. The dry and cool Northwest winds of the EAWM pick up heat and moisture from the Tsushima current influenced waters and lead to heavy snowfall along the central western coast of Japan, which subsequently can lead to severe snow melt floods.

The region of Lake Suigetsu is affected by all three phenomena. In Fig. 0.4 the mean monthly precipitation and the daily maximum precipitation are shown from the meteorological station in Tsuruga, less than 20 km to the East of Lake Suigetsu, for the time frame from AD 1960 to 2012. The mean monthly precipitation shows three clear peaks: The highest in December/January related to the winter monsoon, the second in July related to the Baiu-front and the third in September related to the typhoon season. Days with precipitation over 100 mm/d occurred mainly in May and from July to October, with a clear maximum in September. Days with over 150 mm/d occurred only between July and October. This means that high short term (24h) precipitation causing floods in the Lake Suigetsu region is mainly due to typhoons, and in second order to the Baiu front. However, floods can also be caused by continuing precipitation over several days/weeks and when considering cumulative precipitation over 300 mm over 7 days, the curve (no figure) shows that such occurred once in July and twice in September between AD 1960 and 2012, supporting the findings from the 24h data.

0.5. Materials and methods

Sediment samples were provided to each group within the SG06 project in LL-channels (Nakagawa et al., 2012). For thin section preparation one to two (depending on the core length) 1 m long channels (cross section: 1-2.25 cm^2) from each core and for each core half were available. Since most of the material was used up in thin section preparation only a very limited amount of sediment was available for other analyses. However, many standard analyses were carried out by other SG06 members such as µXRF, geochemistry (TOC, N, biomarker, $\delta^{13}C_{org}$, $\delta^{15}N$), pollen, diatoms, ^{14}C and tephra analysis.

The methods carried out by the PhD candidate are described in the individual manuscripts. Analyses which are not yet published are briefly described in chapter *VI.2.4 Unpublished Methods and Preliminary Results*. An overview of the methods is given below:

- **thin section preparation and analysis:** see chapter II and V
- **μXRF measurements on impregnated samples from thin section preparation:** see chapter VI.2.4
- **XRF measurements on field samples:** see chapter V
- **δ^{18}O and δ^{13}C measurements on siderite:** see chapter VI.2.4

Methods to which the PhD candidate contributed, without being leading researcher:

- **diatom sampling and analyses at major Late Glacial climate boundaries:** see Kossler et al. 2011
- **stable Fe isotope measurements on Fe in siderite layers:** see Maekeler (2012) and chapter VI.2.4

0.6. Thesis structure

This thesis is organized as a 'cumulative thesis' consisting of 5 manuscripts, from which 4 have been published in peer-reviewed journals and 1 is submitted. Each individual chapter (I–V) represents one manuscript, while in the last chapter (VI) the results are summarised, discussed with respects to the aims of the PhD study but also with respect to the strength and weaknesses of the methods developed here and an outlook is given. Chapters II, III and V contain the three central manuscripts, for which the PhD candidate was a leading author.

The chapters I–V correspond to the following manuscripts:

Chapter I: SG06, a fully continuous and varved sediment core from Lake Suigetsu, Japan: stratigraphy and potential for improving the radiocarbon calibration model and understanding of late Quaternary climate changes
(Nakagawa et al., 2012)
Authors: *Takeshi Nakagawa, Katsuya Gotanda, Tsuyoshi Haraguchi, Toru Danhara, Hitoshi Yonenobu, Achim Brauer, Yusuke Yokoyama, Ryuji Tada, Keiji Takemura, Richard A. Staff, Rebecca Payne, Christopher Bronk Ramsey, Charlotte Bryant, Fiona Brock,* ***Gordon Schlolaut****, Michael Marshall, Pavel Tarasov, Henry Lamb, Suigetsu 2006 Project Members*

Introduces the 'Suigetsu Varves 2006' project (SG06) and its general aims. It also addresses the core retrieval and the initial processing of the sediment (before it was supplied to the individual groups within the SG06 project).

The contribution of the PhD candidate to this manuscript was about 5%, mainly to section '5.2 Varved sediment', but also to the general discussion of the manuscript.

Chapter II: An automated method for varve interpolation and its application to the Late Glacial chronology from Lake Suigetsu, Japan (Schlolaut et al., 2012)
Authors: ***Gordon Schlolaut****, Michael H. Marshall, Achim Brauer, Takeshi Nakagawa, Henry F. Lamb, Richard A. Staff, Christopher Bronk Ramsey, Charlotte L. Bryant, Fiona Brock, Annette Kossler, Pavel E. Tarasov, Yusuke Yokoyama, Ryuji Tada, Tsuyoshi Haraguchi and Suigetsu 2006 project members*

Introduces a novel interpolation method for incompletely varved records. A detailed description of the SG06 varve structure is given and the microscopic varve count is introduced. The interpolation algorithm is applied to the microscopic varve count of the LGIT.

This manuscript was written by the PhD candidate, with the co-authors giving general advises on the structure and checking grammar and style of the manuscript. The overall contribution of the PhD candidate was about 80%. Thin section preparation, varve counting by thin section microscopy, the development of the interpolation program and its application to the microscopic varve count (including manual re-evaluation of CDF plots) were carried out by the PhD candidate. Results were mainly discussed with Michael Marshall (comparison with μXRF count, see next manuscript/chapter). Co-authors contributed the μXRF data, ^{14}C data and stratigraphic information and were involved in general discussions about the method and the manuscript.

Chapter III: A novel approach to varve counting using μXRF and X-radiography in combination with thin-section microscopy, applied to the Late Glacial chronology from Lake Suigetsu, Japan (Marshall et al., 2012)

Authors: *Michael Marshall,* ***Gordon Schlolaut****, Takeshi Nakagawa, Henry Lamb, Achim Brauer, Richard Staffe, Christopher Bronk Ramsey, Pavel Tarasovf, Katsuya Gotandag, Tsuyoshi Haraguchi, Yusuke Yokoyama, Hitoshi Yonenobu, Ryuji Tadai and Suigetsu 2006 Project Members*

Describes how varve counting was accomplished using μXRF data. It gives the technical specification of the μXRF measurements and it is shown how the μXRF count of the LGIT was combined with the microscopic varve count.

This manuscript was written by Michael Marshall and the PhD candidate, with the latter producing the majority of the text and the figures from subsection 4.3 onwards. The overall contribution of the PhD candidate to this manuscript was about 40% (about equalling that of the first author). Except for the μXRF measuring itself, the candidate was directly involved in all steps. Micro-XRF counting was carried out by Michael Marshall but intermediary results were discussed with the PhD candidate and the criteria for quality selective μXRF counting were set by Michael Marshall together with the PhD candidate. Interpolation of the count results was carried out by the PhD candidate as well as the combination of microscopic and μXRF results. Discussion of the results (controls on siderite formation, results from overlapping core sections, reasons for count differences between μXRF and microscopic count etc.) was done by the PhD candidate together with Michael Marshall.

Chapter IV: A Complete Terrestrial Radiocarbon Record for 11.2 to 52.8 kyr B.P. (Bronk Ramsey et al., 2012)

Authors: *Christopher Bronk Ramsey, Richard A. Staff, Charlotte L. Bryant, Fiona Brock, Hiroyuki Kitagawa, Johannes van der Plicht,* ***Gordon Schlolaut****, Michael H. Marshall, Achim Brauer, Henry F. Lamb, Rebecca L. Payne, Pavel E. Tarasov, Tsuyoshi Haraguchi, Katsuya Gotanda, Hitoshi Yonenobu, Yusuke Yokoyama, Ryuji Tada and Takeshi Nakagawa*

Introduces the SG06 ^{14}C record and shows how it can be used in combination with the varve based age model to contribute to the international atmospheric radiocarbon calibration curve.

The contribution of the PhD candidate to this manuscript was about 15%. As fundamental contribution the calendar age scale was provided back to 40 kyr, without which

^{14}C calibration would not have been possible. Furthermore, SG06-SG93 fitting was supported by micro-facies analysis and the candidate was also involved in the discussions of the quality of the data and the treatment of uncertainties as well as general discussions about the methodology and the manuscript.

Chapter V: A 40,000 year flood history from Lake Suigetsu, Japan (Schlolaut et al., submitted)

Authors: ***Gordon Schlolaut***, *Achim Brauer, Michael Marshall, Takeshi Nakagawa, Richard A. Staff, Christopher Bronk Ramsey, Henry F. Lamb, Charlotte L. Bryant, Rudolf Naumann, Peter Dulski, Fiona Brock, Yusuke Yokoyama, Ryuji Tada, Tsuyoshi Haraguchi and Suigetsu 2006 project members*

Describes and characterises the event layers in the SG06 core. Special focus is put on the flood history of the Lake Suigetsu area and climatic implications are discussed.

This manuscript was written by the PhD candidate, with the co-authors giving general advises on the structure and checking grammar and style of the manuscript. The overall contribution of the PhD candidate to this manuscript was about 80%. Thin sections and thin section scans were made by the PhD candidate, while core photos and μXRF data were produced by co-authors. Additional μXRF data from impregnated thin section samples were measured in cooperation with Peter Dulski and even though eventually not published here, these data were used intensively in the in the beginning of the study. Identification and characterisation of the event layers in the core photographs, in the μXRF data and in the thin sections was carried by the PhD candidate. Furthermore, interpretation of the event layers as well as discussion of the climatic implications was done by the PhD candidate with co-authors providing general remarks on the latter. Co-authors contributed stratigraphic information, ^{14}C data and converted the Lake Biwa chronology to the $SG06_{2012}$ age model. They were also involved in general discussion of the manuscript.

Publications not included in the thesis

More manuscripts with contributions from the PhD candidate were produced but are not included here. These are:

- **New ^{14}C Determinations from Lake Suigetsu, Japan: 12,000 to 0 cal BP** (Staff et al., 2011): Introduces the upper ^{14}C chronology (from the top to the tree-ring limit of IntCal09 (Reimer et al., 2009)). The PhD candidate provided preliminary sedimentation rate data from varve counting, which was used to assess parameters for the ^{14}C modeling. The contribution of the PhD candidate to this manuscript was about 5%.

- **Onset and termination of the late-glacial climate reversal in the high-resolution diatom and sedimentary records from the annually laminated SG06 core from Lake Suigetsu, Japan** (Kossler et al., 2011): Uses micro-facies information on microscopic, detrital layers and compares it to diatom and pollen data in order to identify response times of different proxies to climatic change. The contribution of the PhD candidate to this manuscript was about 30%.

- **The multiple chronological techniques applied to the Lake Suigetsu SG06 sediment core, central Japan** (Staff et al., 2013a): Gives an overview of the different dating techniques that are applied to the SG06 sediment core. The PhD candidate contributed about 10% to this manuscript, mainly to the sub-sections

'2.1 Varve counting', '2.3 Incorporation of SG93 dataset' and '3. Integration of chronological methods'.

- **Integration of the old and new Lake Suigetsu (Japan) terrestrial radiocarbon calibration datasets** (Staff et al., 2013b): Describes how the SG06 and SG93 sediment profiles were stratigraphically matched. For the intervals where thin sections from SG93 were available, microfacies data were used (by the PhD candidate) to improve the correlation. The contribution of the PhD candidate to this manuscript was about 10%.

I. Introduction: The SG06 sediment core

This chapter has been published as *SG06, a fully continuous and varved sediment core from Lake Suigetsu, Japan: stratigraphy and potential for improving the radiocarbon calibration model and understanding of late Quaternary climate changes* by *Takeshi NAKAGAWA, Katsuya GOTANDA, Tsuyoshi HARAGUCHI, Toru DANHARA, Hitoshi YONENOBU, Achim BRAUER, Yusuke YOKOYAMA, Ryuji TADA, Keiji TAKEMURA, Richard A. STAFF, Rebecca PAYNE, Christopher BRONK RAMSEY, Charlotte BRYANT, Fiona BROCK, Gordon SCHLOLAUT, Michael MARSHALL, Pavel TARASOV, Henry LAMB and Suigetsu 2006 Project Members* in *Quaternary Science Reviews, 2012, Vol 36 164-176*

Abstract

The high potential of the varved sediments of Lake Suigetsu, central Japan, to provide a purely terrestrial radiocarbon calibration model and a chronology of palaeoclimatic changes has been widely recognised for the last two decades. However, this potential has not been fully realised since the only available long sediment core from the lake ('SG93') was extracted from a single bore hole and was therefore interrupted by gaps of unknown duration between successive core sections. In the summer of 2006, a new sediment core ('SG06') was recovered from the lake. Four separate bore holes were drilled and the parallel sets of cores recovered were found to overlap completely, without gaps between segments. This new record provides the ability to test existing atmospheric radiocarbon calibration models, as well as to assess the scale of inter-regional leads and lags in palaeoclimatic changes over the last glacial-interglacial cycle. Multi-disciplinary analyses from SG06 are still ongoing, but a reliable description of the sedimentary sequence needs to be provided to the wider science community before major outputs from the project are released, thereby allowing fully-informed critical evaluation of all subsequent releases of data based on the SG06 record. In this paper, we report key litho-stratigraphic information concerning the SG06 sediment core, highlighting changes in the clarity of annual laminations (varves) with depth, and possible implications for the mechanism of the climate change. We also discuss the potential of the SG06 record to meet the fundamental goals of the INQUA-INTIMATE project.

I.0. Definitions

SG93 vyr BP: The specific age unit for the varve chronology established by Kitagawa and van der Plicht (1998a,b) from the 75 m long sediment core ('SG93') recovered from Lake Suigetsu, central Japan, in 1993. This age unit has also been shortened to "SG vyr BP" by Nakagawa et al. (2003, 2005, 2006), but is the same thing as SG93 vyr BP. Year 0 is defined as 1950 AD.

IntCal09 yr BP: The absolute age scale assigned to the IntCal09 radiocarbon calibration model (Reimer et al., 2009). It is based on continuous tree ring chronologies from the present to 12,550 cal BP, combined with data from various marine sources from 12,550 to 50,000 cal BP. Year 0 is defined as 1950 AD.

^{14}C BP: Radiocarbon age calculated by convention (Stuiver and Polach, 1977) using the 'Libby half-life' of 5,568 ± 30 years (Anderson and Libby, 1951). Year 0 is defined as 1950 AD.

cal BP: Conceptual absolute age scale defined as '1950 minus yr AD' or '1949 plus yr BC'.

SPECMAP BP: Age inferred by correlating to a marine core, the age of which has been determined by matching δ^{18}O curve to the SPECMAP model (Imbrie et al., 1984).

Note: In this paper, we do not use the 'b2k' notation (defined as before 2000 AD; Andersen et al. 2006; Svensson et al. 2006).

I.1. Introduction

Establishing leads and lags of past climate changes is one of the major focuses of today's Quaternary science. It gives almost direct information about triggers and responses to the climate change, which is crucial to the better prediction of our likely future. INQUA-INTIMATE is an international project striving to correlate ice core, marine, and terrestrial records using independent chronologies in an attempt to reveal the relative timing of Lageglacial to early Holocene (60,000 - 8,000 cal BP) abrupt climate changes between different regions and different environments (Lowe et al., 2008; Blockley et al., 2012).

Lake Suigetsu, central Japan, is one of the most suitable study sites to meet the INQUA-INTIMATE aims. The lake has been known to the Quaternary Science community for the last two decades for its annually-laminated (varved) sediment record that spans the last c. 70 kyr. Four short sediment cores ('SG1-4') were obtained from the centre of Lake Suigetsu by Yasuda and co-workers (Takemura et al., 1994; Kitagawa et al., 1995; Yasuda et al., 2004) using piston-corers in 1991 (SG1-2, less than 4 m) and 1993 (SG3-4, c. 16 m). A longer, 75 m core ('SG93', also referred to as simply "SG" in previous studies) was also obtained by the same group in 1993, and reached the base of the sediment profile (Takemura et al., 1994; Kitagawa et al., 1995). These researchers were the very first to demonstrate the occurrence of varved sediment in Japan, which triggered a series of research projects based on analysis of the SG93 core. Most notably, Kitagawa and van der Plicht (1998a,b, 2000) established a high-precision independent chronology for the core through counting of the annual layers (varves). Combining this with >300 radiocarbon determinations measured on terrestrial plant macrofossil remains (mostly comprising leaves and small twigs), these authors generated a radiocarbon age calibration model stretching back to close to the radiocarbon detection limit (c. 50 kyr cal BP). This study was an early attempt to extend the radiocarbon calibration model beyond the tree-ring limit (11,400 cal BP at that time; Kromer and Becker 1993), and even now remains the only purely terrestrial radiocarbon calibration dataset that: (i) is free from 'dead carbon fraction' correction (unavoidable with speleothem data, *e.g.* Beck et al. 2001); and (ii) extends back to the radiocarbon detection limit.

Supported by the exceptionally high precision chronology of the SG93 core, Nakagawa et al. (2003, 2005, 2006) conducted high-resolution (average analytical interval = 14.86 yrs) pollen analysis and pollen-based quantitative climate reconstruction through the deglacial interval to the early Holocene section of the core (15,701 to 10,217 SG93 vyr BP). They claimed that if the respective Lake Suigetsu, Greenland and Cariaco Basin chronologies were correct, then Lateglacial events in Japan were not synchronous with those of circum N. Atlantic regions such as Greenland (Alley et al., 1993; Björck et al., 1998) and the tropical Cariaco basin (Hughen et al., 1996, 1998, 2000).

Despite the potentially huge importance of these studies, Lake Suigetsu did not attain acceptance as a reference site for either radiocarbon calibration or the anchoring of the

Lateglacial event stratigraphy. Subsequent radiocarbon calibration datasets obtained from marine sediment (Hughen et al., 1998), corals (Fairbanks et al., 2005) and cave speleothems (Beck et al., 2001) were adopted by IntCal, although all of these datasets relied on assumptions about radiocarbon reservoir age. The ensemble of available data nevertheless strongly implied that the absolute age range assigned to the SG93 core was significantly underestimated (*e.g.* van der Plicht et al. 2004).

There are three potential explanations for the apparently "too-young" SG93 varve chronology: (i) undercounting of the number of varves in SG93; (ii) over-counting of annual bandings in all other sites; and (iii) discontinuities within the SG93 core. Unreliable correction of the carbon reservoir effects in all other sites could explain short-term (annual to millennial) differences in the structure of ^{14}C age scatter between the SG93 and other datasets. However, such an explanation would seem unlikely for the longer-term deviation between SG93 ^{14}C ages and those obtained from other sites, since there is no feasible mechanism that could allow carbon reservoir ages to become progressively greater further back in time. It is mainly for this reason that the SG93 dataset has never become formally incorporated into the IntCal calibration model (Stuiver et al., 1998; Reimer et al., 2004, 2009).

Perceived problems with the SG93 independent age scale also had serious implications for the assessment of the timing of Lateglacial events. If it is indeed unreliable, then the temporal offset proposed by Nakagawa et al. (2003, 2005) could simply be an artefact of an erroneous age model. Specifically, when an event in SG93 is claimed to post-date those of other regions (*e.g.* the Younger Dryas-equivalent cold reversal), this could affect the fact that the SG93 varve chronology tends to be younger than the age models derived for other reference sites.

Recently, Staff et al. (2010) performed a statistical re-analysis of the SG93 data, calibrating the data to the IntCal04 (Reimer et al., 2004) and Cariaco Basin Hughen et al. (2006) datasets, and concluded that the previously unquantified age gaps between successively drilled SG93 core segments constituted the more likely cause for discrepancy between the SG93 record and other radiocarbon age models. Such a finding was considered encouraging since it implied that the Lake Suigetsu sediment record offered the potential to achieve the aims set in preceding studies, providing that a fully continuous sediment core could be obtained.

In summer 2006, a research team funded by the UK Natural Environment Research Council (NERC) conducted a new sediment coring exercise at Lake Suigetsu, reaching the base of the sedimentary profile (73.19 m below the lake bottom). Cores were recovered from four parallel boreholes with fully overlapping core segments, leaving no room for chronological gaps in the entire sequence. The aim of this paper is to provide detailed litho-stratigraphic information for the new "SG06" sediment core, which will underpin all future studies of the sequence. Special emphasis is given to the potential of the SG06 core to contribute to the overall objectives of the INQUA-INTIMATE project (Blockley et al., 2012).

I.2. Site description

Lake Suigetsu (35°35′N, 135°53′E, 0 m above present sea level (a.p.s.l.)), is a tectonic lake located proximal to the Sea of Japan coast, Honshu Island, central Japan, and is situated on the western side of the active Mikata fault (Fig. I.1). The lake is 34 m deep, and covers an area of c. 4.3 km^2 with a diameter of c. 2 km in both N-S and E-W directions. Both SG93 (35°34′51″N, 135°53′7.5″E) and SG06 (35°35′0″N, 135°52′57″E) cores were recovered from the depocentre of the lake. The SG06 coring point is about 250 m offset to the north (Fig. I.1). Lake Suigetsu is naturally protected from winds by surrounding hills (max 400 m), as well as from river influx by the neighbouring Lake Mikata. The

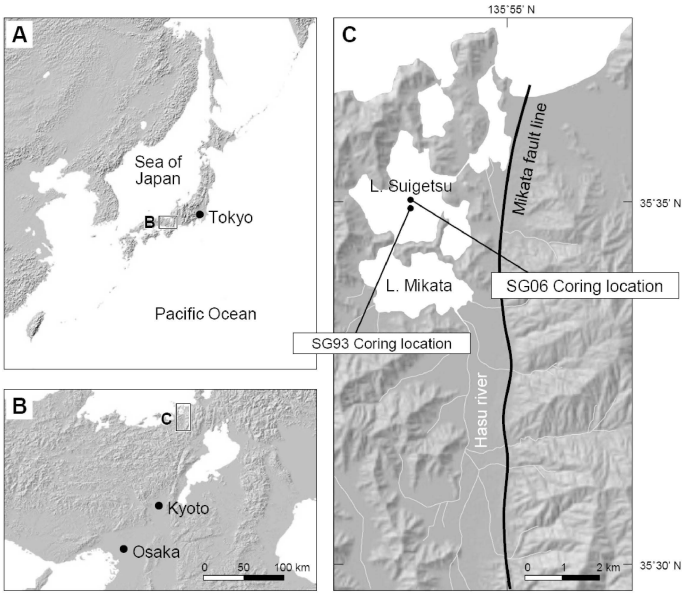

Figure I.1.: location of Lake Suigetsu (modified after Nakagawa et al. (2005))

Hasu River is the only significant water supply into Lake Suigetsu, but the hydrology of the lake system (Fig. I.1c) is such that water from the river first flows into Lake Mikata, which is connected to Lake Suigetsu only by a very shallow (max c. 4 m) and narrow (c. 45 m) channel, and therefore any high-energy hydrological events (such as floods) cannot disturb the sediments deposited at the bottom of Lake Suigetsu.

The regional climate around Lake Suigetsu is typically characterised by both summer and winter monsoons. In summer, Japan receives predominantly south-easterly winds and humidity from the Pacific Ocean, whereas in winter the dominant north-westerly winds come from Siberia (Fig. I.2). It should be noted that the winter monsoon in Japan, unlike in China, does not bring about dry conditions to the archipelago; the wind over the relatively warm surface water of the Sea of Japan picks up much moisture and eventually provides heavy winter precipitation to Japan, particularly along the western side of the country, including the Lake Suigetsu region. Present day climatic data recorded at the Tsuruga meteorological observatory (35°39'00" N, 136°03'54" E, 16 m a.p.s.l.), about 15 km ENE of Lake Suigetsu, is as in Table I.1.

Because of the strong seasonality, different types of material are deposited at the lake bottom throughout the different seasons. This original sedimentary structure, with seasonally alternating material, is well preserved in Lake Suigetsu because of the abiotic and very stable conditions at the lake bottom, and is recognised as varves when observed in the sediment core section (Marshall et al. 2012 report technical details, results, implications, precision and accuracy of varve counting using ultra-high resolution XRF and X-radiographic data; Schlolaut et al. 2012 report technical details, results, implications, precision and accuracy of varve counting using thin section microscopy).

Table I.1.: Climate indices observed at Tsuruga, the nearest meteorological observatory to Lake Suigetsu Japan Meteorological Agency (1998a,b). Values were averaged for the 30 year period from 1961 to 1990

Mean annual temperature	14.8 °C	Annual precipitation	2419 mm
Mean temperature warmest month	27.0 °C	Precipitation Apr to Sep	1081 mm
Mean temperature coldest month	3.3 °C	Precipitation Oct to Mar	1338 mm

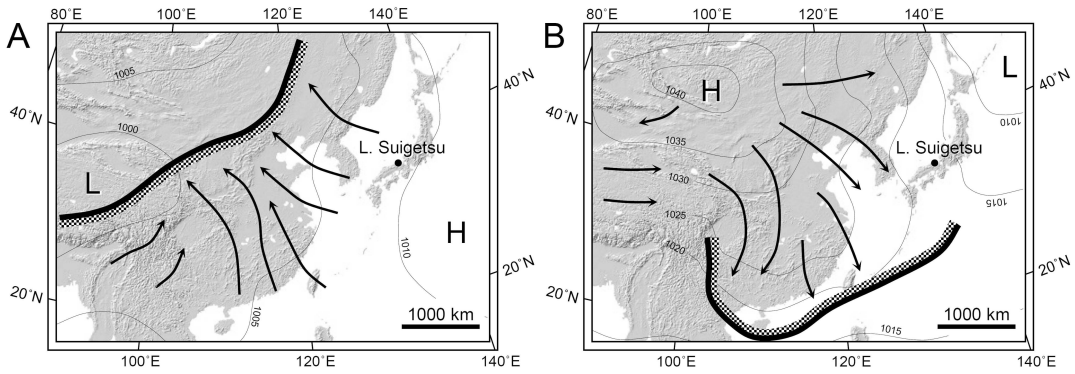

Figure I.2.: atmospheric circulation around Japan. A: summer, B: winter (modified after Porter and An (1995))

I.3. Coring, logging and storage methods

Sediment coring was conducted from 03 July to 11 August 2006 using a hydro-pressure thin-walled piston sampler installed on a floating platform (Fig. I.3). The inner diameter of the sampling tube was 7.8 cm. There was no need to use a smaller diameter corer for recovery of bottom sediments because, unlike other commonly-used percussion systems (e.g. Mingram et al., 2006), the hydro-pressure sampler does not undergo significant power loss as it penetrates into deeper horizons. Some core sections were magnetically oriented using newly developed in-situ magnetic field sensors or, more simply, a mark on the drilling rod. Sediment core sections were extracted from their sampling tubes within a few days (at the latest) of recovery from the lake. A mechanical piston was used for extraction, which inevitably meant that the top c. 5 cm of each core section was compressed and/or disturbed. No significant disturbances caused by the piston were observed beyond 5 cm from the top of each core segment. Extracted cores were immediately split into two half cylinders and a 'quasi-real scale' digital photograph was taken of the freshly exposed core section surface, before any colour changes through oxidisation could occur (observable within a minute of exposure to the air). The core images were taken under natural daylight, which was not controlled to be constant. In order to compensate for this problem: (i) a colour chart was always placed alongside the sediment in each photograph; and (ii) surface colour was instrumentally measured using a Konica Minolta CM-2002 Colorimeter at every

Figure I.3.: The drilling platform used for the Lake Suigetsu sediment coring campaign conducted in the summer of 2006.

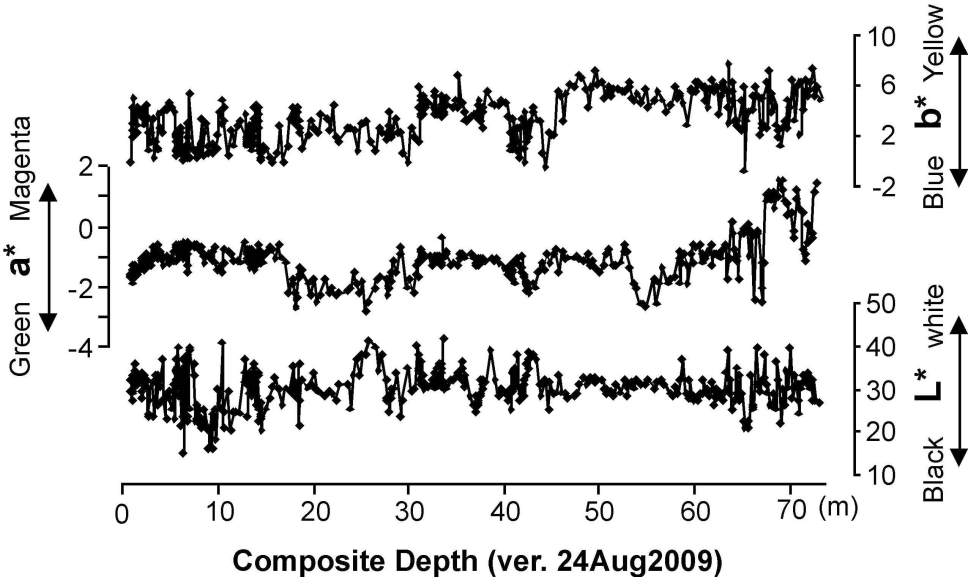

Figure I.4.: SG06 core freshly exposed sediment colour in L*a*b* system.

10 cm from the top of each core segment (Fig. I.4). Where available, layers with clearly identifiable characteristics (including tephra layers, clay layers, laminae with characteristic colouration, etc.) were chosen at c. 10-20 cm intervals and assigned numbers (Fig. I.5). The positions of these numbered laminae were defined at 1 mm precision using the scale in the digital photographs.

Sediment cores were obtained from 4 separate bore holes (A, B, C and D), all within 20 m horizontal distance from each other, with the core sections fully overlapping such that material from any given Lake Suigetsu sedimentary horizon would be represented by at least one of the individual sediment cores. This overlapping of cores was simultaneously monitored using the core section images, which was particularly necessary since the lake level was oscillating from day to day by several tens of centimetres reflecting the changeable weather of the Japanese summer monsoon season. After taking comprehensive core photographs and subsequent subsampling by 'double-L (LL) channel' (Fig. I.6 - a.k.a. 'Nakagawa channel') (Nakagawa, 2007) for later multi-proxy analysis, cores were wrapped with moist flower foam (Oasis™) (avoiding direct contact with the core material) using plastic (Saran) film to avoid desiccation. The wrapped cores were transported to cold storage (+4°C) near the lake as soon as possible. For logistical reasons, however, some core sections had to stay in ambient temperatures (between 20 and 40°C) for a few days prior to storage. Cores were finally shipped using a cold container (+4°C) to their permanent cold storage site (+4 °C) at the University of Newcastle, UK.

I.4. Stratigraphy of the SG06 core

I.4.1. General rule for coding and depth control

Core segments are coded according to bore hole (A, B, C, and D) (Fig. I.7) and numbers given to the successive core segments within each bore hole (01 at the top of the sediment profile). Bore holes A, B, C, and D yielded 46, 47, 21, and 4 core segments, respectively. Position within each segment is defined by the distance from each core segment top, which in turn is defined by the scale in the digital photographs of the core. Laminae with strong character/visibility are labelled by number starting from 01 at the top. For example, lamina A-20-05e in Fig. I.5 can also be expressed as A-20-75.1cm. Sometimes lamina labels were added later in order to facilitate more precise correlation. Such additional laminae are identified with Greek alphabet codes (α, β, etc.).

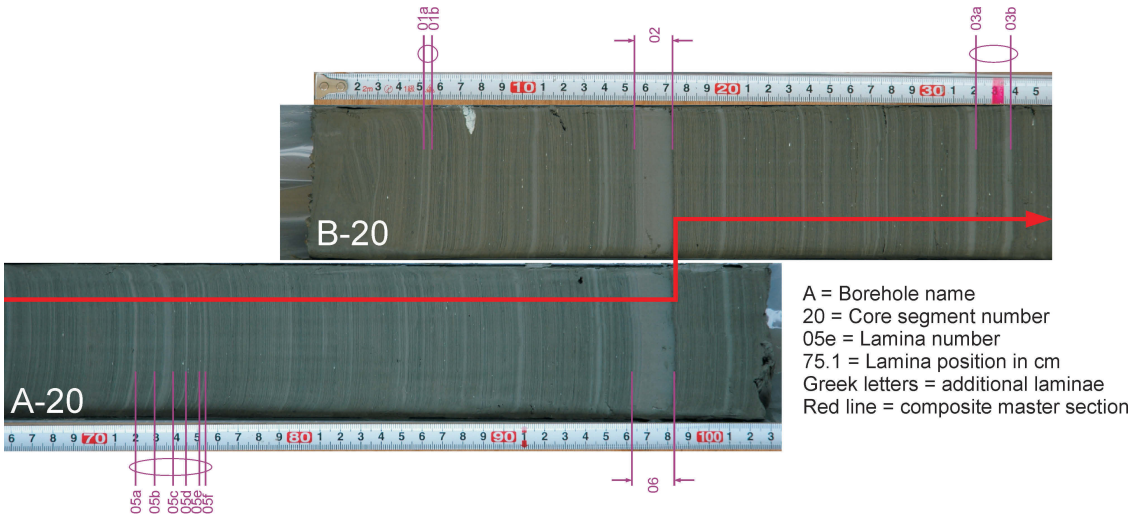

Figure I.5.: Example of the SG06 lamina numbering and correlation system. Lamination patterns are clearly duplicated in parallel cores, leaving no room for doubt in correlation. Red line denotes composite master section, which always moves from one core to the next at only one correlation point.

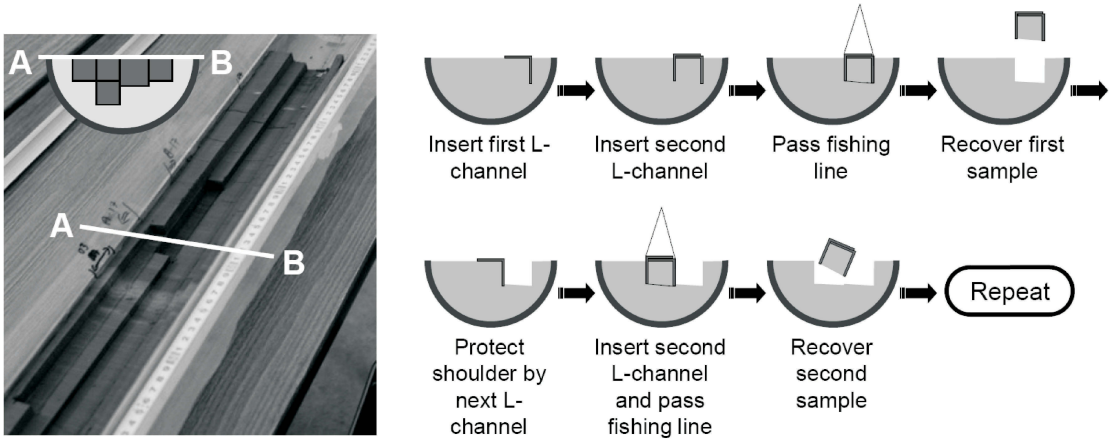

Figure I.6.: Subsampling from the SG06 core using the double-L (LL) channel extraction procedure (Nakagawa, 2007). The core is much reduced after taking several samples but remains intact and suitable for further sampling using the same technique.

Figure I.7.: Photographic record of the litho-stratigraphy of the SG06 core. Colours of core No.: red = magnetically oriented using in situ sensor; orange = Geographically oriented using marks on rods; white = no orientation. Red shades on core images = disturbed sediments.

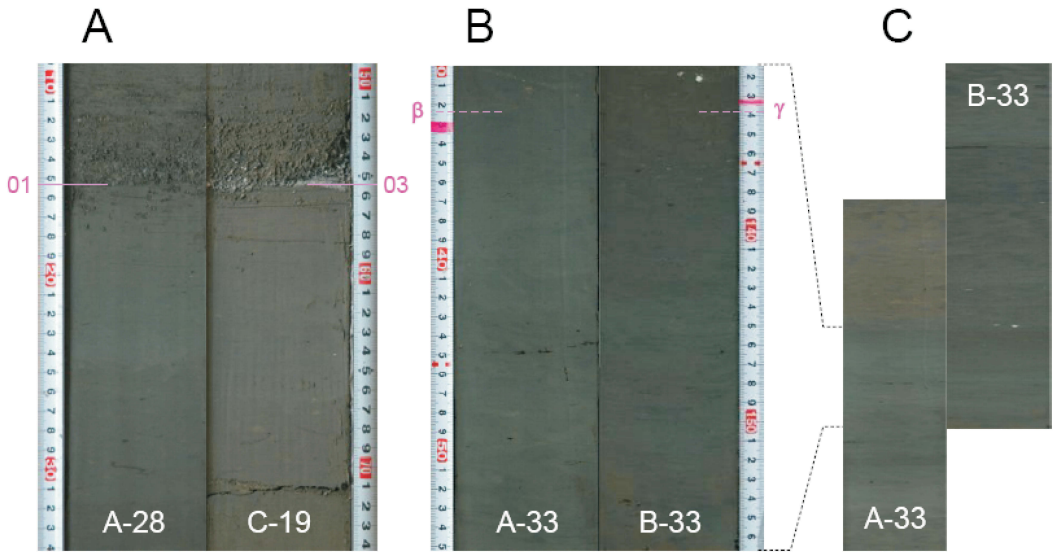

Figure I.8.: Correlation of non-laminated core segments. A: reliable correlation using tephra. B: uncertain correlation due to lack of fine sedimentary structure. C. The same segment as B in smaller scale which shows larger structure of the core that can be used for low-precision correlation.

I.4.2. Construction of the composite section

A composite master section was generated by connecting middle parts of the core segments, bound by labelled lamina both above and below (except for the first and the last sections, namely A-01 and B-47 cores, for obvious reasons). The top 5 cm of cores were avoided from the master section wherever possible, because of compression or disturbance of the core being likely, as mentioned in section I.3. The "composite depth", a depth scale assigned to the composite master section, was defined simply as the combined lengths of the segments in the master section. Segment lengths were defined by the scale in the digital core images. Composite depth of the segments that are not in the master section was determined by correlation to the master section. Fig. I.7 plots all of the core section images arranged against the composite depth scale thus generated. Correlation between neighbouring cores was principally established through visual matching of the lamination pattern, using especially those characteristic event horizons observed. Correlation points used to define composite master section are indicated by red horizontal lines in Fig. I.7. We consider that there is no correlation error for the top c. 46 m and bottom c. 10 m of the SG06 core, where sediments are rich in fine structure such as varves. The section from c. 46 m to c. 63.5 m is more problematic because the sediment does not have much obvious structure, apart from large scale (of the order 10^0 to 10^1 cm) colour changes and occasional tephra layers. Visual correlation was nevertheless undertaken for this section using small-scale core photographs (Fig. I.8), but the correlation of this part of the SG06 core potentially includes some error. All uncertain correlations are indicated in Fig. I.7 by dotted red horizontal lines connecting parallel cores. Our correlation model has had no revisions on the composite master section and only very minor adjustments for parallel sections over the 4 years since coring. However, we are always aware of the potential for our current correlation model (version: 24^{th} August 2009) to be updated once we have generated more high-resolution analytical data from the overlapping cores, since 'wiggle matching' of proxy curves might enable correlation at much higher precision than comparison of the optical images.

A note must also be made on core section A-14, which is severely disturbed and does not properly bridge between the neighbouring B-13 and B-14 core sections. However, because

the B-13 core contains the undisturbed top of the very thick AT-tephra layer (Machida and Arai, 2003; Miyairi et al., 2004) and the B-14 core contains the undisturbed bottom of the same tephra event, we consider that all missing material between the B-13 and B-14 cores is the middle part of the AT-tephra. In other words, the core is stratigraphically discontinuous here but there is no missing "period" represented by the regular deposition pattern of clay and organic material. In order to define the composite depth beyond the AT-tephra, we arbitrarily assumed a 24 cm loss of material between the B-13 and B-14 cores.

Indirect evidence that supports the robustness of our correlation model is the trend in departure of the composite depth from that of the raw drilling depth. Due to the porous and elastic nature of sediment and the high over-loaded pressure, sediment cores generally expand once they are exposed to atmospheric pressure. Because of this, as well as the fact that the composite depth of the sediment profile is defined as the combined segment length between correlation points measured by the scale in the optical core images (*i.e.* under atmospheric pressure), composite depth tends to become increasingly greater than the original drilling depth (which is defined as *in situ* distance from the lake bottom). The departure of composite depth from drilling depth in the SG06 core increases gradually and quasi-homogeneously (Fig. I.9). This strongly supports our hypothesis of there being no major correlation error throughout the entirety of the sequence. The diagram shows a plateau between 46 and 63.5 m. Because this plateau includes segments that are correlated by clear marker layers such as tephra (*e.g.* C-19 and A-28 correlated at 4962.6 cm composite depth; B-29 and A-29 correlated at 5180.5 cm composite depth) where there is no correlation uncertainties, this is more likely to indicate lower elasticity of the non-laminated sediment in this part of the sequence, rather than error in correlation.

I.4.3. Varved sediment

Because a large part of the SG06 core is finely laminated and thus has sub-millimetre scale structure, it is not realistic to make a full conventional description of the core. Instead, we produced an objective index to quantify the visibility of fine lamination (the "Lamination visibility index", LVI) and substituted this into a more conventional description (Fig. I.10A). The LVI was defined as the standard deviation of the core image greyscale for the vertically adjacent 30 pixels ($\approx$ 5.1 mm) (with greyscale values having been averaged across the horizontally neighbouring 30 pixels before calculating the index). Because the standard deviation is not correlated to the absolute level of the original greyscale value, the index has the capacity to cancel out the effect of the changing natural light levels and to extract information on the variability of sediment colouration with depth.

As can be seen in Fig. I.10D, sediments with LVI values around 1 and 2 have virtually no structure (*i.e.* impossible to establish a chronology by counting varves). Sediments with LVI values around 3 are more structured: some sections are not yet clearly varved but show a high LVI value due to the presence of material with very differing greyscale values; others are finely laminated but do not show very high LVI values because the varves consist of materials with less differing greyscale values. Varves are generally very clearly visible for the sediments with LVI values around 4 or higher (Fig. I.10D).

For the composite core section representing the time period between the IntCal09 tree-ring limit and radiocarbon detection limit (12,550-50,000 IntCal09 BP - see section I.4.5 for the preliminary chronology of the SG06 core), the LVI value typically oscillates around 4, indicating the generally well varved nature of the core for this section. However, the LVI values change over very short intervals and there are still a considerable number of fragmented sections with LVI values lower than 3 within this time period. The frequency of the 30 pixel window showing LVI values lower than 3 for this particular section was 37%, whilst the frequency of windows demonstrating a LVI value greater than 3.5 for the same section was 51%. These facts in combination imply that it is possible to establish a varve

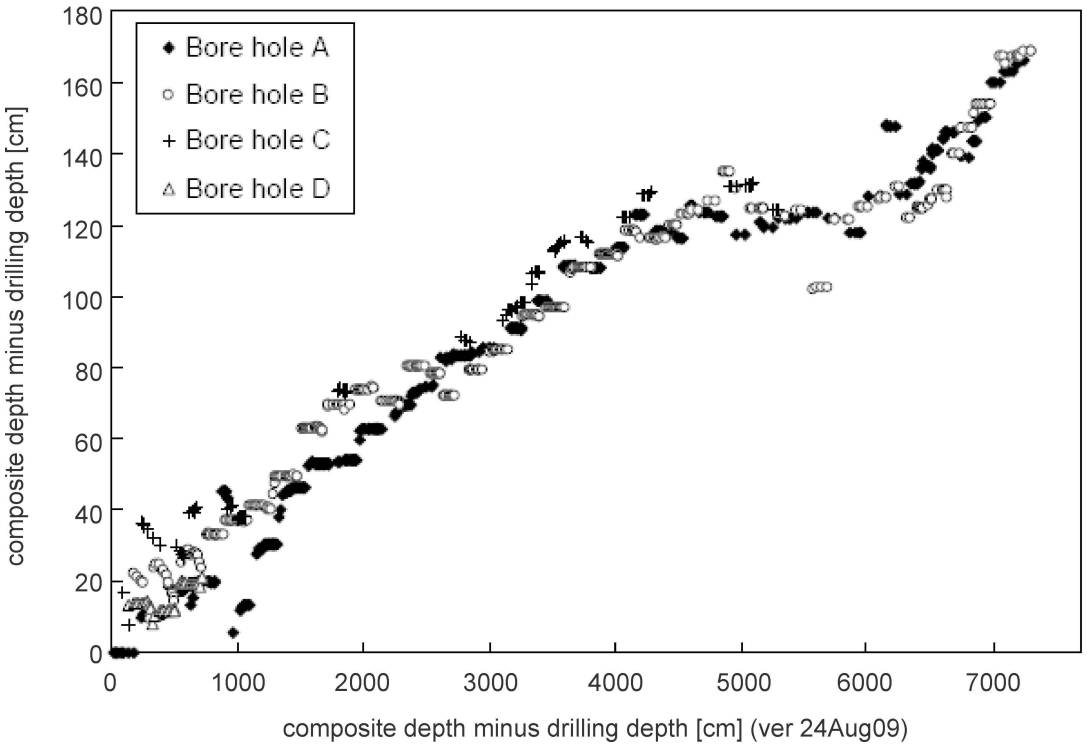

Figure I.9.: Departure of composite depth from drilling depth, calculated at all numbered laminae in the SG06 sediment core. The general trend of the scatter is very linear, supporting the overall continuity of the core. Data points do not fit perfectly on a single line because of the uncertainty in the drilling depth control (cores were recovered from a floating platform and the water depth changed almost every day reflecting the very changeable weather of the Japanese summer monsoon season). A few outliers represent secondary movement of the core within the sampling tube.

chronology for the SG06 core, but that at places this needs to be supplemented with an interpolation method to compensate for missing varves (Schlolaut et al., 2012). Combined uncertainties of counting and interpolation were estimated using the core section overlapping with the tree ring part of the IntCal09 calibration model. The sedimentation rate of this section was calculated by two independent methods: varve counting/interpolation and ^{14}C wiggle matching. Within this section the interpolated varve model lies well within the 2-sigma (95.4%) probability range of the calibrated age (Schlolaut et al., 2012; Marshall et al., 2012). However, in some deeper core sections where LVI values are reduced, the varve counting uncertainty is likely to be greater (Schlolaut et al., 2012; Marshall et al., 2012).

Oscillation of the LVI value seems to exhibit millennial scale structure. There are 19 distinct peaks in the smoothed LVI curve between the K-Ah tephra (dated at ca. 7300 cal BP, Machida and Arai (2003)) and the radiocarbon detection limit, with possibly a further 2 (or more) less distinct peaks over the same section (black and white triangles, respectively, in Fig. I.10A). The typical time interval between these peaks is roughly estimated to be in the region of 2.0 - 2.3 kyr. Whether or not these oscillations are related to the known millennial scale climate changes during the glacial period (such as Dansgaar-Oecshger (D-O) events) needs to be further investigated using other palaeoclimatic proxies. If such a relationship were to be demonstrated, however, this might imply: (i) a more fundamental causal mechanism external to the global climate system; and (ii) East Asia responded more sensitively to such a mechanism than the N. Atlantic regions, since: (a) the observed "cycle" in the LVI is persistent throughout both the glacial period and the Holocene; and (b) the amplitude of the LVI oscillation does not seem to become smaller

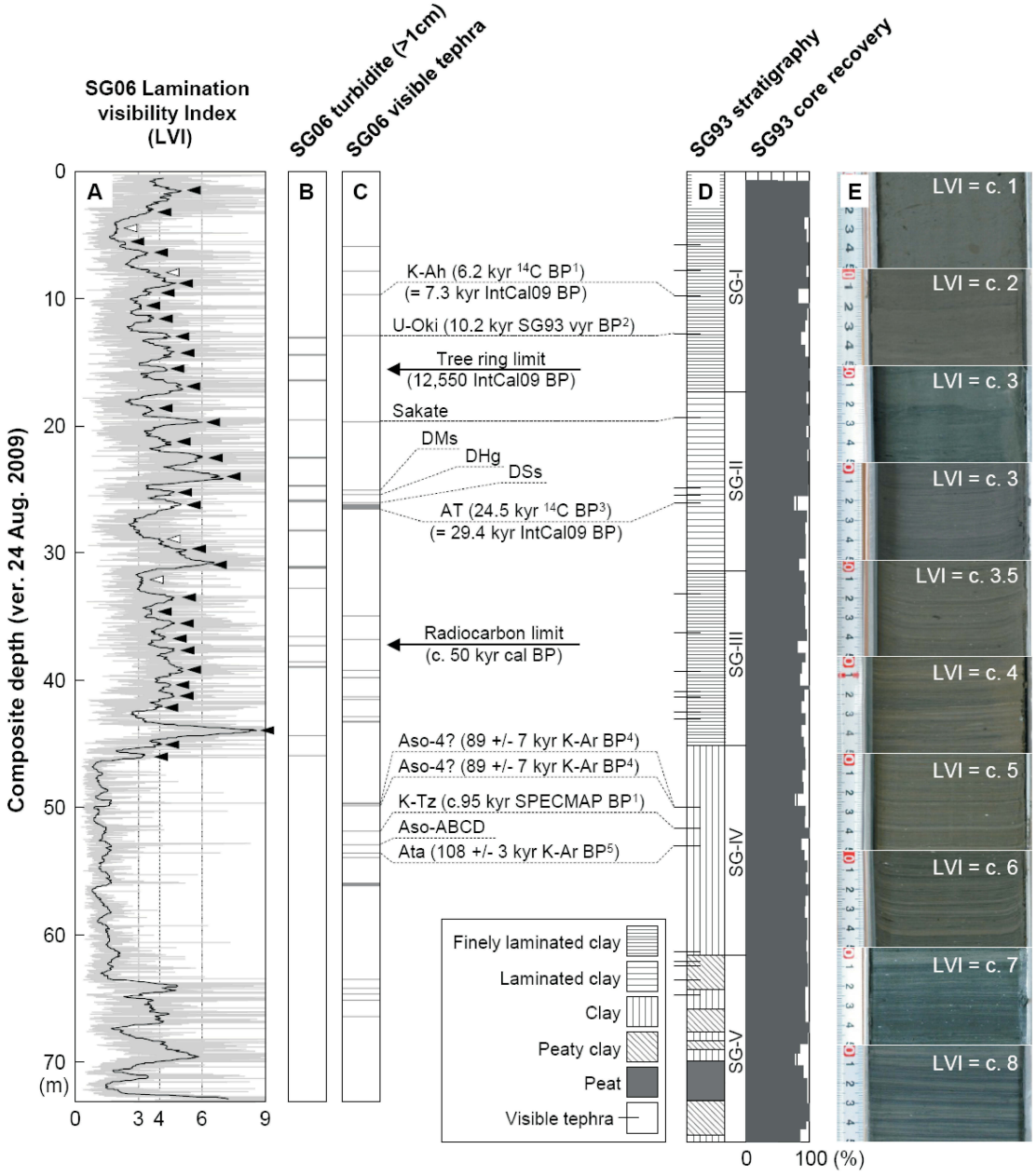

Figure I.10.: Summary of the lamination, event, and tephra stratigraphy of the SG06 core. A: lamination visibility index (LVI). Grey curve: raw data; Black curve: 50 cm moving average; Black triangles: distinct peaks in the LVI moving average; Open triangles: less distinct peaks in the LVI moving average. B: distribution of turbidites thicker than 3 cm. C: distribution of visible tephras and their identification, where known. D: SG93 core stratigraphy with visible tephra layers (Takemura et al., 1994) and core recovery rate. E: appearance of fresh core section surface classified by LVI. Reference for tephra ages: [1]Machida and Arai (2003); [2]*Kitagawa (unpublished data)*; [3]Miyairi et al. (2004); [4]Matsumoto (1996); [5]Matsumoto and Ui (1997).

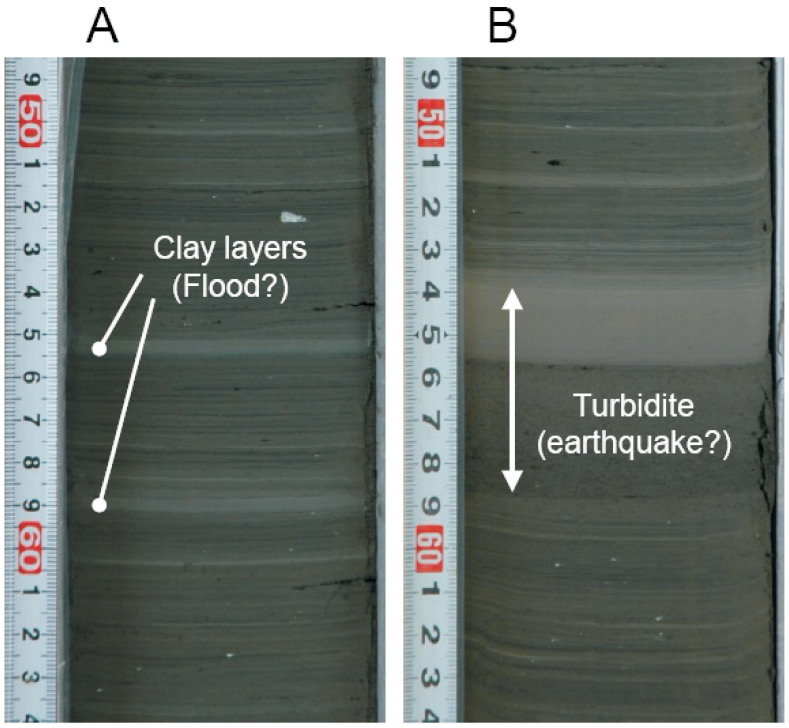

Figure I.11.: Two typical event layers that frequently appear in the SG06 core. A: clay layers. B: turbidite(?). (Distribution of the turbidite-like layers thicker than 3 cm is shown in Fig. I.10B.)

even during the period when a D-O cycle is not well pronounced (such as the period between the last glacial maximum and the onset of GI-1e (Dansgaard et al., 1993; Björck et al., 1998)).

As noted above, the sediment between 4601.4 cm and 6375.2 cm composite depth (ver. 24 Aug. 2009) is not laminated. This section corresponds to unit 'SG-IV' of the SG93 core stratigraphy which represents the period when the lake was not deep enough to maintain an abiotic bottom water environment (Takemura et al., 1994). Sediments below 6375.2 cm down to the core bottom are composed of alternations of peat, massive inorganic clay layers, and occasionally finely laminated organic clays. This is a counterpart of unit 'SG-V' in the SG93 core, which represents alternating fluvial and shallow water environments that occurred after the initial tectonic formation of the basin.

I.4.4. Event layers

The varved sediment of the SG06 core is occasionally intercalated by thick layers lacking such fine structure. These are classified into two empirical types: (i) a relatively light-coloured massive clay layer, directly overlying the regularly-deposited varved sediment (Fig. I.11A); and (ii) a very similar clay layer, but generally much thicker and accompanied by an underlying dark-coloured and slightly coarser layer (Fig. I.11B). It is hypothesised that the clay layers of the former type were formed by large flood events. These layers lack coarse material, which would normally underlie clay layers derived from flood events affecting lake sites, but this can be explained because the coarser materials carried by the Hasu River (the only significant water source into the multiple lake system) would be deposited within Lake Mikata and hence would not reach Lake Suigetsu. Only fine clay that can remain in suspension for a longer time could subsequently be deposited in Lake Suigetsu. The thicker event layers with coarser material towards the bottom and finer material towards the top are interpreted as small-scale turbidites, textiti.e. thick layers

Figure I.12.: An example of a plant macrofossil sample from the SG06 core. Even without species-level identification, this is obviously a terrestrial deciduous tree leaf, which is free from any (terrestrial, marine, and lacustrine) carbon reservoir effect.

formed by reworking of the deposits from the basin wall, which contain both fine grain-sized clay and coarser particles transported from slopes around the lake by surface runoff. The most likely cause to trigger such turbidites is earthquakes. According to the most preliminary age-depth model based on tephra ages, the turbidite layers seem to have been formed every 2.8 kyr on average (min-max: 1.2-5.3 kyr) (Fig. I.10B). This may represent the typical activity frequency of major displacement of the Mikata fault (Fig. I.1, (cf. Kawakami et al., 1996)).

I.4.5. Tephrostratigraphy and preliminary chronology

A total of 30 visible tephra layers were recognised within the entire SG06 core sequence, 11 of which are being identified using mineral composition, shard morphology, and shard refractive indices. (More robust identification by glass chemistry is being carried out; *Smith and Blockley, personal communication*) The distribution of these visible tephra layers, as well as their ages according to the existing literature, are summarised in Fig. I.10C. The age of the SG06 core bottom is yet to be determined, but is subject to further investigation. If the sediment accumulation rate is assumed to have been constant between the core bottom and the Aso-4 tephra layer (composite depth c. 4960cm), then the age of the core bottom may be as old as 200 ka. Even if the sedimentation rate below the Ata tephra (composite depth c. 5350 cm) was twice as high as the overlying section, the estimated age for the core bottom would still be around 150 ka. Low resolution fossil pollen assemblage data from the core bottom is dominated by boreal conifer trees and herbs, indicating generally cold climate (*Nakagawa, unpublished data*). Based on these facts, we provisionally conclude that the base of the SG06 core is older than marine isotope stage (MIS) 5 and that sediment deposition in Lake Suigetsu commenced during the MIS 6.

I.4.6. Plant macro remains

Lake Suigetsu is located in the mid-latitude temperate zone, and has never been covered by Quaternary ice sheets. Since the lake has always been surrounded by forest even during the Last Glacial Maximum (Gotanda et al., 2002; Gotanda and Yasuda, 2008), tree leaves, twigs, and bark have been constantly falling on to the lake surface throughout the lake's existence. Some of these eventually sink to the lake bottom and are preserved as fossils

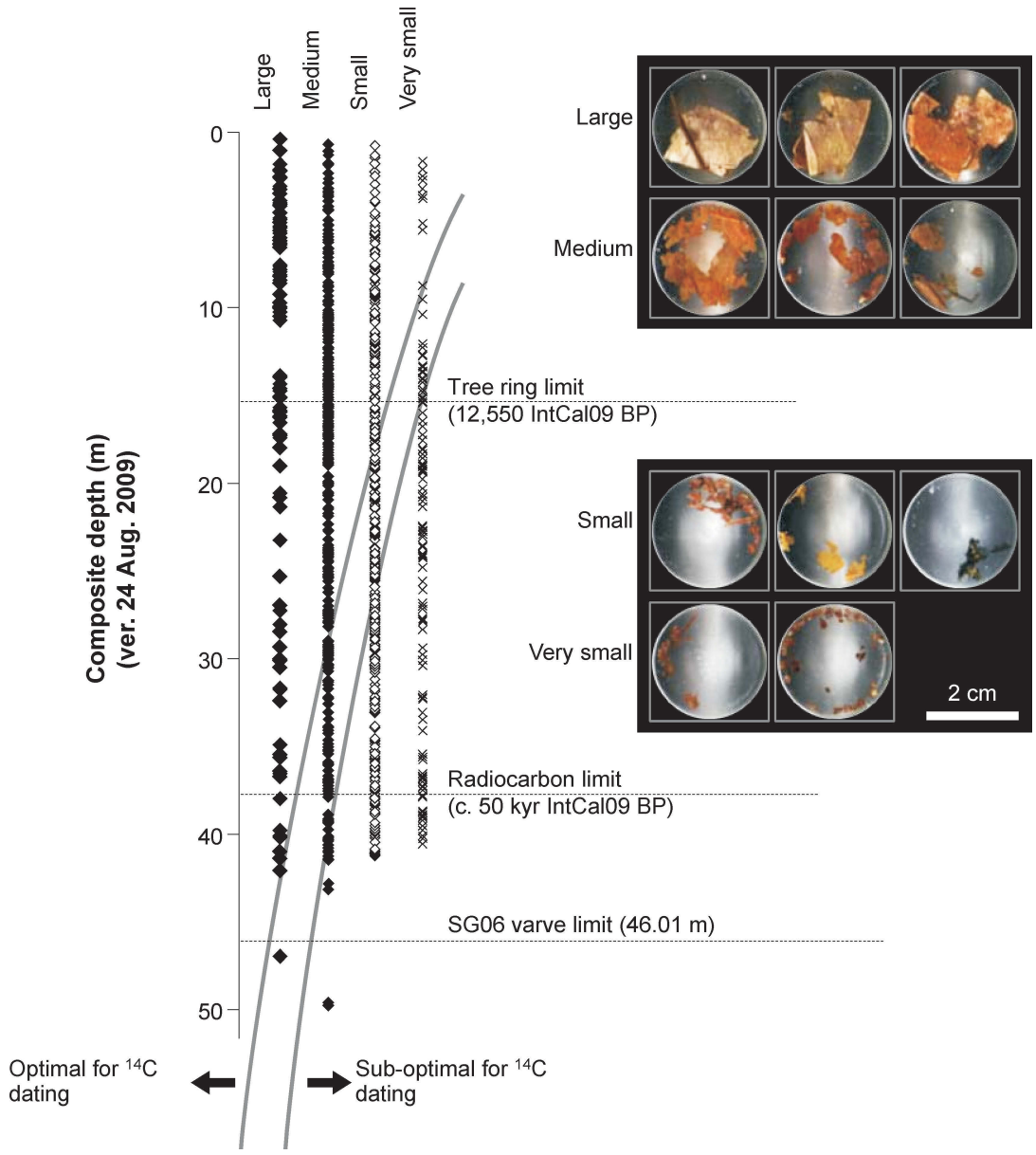

Figure I.13.: Size and distribution of terrestrial plant macro remains in the SG06 sediment core. Definition of size classes is qualitative and based on our laboratory note. A fossil leaf as in Fig. I.12 is typically described as "Large" in Fig. I.13. "Large" basically means sufficient to share between two institutions for comparison. "Very small" is suggesting not to use the sample as long as better alternatives are available (*i.e.* 0.5 mg carbon is not likely to be recovered). Images of vial bottles taken by image scanner illustrate examples of fossils in each size cluster. The grey curves on the diagram are more empirical/qualitative than analytical. The average interval between available samples is about 50 years, and at least half of the samples are large enough for ^{14}C dating by AMS to provide results with sufficient precision to be included in radiocarbon calibration datasets.

in the abiotic and reducing conditions of the varved sediment matrix (Fig. I.12). So far a total of 1176 terrestrial plant macro remains have been recovered, at least half of which are large enough for radiocarbon dating by accelerator mass spectrometry (AMS) (Fig. I.13) to provide results with sufficient precision to be included in radiocarbon calibration datasets. This is about twice the number of samples dated by Kitagawa and van der Plicht (1998a,b, 2000) from SG93 core. Terrestrial plant macrofossils are not concentrated in any specific intervals but are quasi-uniformly distributed.

I.5. Potential contributions for INTIMATE perspectives - coming attractions -

The SG06 sediment core has the potential to make a significant contribution to the overarching aims of INTIMATE (Blockley et al., 2012), covering three principal areas: (i) extension of the terrestrial radiocarbon calibration model; (ii) providing an East Asian regional template of high-resolution palaeoclimate reconstruction, coupled with a high-precision chronology; and (iii) providing intra- and inter-regional tie-points for correlation between SG06 and other study sites. The remainder of this section outlines the multidisciplinary research that is currently being conducted on the SG06 core, also highlighting the potential significance of the expected project outcomes.

I.5.1. Terrestrial radiocarbon calibration model

One of the principal objectives of the Suigetsu Varves 2006 project is to combine a large number (≈600) of terrestrial radiocarbon dates with the continuous and independent varve count chronology of the same core to generate a wholly terrestrial radiocarbon calibration model free from any of the aforementioned carbon reservoir corrections. Because of the improved continuity of the core (as compared to the SG93 study), as well as the more advanced methods of varve counting utilised by the project team (coupled thin-section microscopy and ultra-high resolution X-ray fluorescence (XRF) scanning methodologies (Schlolaut et al., 2012; Marshall et al., 2012)), the SG06 core is expected to generate a more reliable, fully terrestrial radiocarbon calibration model beyond the current IntCal tree-ring limit (12,550 IntCal09 yr BP, (Reimer et al., 2009)) and back to the radiocarbon detection limit (beyond 50 kyr cal BP). It is also hoped that through comparison of the SG93 and SG06 sedimentary structures, there might be the possibility of combining the SG93 and SG06 radiocarbon datasets, thereby significantly increasing the resolution of the final Suigetsu radiocarbon calibration dataset to c. 900 data points (c. 300 from the SG93 dataset and c. 600 from the present project). The average dating interval within the resulting calibration curve would be c. 83-56 yrs (*i.e.* either c. 600 or c. 900 data points covering the radiocarbon dating method, 0 to c. 50,000 cal BP). Unlike the current IntCal09 model, the Suigetsu-based calibration model will be entirely free from the assumed corrections for the marine reservoir effect, meaning that: (i) it will provide a more reliable template for assessing the relative inter-regional event timings; and (ii) the departure of the marine calibration model from the Suigetsu terrestrial model will give a more robust indication of variations in the magnitude of marine reservoir effects through time. The differences between the marine and terrestrial radiocarbon calibration models will in turn also provide important information about the response of the marine circulation system to major climate changes, and vice versa. The extended calibration model will also cover some key periods for understanding the origins of humankind, such as extinction of *Homo neanderthalensis* and the spreading of *Homo sapiens* from Africa to the rest of the world.

I.5.2. Climate changes

Once varve counting has been completed, the SG06 core will provide an almost ideal archive from which to derive terrestrial palaeoenvironmental reconstruction and subsequent inter-regional comparison because: (i) the organic-rich, fine-grained sediment contains a wealth of environmental indicators including pollen, diatoms, biomarkers and other organic compounds, and aeolian dust; (ii) the sediment represents information about mid-latitude terrestrial monsoon regions which cannot be represented by ice cores or marine cores; and (iii) the proxy data will be provided with an independent age scale, thus avoiding the use of climatic signals for correlation purposes, and the consequent circular logic that this frequently entails. This final point is particularly significant for meeting INTIMATE's aims, because the target time period of INTIMATE, from 60,000 to 8000 cal BP, is represented in the SG06 core by finely laminated sediments for the entirety of this period (from c. 41.5 to c. 10.4 m in composite depth - see Fig. I.10A).

Methods of climate reconstruction currently being conducted within the Lake Suigetsu 2006 varved sediment project include the following: pollen analysis and pollen-based quantitative climate reconstruction (Nakagawa et al., 2002, 2003, 2005, 2006, 2008); XRF elemental and major component analyses (Francus et al., 2009; Kido et al., 2006); thin-section microfacies analysis; diatom analysis; biomarker analysis; compound specific stable isotope analysis (Tyler et al., 2010); Aeolian dust flux and origin analyses; and microbial DNA analysis.

I.5.3. Correlation with other study sites

The INTIMATE project ultimately aims to compile all available palaeoclimate information (*i.e.* ice core, marine and terrestrial records) for the period from 60,000 to 8000 cal. BP, examining the relative timings of climatic events across different regions, and understanding the mechanical/causal links between different components of the climate system. Correlation of proxy records using an independent age scale is a logical approach towards this goal (Lowe et al., 2008). However, having a varve counting and terrestrial ^{14}C dated chronology from SG06 is not enough for this purpose for the following reasons. Firstly, varve counting has unavoidable errors that are cumulative with depth (as is the case with the counting of annual layers within ice cores - see *e.g.* Rasmussen et al. (2008)). This makes it extremely difficult to precisely correlate time scales independently generated by annual layer counting at more than one site. Secondly, the purely terrestrial radiocarbon chronology of Lake Suigetsu does not allow direct correlation between the SG06 core and marine/ice cores since: (i) marine cores are subject to an unknown marine reservoir effect; and (ii) ice cores do not contain sufficient atmospheric carbon for radiocarbon dating. In order to overcome these problems, we need to explore methods of more direct correlation.

Tephra seems to be the best tool to correlate SG06 with marine cores from regions near to Japan. There are already 14 visible tephras representing the period covered by the INQUA-INTIMATE project. Additionally, many more microtephra layers can be expected from the same interval. If we can successfully correlate SG06 with Pacific or Sea of Japan sediment cores, then that would immediately mean that we would be able to assign terrestrial radiocarbon ages to the oxygen marine isotope stages (Pacific) and D-O events (Sea of Japan - Tada et al. 1999), respectively.

Correlation between SG06 and ice cores is more problematic. One possibility is to use the D-O event record in the Sea of Japan sediments as a 'stepping stone' and correlate them with δ^{18}O records from Greenland. This, however, would immediately exclude the possibility of assessing the lead or lag relationship of millennial scale climate changes between Greenland and Monsoon Asia, which is contrary to INTIMATE's protocol and targets. Greenland and Antarctic ice cores have been successfully correlated using atmospheric methane content and ^{10}Be flux (Blunier et al., 1998; Blunier and Brook, 2001;

EPICA community members, 2005). The former is not possible for SG06 simply because lacustrine cores do not contain trapped air bubbles. ^{10}Be might be a possibility as lake sediments do contain ^{10}Be particles. However, its interpretation is not straightforward because in lakes, unlike in ice sheets, ^{10}Be flux represents a mixed signal of cosmic ray intensity and catchment dynamics. Lake Suigetsu and Greenland are too distant from each other for most (if not all) of the tephra layers to reach both sites. Finally, we expect that Δ^{14}C in Lake Suigetsu can be correlated to ^{10}Be flux reflected in polar ice cores, as both are considered to be direct indicator of variations in cosmic ray intensity. This is supposedly independent of the climate system, and would therefore allow the possibility to determine leads and lags between the SG06 terrestrial climate proxies and the Greenland and Antarctic δ^{18}O, D and other isotopic and chemical records, without involving climate as a correlation tool.

Acknowledgements

The SG06 core was recovered as a major part of the project funded by the United Kingdom Natural Environment Research Council (NERC) (grant NE/D000289/1). Preliminary analyses of the core were also supported by two other NERC projects (grants SM/1219.0407/001 and NE/F003048/1), as well as a Germany DFG project (grant TA-540/3-1 to P. Tarasov) and a Japanese KAKENHI project (grant 211001002 to H. Yonenobu). Coring was conducted by a team of Seibushisui Co. Ltd. Japan led by Mr. A. Kitamura. The whole coring campaign was fully supported by Wakasa town, the mayor of which in 2006 was Mr. C. Senda. The authors thank Mr. T. Tanabe and Mr. H. Kojima of Wakasa Johmon Museum for their invaluable support for logistics. The authors also thank Hayase Fishermen's Union for having allowed us to use a precious space of their cold storage. Our special thanks go to Prof. Y. Yasuda and Prof. H. Kitagawa, who opened this area of science in Japan and have always given invaluable support and encouragement to our project. The authors thank Dr. K. Aoki for providing latest information about Japanese tephra ages, and Prof. J. Lowe and an anonymous reviewer of the paper for their constructive suggestions.

II. Dating the SG06 sediment core: Varve counting by thin-section microscopy and varve interpolation

This chapter has been published as *An automated method for varve interpolation and its application to the Late Glacial chronology from Lake Suigetsu, Japan* by *Gordon SCHLOLAUT, Michael H. MARSHALL, Achim BRAUER, Takeshi NAKAGAWA, Henry F. LAMB, Richard A. STAFF, Christopher BRONK RAMSEY, Charlotte L. BRYANT, Fiona BROCK, Annette KOSSLER, Pavel E. TARASOV, Yusuke YOKOYAMA, Ryuji TADA, Tsuyoshi HARAGUCHI and Suigetsu 2006 Project Members* in *Quaternary Geochronology, 2012, Vol 13 52-69*

Abstract

The Lake Suigetsu sediment has been recognised for its potential to create a wholly terrestrial (i.e. non-reservoir-corrected) ^{14}C calibration dataset, as it exhibits annual laminations (varves) for much of its depth and is rich in terrestrial leaf fossils, providing a record of atmospheric radiocarbon. Microscopic analysis revealed that the varve record is curtailed due to the incomplete formation or preservation of annual laminae, necessitating interpolation. The program for varve interpolation presented here analyses the seasonal layer distribution and automatically derives a sedimentation rate estimate, which is the basis for interpolation, and applies it to complement the original varve count. As the interpolation is automated it largely avoids subjectivity, which manual interpolation approaches often suffer from. Application to the Late Glacial chronology from Lake Suigetsu demonstrates the implementation and the limits of the method. To evaluate the reliability of the technique, the interpolation result is compared with the ^{14}C chronology from Lake Suigetsu, calibrated with the tree-ring derived section of the IntCal09 calibration curve. The comparison shows that the accuracy of the interpolation result is well within the 68.2% probability range of the calibrated ^{14}C dates and that it is therefore suitable for calibration beyond the present tree-ring limit.

II.1. Introduction

Varved (annually laminated) sediments are palaeo-environmental archives that at the same time allow the construction of high precision age models, potentially down to a seasonal resolution (Brauer et al., 1999). However, a common problem is the occurrence of incompletely varved sections. Changes in the depositional environment may interrupt varve formation or result in partially indistinct records (Zolitschka et al., 2000), which therefore require interpolation. Commonly, interpolation is carried out manually, using sedimentation rate estimates from neighbouring, well varved sections. The main error source of this conventional interpolation approach is that sedimentation rates in compromised intervals (i.e. intervals with an incompletely developed varve record) and well varved intervals can be different. Also, the conventional interpolation cannot be applied to sediment profiles

that do not show well varved intervals. The new approach presented here is based on an automated analysis of frequency distributions of seasonal layers from the compromised interval itself and therefore avoids this main problem associated with conventional varve interpolation. Moreover, since the interpolation method is computer based and automated it enables the reliable reproduction of a result, which is difficult to achieve when the interpolation is carried out manually. This novel approach is applied to the Lake Suigetsu sediment from the Last Glacial-Interglacial Transition (LGIT, Table II.1), which is an example of such an incompletely developed varve record.

The Suigetsu varves were first analysed by Kitagawa and van der Plicht (1998a,b, 2000), using a sediment core recovered in 1993 (SG93). They showed that, besides being annually laminated for much of its depth, the sediment also provides one of the most comprehensive atmospheric radiocarbon records, as it is rich in terrestrial leaf fossils. This makes it suitable for extending the atmospheric radiocarbon calibration model beyond the present IntCal tree-ring limit (12.55 ka cal BP (Reimer et al., 2009)) to >50 ka cal BP. However, the SG93 data significantly diverged from alternative, marine-based calibration datasets, due to gaps in the sediment profile and varve counting uncertainties (van der Plicht et al., 2004; Staff et al., 2010).

The Suigetsu Varves 2006 project aims to overcome the reported problems of the SG93 project. A new and continuous master profile was constructed (SG06), based on parallel cores from four bore holes, recovered in 2006 (Nakagawa et al., 2012). The varve interpolation program was devised to aid in the construction of an improved calendar age scale for the terrestrial SG06 radiocarbon calibration model. Therefore no information based on the ^{14}C chronology can be used to complement the varve count as the varve chronology must be completely independent.

While this study focuses on the establishment of the new varve interpolation program and the results from microscopic varve counting, a second paper (Marshall et al., 2012, see next chapter) introduces an additional, novel and independent varve counting method utilising μXRF and X-radiography. The comparison of the results from the two methods, their individual strengths and weaknesses and the combination into the final Suigetsu varve chronology are given in Marshall et al. (2012). Hence, the LGIT varve chronology presented here, based on microscopic counting only, does not represent the final SG06 varve chronology.

II.1.1. Study site

Lake Suigetsu is situated in Fukui prefecture on the west coast of Honshu Island, central Japan. It is part of a tectonic lake system (Mikata Five Lakes) with the active Mikata fault running N-S less than 2 km to the east (Fig. II.1). The lake is approximately 2 km in diameter and has a maximum water depth of 34 m (Nakagawa et al., 2005).

In AD 1664 a canal was built connecting Lake Suigetsu with Lake Kugushi (itself already connected to the sea), which resulted in the inflow of salt water into the previously fresh water lake and the subsequent formation of a chemocline between 3 and 8 m water depth, which now separates the lower salt water body and the upper fresh water layer (Masuzawa and Kitano, 1982; Kondo et al., 2009). Due to this artificial change in the hydrology, the majority of the Lake Suigetsu sediment formed under limnological conditions that are only partially comparable to those of the present.

The fresh water, that comprises the upper water body, flows into Lake Suigetsu from Lake Mikata through a shallow sill connecting the two lakes. Lake Mikata is fed by the Hasu river, which constitutes the only major fresh water source to the lake system. In this setting Lake Mikata acts as a natural filter for coarse detrital material from the Hasu river catchment. Therefore the sediment of Lake Suigetsu consists predominantly of autochthonous and authigenic material.

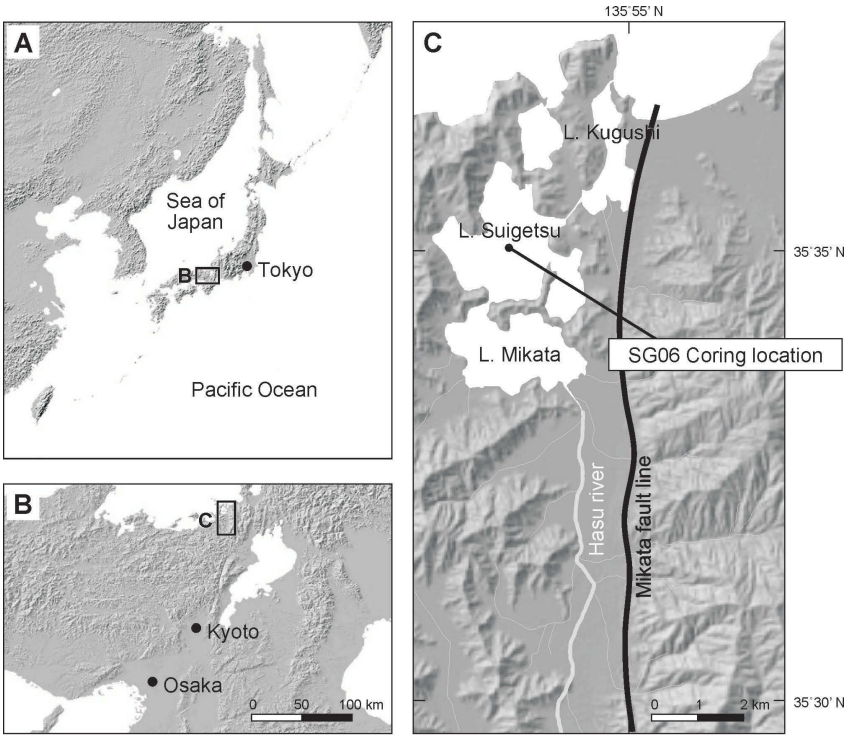

Figure II.1.: location of Lake Suigetsu (after Nakagawa et al. (2012))

II.2. Materials and methods

II.2.1. Varve description and counting

Sediment analysis and varve counting were carried out by thin section microscopy. For thin section preparation the LL-channel sediment sections (Nakagawa et al., 2012) were cut into 10 cm long segments and freeze dried. Afterwards the samples were impregnated with synthetic resin under vacuum. The blocks produced were glued to glass slides with the same resin and then ground and polished down to ≈20 µm (Brauer and Casanova, 2001). A petrographic microscope with magnification from 25× to 400× was used for counting.

An idealised varve with the main seasonal layers is depicted in Fig. II.2a. At the base a spring related layer of *Aulacoseira subarctica* and *Aulacoseira ambigua* diatoms occurs, which may also contain some siderite. Following above is a detrital layer, which is dominated by silt-sized quartz and feldspar and contains only few clay minerals. The detrital layers are deposited mainly in spring, but can also form later in the year. In summer a layer of light amorphous organic material (LAO-layer) follows. Above, a layer of *Encyonema* diatoms occurs, either below or within the base of a following siderite layer. Both varve sub-layers, *Encyonema* and siderite, are related to autumn. Above a clay layer follows, which can partially overlap with the siderite layer and forms in autumn to winter. A full description of how the individual varve sub-layers were assigned to the different seasons is given below.

The layers of *Aulacoseira* spp. are often difficult to distinguish as the overall abundance of these diatoms is high. Since *A. subarctica* and *A. ambigua* cover a wide range of environmental conditions in which they prosper (see Kossler et al. (2011) and references therein) it is difficult to place *Aulacoseira* spp. into a specific season of formation, which is also reflected in the fact that they can occur as a secondary component within every other seasonal layer, except LAO layers, which are either devoid of *Aulacoseira* spp. or in which

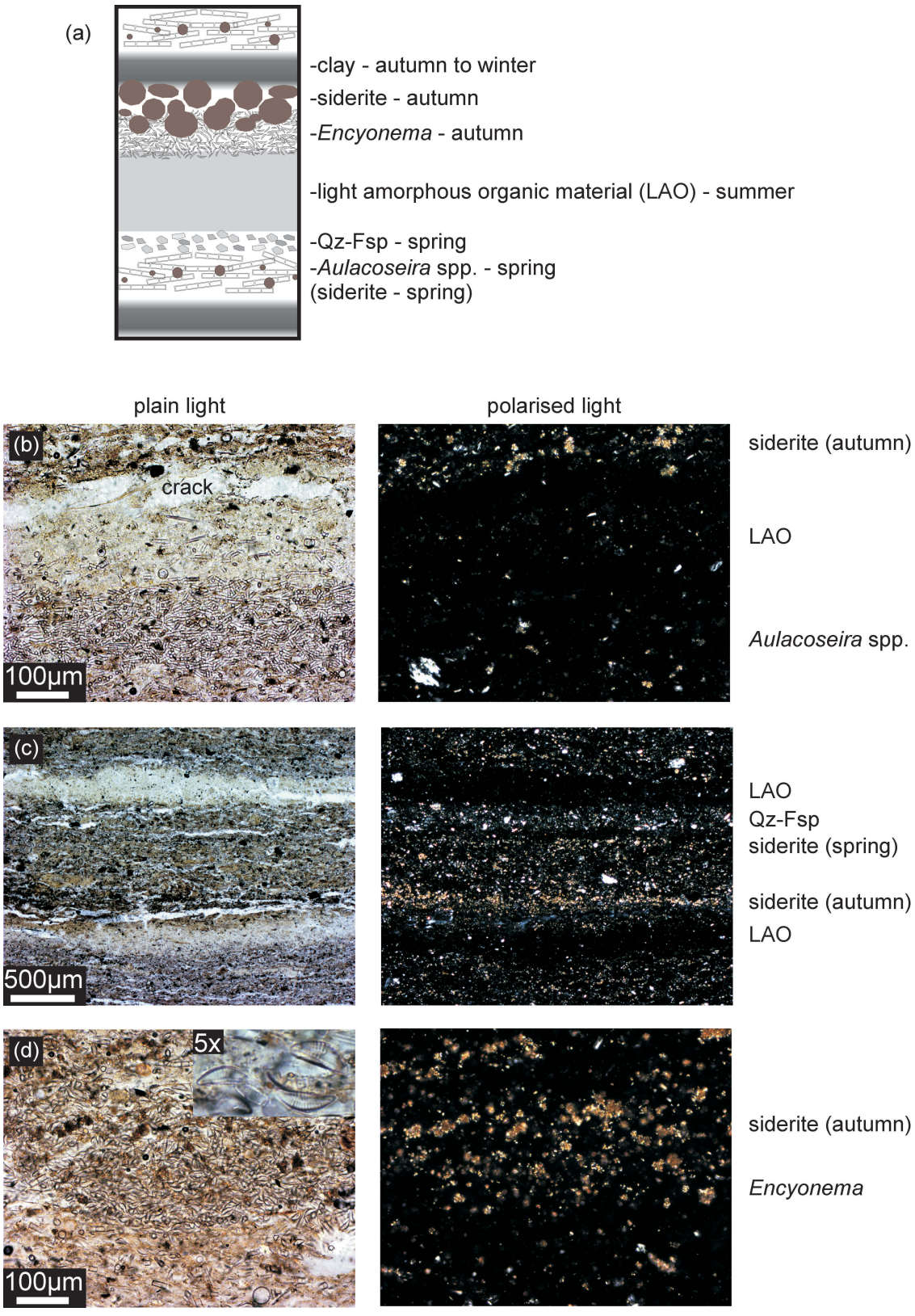

Figure II.2.: (a) schematic, idealised varve structure with main sub-layers - finding more than three of the seven types of seasonal layers together is rare and often only siderite layers, separated by mixed layers, occur; (b)-(d) microscope photos of selected examples for seasonal layers paragenesis

the proportion of *Aulacoseira* spp. is greatly reduced. But as heavily silicified diatoms, they require turbulence to be kept in suspension (Rioual et al., 2007; Gibson et al., 2003). This suggests that distinguishable, occasionally even pure, *Aulacoseira* spp. layers formed predominantly during/after lake overturn, which (if we assume a pre-anthropogenic dimictic lake system) would imply formation in spring and/or autumn, though the relative position to other sub-layers suggests spring over autumn.

Another varve sub-layer that is mostly related to spring consists primarily of silt-sized quartz and feldspar. The majority of these appear below LAO-layers (or siderite layers if LAO-layers are absent). This indicates that they reflect detrital input related to snow melt in spring. Coming from the surrounding mountain slopes the material is not "filtered" by Lake Mikata, as is the material coming from the Hasu river catchment, but is washed into the lake directly. However, wind-blown dust could also produce these layers, as well as strong precipitation events during the rainy season, and therefore such layers may also form in summer.

The absence of *Aulacoseira* spp. in LAO layers suggests formation of these in times of strong stratification with little or no turbulence (which the diatoms require to be kept in suspension), i.e. during summer.

Above the LAO-layers, siderite layers occur. At the base of the siderite laminae *Encyonema* layers occur repeatedly within the LGIT stadial. As *Encyonema* is a littoral, epiphytic diatom, its occurrence in the profundal zone (from where the sediment core was taken) is the result of reworking due to enhanced water turbulence (Kossler et al., 2011), which in turn is likely to be the result of either strong storms, the peak season for which is in August/September (Japan Meteorological Society, http://www.jma.go.jp/) and/or lake overturn in autumn, considering that *Encyonema* occurs above the summer related LAO layers. Hence, the formation of siderite layers occurred predominantly during or shortly after lake overturn in autumn. However, a minor fraction of siderite layers also occurs below LAO layers or within *Aulacoseira* spp. layers, and are therefore likely to have formed as a result of spring overturn.

The observation that siderite layers are related to lake overturn is supported by Bahrig (1988), whose suggested model for annual siderite formation requires mixing of the water body. In this model the water body below the thermocline is depleted in oxygen during stratification and thus becomes enriched in dissolved Fe^{3+} ions. During lake overturn this water body mixes with oxygen-rich surface water, leading to the formation of Fe_2O_3, which sinks to the lake bottom. There anoxic, reducing conditions form after re-established stratification and the iron is brought back into solution as Fe^{2+}, which reacts with CO_3^{2-} forming $FeCO_3$ (siderite). The CO_3^{2-} is likely to be a product of organic decomposition.

Layers rich in clay minerals may occur at, sometimes in, the top of siderite laminae and were hence deposited in late autumn to winter. Since this is unlikely to represent the season of maximum clay inwash, which would rather be expected in the summer rainy season, the clay deposition is assumed to be governed by hydrological changes within the lake. During summer the thermocline can act as a sediment trap, keeping inwashed clay in suspension (Sturm and Matter, 1978). With lake mixing the clay reaches the deeper parts of the lake and is deposited in quiescent conditions after overturn or under ice cover in winter (Lamourex, 2000). Above the clay/siderite layers, the *Aulacoseira* spp. layers occur again.

Usually not all of the sub-layers formed every year and in a considerable proportion of years no seasonal layers formed at all, in which case non-seasonal, mixed layers formed. The mixed layers are dominated by *Aulacoseira* spp. and organic material, but also contain diffuse siderite and detrital material. Presumably, these formed when stratification of the lake did not form or was weak and no seasonal lake overturning occurred. Without this the deposition of the different sediment components was not seasonally separated and the homogenous mixed layers formed. The thickness of mixed layers ranges from a

sub-millimetre scale up to 12 cm and they therefore represent time windows of 1 year to over 120 years (the mean sedimentation rate in the LGIT is less than 1 mm/a).

Siderite layers are the most frequently and consistently occurring type of seasonal layer and often delimit the mixed layers. Hence, counting is mainly based on (the base of) siderite layers. In the absence of distinguishable siderite layers, alternative seasonal layers were used where present, e.g. the top of LAO layers or the base of *Encyonema* or clay layers.

A potential error source for counting is the occurrence of spring related siderite layers that are bounded by mixed layers, as these can be mistaken as autumn related layers. However, since well varved intervals indicate that the spring related layers represent only a minor fraction of the siderite layers, the effect on the interpolation is considered to be minor.

term	**definition**
bs	bin size
pv	peak value
$\kappa(p)$	mode variance window
μ	mean of Gaussian distribution
σ	standard deviation of Gaussian distribution
BP	before present (AD 1950 = 0)
cd	composite depth (version 24Aug2009 (Nakagawa et al., 2012))
CDF	count distances frequency (plot / distribution)
efd	event-free depth (thickness of macroscopic, instantaneous deposits is set 0)
LAO	light amorphous organic (material)
LGIT	last glacial-interglacial transition
LQS	section quality selective (count)
SQS	layer quality selective (count)
SR	sedimentation rate [mm/a]
sr	mean annual sediment accumulation [mm] (equals the SR in value)
section	an arbitrary core interval
sub-section	a core interval defined by the interpolation program which is interpolated with a mean SR estimate derived from count distances within the sub-section; the core is divided into multiple, overlapping sub-sections
well varved section	a core interval defined by the user, depending on the quality and continuity of the seasonal laminations
LGIT	the period between the end of the last Glacial and the Holocene onset; synonymous with the terms Late Glacial and Last Termination
LGIT stadial	climatic equivalent of the Younger Dryas (YD) biozone as defined in Europe (Mangerud et al., 1974; Jessen, 1935)
LGIT interstadial	climatic equivalent of the Bølling/Allerød (B/A) biozone as defined in Europe (Mangerud et al., 1974; Jessen, 1935)

Table II.1.: overview variables, abbreviations and terminology

II.2.2. Interpolation

Since mixed layers occur frequently in the Suigetsu sediment, and since these represent time intervals of multiple years without any distinguishable seasonal layers, the microscopic count of the LGIT is necessarily incomplete. That is, the number of counted layers is smaller than the number of years that passed during the formation of the studied part of the core. Therefore the count must be complemented by varve interpolation.

The main prerequisite for interpolation is the knowledge of the mean sedimentation rate (SR) which is the mean sediment accumulation in millimetre per year within a predefined sediment interval. When the thickness of a mixed layer is a multiple of the mean SR it can be assumed that the time that passed during the formation of the layer is its thickness divided by the mean SR (Fig. II.3a). Explicitly, the factor by which the mean SR needs to be multiplied has the unit year [a].

It is common to use the mean SR from a neighbouring, well varved core section for interpolation (e.g. Hughen et al., 2004). However, the well varved section might represent a different micro-lithofacies than the compromised interval, which makes the assumption that the mean SR in the two parts of the core is the same questionable. Moreover, varve interpolation is usually carried out manually, which can lead to inaccuracies due to subjective interpretation. An exemplary problem is, that the thickness of the mixed layers is usually not an integer multiple of the mean SR, and individual differences in the rounding, resulting from interpretation of the sediment, can lead to considerable cumulative differences. Such subjective differences, either in the estimation of the mean SR or in the interpolation itself, also impede the reproduction of an accurate result.

The approach presented here is computer based and therefore largely avoids subjectivity. It also derives the mean SR estimate from a compromised interval itself. As such it avoids some of the major problems associated with manual varve interpolation.

To derive the mean SR estimate the program analyses the distances between successive counts from a compromised interval (Fig. II.3a). For this the interval is divided into overlapping sub-sections. Within each sub-section a constant mean SR is assumed, i.e. over the sub-section the SR has a linear trend and the trend has a gradient of approximately zero. For each sub-section the distance between the individual counts is analysed in a count distance frequency (CDF) plot. Figure II.3c shows what a CDF plot of a complete count (i.e. when the sediment is perfectly varved) may look like. Since all counts are one year apart, the mean of all count distances yields the mean SR. Figure II.3d shows the CDF plot of an incomplete count, which is derived from the data in Fig. II.3c by removing counts with a random function. Similarly to the complete count a mean of the distance values must be calculated to gain an estimate of the mean SR from the incomplete count. For this, a "mode variance window" (κ) is defined around the mode (Fig II.3g), which includes all values that are within

$$\kappa(p) = [0...mode * (1 + p)] \tag{II.1}$$

$$p = const. \quad 0 \leq p \leq 1 \quad p \in \mathbb{R}$$

Values for p larger than one would include a high number of values derived from distances between counts that are two years apart and hence from double the annual sediment accumulation.

The mean of all count distances within the window yields the estimate of the mean annual sediment accumulation (in mm) and directly translates into the mean SR estimate (in mm/a). However, there are three variables, which need to be determined beforehand: i) the bin size (bs), which controls the resolution of the plot; ii) the peak value (pv) threshold, with the pv being the value of the mode bin and the pv threshold controlling the length of the sub-sections and iii) the size of the mode variance window ($\kappa(p)$). All of these variables depend ultimately on the SR and for the mode variance window size

also on the percentage of distinguishable, counted seasonal layers relative to the number of years that actually passed during the formation of the sediment interval.

The effect of the *bs* and its dependence on the mean SR is illustrated in Fig. II.3g-j. Figures II.3g-i show data from largely overlapping sub-sections and hence with a similar, if not the same, mean SR, with a small (0.01 mm, Fig. II.3h), intermediate (0.1 mm, Fig. II.3g) and large (0.5 mm, Fig. II.3i) *bs*. The small *bs* produces a very noisy plot, which makes the mode determination unreliable. The large *bs* on the other hand produces a plot with a very low resolution and the mode determination is hence not very accurate. The intermediate *bs* offers a compromise between the two, with a low noise level and a good accuracy. However, it should not be concluded that *bs*=0.1 mm is generally a suitable value. Figure II.3j shows data with an approximately five fold increased mean SR using the same *bs*=0.5 mm as in Fig. II.3i (the data used in Fig. II.3j are artificial, as such high mean SRs do not occur in the Suigetsu sediment). It can be seen that the large *bs* produces a well defined plot for the larger mean SR. This illustrates that for large mean SRs, large *bs* need to be used and vice versa. Based on such observations we empirically concluded that a *bs* that is about a tenth of the mean annual sediment accumulation is a suitable value, i.e. a value that produces CDF plots with acceptable noise levels and a sufficiently high resolution. Since the mean annual sediment accumulation [mm] has the same value as the mean SR [mm/a], we will abbreviate it with sr, hence *bs*=sr/10.

The second variable, the peakvalue (*pv*) threshold, controls the length of the sub-sections. Sub-sections start every ten counts and each sub-section is extended stepwise 1 cm until a predefined *pv* is reached (or exceeded) in the CDF plot. This is illustrated in Fig. II.3e-f. The *pv* threshold is set at 15. The first plot (Fig. II.3e) is from a 1 cm long sub-section and only reaches a *pv* of 2, producing an inconclusive plot. Inconclusive means here that the mode is not well defined and its position is unreliable as the low number of counts is not representative. In Fig. II.3f the sub-section has been extended to 10 cm and the frequency distribution has a better defined shape. In Fig. II.3g the set *pv* threshold is reached/exceeded at a sub-section length of 22 cm and the frequency plot is well defined with a clearly distinguishable mode (around which the mode variance window is defined). The value of the *pv* threshold needs to fulfil two requirements: (i) the sub-section must contain a sufficient number of counts (i.e. must be long enough) so that a well defined, conclusive frequency distribution is produced and (ii) it should be as low as possible (producing short sub-sections) since we assume a constant mean SR within sub-sections and shorter sub-sections are more likely to meet that assumption. Furthermore, the sub-section length is also dependent on the *bs*. The wider the *bs*, the more counts are grouped into the mode bin and hence the *pv* threshold is reached more quickly, resulting

---

Figure II.3. ***(facing page)*:** (a) schematic sediment section with incomplete seasonal layer formation/preservation, grey arrows show distances between counts from which the Count Distance Frequency (CDF) plots are derived; in detail is shown how a count distance that is a multiple of the mean SR is interpolated by checking how often the mean SR fits in between the two counts; the last step shows the interpolated sediment section; (b) artificial varve thickness frequency distribution from which varve thickness values are drawn to build the artificial count dataset; (c) CDF distribution of artificial count; (d) CDF distribution of artificial, incomplete count; (e)-(g) development of CDF distribution when the length of a sub-section is increased until the peak value (*pv*) threshold is reached, (g) also shows the mode variance window (grey coloured, in the background); (h) CDF distribution with a small bin size (*bs*) relative to the SR value; (i) CDF distribution with a large *bs* relative to the SR value, dark grey and light grey bins show the effect of different sub-section lengths; (j) artificial CDF distribution with the same *bs* value as (i) but using a dataset with a relatively large mean SR

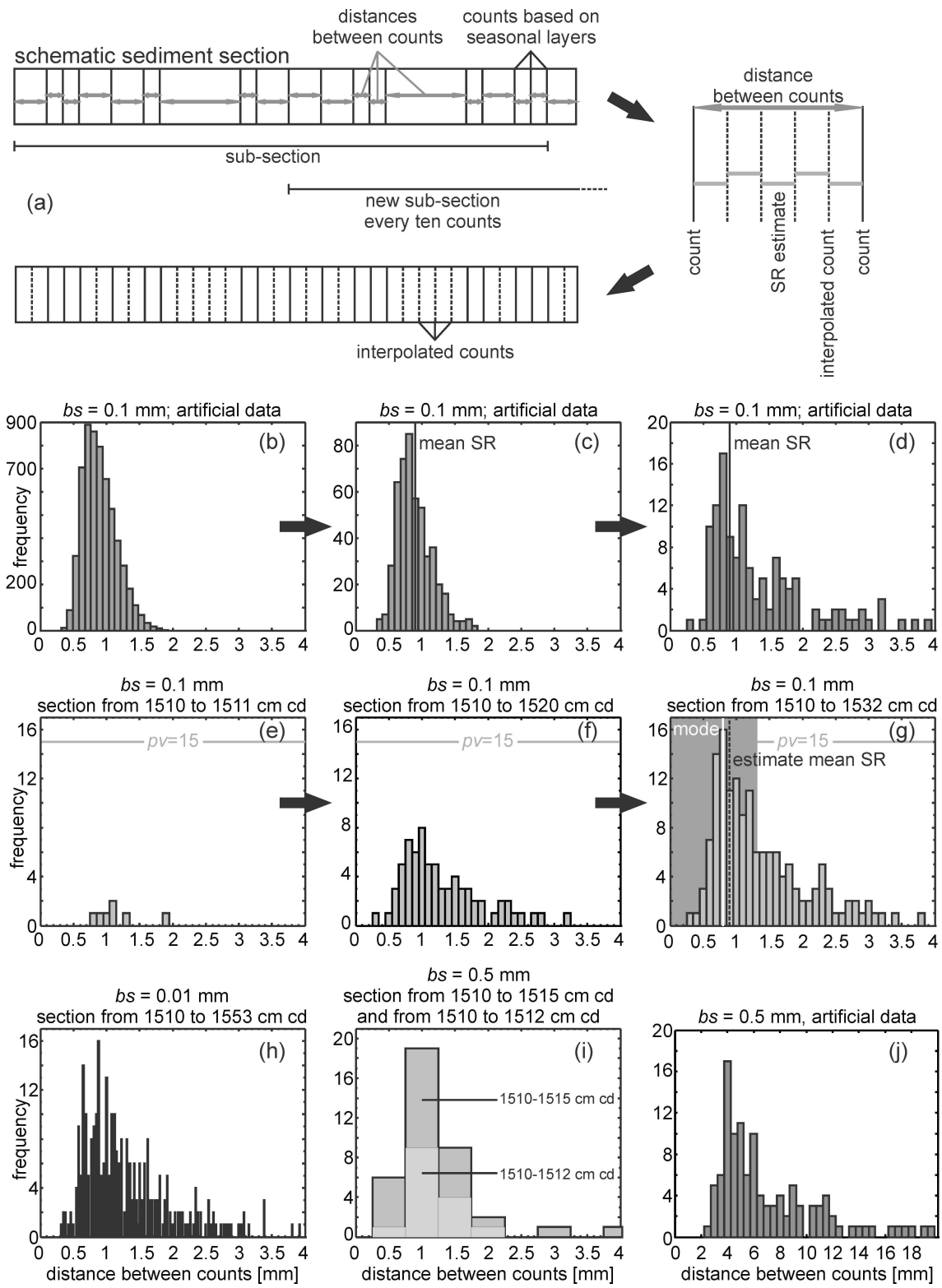
distances between counts
counts based on seasonal layers
schematic sediment section
sub-section
(a)
new sub-section every ten counts
interpolated counts
distance between counts
count
SR estimate
interpolated count
count
bs = 0.1 mm; artificial data
(b)
frequency
bs = 0.1 mm; artificial data
mean SR
(c)
bs = 0.1 mm; artificial data
mean SR
(d)
bs = 0.1 mm
section from 1510 to 1511 cm cd
pv=15
(e)
frequency
bs = 0.1 mm
section from 1510 to 1520 cm cd
pv=15
(f)
bs = 0.1 mm
section from 1510 to 1532 cm cd
mode
pv=15
estimate mean SR
(g)
bs = 0.01 mm
section from 1510 to 1553 cm cd
(h)
frequency
distance between counts [mm]
bs = 0.5 mm
section from 1510 to 1515 cm cd
and from 1510 to 1512 cm cd
(i)
1510-1515 cm cd
1510-1512 cm cd
distance between counts [mm]
bs = 0.5 mm, artificial data
(j)
distance between counts [mm]

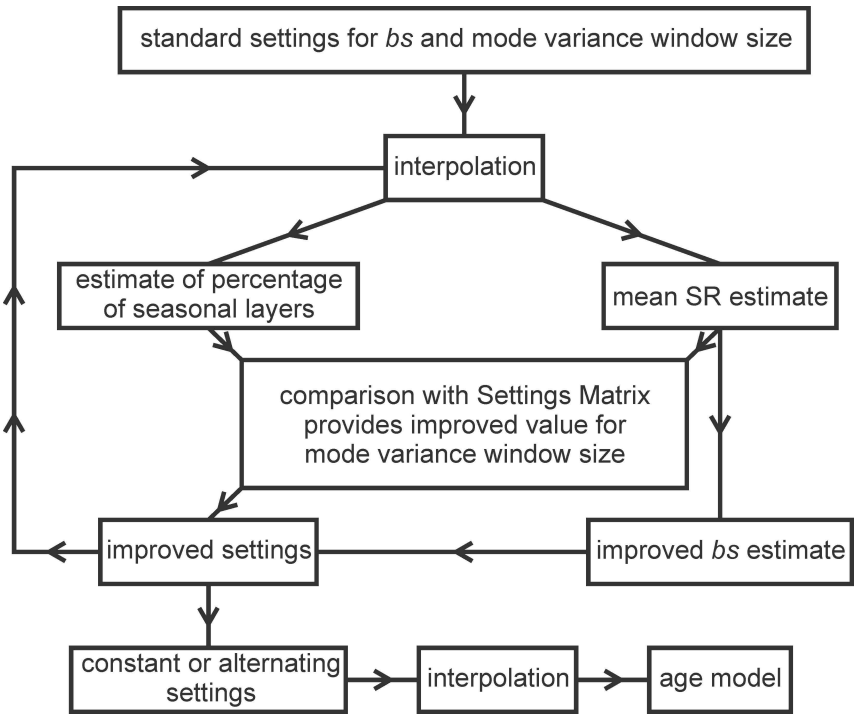

Figure II.4.: work flow of the varve interpolation program

in shorter sub-sections. This relationship is reflected in Fig. II.3g-i, all of which use data from the same part of the core and have the same *pv* threshold but different *bs*. While the sub-section with the smallest *bs*=0.01 mm produces a sub-section of 43 cm length, the intermediate *bs*=0.1 mm produces a sub-section of 22 cm length and the large *bs*=0.5 mm only produces a 5 cm long sub-section.

Ultimately the *pv* threshold depends upon the *bs*, as larger *bs* values allow the use of a smaller *pv* threshold, which is illustrated in Fig II.3i. The frequency distribution from the long sub-section (*pv*=18) is just as conclusive as the distribution from the short sub-section (*pv*=9). For *bs*=sr/10 we empirically derived a value of *pv*=15 to produce statistically conclusive plots. It is note-worthy that a constant *pv* threshold will automatically result in longer sub-sections when only few distinguishable seasonal layers occur and vice versa.

The last variable, the mode variance window size, is more complex to determine, as there is no obvious linear dependence on any of the other variables. To gain an estimate of the mode variance window size, an artificial varve count dataset is created (Fig. II.3c), from which a certain percentage of counts is randomly removed (Fig. II.3d). This incomplete, artificial dataset is then interpolated with different values for the mode variance window size and the interpolation results are compared to the complete artificial age model. Through this comparison the mode variance window size that produces the closest fit with the original, complete count can be determined. This procedure is carried out for different mean SR values and a range of different percentages of removed counts. This way the optimal mode variance window size for any situation is determined.

The circular problem, that the mean SR and the percentage of distinguishable, counted seasonal layers are variables in the mean SR determination process is solved by a recursive iteration (Fig. II.4). A first interpolation is run with standard settings for the *bs* and the mode variance window size. This interpolation yields an estimate of the mean SR and the percentage of distinguishable, counted seasonal layers, from which improved values for the *bs*=sr/10 and the mode variance window size can be derived. Interpolation with the improved settings provides an improved estimate of the mean SR and the percentage of distinguishable seasonal layers, which yield further improved values for the *bs*=sr/10 and

the mode variance window size. This loop continues until constant values for the mean SR and the percentage of distinguishable, counted seasonal layers are reached.

In the following sections the generation of the artificial data, their application to the real count, the error estimation and the requirements for interpolation are explained in more detail.

Generation of artificial varve count data and the Settings Matrix

The creation of an artificial varve count dataset is carried out in two main steps. First, a dataset is created which contains a large number (on the order of 10^3-10^4) of varve thickness values. The varve thickness values follow a frequency distribution as exemplified in Fig. II.3b. The second step is to randomly select a number of varve thickness values from this dataset, which are used to create the actual artificial varve count. The number of values that is selected determines the length of the artificial varve count dataset in years. After that step some white noise is added to the varve thickness values in the artificial varve count. The varve thickness frequency distribution of the resulting artificial varve count is shown in Fig. II.3c. The effect of this two step approach becomes clear when comparing Fig. II.3b and II.3c: The varve thickness frequency distribution of the artificial varve count is noisier and its shape less perfectly defined and therefore more realistic.
The dataset for the first step is built from two Gaussian distributions:

$$f_l = f(\sigma_l) \quad f_r = f(\sigma_r) \tag{II.2}$$

with

$$f(x, \mu, \sigma) = \frac{1}{\sigma\sqrt{2\pi}} e^{-\frac{(x-\mu)^2}{2\sigma^2}} \tag{II.3}$$

Both have a common mean (μ), which equals the mode of the artificial varve thickness distribution, but different standard deviations (σ_l and σ_r). The two distributions are normalised and all values $\leq \mu$ from f_l are used as left sided component of the artificial varve thickness distribution and all values $> \mu$ from f_r as right sided component. This approach allows independent adjustment of the two sides of the distribution. The resulting distribution is multiplied by 100 and the values are rounded to two decimal places (Fig. II.3b).

To create the actual artificial varve count, a number of artificial varve thickness values (years) is selected from the distribution using a uniform random function (the Matlab function `rand`). Lastly, white noise is added to each varve (max. ± 0.005 mm).

The values used for μ depend on the expected mean SRs in the sediment. However, it should be kept in mind that μ and the mean SR of the artificial varve count are only identical when the artificial count has a symmetrical varve thickness frequency distribution. For the Suigetsu sediment different standard deviations were used for the left and right sided components of the varve thickness frequency distribution. The resulting asymmetry, with a greater number of thick varves relative to the mode, accounts for thicker varve sub-layers - either detrital in years of increased surface runoff into the lake or organic in years of augmented productivity, respectively. Moreover, different standard deviations were used for the Holocene/LGIT and the Glacial. For the Holocene/LGIT values of σ_l=$\mu/6$ and σ_r=$\mu/2$ were used, while for the Glacial the values were σ_l=$\mu/6$ and σ_r=$\mu/4$ (Fig. II.5a,b). The reason for this is that the occurrence of *Aulacoseira* spp. layers results in a larger varve thickness variability within the Holocene and LGIT. In the Glacial, these layers are virtually absent, and therefore a more symmetric distribution is needed. This is supported by the µXRF based varve count from SG06 by Marshall et al. (2012). In Fig. II.5c,d CDF (Count Distance Frequency) plots from the Late Glacial and the Glacial are shown, using the µXRF raw count (which equals the µXRF quality 1-4 data in Marshall et al. (2012)), supporting a more symmetric distribution in the Glacial. The µXRF data have

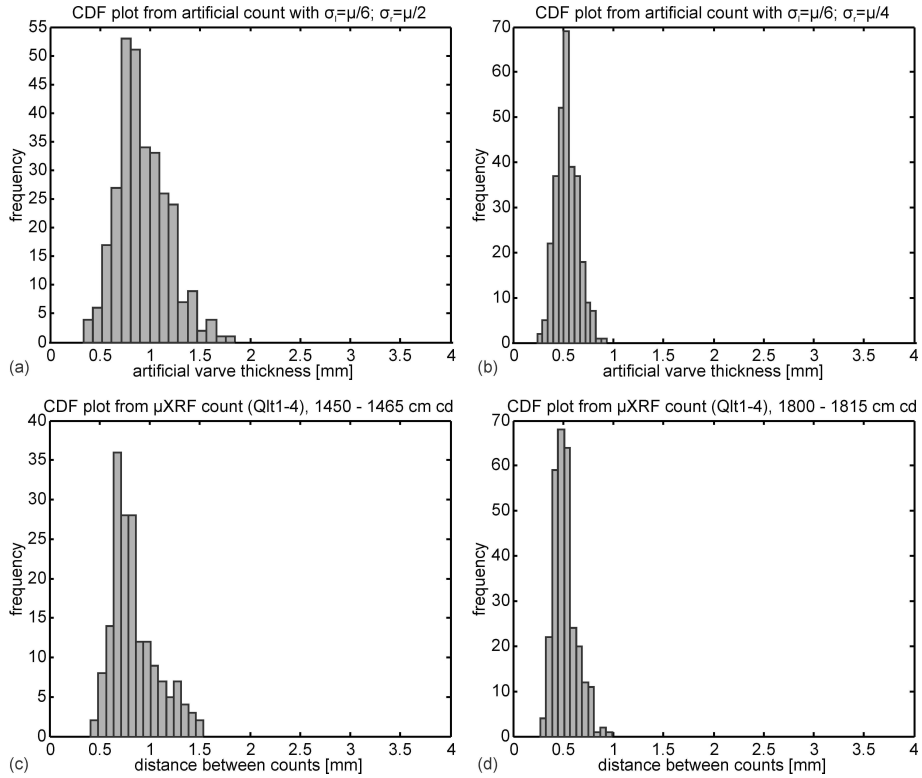

Figure II.5.: count distances frequency (CDF) plots from artificial datasets with (a) σ_l=μ/6 and σ_r=μ/2 (b) σ_l=μ/6 and σ_r=μ/4; CDF plots from µXRF count Qlt1-4 for (c) a Late Glacial section and (d) a Glacial section (µXRF data from Marshall et al. (2012))

a considerably higher raw count than the microscopic data and therefore provide a more complete CDF distribution. However, the data might be partially compromised due to noise in the µXRF data and by an increased uncertainty in the distinction between spring and autumn siderite layers, as diatom and organic layers that are seasonally indicative cannot be distinguished by XRF scanning. Therefore µXRF count cannot be considered a better dataset *per se* than the microscopic count.

To mimic the real, incomplete varve profile, a certain percentage of artificial varves is removed, using a random function (the Matlab function `randi`). The resulting CDF plot of the incomplete artificial varve count is shown in Fig. II.3d and can be compared to a CDF plot from the real varve count (Fig. II.3g). The two distributions display a high degree of similarity, which supports the selected values for artificial data generation.

As mentioned in section II.2 the next step is to calculate artificial varve counts for different mean SRs and different percentages of removed counts. The values used for the Suigetsu sediment were μ = [0.2 ; 0.3 ; ... ; 1.1 ; 1.2] and the percentages of removed counts were [20% ; 30% ; ... ; 70% ; 80%]. Next, different values for the mode variance window size are applied to the incomplete artificial counts, for SG06 these were $\kappa(p$=[0.3 ; 0.4 ; ... ; 0.8 ; 0.9]), yielding different mean SR estimates, which are used for interpolation. When the distance between two counts (d) is:

$$(y - 0.5) * \mathrm{SR} \leq d < (y + 0.5) * \mathrm{SR}; \quad y = 2, 3, ... \tag{II.4}$$

(y-1) years are inserted.

The result of the interpolation is then compared to the complete artificial count in order to assess the offset of the interpolation result ("art-error"), which depends on the setting.

The results are summarised in the Settings Matrix, which contains the determined art-error for each setting, i.e. it gives for each mean SR and each percentage of removed counts which $\kappa(p)$ produced the best interpolation result (the smallest art-error).

Since random functions are used to create the artificial varve count and to remove the counts, the complete and incomplete artificial varve counts are never exactly the same, even when the same setting is used to create them. Thus by repeating the above described calculations 200 times for each setting a statistical quality is added to the art-error estimation. The art-error is then represented by the mean of all 200 error estimations. More repetitions (500) did not show a significant improvement of the art-error values and more repetitions also prolong the calculation time accordingly.

Applying the Settings Matrix to a real count

For application to the real count (Fig. II.4) an interpolation with standard settings (bs=0.05, pv=15, p=0.5) is first run, which yields an initial estimate for the mean SR and the percentage of distinguishable, counted seasonal layers (relative to the time that passed during the formation of the sub-section). Using these two values, the mode variance window size with the smallest art-error is selected from the Settings Matrix and the interpolation is repeated, yielding a new, improved estimate for the mean SR and the percentage distinguishable seasonal layers. This is repeated in a loop until constant values for the mean SR and the percentage of distinguishable seasonal layers are reached or until a set of values repeats itself (i.e. if setting (a) leads to setting (b) which again leads to setting (a)). In the latter case the number of sub-sections increases accordingly, as each setting produces an independent sub-section. Since sub-sections are also always overlapping (new ones start every ten counts) this results in different interpolation results for every part of the core, as different overlapping sub-sections can suggest different numbers of years that should be interpolated between two counts. In order to combine these different results into one age model, a matrix (Interpolation Matrix) is created, that for every two adjacent counts lists how many sub-sections suggest a certain number of years (including zero) to be inserted between the two counts (in percent by division by the total number of overlapping sub-sections (Table II.2)). For example, between two counted seasonal layers seven sub-sections overlap and one of the sub-sections produces alternating settings adding an extra three sub-sections. Therefore the total number of sub-sections is ten. In six subsections 15 interpolated counts are inserted between the two counts, in three sub-sections 16 counts are inserted and in one sub-section 14 counts. Therefore 15 counts have a probability of 60%, 16 counts 30% and 14 counts 10%. Then the number of counts with the highest probability is inserted, which in the example would be 15 counts. Since the situation can arise in which equal maximum probabilities occur (e.g. 50%-50%, 40%-40%-20%, ...), the interpolation produces an oldest and a youngest, equally likely, age model.

It is also possible to apply multiple Settings Matrices to one count and combine the results by combining the Interpolation Matrices. For instance, for the SG06 core we varied the bin size with values of bs=[sr/8, sr/10, sr/12] keeping the peak value threshold constant at pv=15. Additionally we varied the pv threshold with pv=[10, 20], keeping the bs=sr/10 constant, using a total of five different Settings Matrices. Varying these values aims to decrease the uncertainty that is associated with the empirical derivation of bs and the pv threshold. Each Settings Matrix produces a separate Interpolation Matrix and these are combined by adding up the Interpolation Matrices before the number of models is converted into percent and only then divide by the total number models.

Error estimation

The total error range of the interpolation is obtained when using the lowest and highest number of counts suggested in the Interpolation Matrix for interpolation. But since it is

Probability of number of counts to be interpolated																			
Position of	number of counts to be interpolated between this and the next count																		
counts [cm cd]	0	1	2	3	4	5	6	7	8	9	10	11	12	13	14	15	16	17	18
1619.4196	0%	0%	0%	0%	0%	0%	0%	0%	0%	0%	3%	13%	40%	10%	3%	20%	7%	3%	0%
1620.6000	0%	0%	67%	33%	0%	0%	0%	0%	0%	0%	0%	0%	0%	0%	0%	0%	0%	0%	0%
1620.8898	7%	93%	0%	0%	0%	0%	0%	0%	0%	0%	0%	0%	0%	0%	0%	0%	0%	0%	0%
1621.0428	100%	0%	0%	0%	0%	0%	0%	0%	0%	0%	0%	0%	0%	0%	0%	0%	0%	0%	0%
1621.1152	0%	67%	33%	0%	0%	0%	0%	0%	0%	0%	0%	0%	0%	0%	0%	0%	0%	0%	0%
1621.3125	0%	0%	10%	63%	27%	0%	0%	0%	0%	0%	0%	0%	0%	0%	0%	0%	0%	0%	0%
1621.6546	0%	80%	20%	0%	0%	0%	0%	0%	0%	0%	0%	0%	0%	0%	0%	0%	0%	0%	0%
1621.8397	100%	0%	0%	0%	0%	0%	0%	0%	0%	0%	0%	0%	0%	0%	0%	0%	0%	0%	0%
1621.9082	100%	0%	0%	0%	0%	0%	0%	0%	0%	0%	0%	0%	0%	0%	0%	0%	0%	0%	0%
1621.9525	0%	0%	67%	23%	10%	0%	0%	0%	0%	0%	0%	0%	0%	0%	0%	0%	0%	0%	0%
1622.3389	77%	23%	0%	0%	0%	0%	0%	0%	0%	0%	0%	0%	0%	0%	0%	0%	0%	0%	0%

Table II.2.: example for Interpolation Matrix; probability values are rounded to integers; [cm cd] in first column means centimetre composite depth

unlikely that constantly the youngest or oldest model is true, the program defines a 68.2% probability range. This means that if the likeliest number of counts to be interpolated has a probability of less than 68.2% in the Interpolation Matrix, the adjacent number of counts with the highest probability is also considered for the error range and the probabilities are added. This is repeated until the sum of the probabilities reaches at least 68.2%. Eventually, the youngest and oldest model within the error range are used as error estimates. For example, in Table II.2, line one, the highest probability is 40% and suggests the insertion of twelve counts. Since this is below 68.2%, the eleven counts with 13% probability are also included in the error range, giving a total probability of 53%. Next, the thirteen counts with a probability of 10% are included in the error range and the total probability reaches 63%. Eventually a total probability of 68.2% is reached/exceeded when the count numbers from ten to fourteen are considered. Therefore the number of interpolated counts is 12 ± 2. The cumulative sum for all counts yields the interpolation error for the age model.

Limitations and requirements for interpolation

Firstly, the position of each counted seasonal layer must be ascertained precisely on the depth scale, so as to allow the program to calculate the exact count distances. Once the varve count is established, the quality and reliability of the interpolation result are controlled by certain characteristics. Beneficial are:

- a low inter-annual accumulation variability:
  A variability that is equal to or lower than 50% of the mean annual sediment accumulation (annual accumulation = sr $\pm$ sr/2) is considered ideal.

- low mean SR variability:
  Since the program assumes a constant mean SR within sub-sections, this criterion should be met. The permitted mean SR variability depends on the percentage of countable, seasonal layers relative to the actual number of years that passed during the formation of the sediment. A high count leads to short sub-sections and therefore the mean SR only needs to be constant in these shorter intervals, which in turn allows a higher mean SR variability.
  This is not the same as the first point, as it is possible to have a constant mean SR (i.e. no mean SR variability) and still a high inter-annual accumulation variability.

- random formation/preservation of seasonal layers:
  A potential problem is a systematic non-formation/preservation of seasonal layers. For instance, if in years with a small sediment accumulation seasonal layers did not

form as often as they did in years with a higher sediment accumulation, this would lead to an overestimation of the annual sediment accumulation in the CDF plot.

In practice, it can be difficult to quantify the degree to which these criteria are fulfilled. While a first estimate can be made during counting, the visual analysis of the CDF plots provides a mean to verify these. Furthermore, high interpolation errors might point towards a high annual accumulation or SR variability, as high variabilities can lead to noisier CDF plots, which in turn produce higher errors. Examination of potentially random seasonal layer preservation can be aided by the comparison of interpolation results from quality selective counts, which are explained in the following section. The comparison is demonstrated in section II.3.

Combining results from different counts from the same core

As a last step we aim to reduce uncertainties that arise from counting rather than from interpolation. The uncertainties mainly result from low quality layers that are difficult to distinguish as they are either diffuse, variable in thickness and/or not perfectly aligned with adjacent layers. Thus we established two quality selective counts from the raw count. First, each layer was labelled from 1 (clear layer) to 4 (uncertain layer) (Fig. II.6). By including only counts that were related to layers of at least quality 3 the layer-quality selective (LQS) count was built. Additionally, the core was divided into sections depending on the quality of the annual laminations (Fig. II.6). Sections were labelled quality 1 when multiple seasonal layers formed within one year, allowing a clear distinction between spring and autumn siderite layers, and when there was no indication that seasonal layers did not form every year. Also, a section of quality 1 contains a minimum of three varves. Sections of quality 1 do not explicitly exclude low quality layers, but good quality layers prevail in these sections. In sections of quality 2, multiple seasonal layers occur in most varves, and years in which seemingly no seasonal layer formed are rare. Sections of quality 3 reflect a regular lamination, but contain usually only one type of seasonal layer. Sections of quality 4 are only irregularly laminated or may contain no lamination at all. The section quality selective (SQS) count contains only counts that were within sections of at least quality 3.
The interpolation of the three quality selective counts (raw, LQS, SQS) should ideally produce similar results as they derive from the same sediment. Explicitly, no count dataset can be considered superior to another, as all three have their individual strengths and weaknesses. In turn this means, if one interpolated quality selective count diverges from the other two, it is less likely to represent an accurate result. If all three models diverge, it must be carefully examined what causes this (e.g. by manual CDF plot re-evaluation - compare with section II.3.2). This is used to combine the different results into a single, more robust chronology. The program provides an automated algorithm, which compares the interpolated models for each centimetre, using the mean of the two most parallel models in each centimetre to produce the single, resulting chronology. However, as noted above, in intervals with high differences between individual models it is advisable to manually ascertain the results.
Generally, this combination approach is also applicable to different counts that result from re-counting, counting parallel cores or applying different counting techniques (e.g. Marshall et al., 2012).

II.3. Results

To anchor the floating SG06 varve chronology the SG06-1288 (U-Oki) tephra at 1288.0 cm composite depth (cd) (version 24Aug2009 (Nakagawa et al., 2012)) was used, which has an wiggle matched ^{14}C age between 10.255 and 10.177 ka cal BP (at 95.4% probability range), with the median age being 10.217 ka cal BP (Staff et al., 2011).

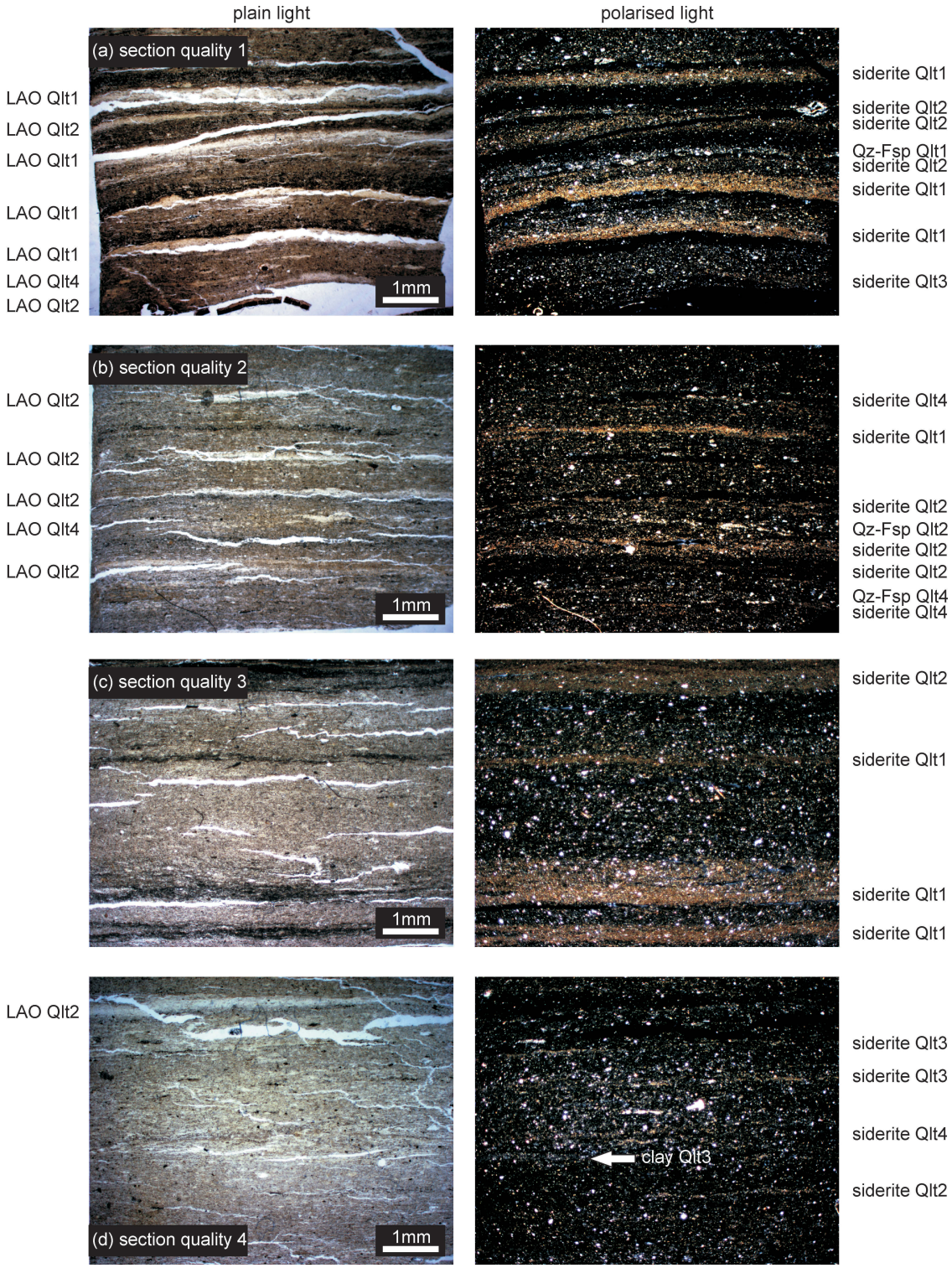

Figure II.6.: microscope photos showing examples for different layer and section qualities, on the left side in plain light and on the right side in polarised light; layer types and qualities are annotated on the left and right side, depending upon the light under which they are easier to distinguish: (a) section quality 1: multiple, seasonal sub-layers per year, highly regular lamination; (b) section quality 2: multiple, seasonal sub-layers per year, relatively regular lamination; (c) section quality 3: only siderite layers, separated by mixed layers, relatively regular lamination; (d) section quality 4: mainly indistinct seasonal layers of low quality, lamination in this example still relatively regular

Chronologically important micro-lithofacies boundaries occur at the onset of the LGIT interstadial (≈1729 cm cd) as well as the onset (≈1554 cm cd) and termination (≈1436 cm cd) of the LGIT stadial (Kossler et al., 2011). The boundaries are shown in the following figures for orientation and easier comparison between figures.

In the following we will first examine the interpolation results from the application of the different Setting Matrices and the result of their combination (by combining the Interpolation Matrices (see section II.2.2)). The second step is then to compare and combine the interpolation results from the different quality selective count datasets. In the second step we will also give examples for the manual re-evaluations of CDF plots, while we will only give the results of the manual re-evaluation for the results of the first step.

II.3.1. Varve counting and first step interpolation results

Counting and interpolation starts at the SG06-1288 tephra and is directed down the sediment profile to 1815.0 cm cd, at present. The microscopic varve count results from Lake Suigetsu for the raw count, the layer quality selective (LQS) and the section quality selective (SQS) count are shown in Figure II.7a. Before the interpolation algorithm was applied, macroscopic event layers, i.e. instantaneous deposits such as tephras or turbidites, were removed to avoid interpolation within those, resulting in an event free depth (efd). After interpolation the event layers were reintegrated, returning to composite depth (cd). The effect of event layers eroding the underlying sediment is not accounted for here for various reasons: (i) The base of event layers in the LGIT is usually well defined and does not suggest major erosion. (ii) Staff et al. (2011) showed with a high resolution ^{14}C chronology, that the Holocene in Lake Suigetsu is continuous and found no indication of major hiatuses. This suggests that the sedimentation in the lake is not generally prone to hiatuses. However, their study does not exclude micro-hiatuses. (iii) The comparison of distances between marker layers in parallel cores showed no major differences. Marker layers in the top 15 cm of a core were not considered as the top of cores is often compressed (Nakagawa et al., 2012). On average the differences in the distances between marker layers were 3.5 mm. No distance difference was larger than 9 mm and only in 4 out of 26 cases the difference exceeded 5 mm in the studied core interval. The differences could indicate micro-hiatuses, but could also be the result of slight, local sediment accumulation differences or might result from sediment expansion or contraction after opening of cores. In Summary, this suggests that if erosion occurred at all, it was very minor and therefore negligible compared to the interpolation error.

Results from the different quality selective count datasets, using different settings for the *bs* and the *pv* threshold, as well as the result of their combinations, are shown in Figure II.7b,c,d. When comparing the results from the different settings, it can be seen that a decreasing dataset results in a higher variability of age models, i.e. the results from different settings show an increased divergence. This is mainly due to an increased sub-sections length and therefore a higher SR variability within sub-sections, which produces less well defined CDF plots. However, the differences between the individual age models from one count do not increase linearly. In case of the LQS count the interpolated models show the greatest divergence between 1350 - 1390 cm cd, 1510 - 1550 cm cd and between 1640 - 1680 cm cd (Fig. II.7c). Manual re-evaluation of the CDF plots and comparison with the CDF plots from the raw count support the combination result. The results from the SQS count show the greatest variability between 1300 - 1380 cm cd and 1730 - 1815 cm cd (Fig. II.7d). Both intervals are characterised by a very low number of well varved sections, which explains the divergence (Fig. II.7e). Again, the combination result is supported by manual CDF plot re-evaluation, but it must be kept in my mind that these intervals have a high uncertainty due to the low number of well varved sections within them.

The percentage of interpolated years and the interpolation errors for all three resulting models are given in Table II.3. The errors increase from the interpolated raw count over

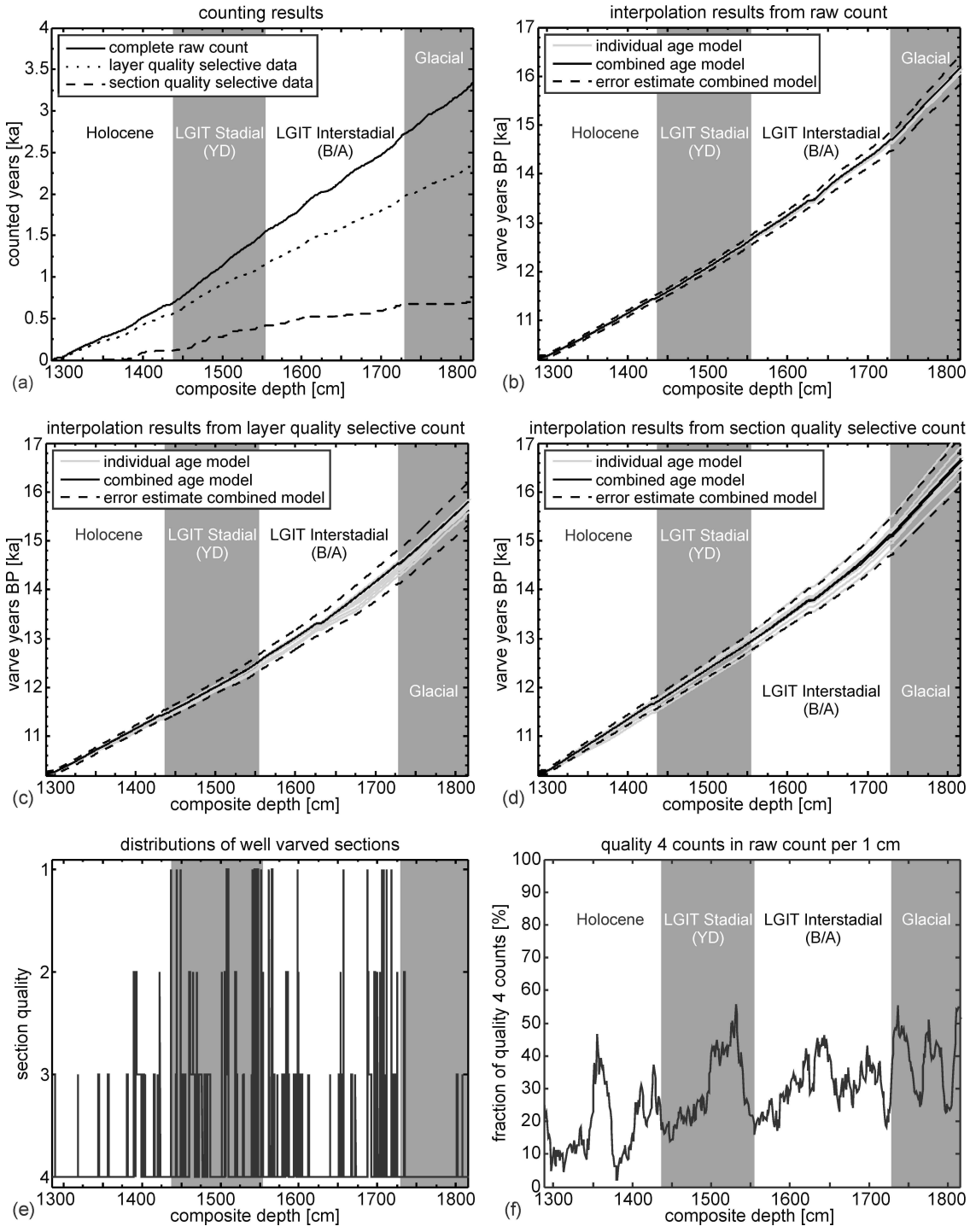

Figure II.7.: (a) microscopic varve count results; interpolation results from the different *bs* and *pv* threshold values (grey) and their combination result (black) from the (b) raw count, (c) layer quality selective count and (d) section quality selective count; (e) distribution of well varved sections; (f) distribution of counts related to quality 4 layers

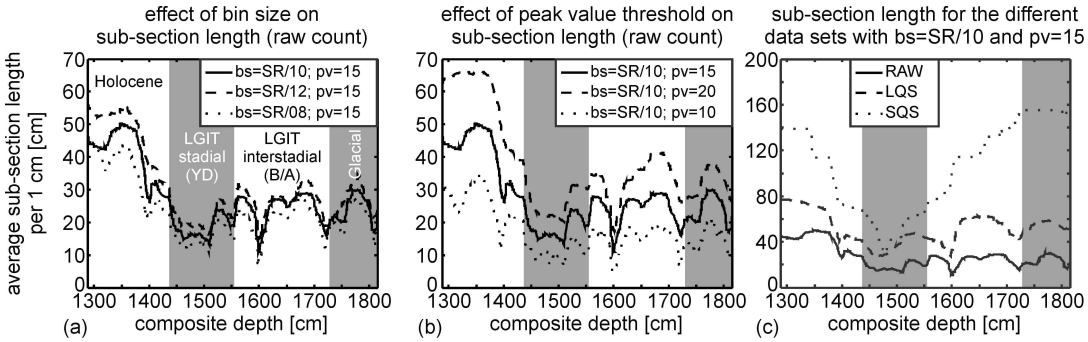

Figure II.8.: average sub-section length depending on count dataset and setting

count dataset	percent interpolated	upper error absolute	upper error relative	lower error absolute	lower error relative
raw count	44 %	+252 a	+4.2 %	-343 a	-5.8 %
LQS count	58 %	+398 a	+7.2 %	-481 a	-8.7 %
SQS count	89 %	+479 a	+7.5 %	-527 a	-8.2 %

Table II.3.: interpolation errors for the different count datasets

the LQS to the SQS age model. This is mainly due to an increased length of sub-sections and therefore a higher SR variability within sub-sections, which produces less well defined CDF plots. The dependence of the sub-section length on the different quality selective counts, the *bs* and the *pv* threshold is shown in Figure II.8.

II.3.2. Comparison of first step interpolation results and combined chronology

Before combining the resulting age models from the three count datasets, they are compared manually to identify problematic core intervals:

- Holocene section
  While in this section the interpolated raw count and the interpolated LQS count are rather similar, the interpolated SQS count gives considerably older ages (Fig. II.9a-c). As discussed earlier, the low number of well varved sections within the upper part of the Holocene section decreases the reliability of the SQS count (Fig. II.7e). However, the raw count and the LQS count are also compromised, both being rather similar due to the low percentage of quality 4 counts in this section. In Fig. II.10a the CDF plot from the raw count for a part of the Holocene section is shown. Various peaks are distinguishable and those that are potentially multiples of the mean SR, i.e. where more than one year passed between the formation of two successive seasonal layers, are labelled accordingly. Seemingly two different mean SRs are supported by the plot, one around 0.8 mm/a and one around 1.25 mm/a. This could mean that the relatively long sub-sections in the Holocene, which are a result of a low frequency of seasonal layers, enclose a change between two SRs. Alternatively it could mean that the seasonal layer preservation is not random, but that in years with a low accumulation rate less seasonal layers formed or were preserved and hence the mode bin is at a higher distance value (than 0.8 mm). In this case most of the measurements that contribute to the different peaks would relate to a SR of about 0.8 mm/a. Careful examination of further Holocene CDF plots from the three quality selective counts suggests the latter, supporting the SQS result. But since all three datasets are afflicted by uncertainties in the Holocene we must label it as problematic in the microscopic count.

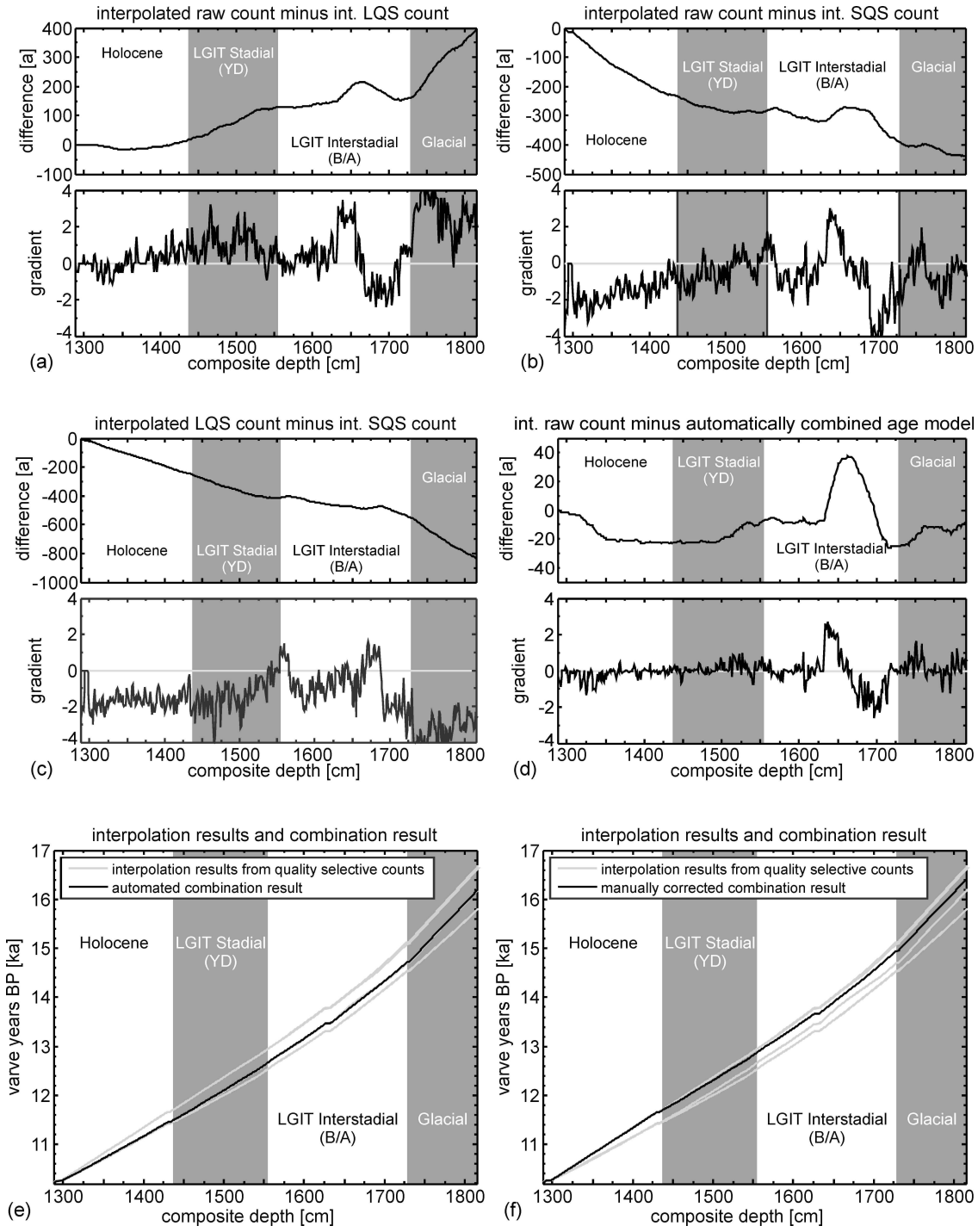

Figure II.9.: (a) difference between the interpolated raw and layer quality selective count (upper: difference, lower: gradient of difference curve); (b) difference between the interpolated raw and section quality selective count (c) difference between the interpolated layer quality and section quality selective count (d) difference between the interpolated raw count and the automated combination result (d) result of automated combination (black) and interpolated quality selective counts (grey) (f) combination result with manual age model pre-selection

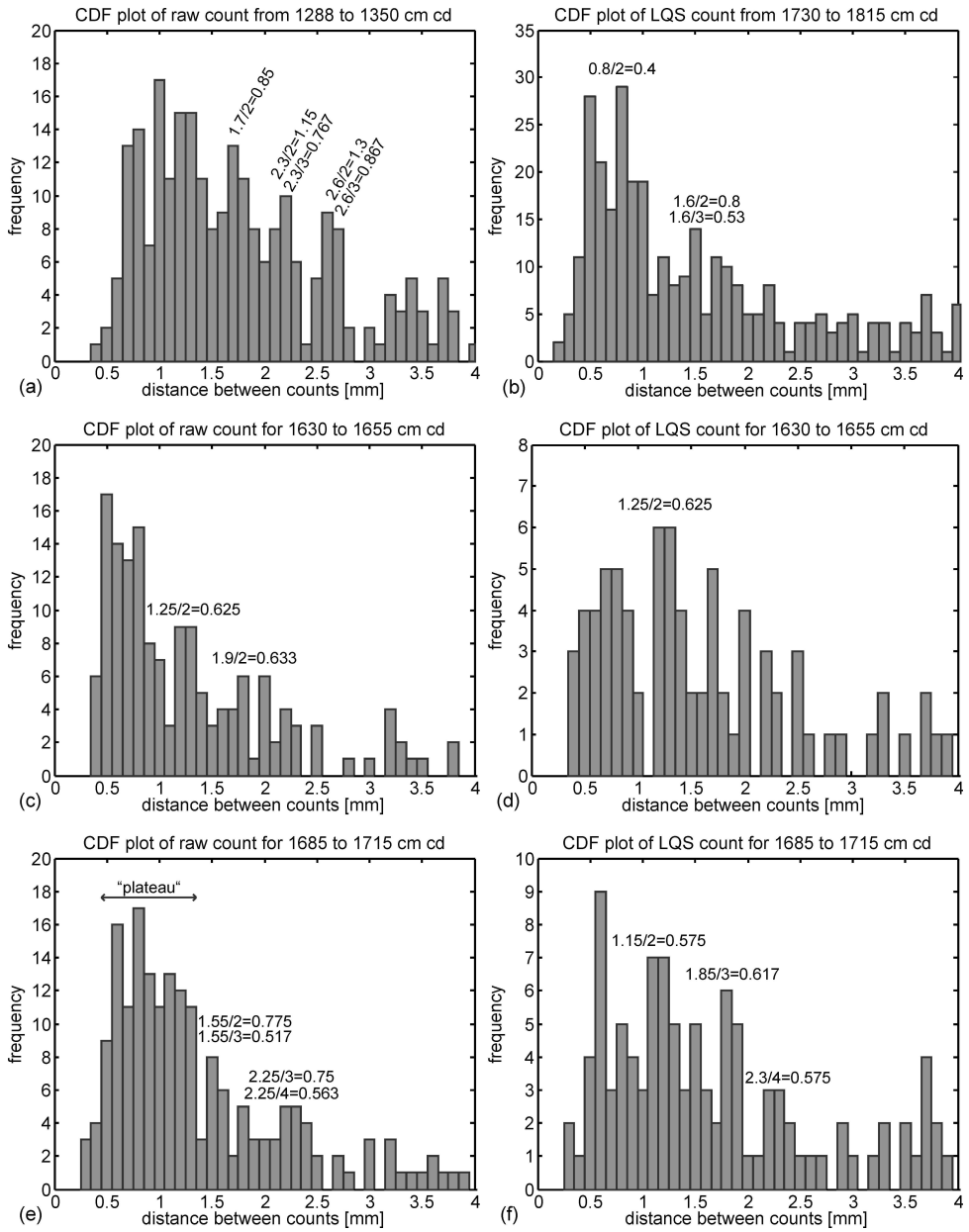

Figure II.10.: CDF plots from intervals with the greatest differences between the three different quality selective age models; for details refer to text, section II.3.2

- LGIT stadial section
  In this core section the interpolated raw count and the SQS age model generally show a good fit, while the LQS age model gives younger ages (Fig. II.9a-c). Examination of the CDF plots from the LQS count shows that peaks with double the mean SR dominate the CDF plot, which leads to an overestimation of the mean SR.

- LGIT interstadial section
  In the upper part of this core section the datasets agree reasonably well with each other (Fig. II.9a-c). But between 1630 and 1655 cm cd the LQS and SQS age models give younger ages than the interpolated raw count (i.e. have a higher mean SR). This coincides with a core interval with only few well varved sections (Fig. II.7e) and therefore the SQS data must be viewed with caution. Examination of the CDF plot from the raw count (Fig. II.10c) and the LQS count (Fig II.10d) for this core interval shows that the LQS count is again dominated by a peak that is likely to be related to double the mean SR. Since this peak in the LQS CDF plot supports

the result from the raw count the latter represents the best model in this interval. Further down core, between 1685 and 1715 cm cd, the relation between the three count datasets is reversed and the interpolated raw count gives younger ages than the other two models. This is due to a relatively large "plateau" around the mode in the CDF plot of the raw count (Fig. II.10e), which makes the mode bin less distinct. Furthermore, the peaks that presumably relate to a multiple of the mean SR support the results from the LQS (Fig. II.10f) and SQS count. Hence the raw count is considered compromised in this interval.

- Glacial section
  Here the LQS data gives younger ages again, while the interpolated raw count and the SQS data agree rather well (Fig. II.9a-c). Again this is due to the dominance of count distances that are double the SR in the LQS data (Fig. II.10b) as examination of CDF from all three datasets reveals. Hence the LQS data are compromised here. However, we must also acknowledge problems in the other two datasets, as: (i) there are only very few well varved sections that make up the SQS data and (ii) the total number of quality 4 layers in the raw count is considerably increased.

The automated combination result of all three models, which equals the mean of the two most parallel models at a one centimetre resolution, shows a high degree of similarity with the interpolated raw count (Fig. II.9d,e), as this dataset usually combines with either the LQS or the SQS age model. The only clear deviation occurs between 1630 and 1715 cm cd (about 50 years deviation from the interpolated raw count), where the LQS and SQS age models are most similar. However, after the manual re-evaluation we discard the raw and LQS count in the Holocene and the LQS and SQS count between 1630 and 1655 cm cd, as in these two sections the two most similar models are unlikely to give the best result. The effect of the manual age model pre-selection on the combination result can be seen in Figure II.9e,f.

II.4. Discussion

II.4.1. Seasonal layer formation/preservation

The formation of mixed layers, which represent time windows of multiple years, is the main cause for the incomplete raw count. As already noted in the layer description, the mixed layer formation is possibly the result of years with a less pronounced or no stratification of the water body, and subsequently no seasonal lake overturn. This would still allow the production of the autochthonous and authigenic sediment components, but no mechanism for a separate deposition would be provided, resulting in a mixed layer without sedimentological transitions between years. Also, a temporary oxygenation of the lake bottom could result in the dissolution of siderite. Furthermore, this could allow bioturbation, but the generally low thickness of the mixed layers suggests that bioturbation, if occurring at all, had only a minor impact in the LGIT. Lastly, siderite layers (which usually delimit the mixed layers) do not form homogenously over the whole lake bottom. For example, in Fig. II.6b,c siderite layers can be distinguished that are laterally not continuous. The reason for this could be very localised differences in the chemical conditions, such as Fe fugacity or O_2 concentration as a result of small scale fluid dynamics at the water-sediment interface. Hence, even when siderite formed in a certain year, it may not be present in the SG06 sediment cores.

II.4.2. Accuracy and precision of the interpolation result

In order to assess the reliability of the interpolation, we compare the result with the calibrated, unmodelled ^{14}C chronology from Lake Suigetsu (Staff et al., 2011) down to the

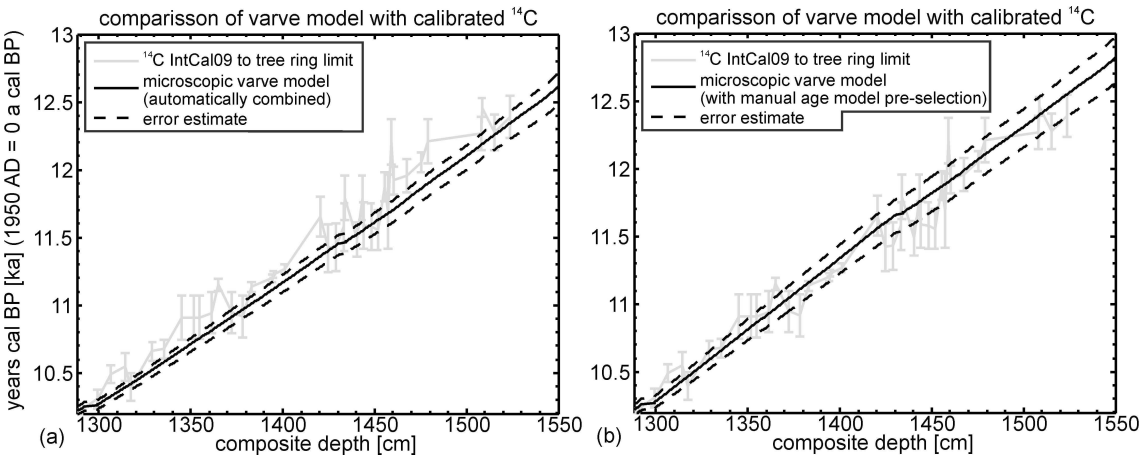

Figure II.11.: ^{14}C dates calibrated with IntCal09 (Reimer et al., 2009) versus (a) automated combination result and (b) combination result with manual pre-selection of varve models

tree-ring limit of the IntCal09 calibration curve (12.55 ka cal. BP) (Reimer et al., 2009). Since IntCal09 is considered accurate within this period and both, IntCal09 and the SG06 ^{14}C chronology, are composed of terrestrial (i.e. non-reservoir-corrected) data, the result from the varve interpolation should show a high degree of similarity with the calibrated SG06 ^{14}C age determinations.

In Fig. II.11a the varve model from the automated combination (of the three interpolated quality selective counts) is shown versus the calibrated ^{14}C dates at the 68.2% probability range. Although the model demonstrates the same trend as the ^{14}C curve, it gives mostly ages that are too young. The mean difference between the varve model and the individual mean ^{14}C ages is -124 years. When comparing the ^{14}C curve with the varve model where a manual age model pre-selection was done prior to combination, the fit is highly improved, the mean difference to the ^{14}C dates is reduced to +67 years (Fig. II.11b), while the mean error of the ^{14}C dates is ±120 years. This shows that despite the fact that the program can be run totally automated, the result should be manually ascertained.

The interpolation error estimates of the varve models shown in Fig. II.11a,b are anchored to the upper and lower ^{14}C error of the SG06-1288 tephra at the 95.4% probability range (10.255 and 10.177 ka cal BP (Staff et al., 2011)). The interpolation error of the age model with manual pre-selection is greater than that of the automated combination result. This is due to the use of the SQS interpolation result at the top of the age model, which has a larger error (compare Table II.3). The total error from 1288 to 1815 cm cd for the manually pre-selected model is -7.2% and +5.2%. This is about two to three times the error that is generally associated with varve counts (without major interpolation), which is on average estimated to be between 2 to 3% (Ojala et al., 2012). Naturally, an interpolated chronology is bound to have a greater uncertainty than the varve count from well varved sediment, and were estimated to reach values up to 20% (Brauer, 2003). Since only about 50% of the varves were distinguishable in the microscopic count from Lake Suigetsu, we consider the errors to be acceptable. How the result can be further improved is discussed in section II.4.4.

II.4.3. Comparison with conventional varve interpolation

The main advantages of the interpolation approach presented here have already been listed in the introduction, which were the mean SR estimation from the compromised interval itself, the reduction of subjectivity in the interpolation process and the reproducibility of results. Of these, the second point especially requires a more detailed discussion. Though

the interpolation can be run fully automated and hence absolutely objective it has been shown that results should be manually ascertained, mainly through the mean of CDF plot re-evaluation, which allows subjectivity to a certain degree. However, the discussion of (unclear) CDF plots in publications allows quantification of the uncertainties in problematic intervals and decisions made are easily retraced by readers.
Another major advantage of the interpolation approach presented here is objectivity in the error estimation. While varve counts can be validated by cross dating (Neugebauer et al., 2012), no protocol for the estimation of errors by conventional varve interpolation is established and errors are, if given at all, only roughly estimated. The only exception is the comparison with independent chronologies like for example from ^{14}C, ^{210}Pb or ^{137}Cs dating. However, often the alternative chronology is used to aid in the interpolation, in which case the comparison invites circularity and the errors give only a combined uncertainty of varve interpolation and that of the alternative chronology (Tian et al., 2005).

Although the automated interpolation approach has many advantages, manual interpolation can yield better results in certain situations. For example, the interpolation program uses only the distance between two counted seasonal layers as basis for interpolation. It does not incorporate information from other, non-counted seasonal layers. For instance, if between two counts an unusually thick seasonal layer occurs, e.g. a diatom layer, this information can be used in manual interpolation to interpolate fewer or no years. Especially in sediment records where only a few/single varves are indistinguishable, manual interpolation could provide better results. Moreover, it should be recalled that incompletely varved records need to fulfil the requirements described in section II.2.2.

II.4.4. Outlook: Further improvements to the SG06 varve chronology

In order to further increase the reliability and accuracy of the SG06 varve chronology a second, independent and novel approach to varve counting is applied, utilising μXRF and X-radiography (Marshall et al., 2012). Especially for core intervals that exhibit a decreased degree of certainty, due to ambiguous CDF plots or low lamina quality, this complementary counting approach will help to reduce uncertainties.

Two problems that are commonly associated with varve counting also apply to the interpolation. First, an erroneous age estimation in a certain interval will affect all subsequent sections, as the interval gives an incorrect starting age for the following sections. The second problem is the cumulative nature of the error estimation. Over the long timeframe that we aim to cover in the Suigetsu Varves 2006 project (10 ka cal BP to ≈60 ka cal BP) this will result in unsuitably large errors towards the oldest parts of the chronology. To eventually overcome these problems, distinctive features in the radiocarbon data from lower down the SG06 core (beyond the present tree-ring limit of IntCal09) will be compared to the marine portion of the IntCal calibration curve. (Although finer scale structure of the calibration curve may be 'smoothed' in the marine datasets, pronounced events in the calibration curve would be shared between the atmospheric and marine datasets - most notably to large-scale events such as the Laschamp geomagnetic excursion.) Thus, the overall trend of the IntCal data will be used to minimise the cumulative deviation of the SG06 varve year age scale from the international consensus IntCal timescale. It is important to note that the short and medium-term structure of the SG06 calibration dataset will remain independent of the marine data (and any assumptions pertaining to the marine reservoir effect that this would introduce), with only the long-term trend of the dataset adjusted by comparison to IntCal. To further constrain the cumulative varve count error, additional ^{40}Ar/^{39}Ar-dated tephra layers (Smith et al., 2011) will be used as age supplementary, thoroughly independent control points through the entire SG06 sequence (Staff et al., 2013a).

II.5. Conclusion

It has been shown that the new, automated varve interpolation method produces reliable results from varve records where on average as many as 50% of the varves are indistinguishable. Where manual interpolation approaches often suffer from subjectivity, the varve interpolation program (VIP) provides objectivity in the interpolation and error-estimation. Although the interpolation is automated, a detailed understanding of the data is necessary to evaluate the results and understand possible weaknesses within them and to account for these.

With respect to the aim of the SG06 project, to extend the atmospheric radiocarbon calibration curve to 50 ka cal BP, it was shown that the accuracy of the interpolation is within the 68.2% probability range of calibrated ^{14}C for a ≈2500 year period, and therefore is considered a suitable dataset for extension of the purely terrestrial calibration curve further back in time.

The VIP will be made publically accessible on the internet after a closed beta testing. Since the program so far has only been applied to and optimised for the SG06 varve record, the application to other records might show possible weaknesses in the program and thus application should be supervised. If you have data that is potentially suitable for the interpolation method described here, please contact the first author of this paper.

Acknowledgements

We thank the German Research Foundation (DFG grants TA-540/3-1, BR 2208/7-1), the UK Natural Environment Research Council (NERC grants NE/D000289/1, NE/F003048/1, SM/1219.0407/001), the KAKENHI project of Japan (grant 211001002) and INTIMATE EU cost for funding. Furthermore, we thank two anonymous reviewers and S. Lauterbach for their constructive and helpful suggestions on the manuscript. We also thank H. Kitagawa and J. van der Plicht for inspiration for the project.

III. Dating the SG06 sediment core: Varve counting by μXRF and combination with the thin-section count

This chapter has been published as *A novel approach to varve counting using μXRF and X-radiography in combination with thin-section microscopy, applied to the Late Glacial chronology from Lake Suigetsu, Japan* by *Michael H. MARSHALL, Gordon SCHLOLAUT, Takeshi NAKAGAWA, Henry F. LAMB, Achim BRAUER, Richard A. STAFF, Christopher BRONK RAMSEY, Pavel E. TARASOV, Katsuya GOTANDA, Tsuyoshi HARAGUCHI, Yusuke YOKOYAMA, Hitoshi YONENOBU, Ryuji TADA and Suigetsu 2006 Project Members* in *Quaternary Geochronology, 2012, Vol 13 70-80*

Abstract

The Lake Suigetsu 2006 Varved Sediment Core Project (SG06 Project) aims to contribute to the international terrestrial radiocarbon calibration model, extending it to >50,000 cal years BP using the new SG06 sediment record, which shows annual laminations (varves) for most of this period. For varve counting, a novel approach using high resolution X-ray fluorescence (μXRF) and X-radiography was applied, described here in detail for the first time, and applied to the Late Glacial sediments of core SG06. This new technique was carried out alongside conventional varve counting by thin-section microscopy (Schlolaut et al., 2012). This dual approach allows comparison of results from the two independent counting methods on metre to sub-mm scales, enabling the identification and characterisation of differences between the techniques, and quantification of their weaknesses. Combining the results produces a more robust chronology than either counting method could produce alone. The reliability of this dual approach is demonstrated by comparison of the combined chronology with the radiocarbon dataset of SG06, calibrated with the tree-ring derived Late Glacial section of IntCal09.

III.1. Introduction

Annually laminated (varved) lake sediments are important palaeoclimate archives as they provide high-resolution chronological control for sedimentary records of environmental change (Lamoureux, 2001; Brauer, 2004; Zolitschka, 2003, 2006). Traditionally varve counting is carried out using thin-section microscopy, which, when integrated with microfacies analyses, provides crucial information on the seasonal signals in varve records (Brauer, 2004). By integrating microscope analyses with micro-X-ray fluorescence (μXRF) elemental scanning, detailed quantitative element profiling across individual varves is possible (Brauer et al., 2009). Here we use this μXRF information to establish a new approach to varve counting, which can be carried out independently of, but complementary to, thin-section varve counting.

For elemental scanning in this study, the Itrax™ XRF core scanner was used (see Croudace et al., 2006; Francus et al., 2009). It takes very high resolution radiographic and optical

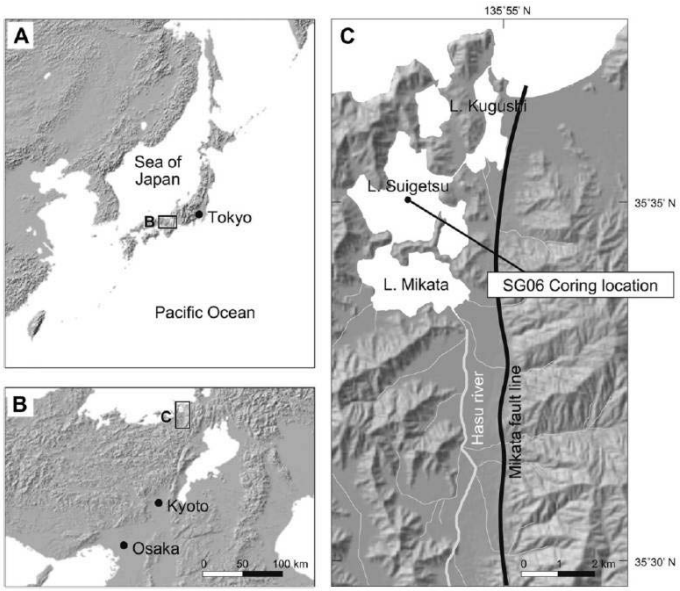

Figure III.1.: Location of Lake Suigetsu (modified after Nakagawa et al. (2012))

images at the same time as XRF measurements, with improved count rates and detection limits as compared to most alternative scanners. Furthermore, rather than using a single spot X-ray beam, it is equipped with a unique flat X-ray beam which means that grain-to-grain variance is averaged in the horizontal core axis, ensuring a stronger signal and predominance of the environmental signal through depth. This is a particular advantage when measuring laminated sediments at very high resolution. The X-radiographic greyscale density profiles provide additional information on the varve structure, and allow detection of hidden clasts and sedimentary structures that are not visible at the sediment surface.

As part of the Suigetsu Varves 2006 project, the method was applied in parallel with microscopic varve counting (Schlolaut et al., 2012). This dual method approach is designed to reduce count uncertainties reported from an earlier Suigetsu Project (SG93) conducted by Kitagawa and van der Plicht (1998a,b, 2000) (van der Plicht et al., 2004; Staff et al., 2010). Here, the method is demonstrated on the section of the SG06 sediment core that covers the Last Glacial - Interglacial Transition (LGIT). Comparison with the current SG06 radiocarbon dataset, calibrated using IntCal09 to the limit of the tree-ring data set (12,550 cal yr BP; Reimer et al. 2009), demonstrates the reliability of the method.

Eventually, the varve count data will be used to extend the international terrestrial radiocarbon calibration dataset beyond the current tree ring limit, as the Lake Suigetsu sediment profile not only exhibits annual laminations, providing a calendar age scale, but is also rich in terrestrial leaf macrofossils, which provide a unique, 'wholly terrestrial' (i.e. non-reservoir-corrected) record of atmospheric radiocarbon back to >50 cal kyr (Nakagawa et al., 2012).

III.2. Regional setting

Lake Suigetsu (35°35′N, 135°53′E, 0 m above present sea level), is a tectonic lake located close to the Sea of Japan, Honshu Island, central Japan, and is situated on the western side of the active Mikata fault (Fig. III.1). The lake is 34 m deep, and covers an area of c. 4.3 km^2, with a diameter of c. 2 km in both N-S and E-W directions. Lake Suigetsu is naturally protected from winds by surrounding hills (max 400 m). The Hasu River is the only significant fresh water supply, but the river first flows into Lake Mikata, which is connected to Lake Suigetsu only by a very shallow (maximum depth c. 4 m) and narrow

(c. 45 m) natural channel (Fig. III.1c). Therefore, sediments on the floor of Lake Suigetsu are well protected from high-energy hydrological events (such as floods) and only receives a small proportion of detrital material from the Hasu River catchment (Nakagawa et al., 2012).

In AD 1664 a channel was constructed, connecting Lake Suigetsu with Lake Kugushi, which is connected to the Sea of Japan. As a result, salt water flowed into the freshwater Lake Suigetsu and led to the formation of a chemocline at c. 8 m depth (Masuzawa and Kitano, 1982; Kondo et al., 2009). The present-day hydrology is therefore only partially comparable to that of the LGIT.

The regional climate around Lake Suigetsu is characterised by both summer and winter monsoons. In summer, when the monsoon front is to the north of the lake, predominantly south-easterly winds bring humidity from the Pacific Ocean, whereas in winter, when the monsoon front is to the south, the dominant and cool north-westerly winds come from Siberia, taking up humidity over the Sea of Japan (Nakagawa et al., 2005).

III.3. Material and methods

III.3.1. Coring and logging

Sediment cores were obtained from four separate bore holes (A, B, C and D) near the depocentre of the lake (35°35′0″N, 135°52′57″E). Cores were split and the half-cores labelled 'N' (North) and 'S' (South). A composite stratigraphy was constructed using marker layers identifiable in all parallel cores (e.g. tephras, turbidites, flood layers, etc.). This was followed by 'LL-channel' sub-sampling (100 × 1.1 × 1.1 cm; Nakagawa et al. 2012). For core sections longer than 1 m, four 'LL-channels' were taken from each section: North Upper (NU; 0-100 cm), North Lower (NL; 100 cm - core section base), South Lower (SL; core base - 100 cm from core base), South Upper (SU; 100 cm from core base - core top). This sampling method ensured complete overlap for all core sections. A more detailed description of the coring process and core stratigraphy can be found in Nakagawa et al. (2012).

III.3.2. High resolution μ-XRF and X-radiography

Optimisation of scanner settings

XRF works on the principle that when X-rays irradiate a surface, that surface emits secondary X-rays due to the photoelectric effect; incoming X-ray photons knock K-shell electrons out of the atoms in the sample. The energy released by other electrons that fall into the vacated positions results in the production of new X-ray photons, whose wavelength is characteristic of the atoms involved, and therefore the elements present. The rate of emission is largely a function of the concentration of the element and absorption of the outgoing X-rays by the sample.

The Itrax™ scanner used has a 3 kW X-ray generator with a 3 kW molybdenum target tube. The X-rays that emerge through the shutter of the tube turret are focused by means of a proprietary flat-beam optical device, which generates a 20 × 0.2 mm rectangular beam with its long axis perpendicular to the main axis of the sample (Croudace et al., 2006). The X-ray detector is a silicon-drift detector. The core scanner is also fitted with an optical line camera system which incorporates a light sensitive 2048 pixel CMOS device that has a maximum resolution of 50 μm/pixel. The intensity of X-radiation transmitted through the core is recorded by a digital X-ray line camera, which consists of 1024 X-ray sensitive diodes arranged linearly.

Using a Mo X-ray tube, light elements such as Al and Si require long dwell time (>20 sec.), while heavier elements, such as Fe, Ca, Ti, are more easily detected with reduced

dwell times. Numerous factors related to the sediment matrix, such as water content, organic matter content, grain size, mineral crystallinity and porosity may have a significant impact on the production and the detection of fluorescent photons (Weltje and Tjallingii, 2008). Results are presented as spectral peak areas (or counts per second cps; cps = peak area/XRF count time in seconds) and can be calibrated to concentration, although this is problematic in some sediments because of the high variability of the matrix factors mentioned above.

The overlapping LL-channel core sections were loaded onto a LL-channel sample holder and placed into the horizontal cradle of the scanner. The standard proprietary flat-beam of the scanner was updated to reduce the vertical dimension of the beam to 0.1 mm to facilitate higher resolution scanning, and a more sensitive detector was added. The unique flat beam of the Itrax™ core scanner was essential to cancel grain-to-grain variance within the geochemical signal that becomes more significant at higher scanning resolutions. Pilot studies were carried out to determine the optimum settings of the scanner for this project. The same SG06 core interval was repeatedly XRF-scanned using a number of different measurement intervals (200, 100, 60, 20 μm), count times (20, 10, 6, 5 and 4 seconds), voltage (60, 50, 40, 30 kV), and current (40, 30 mA) settings. Two different detector nozzles (8 and 4 mm perpendicular to the main core axis) were also trialled. The output data were analysed and the number of peaks observed in certain key elements were counted. Correlated peaks in elements represent discrete sub-layers in the varve structure. The total counts from each setting configuration were compared. As well as representing the optimum settings for the distinction of the elements of interest (dependent on sub-layer composition), the final operating procedure also had to fulfil two pre-defined criteria to allow complete consistency for all LL-channels analysed: (1) a minimum of 10 measurements must be made in one annual cycle, to allow precise distinction of key element peaks that are representative of the dominant varve sub-layers; (2) each LL-channel 1 m section should be analysed in approximately 24 hours; and (3) the detector nozzle width needs to be small enough so that non-horizontal layers can still be resolved.

According to the results from Kitagawa and van der Plicht (1998a,b) varve thickness in the Suigetsu core varies between approximately 610 μm (in the Glacial) and 1200 μm (in the Holocene), and hence a 60 μm step size achieved the first criterion without any significant increase in the signal : noise ratio. Although the width of the flat beam is 100 μm, the sample stage allows a minimum of 20 μm measurement intervals, with any step size smaller than the beam width resulting in naturally smoothed results (by a moving average).

Scanning at such high resolution (1.67×10^4 measurements per metre) meant that for the second scanning criterion to be fulfilled, the XRF count time would have to be reduced, whilst ensuring that the signal was not compromised. Although prolonged count times are necessary for accurate detection of the lighter elements (particularly Al and Si), the main elements required to fulfil the project objectives are heavier (mainly Fe and Mn, but also K, Ca, Ti, Zn, Rb, Sr, Zr) and were detected consistently and accurately with count times as low as 4 seconds (with no difference in total peaks counted between 20 and 4 seconds). The detection limits of these elements using a XRF count time of 4 seconds were also estimated based on a 95% confidence level of actual detection of the element from its characteristic emission line. Thus, the total XRF count within the peak area must be significant in relation to the corresponding (non-fluorescent) background below the particular element peak. The detection limits were calculated using certified reference material, by calculating the minimum peak area that could be significantly detected for that particular background recorded. For most elements of interest, if they constituted between 0.0001 and 0.5% of the total peak area, then the data could be taken as accurate, but for Si the figure was closer to 5%. For a scan of the Suigetsu sediment, all of the

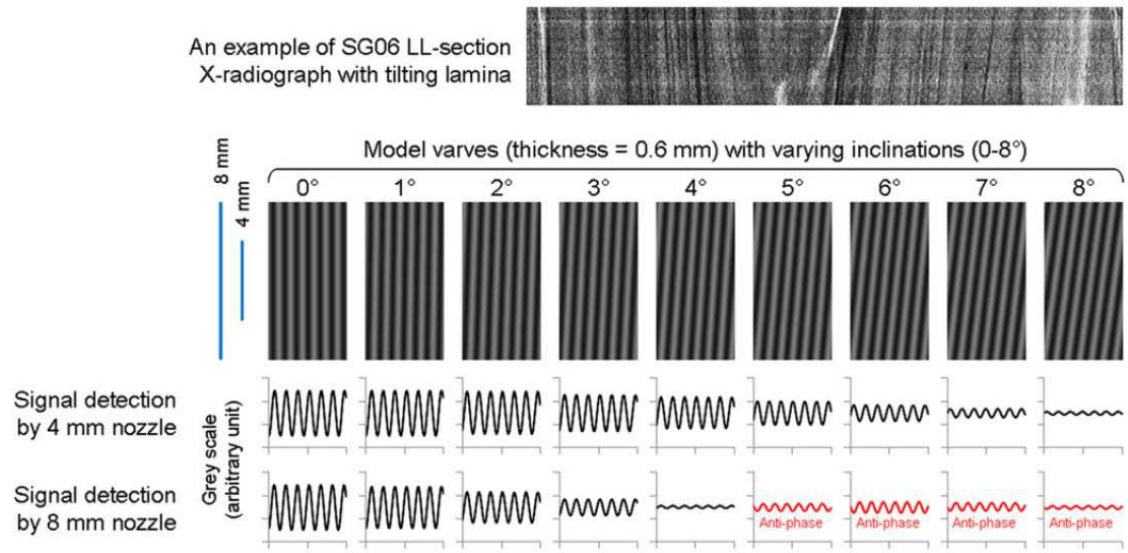

Figure III.2.: X-radiograph image showing tilting lamina. Detector nozzle width (mm) is also shown, together with model varves with varying inclinations (0-8°) and the signal detection using both 8 mm and 4 mm nozzle widths

elements of interest were found to satisfy these requirements and therefore a XRF count time of 4 seconds was used.

As expected, increasing the power led to a higher overall XRF count rate detection, but did not change the shape of the output profiles (of each element) and hence the number of peaks counted. However, increasing the voltage and current caused a 'double line' in the output spectra for the most abundant elements detected in the sediment. In the case of the Suigetsu sediment, even at standard setting values of 30 kV and 30 mA, a secondary Fe peak was identified at 12.8 KeV (double the 6.4 KeV emission line of Fe). Although this may reduce the accurate detection of elements whose emission lines are close to the double line of Fe, the line can be marked as such and therefore modelled in the output spectra. Lower power settings reduced the size of this double emission line of Fe, but also reduced the sensitivity of detection (and peak count). Hence, setting values of 30 kV and 30 mA were used.

Another important variable is the width of the detector nozzle (either 4 or 8 mm), particularly when measuring horizontal laminae across a ≈1 cm wide core surface at extremely high resolution. The 8 mm detector nozzle allowed a greater rate of photon detection compared to the 4 mm nozzle when all other settings were equal, but there was no difference in the number of peaks counted in the indicator element profiles (representative of key sub-layers deposited in a single season). However, scanning fine non-horizontal laminae using the wider detector nozzle might result in the number of indicator element peaks detected (and counted) being greater than the actual number of peaks that represent the key indicator varve sub-layers present in the sediment. In the case of a sedimentation rate of 0.6 mm/year (typical value for Glacial age), detection of the annual cycle by the 8 mm nozzle becomes inaccurate if laminae are tilted by c. 4.2° (= arctan (0.6/8)), whereas the 4 mm nozzle can still detect the annual cycle signal up to c. 8.5° (= arctan (0.6/4)). In general, the 4 mm nozzle is twice as tolerant of the off-horizontal laminae (Fig. III.2). This weakness of the wider nozzle is of purely geometric nature and thus cannot be compensated by improving detection limits. The 4 mm nozzle is hence more likely to produce output data that are most representative of the actual number of annually-deposited sub-layers in the sediment and was therefore chosen as preferable and used throughout. Therefore the 4 mm detector nozzle was used.

The use of LL-channel sub-sample cores meant that a consistent sediment thickness was maintained throughout the entire composite core, and therefore that the X-radiographs were comparable between core sections. X-radiographic setting tests across contrasting sediment lithologies (highly organic, with low X-ray absorbance, to highly minerogenic, with high X-ray absorbance) allowed the choice of suitable power settings that did not lead to over- or under-exposure of the X-radiographic images, even across the range of sediment densities. A voltage of 60 kV, current of 50 mA, and exposure of 200 ms, achieved this. The slit system (which focuses the X-ray into the line camera) was adjusted so that the X-rays were confined to 60 µm, maintaining the same resolution as the XRF measurement step size.

All LL-channel sub-samples (i.e. NU, NL, SU, SL) from each core section of the laminated part of the SG06 core (A-07 to B-23, 1286.1 to 4497.7 cm composite depth (cd)) were scanned using these settings.

Counting

An increasing number of studies are utilising digital analysis of optical and X-ray images as an objective method of analysing sediment features, including varves, both manually and automatically (Ripepe et al., 1991; Cooper, 1993; Petterson et al., 1999; Saarinen and Petterson, 2001; Ojala and Francus, 2002; Haltia-Hovi et al., 2007). Automated peak counting software has been developed for use in characterising laminated sediments and varve counting, using profiles derived from images, but also geochemical data, and allow the option of spectral analysis on such datasets (Weber et al., 2010). However, for such approaches to be viable, the laminations must be extremely well preserved, clearly and consistently distinguishable, and continuous for the entire period of interest. In most laminated and varved sediment sequences this is not the case. These methods also detract from actually studying and characterising sediment composition and understanding the process of deposition. Therefore, these rapid approaches can only ever be used alongside conventional counting, for which there is no stand-alone substitution.

Manual counting of the SG06 sediment was performed with help of the freely available *PeakCounter* software (*http://dendro.naruto-u.ac.jp/~nakagawa/*). This program was specifically developed by Takeshi Nakagawa to aid manual varve counting (and other fine-scale analysis) using multi-parameter data from the Itrax™ core scanner.

Using the software, the X-radiograph and the optical images can be viewed adjacently (Fig. III.3). An active window selector plots up to six different parameters derived from the scanner in separate (magnified) windows using the equivalent X-radiograph image as the background image. The active area of the optical image can also be viewed in a separate window, from which greyscale (i.e. surface reflectance), Red Green Blue, and L*a*b* (CIELAB) plots can be derived. In this study, the optical images used alongside element profiles were digital core photographs taken immediately after core retrieval, rather than the optical images taken by the Itrax™ scanner, which were more likely to have been obscured by subsequent oxidation of the sediment surface. A cursor line moves simultaneously in all active windows, making it easy to mark correlating peaks in specified indicator elements (or element ratios) and greyscale plots. Elements that are close to the lower detection limits of the scanner, due either to their low atomic weight or low concentration in the sediment, may result in unrealistically high frequency profile variations (emphasised by the extremely high resolution of the scans). This can be overcome by considering their moving average (3 or 5 neighbouring data points, either equally or centrally weighted). Peaks, as well as sedimentary structures, can be marked and described, with these new data appearing as four additional columns in the output (.csv) file: greyscale from X-radiograph (user selected image area from which values derive), position of annual peak (including signal quality), marker layer number (where available; see Nakagawa et al. 2012), and further notes.

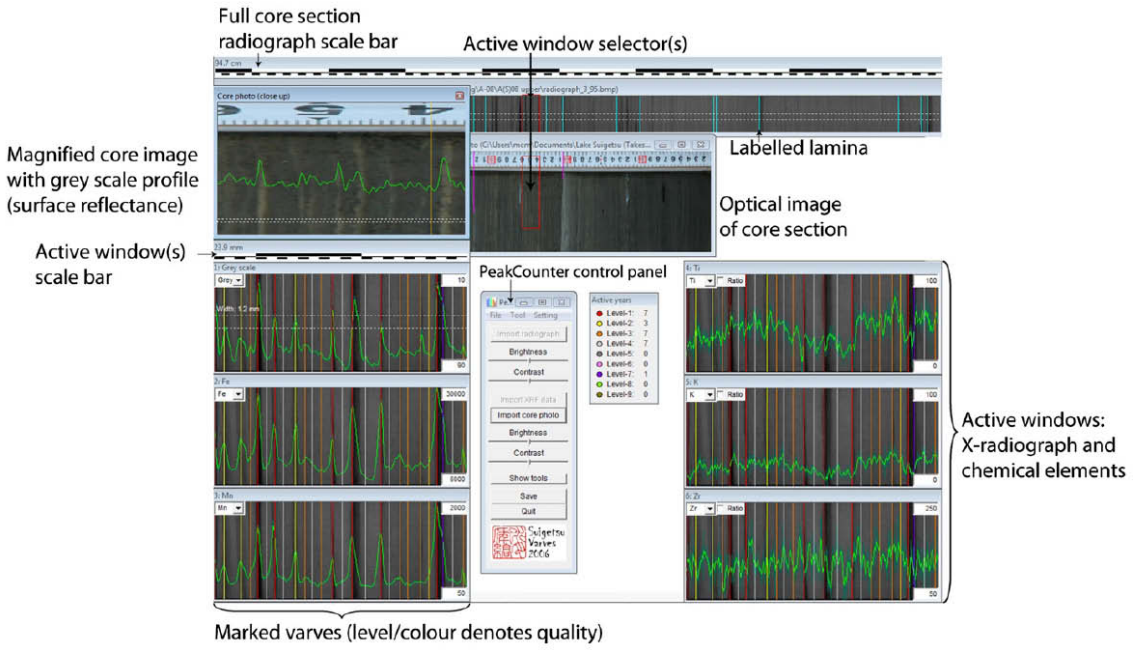

Figure III.3.: PeakCounter 2.0.0 software (*http://dendro.naruto-u.ac.jp/~nakagawa/*) for a multi-parameter approach to varve counting. Note that greyscale from the background X-radiograph is plotted on a reverse y-axis. The varve thickness of the example of core shown is ≈0.8-1 mm.

III.4. Results

III.4.1. Varve structure

The varve structure of core SG06 has been described by Schlolaut et al. (2012), with the most important varve sub-layers being: a diatom-rich layer of the genus *Aulacoseira* (spring), amorphous organic material (summer), siderite (autumn) and clay (autumn/winter). Occasionally, siderite may also form in spring. All seasonal layers are variable in occurrence, with siderite laminae being the most consistently occurring. The μXRF analysis revealed that the siderite is not pure iron carbonate but is enriched in manganese ($[Fe,Mn]CO_3$).

Siderite formation is controlled by changes in the redox conditions within the lake, which determine the chemical nature of the Fe ions at the sediment-water interface (Brauer, 2004). The model of formation was first proposed by Bahrig (1988). The siderite precipitates when oxidised forms of Fe (Fe^{3+} precipitated as hydroxides during lake overturn) are reduced by the decomposition of organic matter (to Fe^{2+}) at the sediment-water interface and brought back into solution, before bonding with the available carbonate (CO_3^{2-}) ions (a product of the degradation of organic matter). The necessary reducing conditions are either established as the sediment-water interface remains anoxic (due to incomplete overturn) or with the onset of re-stratification. Manganese (Mn^{2+}) is also precipitated in this way, either substituting for Fe^{2+} in the $FeCO_3$ crystal lattice or (and rarely) as rhodochrosite. As manganese oxyhydroxides are extremely unstable (compared to ferric hydroxide colloids), complete mixing (no permanent anoxia) of the water column must occur to allow them to reach the sediment-water interface in this form (cf. Dean, 1993). When anoxia is established with the onset of stratification they are likely to be preferentially brought into solution and bond with the bicarbonate ions. Siderite formation not only requires an environment with very low redox potential, but also very low concentrations of sulphur, and thus low fluxes of sulphate, or else pyrite may form.

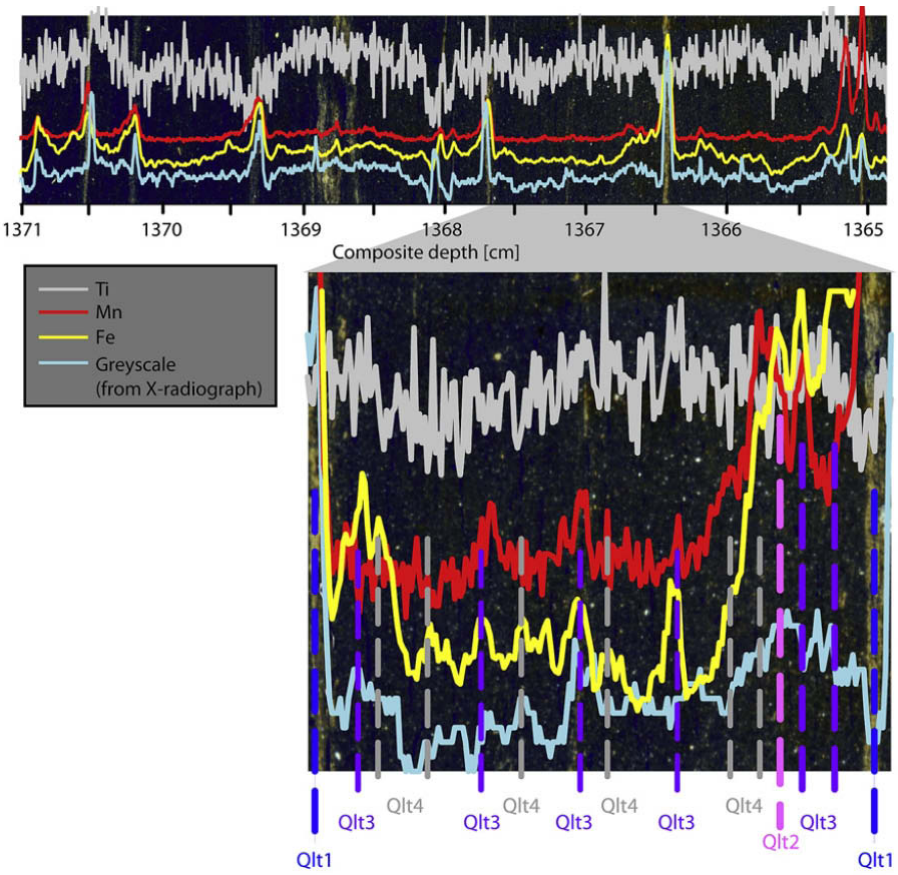

Figure III.4.: Sub-mm comparison from core B(N)07 upper, showing the thin section photograph overlain with indicator μXRF element- and X-radiograph grey scale profiles. Multiparameter peaks of varve sub-layers and corresponding μXRF quality (Qlt) counts are shown.

III.4.2. Varve structure in the μXRF signal

The siderite layers deposited during autumn are clearly evident within the XRF data as distinct and correlating peaks of Fe and Mn, as can be seen in comparison with polarised thin section images (Fig. III.4). The siderite layers are also optically distinct in core photos taken in the field; siderite layers rich in Fe tend to be light reddish-brown, whereas those dominated by Mn are dark brown to black. Furthermore, they are high in density as can be seen in X-radiographic images. Detrital layers are also geochemically distinct, characterised by peaks in the lithogenic elements Ti, K, Rb, and sometimes Zr, and are high in density. These elements are relatively immobile in the surficial environment and are generally insoluble. During transport, by water or wind, Zr, Ti and Rb have a tendency to become concentrated in particular sediment size fractions. According to Oldfield et al. (2003), Zr is concentrated in the silt to fine sand fractions of lacustrine sediments whereas Ti (and Rb) is usually enriched in the clay-size fraction. Thus, autumn/winter clay layers are usually dominated by peaks in Ti, K, and Rb. Larger detrital layers (e.g. turbidites) are often enriched in Zr towards their base, and in Ti, K, and Rb within the top, indicative of grain size sorting. Some detrital layers are also enriched in Ca and result from a change in dominant source lithology and mineralogy.

As autumn siderite layers are the most frequently occurring seasonal layer, and are easily distinguishable in the XRF, X-radiographic and optical signals, counting is mainly based on these. A quality score was assigned to each count, ranging from 1 (excellent quality) to 4 (poor quality). Large and distinct peaks in Fe, Mn, surface reflectance of optical image (greyscale) with a low greyscale from X-radiograph (dark/dense; siderite), and being

immediately below peaks in the lithogenic elements (being indicative of autumn/winter clay layers and thus allowing the distinction between autumn and spring related siderite layers), were marked as 'quality 1' counts (Fig. III.4). Reduced and less distinct, but correlating, peaks in all of the indicator parameters were marked as 'quality 2' counts (Fig. III.4). Further reduced and less distinct peaks, but with correlation between some (two or more) of the parameters, were marked as 'quality 3' counts (Fig. III.4). Low and indistinct peaks in (at least) one parameter were marked as 'quality 4' counts (Fig. III.4). Quality 4 counts therefore represent siderite layers that are extremely indistinct and poorly preserved so that the reliability of these counts is questionable. It is likely that they partially represent 'noise' of diffuse siderite within the background sediment matrix. Also one needs to be aware that spring-related siderite layers are a potential source of error. However, based on microscopic observation, spring siderite layers represent only a minor fraction of all siderite layers (Schlolaut et al., 2012) and the consideration of clay-related parameters, indicative of autumn, further reduces this uncertainty. With respect to the terminology, it must be made clear that the method does not count varves or seasonal layers, but elemental peaks that are related to seasonal layers.

III.4.3. μXRF count results

Counts produced using μXRF are considered for the Last Glacial - Interglacial Transition (LGIT; Fig. III.5). The upper boundary is close to the start of the more clearly laminated core section (1288.0 cm cd) while the lower boundary is during the later stages of the Glacial period (1815 cm cd). In order to compare the count and interpolation results they are anchored at the very top using the base of the distinct SG06-1288 tephra (Nakagawa et al., 2012), which has been dated by Staff et al. (2011) to 10,219 ± 20 cal yr BP (mean ± 1 sigma value; 10,255 to 10,177 cal yr BP 95.4% probability range). For comparison an anchor point at the top is beneficial as resulting curves don't cross each other in figures and cumulative differences can be better distinguished. The final chronology will be anchored further downcore, to minimise cumulative error in varve chronology (see section III.5.2). Chronologically important micro-facies boundaries of the LGIT in SG06 are related to the onset of the LGIT interstadial, equivalent of the North Atlantic Bølling/Allerød, at ≈1729 cm cd, the onset of the LGIT stadial, equivalent of the North Atlantic Younger Dryas, at ≈1554 cm cd and its termination at the Holocene onset at ≈1436 cm cd (Kossler et al., 2011).

Due to the fact that there is likely to be an unknown proportion of 'noise' in the μ-XRF quality 4 counts, two separate datasets are considered; 'μXRF Qlt1-4', where all counts are included, and 'μXRF Qlt1-3', where quality 4 counts are excluded.

The distribution of the different quality counts is shown in Figure III.6. The most distinctive change is a steep decrease of quality 4 counts at the transition from the Glacial to the LGIT interstadial (≈1729 cm cd), which coincides with a clear increase in quality 1 and 2 counts. The LGIT stadial shows the lowest proportion of quality 4 counts, but also a decreased amount of quality 1 counts, relative to the Holocene and LGIT interstadial. In summary, the higher counting uncertainty lies within the Glacial, while the LGIT and Holocene clearly show less ambiguity.

Count reliability was assessed by comparison of counts from overlapping LL-channels (e.g. NU vs. SL - see section III.3.1) as well as from overlapping cores taken from different boreholes. In the former instance, differences were <2% for single overlapping sections as well as for the cumulative difference across the whole studied interval. The total overlap of LL-channels was 255 cm, composed of ≈2950 counts. This shows that the method produces low count errors that compare positively to errors estimated in other studies of <3% (e.g. Zolitschka, 1991; Snowball et al., 1999; Ojala and Tiljander, 2003).

When comparing counts from overlapping cores from different boreholes, an alternative picture emerged. Although differences were low when considering the whole studied core

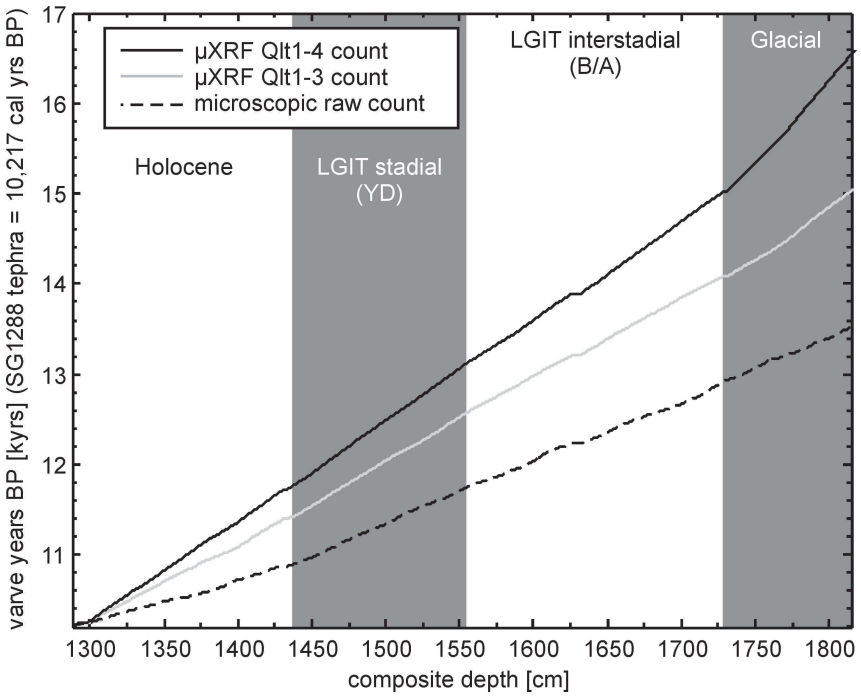

Figure III.5.: Plot showing the age-depth models from raw μXRF (Qlt1-3 and Qlt1-4) and raw microscopic counts. Steps in the models are due to event layers, visible when plotted against composite depth.

interval (μXRF Qlt1-4: 2.2%, μXRF Qlt1-3: 1.6%), they increased when only comparing single overlapping sections between marker layers (μXRF Qlt1-4: up to 13%, μXRF Qlt1-3: up to 10%). A negative correlation between section length and count difference was evident. In overlapping sections of more than 200 counts differences decreased to values of less than 5%, and with more than 350 counts to about 2%. We therefore do not relate these differences to the counting method, but to a limited lateral extension of siderite layers. As a result, layers occurring in a core from one borehole do not necessarily appear in the parallel core as well (boreholes up to 40 m apart). Such differences between cores from different boreholes cancel out over longer core intervals, which is supported by the observation that there is no systematic difference between cores, that is, analysis of any particular single borehole did not consistently result in a greater (or lower) number of siderite layers being identified. Therefore, as a result of their incomplete formation and/or preservation, the number of autumnal siderite layers identified from the composite core profile is less than the actual number of years that passed during deposition. This therefore necessitates interpolation of the incomplete count. Before interpolation the results are compared to those from the independent microscopic varve count.

III.4.4. Comparison with results from microscopic varve counting

Comparison of raw counts

The microscopic varve count results are described in detail in Schlolaut et al. (2012) but shall be briefly summarised here for clarity. There are three microscopic count datasets: (i) the raw count, which includes all counts (ii) the layer quality selective, which excludes low quality counts, and (iii) the section quality selective, which includes only counts from well varved intervals. The number of counts in the three datasets decreases in this order.

The comparison of the count results from the two independent counting approaches show significant offsets, with many more counts made using μXRF (Fig. III.5). The μXRF Qlt1-4 dataset contains 2921 more counts than the microscopic raw count (+88%) while the

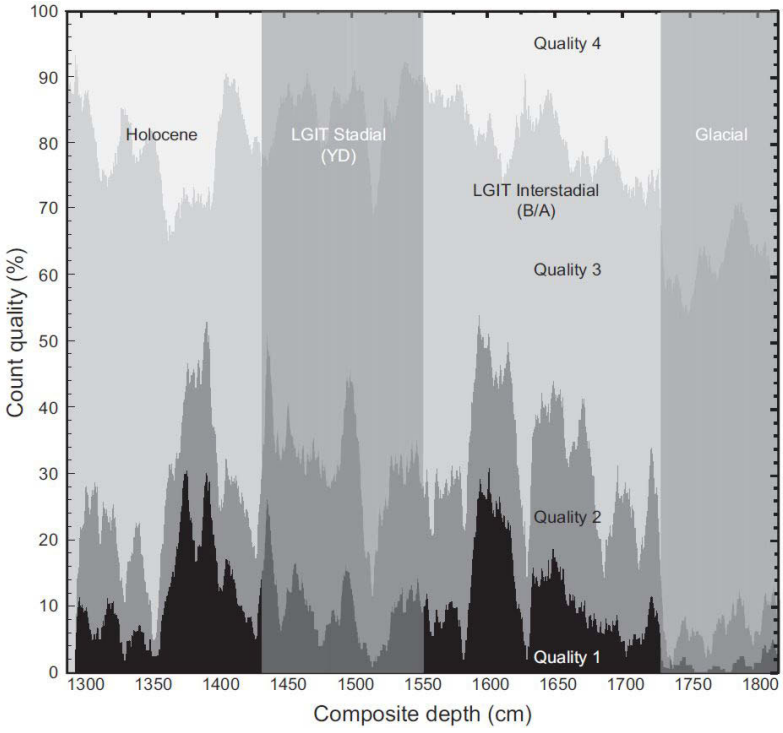

Figure III.6.: Plot showing the distribution of the different quality (Qlt) counts derived from µXRF counting.

µXRF Qlt1-3 dataset contains 1493 more counts (+45%). To better understand these differences, raw data comparisons were made on increasingly small sections of core, from a dm down to a sub-mm scale. On a dm scale, the largest differences were observed where seasonal layer quality was poorest. At a sub-mm scale it became clear that low-magnitude geochemical peaks often have no visible counterpart in the thin sections (Fig. III.4) and are thus the primary cause for the count differences.

Interpolation of µXRF counts

Interpolation of the two µXRF counts (Qlt1-3 and Qlt1-4) was carried out using the Varve Interpolation Program (VIP v1.0.1) from Schlolaut et al. (2012), using the standard settings suggested therein. This new method is based on the automated analysis of frequency distributions of counted annual layers to derive a sedimentation rate estimate that is used for interpolation of the core section where varve preservation is imperfect or formation is irregular. It represents a more objective approach than manual interpolation.

The interpolated µXRF models, with the resulting error estimates, are shown in Figure III.7. Varying the peak value and bin size settings as outlined by Schlolaut et al. (2012) had very little impact on the interpolation results due to the relatively high number of counts in the raw µXRF datasets. The interpolation errors, relative to the respective models, for the µXRF Qlt1-3 model are +0.2% and -2.1%, and for the µXRF Qlt1-4 model are +0.1% and -0.7%. The errors are very low and indicate that an over-interpolation is more likely than an under-interpolation. Both characteristics are the result of the high raw counts, which require only little interpolation. However, the interpolation results of the two models are not parallel (although the divergence has been greatly reduced relative to the raw counts), nor are the errors overlapping, which points towards a systematic count difference.

The difference between the two interpolation results is most pronounced in the Glacial section. Over 40% of the cumulative differences are produced in these 85 cm, with approximately a three-fold increase in the gradient of the difference (Fig. III.8) compared to the

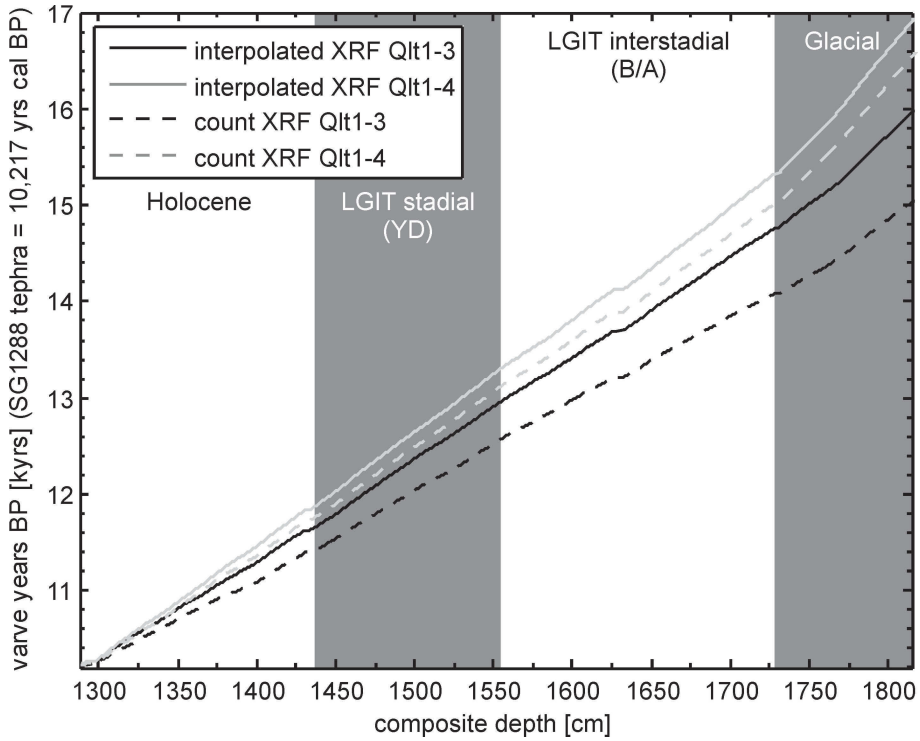

Figure III.7.: Plot showing the two different age-depth models derived from the µXRF counts, including interpolated counts.

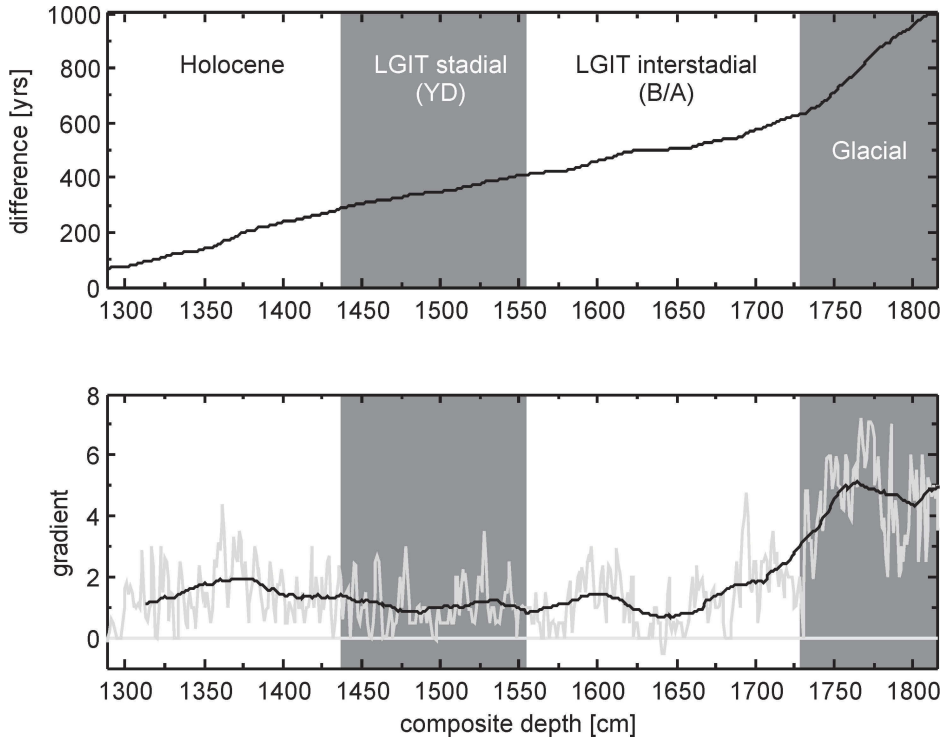

Figure III.8.: Plot showing the difference in years between interpolated µXRF Qlt1-4 and µXRF Qlt1-3 models and the gradient of the difference between interpolated µXRF Qlt1-4 and µXRF Qlt1-3 models.

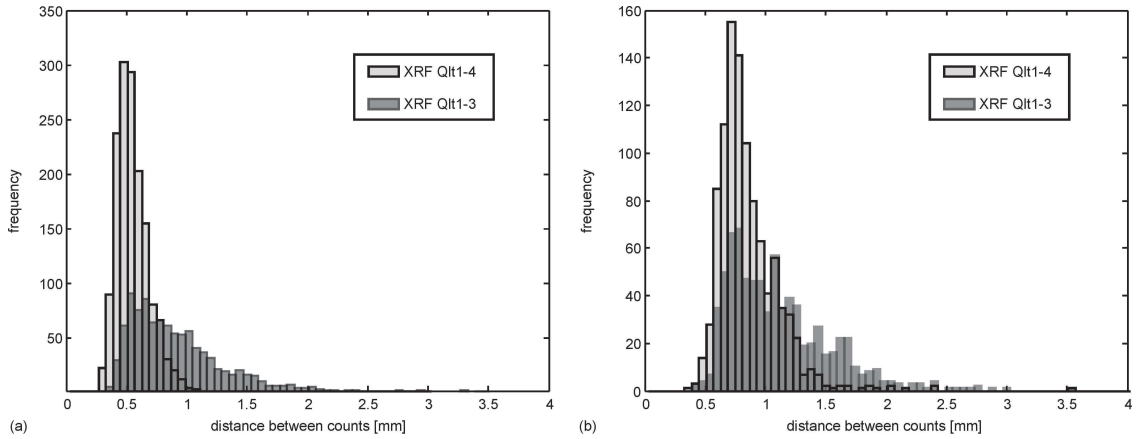

Figure III.9.: a: Plot showing the difference in count distance frequency between μXRF Qlt1-3 and μXRF Qlt1-4 datasets for a core section from the glacial. b: Showing a core section of the same length but just after the end of the glacial.

Late Glacial and Holocene. The main reasons for this behaviour are: (i) a clear decrease in lamination quality (Fig. III.6), which means that a considerable number of counts cannot be detected in the μXRF Qlt1-3 data, and (ii) that most of the low-quality counts occur when the distance between counts is particularly small (Fig. III.9a). Count distances <0.5 mm/yr are scarcely detected by the μXRF Qlt1-3 data. This raises the question if the Qlt4 counts represent primarily noise or a true seasonal signal. Since the percentage of low quality siderite laminae is significantly increased in the Glacial (indicated by the increase in Qlt4 counts and supported by microscopic analysis), the percentage of Qlt4 counts that represent seasonal layers increases as well, reducing the percentage of Qlt4 counts that represent noise, and in turn increasing the reliability of the μXRF Qlt1-4 count. This can be illustrated by consideration of a sediment interval with a perfect quality of laminae, in which all low quality peaks would therefore represent noise. Conversely, in an interval with an extremely bad quality of laminae a significant amount of low quality counts would actually relate to a seasonal signal. In the Late Glacial and Holocene the higher sedimentation rate and better lamination quality result in more similar interpolation results (Fig. III.7). However, there still remains a systematic difference between the two interpolation results. In principle the same two explanations as for the Glacial are possible. Years with low accumulation rates are more frequently associated with low quality laminae, or noise in the μXRF Qlt1-4 data leads to an underestimation of the sedimentation rate. However, the increase in the sedimentation rate and the lamination quality suggest that the latter explanation has a higher impact here. The higher sedimentation rate ensures that all occurring annual accumulation rates are detected in both counts (Fig. III.9b), while the better quality of the siderite laminae decreases the percentage of Qlt4 counts that represent a seasonal signal.

The next step is to compare these results with those from the microscopic varve count in order to resolve such ambiguities, further illustrating the strength of the dual method approach.

Comparison of μXRF with microscopic interpolation results and combination to final SG06 floating varve chronology

The interpolation results from the microscopic varve counts, described in detail by Schlolaut et al. (2012), show that two of the three (raw, layer quality selective and section quality selective) models agree rather well with each other, though not always the same two. An interval that was reported to be associated with considerable uncertainty was that of the Holocene, where two of the three models are believed to produce ages that are

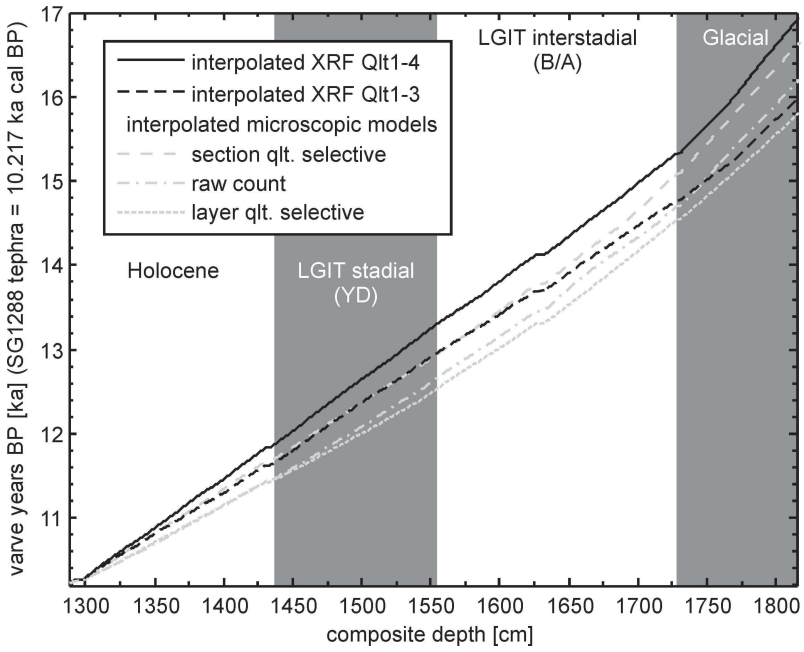

Figure III.10.: Plot showing the individual age-depth models derived from all µXRF and microscopic quality counts.

too young, with the remaining model (section quality selective) providing a rather small basis for interpolation.

When comparing the interpolated µXRF count models with the interpolation results from the microscopic varve count over the whole core interval at least two of the independently-derived models always show a high degree of similarity. A striking feature is the similarity between the interpolated µXRF Qlt1-3 and the microscopic section quality selective dataset in the Holocene and the LGIT stadial (Fig. III.10). However, in some sections single models clearly diverge. For example the µXRF Qlt1-4 data clearly gives older ages than any of the other age models in the Holocene and the LGIT stadial, which indicates that the dataset is compromised by noise. This has implications for LGIT interstadial, as although the µXRF Qlt1-4 data shows an increased similarity with the microscopic age models in this section, there is no sedimentological reason as to why the percentage of µXRF Qlt4 counts that represent noise should decrease. We must therefore consider the µXRF Qlt1-4 dataset to be compromised in the whole LGIT and Holocene sections.

In the Glacial section the agreement between the µXRF and the microscopic age models is variable, with relatively frequent changes in which models are the most similar. However, even the most similar models often agree less well than in the sediment above, which is due to the particularly poor lamination quality in this part of the Glacial. Preliminary data from below 1815 cm cd shows a better agreement again between the age models (especially with µXRF Qlt1-4).

In order to combine the individual age models a tool from the varve interpolation programme is used, which compares the models at 1 cm intervals and selects the two most parallel models for combination (i.e. the mean of the pair of models that gives the closest age increments for the 1 cm interval is used as the final model), as similar models have a higher probability to represent a correct result than diverging ones. In order to ensure equal weighting of the methods one µXRF model and one microscopic model are always used for combination. A manual age model pre-selection is made prior to the automated combination by only including the interpolated µXRF Qlt1-3 dataset in the combination process in the Holocene and LGIT (excluding the interpolated µXRF Qlt1-4) and only including the interpolated µXRF Qlt1-4 dataset in the Glacial (excluding the interpolated µXRF Qlt1-3).

III.5. Discussion

III.5.1. Differences in raw counts

The considerable difference in the raw counts between the two methods (see section III.4.4; Fig. III.5) is explained by the high number of low-quality peaks in the XRF signal. It is thus apparent that Fe and Mn cycling in the lake changed significantly during years which produced low-quality, indistinct counts. The total amount of Fe and Mn deposited decreased considerably, as is evident by the low magnitude of the peaks. A possible explanation for this is a reduced supply of Fe and Mn to the lake, through decreased surface runoff. This is supported by the observation that the best layer quality is found in the LGIT stadial by both counting techniques, and also the demonstration by Kossler et al. (2011) who showed an increased inwash of material into the lake during the LGIT stadial. Alternatively, years with a weaker stratification could have led to less distinct siderite layers being deposited. Furthermore, it is also possible that reducing conditions at the lake floor were not established every year, resulting in dissolution of siderite and/or the formation of Fe (and Mn) oxides or oxyhydroxides, which are not distinguishable under the microscope. Lastly, it must be considered that all of these processes had an impact on the siderite formation/preservation.

III.5.2. Combined count - ^{14}C comparison (to 12,550 cal yr BP)

The age of the final chronology is given in $SG06_{2012}$ vyr BP (varve years before present, where present means 1950 AD; 2012 refers to the model version, and is included to avoid confusion should a revised age model be released in future, for example as result of changes to the interpolation program). The accuracy of this new dual counting approach can be tested by comparison of the combined, final varve model (with errors) to the radiocarbon chronology (Staff et al., 2011) calibrated (but not modelled, as constraining the chronology using varve counts would invite circularity) to the limit of the dendrochronologically dated part of the IntCal09 curve (12,550 cal yr BP; Reimer et al. 2009) at approximately 1530 cm cd. Marker layer B-07-08 (core B07, marker layer 08 (Nakagawa et al., 2012)) is used as the anchor point, which has been dated by Staff et al. (2013a) to 11,241 ± 17 cal yr BP (mean ± 1 sigma value; 11,275 to 11,209 cal yr BP 95.4% probability range) at 1397.4 cm cd. This is different to the anchor point used above for inter-varve model comparison (the SG06-1288 tephra at the top of the varve chronology). The new anchor point (B-07-08, 1397.4 cm cd) is further downcore (but still within the tree ring limit of IntCal09) and therefore partially counteracts the cumulative interpolation error, which increases downcore.

The final LGIT varve age model is depicted in Figure III.11a in comparison to the ^{14}C age model. The varve model shows a high degree of similarity with the calibrated ^{14}C curve. When anchored to B-07-08 the age difference to the modelled U-Oki age is only 7 years (varve model: 11,248 $SG06_{2012}$ vyr BP, ^{14}C model: 11,241 cal yr BP), so considerably smaller than the error estimates of either dating method. This is also a clear improvement in comparison to the purely microscopic varve model from Schlolaut et al. (2012), which had a difference of 73 years (Fig. III.11b). This proves that the accuracy of the final varve model is clearly improved in comparison to the model produced by the more conventional microscope-derived counting method. The low interpolation errors of µXRF models also improve the precision of the final model in comparison to the microscopic model, reducing the errors over the studied core interval to +1.7% and -2.5%. The general similarity between the independent µXRF model and the microscopic model (Fig. III.11b) underlines the robustness of the dual method approach and the resulting final varve model.

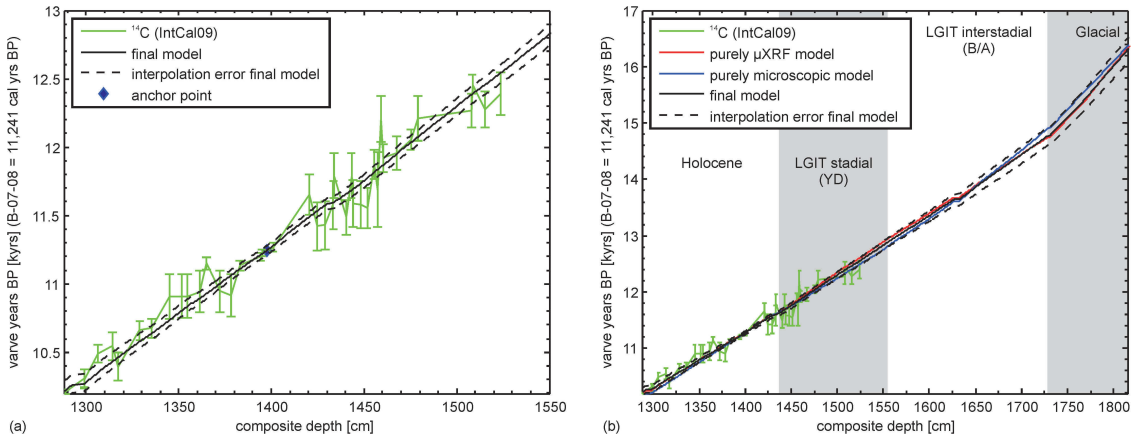

Figure III.11.: a: Plot showing the final varve model with interpolation errors and unmodelled ^{14}C measurements (Staff et al., 2011) calibrated using IntCal09 (Reimer et al., 2009). b: Plot showing individual models derived from µXRF and microscopic quality counts, the resulting final varve model and unmodelled ^{14}C measurements (Staff et al., 2011) calibrated using IntCal09 (Reimer et al., 2009).

III.6. Conclusions

High resolution XRF and X-radiographic core scanning provides the quality of data necessary for accurate geochemical sediment characterisation. The data derived from the Itrax™ µXRF scanner allow a robust, multi-parameter approach to seasonal layer identification and counting, successfully demonstrated here for the Lake Suigetsu sediment, with a high degree of reliability and a low count error. We do not consider it a stand-alone alternative varve counting method to thin-section microscopy because, even with perfect varve formation and preservation, there really is no substitute to thin-section microscopy to properly characterise and understand the physical properties of varved sediments. However, by providing essential, quantifiable geochemical and sediment density data this newly developed method allows discrimination of seasonal layers (and their remnants) that are not identified using thin-section microscopy, and therefore offers a viable companion approach to these more conventional methods. Implementing independent seasonal layer counting using these two approaches allows the internal (to the technique) counting error to be determined and, through the complementary nature of the data, ultimately results in a more accurate and precise varve count model. Although the two approaches produce extremely different raw counts, their necessary interpolation (due to incomplete laminae formation/preservation) results in models that are extremely similar. This supports the accuracy of each independent counting technique as well as the new interpolation method of Schlolaut et al. (2012). The high degree of similarity between the final varve model and the ^{14}C measurements, calibrated using the dendrochronologically-dated part of IntCal09, supports the use of this dual approach to construct a varve chronology to provide the robust and reliable independent calendar age scale for SG06 necessary for the construction of the terrestrial radiocarbon calibration curve to its limit, one of the main goals of the Lake Suigetsu 2006 Varved Sediment Project. It is intended that the future SG06 age-depth model below 1815 cm cd will be further improved by the inclusion of forthcoming data from Ar/Ar and OSL dates (for details see Staff et al. 2013a and Schlolaut et al. 2012).

Acknowledgements

We thank the UK's Natural Environment Research Council (NERC grants NE/D000289/1, NE/ F003048/1, SM/1219.0407/001), the German Research Foundation (DFG grants TA-540/3-1, BR 2208/7-1) and KAKENHI project of Japan (grant 211001002) for funding. We thank Anders Rindby of Cox Analytical Systems for calculating the detection limits of the Itrax scanner using the Suigetsu settings. We thank the anonymous reviewers and the editor for their much appreciated comments on the manuscript. We also thank H. Kitagawa and J. van der Plicht for the inspiration for the project.

IV. Dating the SG06 sediment core: A 40,000 year ^{14}C chronology and constraining the SG06 varve count

This chapter has been published as *A Complete Terrestrial Radiocarbon Record for 11.2 to 52.8 kyr B.P.* by *Christopher BRONK RAMSEY, Richard A. STAFF, Charlotte L. BRYANT, Fiona BROCK, Hiroyuki KITAGAWA, Johannes VAN DER PLICHT, Gordon SCHLOLAUT, Michael H. MARSHALL, Achim BRAUER, Henry F. LAMB, Rebecca L. PAYNE, Pavel E. TARASOV, Tsuyoshi HARAGUCHI, Katsuya GOTANDA, Hitoshi YONENOBU, Yusuke YOKOYAMA, Ryuji TADA and Takeshi NAKAGAWA* in *Science, 2012, Vol 19 370-374*

Abstract

Radiocarbon (^{14}C) provides a way to date material that contains carbon with an age up to ≈50,000 years and is also an important tracer of the global carbon cycle. However, the lack of a comprehensive record reflecting atmospheric ^{14}C prior to 12.5 thousand years before the present (kyr B.P.) has limited the application of radiocarbon dating of samples from the Last Glacial period. Here, we report ^{14}C results from Lake Suigetsu, Japan (35°35′N, 135°53′E), which provide a comprehensive record of terrestrial radiocarbon to the present limit of the ^{14}C method. The time scale we present in this work allows direct comparison of Lake Suigetsu paleoclimatic data with other terrestrial climatic records and gives information on the connection between global atmospheric and regional marine radiocarbon levels.

IV.1. A complete terrestrial radiocarbon record for 11.2 to 52.8 kyr B.P.

Lake Suigetsu contains annually laminated sediments that preserve both paleoclimate proxies and terrestrial plant macrofossils that are suitable for radiocarbon dating. The lake's potential to provide an important archive of atmospheric radiocarbon (^{14}C) was realized in 1993 (Kitagawa and van der Plicht, 1998a). However, the single SG93 sediment core then recovered included missing intervals between successive sections (Staff et al., 2010). This, together with the difficulty of visual varve counting, resulted in inconsistency between the SG93 and other ^{14}C calibration records (van der Plicht et al., 2004). The SG06 core-set recovered in 2006 consists of four parallel cores that together avoid any such sedimentary gaps (Nakagawa et al., 2012). Here, we report 651 ^{14}C measurements covering the period between 11.2 and 52.8 thousand years before the present (kyr B.P.) tied to a time scale derived from varve counting and temporal constraints from other records. Using visual markers, we applied a composite depth (CD) scale to all cores, including SG93. We also define an event-free depth (EFD), which is the CD with substantial macroscopic event layers (such as turbidites and tephras) removed.

Accelerator mass spectrometry radiocarbon dating (for materials and methods see Appendix B) has been conducted on terrestrial plant macrofossils selected from the SG06

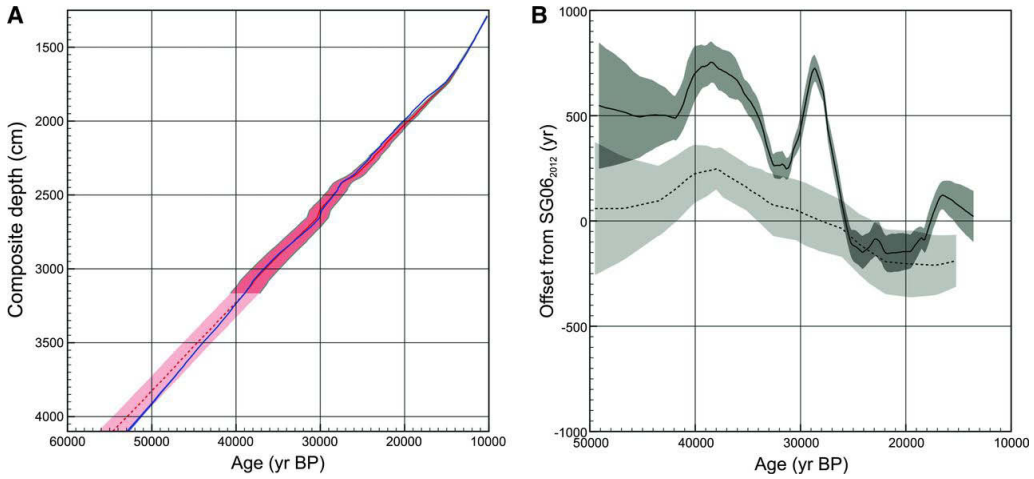

Figure IV.1.: (A) Age-depth model for SG06, based on varves (red), extrapolated by EFD (pink), and constrained by speleothems H82 and GB89-25-3 (blue). (B) Inferred differences in the age models for the Cariaco Basin (Hughen et al., 2006) (solid curves) and Iberian Margin (Bard et al., 2004) (dotted curves) data sets in IntCal09 (Reimer et al., 2009) compared to the SG06$_{2012}$ modeled chronology (higher offset implies that the time scale is older); see Figs. B.9 and B.10

cores to cover the full ^{14}C time range, from the present to the detection limit of the ^{14}C method (0 to 41 m CD) (Table B.1). The results already reported from the control period (0 to 12.2 kyr B.P.) (Staff et al., 2011), covered by the tree-ring-derived calibration curve (Reimer et al., 2009), act to demonstrate the integrity of the sediments and to anchor the floating SG06 varve chronology, because varves do not extend into the Holocene.

The varve-based chronology for SG06 (Appendix B, Marshall et al. 2012; Schlolaut et al. 2012) provides our best estimate of the true age of the cores for the period ≈10.2 to 40.0 kyr B.P., based only on information from the site. It provides good relative chronological precision and has the advantage of being independent of other dating techniques. However, the cumulative counting uncertainty inevitably increases with age (≈6% at 40 kyr B.P.). The full varve chronology (Fig. IV.1A and Table B.1) has been extrapolated on the basis of EFD to cover the period 40 to 53 kyr B.P.

To better constrain the uncertainties in the varve chronology, we can directly compare the Suigetsu data set and other archives that provide information on atmospheric ^{14}C and associated independent ages. The two most useful records for this purpose are the Bahamas speleothem GB89-25-3 (Hoffmann et al., 2010) and the Hulu Cave speleothem H82 (Southon et al., 2012), both of which have extensive ^{14}C- and U-Th-based chronologies. In both cases, we would expect the radiocarbon in the speleothems to respond to changes in atmospheric ^{14}C content, despite the groundwater containing a dead-carbon fraction (DCF) from dissolved carbonates. Estimated DCF for these speleothems was 2075 ± 270 radiocarbon years (^{14}C yr) for GB89-25-3 (Hoffmann et al., 2010) and 450 ± 70 ^{14}C yr for H82 (Southon et al., 2012), each at 1σ. We have modeled these two records onto the SG06$_{2012}$ varve chronology using a Poisson process model (Bronk Ramsey, 2008), which allows for nonlinear random deviation between the SG06$_{2012}$ varve chronology and the U-Th time scale underlying the speleothem records (Appendix B). The model provides independent estimates for the mean DCF of the speleothems of 2500 ± 90 for GB89-25-3 and 440 ± 25 for H82, in agreement with the initial estimates.

The model results can also be used to refine the SG06 chronology by including the constraints provided by the speleothem U-Th dates to 44 kyr B.P. This greatly reduces the uncertainty in the absolute chronology of the age-depth profile (Fig. IV.1A and Table B.1) and ensures that the SG06 data are on a U-Th-moderated time scale. There are

some significant differences between the varve chronology and the model (notably in the period around 12.6 kyr B.P.), possibly associated with changes in the sedimentation rate and sedimentary processes at Suigetsu through that period; however, for most of the core, the agreement between the chronologies is good (Fig. IV.1A), with the ratio between the varve-only and model-inferred deposition rates being 1.01 ± 0.10.

The modeled chronology ($SG06_{2012}$ yr B.P.) is based on all of the available information from both Suigetsu and the other long records of atmospheric radiocarbon. This precise time scale (subcentennial 1σ uncertainties to ≈25 kyr B.P.) allows us to place the detailed paleoclimate data from Suigetsu in a global context, facilitating the identification of potential leads and lags in climate change recorded in key paleoenvironmental archives.

The 651 terrestrial radiocarbon dates from the period 11,241 to 52,820 $SG06_{2012}$ yr B.P. provide a quasi-continuous record of atmospheric ^{14}C for this period (Fig. IV.2), for which the current calibration curve (Reimer et al., 2009) is largely based on reservoir-affected marine data. As such, the Suigetsu calibration data set provides the first backbone upon which a comprehensive atmospheric calibration curve can be built. It will allow, for example, the archeology related to the extinction of Neanderthals and spread of anatomically modern humans into Europe to be calibrated against terrestrial reference data. With its high density of ^{14}C measurements, this data set also allows direct linking between SG06 and any other paleoenvironmental record with terrestrial radiocarbon data.

In addition to its importance for radiocarbon calibration and correlation between different climate records using radiocarbon, a full record of atmospheric ^{14}C has important implications for our understanding of the carbon cycle. The links between atmospheric ^{14}C and primary production are key, as is the connection between the atmosphere and the ocean. Figure IV.3 shows the inferred level of radiocarbon in the atmosphere ($\Delta^{14}C$) at Lake Suigetsu, compared to the ^{10}Be record from Greenland (*Muscheler, personal communication*)(GRIP and GISP2 ^{10}Be flux (Muscheler et al., 2005) are corrected onto the GICC05 time scale (Svensson et al., 2008)). The peak in ^{10}Be production around 41 kyr B.P., assumed to be enhanced by the Laschamp geomagnetic excursion (Muscheler et al., 2005), is clearly visible in the Suigetsu data; the similar timing indicates congruence between the $SG06_{2012}$ and North Greenland Ice Core Project (NGRIP) GICC05 (Svensson et al., 2008) time scales at this point.

Agreement between the Suigetsu radiocarbon record and those of the speleothems (GB89-25-3 and H82) is generally good (Fig. IV.2, A and B), though for the period 28-32 $SG06_{2012}$ kyr B.P., the implied reservoir offset for GB89-25-3 seems higher than for the older sections (Fig. IV.2A). Another ^{14}C record of great importance is the European Late Glacial Pine (LGP) record (Kromer et al., 2004). Figure IV.2C shows the match of this record to that of Suigetsu. The match puts the younger end of the LGP sequence at 12627 ± 35 yr B.P. and gives the average radiocarbon offset of Suigetsu to the LGP data set as 8 ± 6 ^{14}C yr (older). Our modeling supports the fit provided by the linkage of the LGP to Tasmanian Huon Pine (Hua et al., 2009), rather than the suggested ^{10}Be-based fit to NGRIP (Muscheler et al., 2008).

We have used the radiocarbon sequence from Lake Soppensee, Switzerland, as an example of direct comparison with European varved lake sediments (Hajdas et al., 1993). This enables us to place the climate proxy signal associated with the Younger Dryas onset at Soppensee at 12607 ± 85 $SG06_{2012}$ yr B.P., some 156 ± 88 years later than cooling in Suigetsu, which, assuming congruence with GICCO5, probably lags the rapid cooling in Greenland (but only by 83 years, which could be synchronous within error margins). The match to Soppensee also enables us to place the European tephra marker of the Laacher See at 12842 ± 53 $SG06_{2012}$ yr B.P., which agrees well with the independent age estimate of 12880 ± 40 varve years (vyr) B.P. in Meerfelder Maar, Germany (Brauer et al., 1999).

Direct comparison of the terrestrial radiocarbon signal from Suigetsu can also be made to that recorded in marine archives. The long records from the Cariaco Basin, west Atlantic

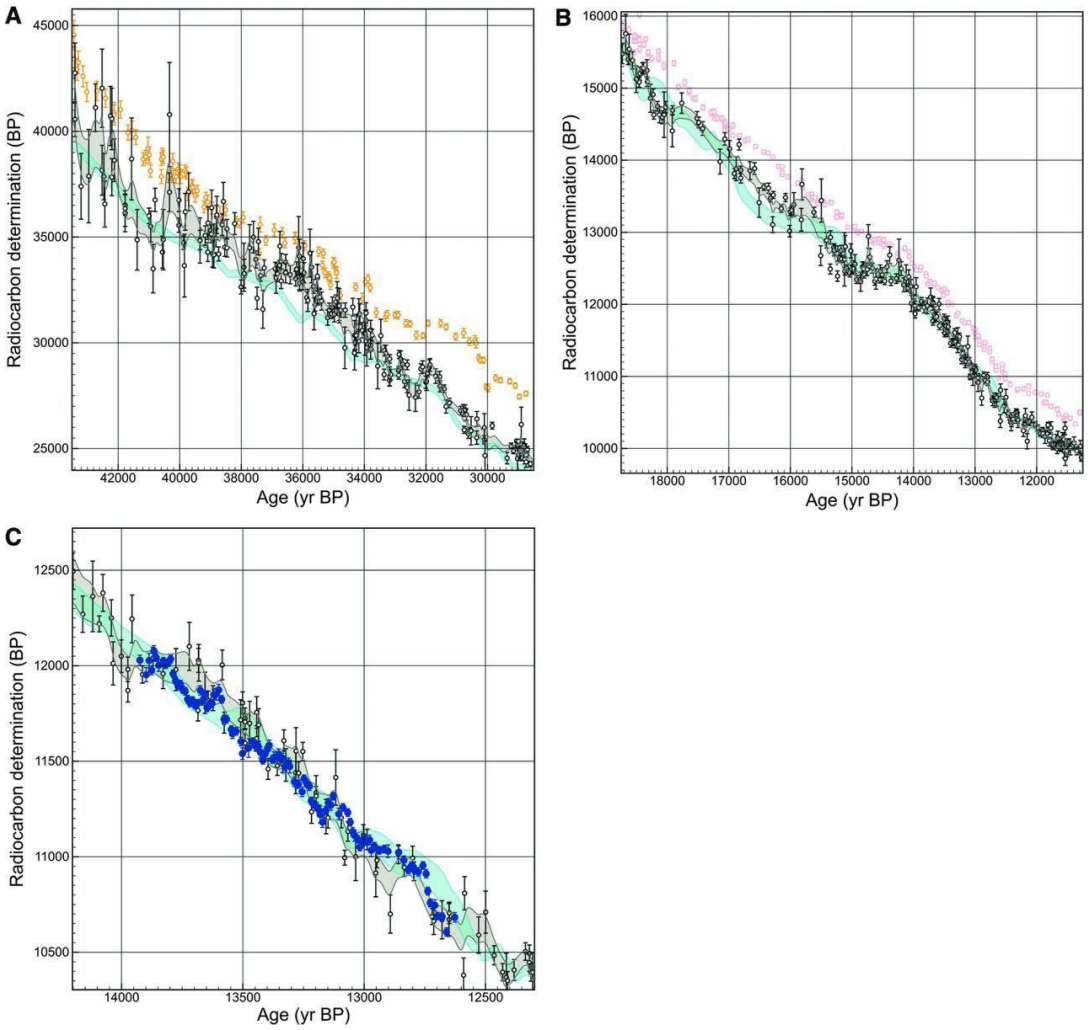

Figure IV.2.: Comparison of raw (black) and five-point moving mean (gray) Lake Suigetsu ^{14}C data against IntCal09 (Reimer et al., 2009) (light blue), as well as (A) GB89-25-3 data (Hoffmann et al., 2010) (orange), (B) H82 speleothem data (Southon et al., 2012) (pink) for the latter part of the H82 time scale, and (C) the LGP record (Kromer et al., 2004) (blue). Whereas the match to the LGP data are good for most individual data points, the match would be improved if the $SG06_{2012}$ chronology were stretched by ≈5% over this period (possible within errors). See also Fig. B.6. Error bars denote 1σ.

(Hughen et al., 2006), and the Iberian Margin record, northeast Atlantic (Bard et al., 2004), are climatically tuned to the Hulu Cave U-Th chronology. By constraining the total marine reservoir age for these two locations within reasonable limits (Appendix B), we are able to quantify offsets between the tuned chronologies and that of SG06 (Fig. IV.1B). The Iberian Margin time scale is mostly consistent with SG06 (within uncertainties), except that it is ≈200 years older at ≈40 kyr B.P. and ≈200 years younger at ≈15 kyr B.P. The latter could be due to greater reservoir ages in the northeast Atlantic at the Last Glacial Maximum (LGM) than have previously been allowed. The Cariaco Basin time scale seems consistent with that for SG06 back to ≈26 kyr B.P., at which point there is a discrete peak (amplitude ≈500 years), perhaps due to specific choices in the climate-tuning. At ≈40 kyr B.P., the Cariaco time scale, like that of the Iberian Margin, is older than that of $SG06_{2012}$, but by a much greater extent (≈700 years). Given that both records are tuned to the same (Hulu) chronology, these differences are more likely to be due to lags in different regional

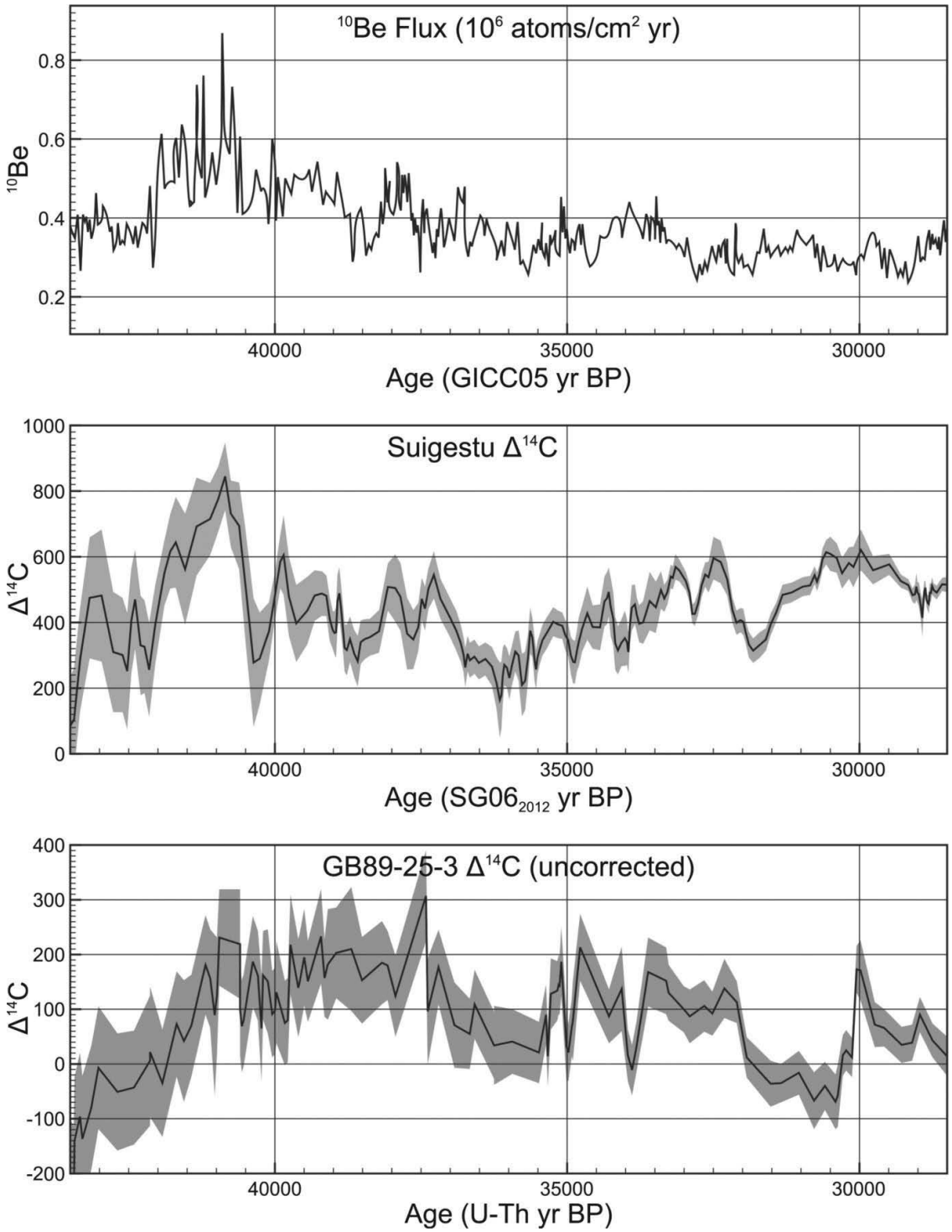

Figure IV.3.: Inferred Δ^{14}C values from Lake Suigetsu compared to data from GB89-25-3 (Hoffmann et al., 2010) uncorrected for DCF. The ^{10}Be flux in Greenland (*Muscheler, personal communication*) is shown for comparison (GRIP and GISP2 ^{10}Be flux (Muscheler et al., 2005) are corrected onto the GICC05 time scale (Svensson et al., 2008)).

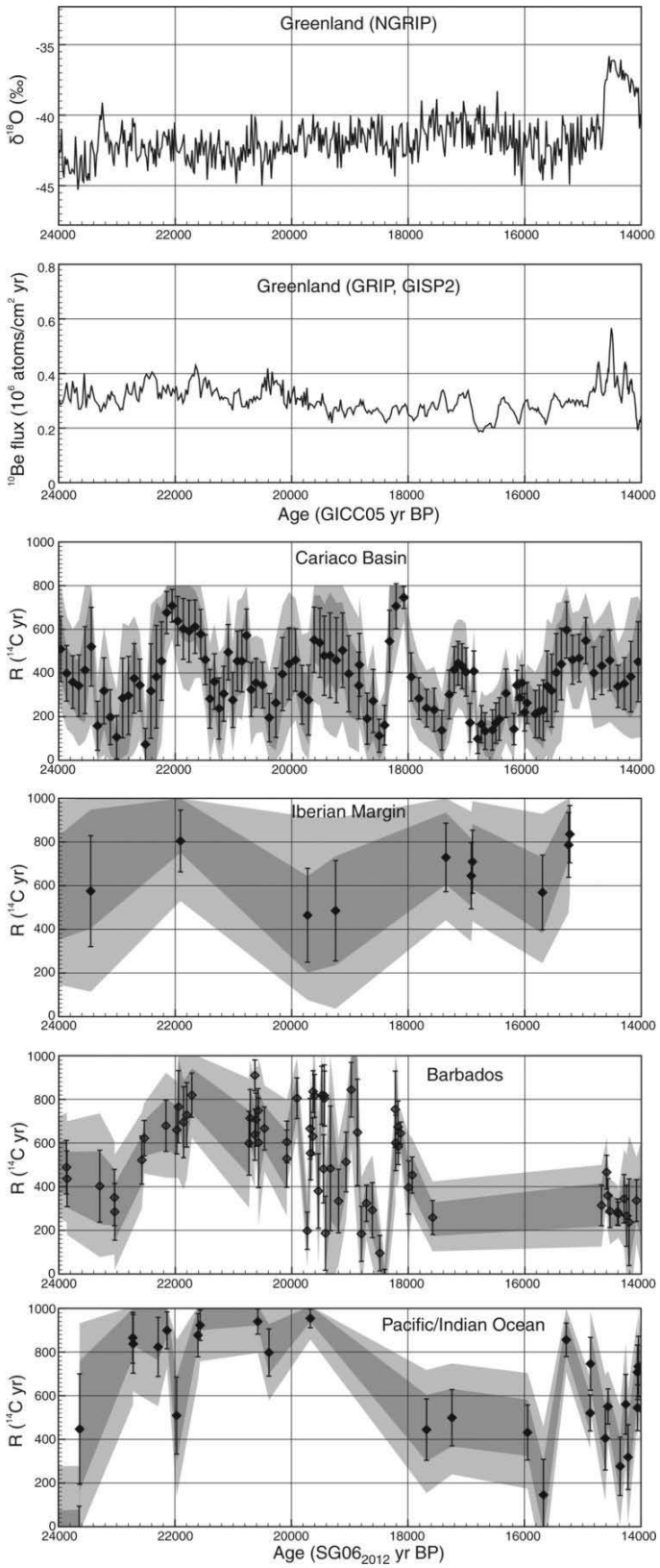

Figure IV.4.: Marine reservoirs relative to atmosphere (R), as deduced from the Suigetsu data on the modeled $SG06_{2012}$ chronology. For comparison, we show the ^{10}Be flux (*Muscheler, personal communication*) (GRIP and GISP2 ^{10}Be flux (Muscheler et al., 2005) are corrected onto the GICC05 time scale (Svensson et al., 2008)) and the δ^{18}O signal from Greenland on the GICC05 time scale (Svensson et al., 2008).

environmental responses to global climate rather than offsets between the fundamental time scales of Hulu and GB89-25-3 (and, hence, $SG06_{2012}$) over this period.

We can also infer total marine reservoir age (R) from these models (Fig. IV.4 and Fig. B.11). In general, most of the signal we see for the Cariaco Basin is due to greater fluctuations in the $\Delta^{14}C$ of the atmosphere from that recorded in marine sediments. Some of the features mirror those of the ^{10}Be production rate in Greenland and might be related to ^{14}C production, others may reflect changes in local ocean dynamics. Although there are fewer data from the Iberian Margin, the rise in R between 16 and 15 kyr B.P. is still apparent, and there is a higher reservoir age inferred at ≈22 kyr B.P., during the LGM.

For the marine coral data from IntCal09 (Reimer et al., 2009), we additionally have direct U-Th dates; thus, R can be calculated more directly. Coral data, however, are not available at regular intervals, so we do not have a continuous record. Pacific coral data (Reimer et al., 2009) in the range 30 to 39 kyr B.P. are consistently higher in $\Delta^{14}C$ than the terrestrial data from Suigetsu (Fig. B.12). We have to deduce that either the $SG06_{2012}$ time scale is substantially too young (a hypothesis not supported by the Iberian Margin data, identification of the Laschamp event as compared to Greenland, or the speleothem data used to correct the modeled $SG06_{2012}$ time scale) or some of the coral data have elevated U-Th ages or overestimated ^{14}C measurements (more likely, given the range of ^{14}C measurements on some coeval samples). It is clear that R for the Pacific and Barbados corals (Reimer et al., 2009), as for the Cariaco Basin and the Iberian Margin foraminifera, is greater at ≈22 kyr B.P. (Fig. IV.4) - possibly a consequence of lower global CO_2 during the LGM. In the period around 16 to 14 kyr B.P., there is a similar pattern in the Pacific/Indian Ocean as in Cariaco: a rapid rise in R, followed by a gradual fall.

The terrestrial radiocarbon record from Lake Suigetsu presented here, together with Holocene measurements (Staff et al., 2011), comprises 808 radiocarbon determinations from two core sites in the center of the lake, measured by three laboratories. Together, these give us a single, quasi-continuous record of purely atmospheric ^{14}C covering the full range of the radiocarbon technique. This will greatly benefit calibration of terrestrial radiocarbon samples in the period 12.5 to 52.8 kyr B.P. and will enable direct correlation between other key climate records and the Lake Suigetsu record itself, without any assumptions of climatic synchrony. An atmospheric record of ^{14}C over this whole time scale also facilitates a more comprehensive understanding of the long marine records in their oceanic context, rather than simply assuming that they represent atmospheric ^{14}C.

V. Palaeo-environmental information: Event layers and a 40,000 year flood record from Lake Suigetsu

This chapter has been submitted as *Event layers in the Japanese Lake Suigetsu 'SG06' sediment core: description, interpretation and climatic implications* by *Gordon SCHLOLAUT, Achim BRAUER, Michael H. MARSHALL, Takeshi NAKAGAWA, Richard A. STAFF, Christopher BRONK RAMSEY, Henry F. LAMB, Charlotte L. BRYANT, Rudolf NAUMANN, Peter DULSKI, Fiona BROCK, Yusuke YOKOYAMA, Ryuji TADA, Tsuyoshi HARAGUCHI and Suigetsu 2006 Project Members* to *Quaternary Science Reviews*

Abstract

Event layers in lake sediments are representatives of past extreme events, mostly the results of floods or earthquakes. Detailed characterisation of the layers allows the discrimination of the sedimentation processes involved, such as surface runoff, landslides or subaqueous slope failures. These processes can then be interpreted in terms of their triggering mechanisms. Here we present a 40 kyr event layer chronology from Lake Suigetsu, Japan. The event layers were characterised using a multi-proxy approach, employing light microscopy and μXRF for microfacies analysis. The vast majority of event layers in Lake Suigetsu was produced by flood events (362 out of 369), allowing the construction of the first long-term, quantitative (with respect to recurrence) and well dated flood chronology from the region. The flood layer frequency shows a high variability over the last 40 kyr, and it appears that extreme precipitation events were decoupled from the average long-term precipitation. For instance, the flood layer frequency is highest in the Glacial at around 25 kyr BP, at which time Japan was experiencing a generally cold and dry climate. Other cold episodes, such as Heinrich Event 1 or the Late Glacial stadial, show a low flood layer frequency. Both observations together exclude a simple, straightforward relationship with average precipitation and temperature. We argue that, especially during Glacial times, changes in typhoon genesis/typhoon tracks are the most likely control on the flood layer frequency, rather than changes in the monsoon front or snow melts. Spectral analysis of the flood chronology revealed periodic variations on centennial and millennial time scales, with 220 yr, 450 yr and a 2000 yr cyclicity most pronounced. However, the flood layer frequency appears to have not only been influenced by climate changes, but also by changes in erosion rates due to, for instance, earthquakes.

V.1. Introduction

Earthquakes and precipitation induced floods are two of the major natural hazards faced in Japan, resulting in the loss of human life and the destruction of infrastructure. For a better understanding of how these risks develop over long time scales, palaeo-records are

necessary since instrumental records only cover recent history. Both kinds of events can leave an imprint on lake sediments (Arnaud et al., 2002; Beck, 2009; Lauterbach et al., 2012; Gilli et al., 2013), enabling the construction of respective chronologies. Lacustrine flood chronologies especially have received increased attention in recent years, since lake sediments are an ideal archive for such studies (Moreno et al., 2008; Vasskog et al., 2011; Kämpf et al., 2012; Gilli et al., 2013) as they are part of the hydrological system and can record flood events as distinct detrital layers (Sturm and Matter, 1978; Mangili et al., 2005; Brauer et al., 2008) over time frames of up to $10^{4\text{-}5}$ years. Furthermore, when these sediments are annually laminated (varved), they also provide excellent chronological control (Cockburn and Lamoreux, 2007; Czymzik et al., 2010; Swierczynski et al., 2012). Such datasets can help us to gain a better understanding of how global climate change forces changes in local to regional flood regimes. However, detailed microfacies analysis of such event layers is necessary in order to distinguish flood events from other major depositional events, such as landslides or subaqueous slope failures (Wilhelm et al., 2012; Swierczynski et al., 2012; Czymzik et al., 2013), which in turn are often the result of earthquakes.

The study of palaeo-floods in Japan has so far mainly relied on the analysis of geomorphological features and sedimentological analysis of fan and terrace deposits, suggesting higher flood magnitudes during the Holocene than during the Last Glacial Maximum (LGM) (Oguchi et al., 2001; Grossman, 2001). However, such studies produce more qualitative than quantitative results. Here we present a 40 kyr event layer stratigraphy from the Lake Suigetsu sediment. The entire Suigetsu composite sediment sequence is about 73 m, which is estimated to cover the last 150 kyr (Nakagawa et al., 2012), with varves occurring between ≈10 and ≈70 kyr BP (Staff et al., 2013a). The first (English) description of the event layers in the Lake Suigetsu sediment was published by Katsuta et al. (2007), who used data from a Scanning X-ray Analytical Microscope (SXAM). They analysed a 6 m long section of the 16 m long 'SG3' piston core recovered in 1993 (Kitagawa et al., 1995). Katsuta et al. (2007) used three tephras as age control points and analysed a core interval that they estimated to be between 19,010 and 5,670 yr cal BP. They counted 30 event layers (excluding tephras) and identified two types: turbidites and clay layers, which they interpreted to derive from earthquakes (turbidites) and floods (clay layers).

In this study we use the composite 'SG06' profile, recovered in 2006 from four bore holes, which is entirely continuous and contains the complete Lake Suigetsu sediment sequence (Nakagawa et al., 2012). The event layers were analysed in the top ≈31 m, which are robustly dated (Bronk Ramsey et al., 2012) and which represent the last ≈40 kyr. A multi-proxy approach was applied, utilising thin section microscopy, micro X-ray fluorescence (μXRF) scanning and core photographs.

V.1.1. Study site

Lake Suigetsu is situated in Fukui prefecture on the west coast of Honshu Island, central Japan. It is part of a tectonic lake system (Mikata Five Lakes) with the active Mikata fault running N-S less than 2 km to the east (Fig. V.1). The lake is approximately 2 km in diameter and has a maximum water depth of 34 m (Nakagawa et al., 2005).

In AD 1664 a canal was built connecting Lake Suigetsu with Lake Kugushi, which resulted in the inflow of salt water (Masuzawa and Kitano, 1982; Kondo et al., 2009). The reason for the channel construction was an earthquake in AD 1662, which displaced the outlet of the lake system, resulting in a lake level rise and the inundation of rice fields and villages around the lakes (Kawakami et al., 1996). The channel was built as drainage for the lake system.

The lake system is fed with fresh water by the Hasu River, which flows into Lake Mikata, which in turn is connected to Lake Suigetsu by a shallow (<4 m deep) sill. In this setting Lake Mikata acts as a natural filter for coarse detrital material from the Hasu

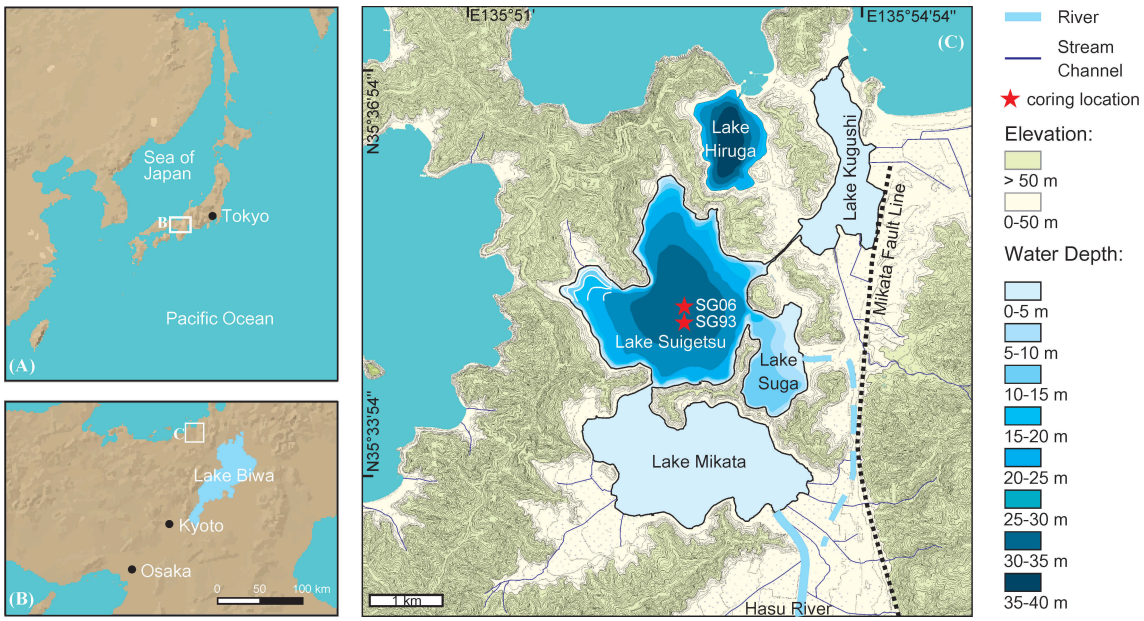

Figure V.1.: Location of Lake Suigetsu (modified after Nakagawa et al. (2012) and topographic map of the Geospatial Information Authority of Japan). The dashed river line shows the hypothesised palaeo river bed of the Hasu River. White bathymetric lines in the western cove of Lake Suigetsu are manually interpolated.

River catchment (Nakagawa et al., 2005), resulting in sedimentation of predominantly autochthonous and authigenic material (Schlolaut et al., 2012).

The geology around Lake Suigetsu is dominated by a large granite pluton to the E and SE. To the S mudstone dominates, but also sandstone, chert, limestone, basalt and dolerite occur. At the NE coast of the lake sandstone occurs, while at the N and W coast basalt, dolerite and chert are dominant (*geological map of the Geological Survey of Japan, Agency of Industrial Science and Technology, 2002*).

The climate at Lake Suigetsu is influenced by the East Asian Monsoon (EAM) system, with the site being north of the monsoon front in winter and south of it in summer (Nakagawa et al., 2006). The summer rainy season lasts from June to July and can lead to catastrophic floods (Fukutome et al., 2003). Precipitation is also high during winter when dry and cold monsoon winds from the Asian continent pick up heat and moisture from the Sea of Japan, leading to increased snowfall along the central western shore of Japan (Takano et al., 2008). The heat is provided by the Tsushima current, which is a branch of the warm Kuroshio current entering the Sea of Japan. Furthermore, Japan is frequently affected by typhoons, for which the peak season is August to September.

V.2. Materials and methods

Core photographs, thin sections and thin section scans were used to identify event layers, and µXRF data to additionally characterise these geochemically. Identification was based on the layers' colour and internal structure. They were considered event layers when they were distinct in both the core photograph and the thin section, and when they were macroscopically identifiable, i.e. when they were clearly distinguishable with the naked eye in the core photograph and the thin section scan. This translates into a minimum thickness of about 1 to 2 mm. Tephras were not considered in this study (results from tephra analysis can be found in Smith et al. (2013)). For the upper 1288 cm composite depth (cd - model version 24Aug2009 (Nakagawa et al., 2012)) of the profile no thin sections and no µXRF data were available, as both methods were primarily intended

for varve counting and lamination is generally poor above 1288 cm cd (≈10,200 yr BP). Hence, event layer identification was based solely on core photographs in the upper part. As a result, the reliability of the dataset is reduced there. However, based on experience from the lower core section, impairment of the identification and classification of layers is expected to be minor. Therefore, the reliability of the dataset in the upper core section is considered acceptable. The analysis was carried out down to 3167.7 cm cd, which marks the current lower end of the varve count-based age model (Bronk Ramsey et al., 2012).

The event layer list presented here is not identical with the event layer list used for calculating the event free depth used in other SG06 publications for interpolating age models (Bronk Ramsey et al., 2012; Schlolaut et al., 2012), where a minimum thickness of about 4 mm for event layers was used, and in which tephra layers were included.

The nomenclature used here is EL for event layer followed by the composite depth of the base of the layer (in cm), e.g. EL-3165.4.

V.2.1. Core photographs

Digital core photographs were taken directly after core opening in the field, before colour changes due to oxidation could occur. The pictures were taken under natural daylight and include a scale and a colour chart (Nakagawa et al., 2012).

V.2.2. Thin section microscopy

For thin section preparation the sediment in the LL-channels (Nakagawa et al., 2012) was cut into 10 cm long segments and freeze-dried. Afterwards, the samples were impregnated with synthetic resin under vacuum. The blocks produced were glued to glass slides with the same resin and then cut, ground and polished down until a ≈20 µm thin slice remained on the glass slide (Brauer and Casanova, 2001). A petrographic microscope with magnification from 25× to 400× was used for analysis. Additionally, thin sections were scanned in polarised light with a 1,200 dpi resolution. These thin section scans provide an ideal tool to link core photographs and thin sections, using standard image processing software.

V.2.3. µXRF analysis of core material

For µXRF analysis continuous measurements were made from 1288 cm cd to the base of the core with an ITRAX core scanner on the sediment in the LL-channels. The distinctive feature of the ITRAX core scanner is the generation of a flat X-ray beam, measuring a rectangular window rather than a single spot. In this way, grain to grain variances are averaged across the horizontal core axis. For the Suigetsu sediment a 20 × 0.1 mm rectangular beam was used, with a step-size of 60 µm, a count time of 4 s, a voltage of 30 kV, a current of 30 mA and a Mo X-ray tube. A more detailed description of the settings used is given by (Marshall et al., 2012).

V.2.4. XRF analysis of catchment samples

In a pilot study 23 catchment samples from around the lake and the proximal watershed of the Hasu River were analysed. Samples included soils, rocks, stream and rivulet sediments. The samples were freeze-dried, powdered and sieved to <62 µm particle size. Samples were prepared as fused disks of Li tetraborate-metaborate (FLUXANA FX-X65, sample-to-flux ratio 1:6). A Panalytical Axios Advanced wavelength-dispersive spectrometer and matrix correction programs were used to calculate concentrations. H_2O^+ and CO_2 were determined using a Vario EL III (ElementarAnalysensysteme GmbH, Hanau/Germany) by means of high-temperature catalytic combustion.

V.2.5. Age model

The age model of the SG06 core (Staff et al., 2013a) after 11.2 kyr BP uses high resolution ^{14}C data from SG06 modelled on to the IntCal09 calibration curve (Staff et al., 2011; Reimer et al., 2009), while the older part is based on a varve count chronology, which has been created using a dual-method counting approach utilising thin section microscopy and μXRF measurements (Schlolaut et al., 2012; Marshall et al., 2012). This varve chronology was then constrained by the Bahamas speleothem GB89-25-3 (Hoffmann et al., 2010) and the Hulu Cave speleothem H82 (Southon et al., 2012) U-Th chronologies, using the low frequency ^{14}C signal from Lake Suigetsu to link with the ^{14}C data from the speleothems (Bronk Ramsey et al., 2012). The resulting chronology is given in "$SG06_{2012}$ yr BP".

V.3. Results

V.3.1. Sediment characterisation and major facies changes

The Lake Suigetsu sediment consists of organic material, diatoms, siderite and detrital mineral grains. All of these components occur diffusely (i.e. form the sediment matrix), but also as distinct (seasonal) layers (Schlolaut et al., 2012). From the top down to 3095.9 cm cd the analysed core section is usually dominated by the autochthonous components, while below it contains a higher proportion of detrital mineral grains. The boundary between the two facies is marked by the top of event layer EL-3107 (event layer type II, see section V.3.2 and Fig. V.3). The facies change is evident in the μXRF signal too, showing a clear drop in Ti, K and Ca in the upper core section. It is also visible in the core photograph, where the colour changes from a light grey in the lower part to a dark grey in the upper.

V.3.2. Event layer types

A total of three different event layer types were distinguished by microfacies analysis, labelled type I, II and III. The total number of event layers is 369, from which 362 are type I, 2 are type II and 5 are type III.

For characterising the clastic event layers in the SG06 profile by μXRF, the elements Ti, K, Ca and Si are most suitable. Ti is a well established tracer element for terrigeneous input (e.g. Yarincik and Murray, 2000), K indicates the presence of clays and/or K-feldspar and Ca may derive from detrital carbonates or plagioclase. The Si signature of the event layers is not as distinct as that of the other elements - the reason being that the sediment is rich in diatoms and hence generally rich in Si. Therefore, the Si signal in the event layer is only slightly elevated compared to the surrounding sediment. However, it is the most suitable element to distinguish the I-B sub-layer in type I event layers (see below). Additionally, Fe and Mn were considered as these two elements play a major role in the hydrology and sedimentation of the lake (Katsuta et al., 2006, 2007; Marshall et al., 2012).

Event layer type I

Event layer type I comprises four main sub-layers (Fig. V.2). The base sub-layer (I-A) consists primarily of quartz and feldspar intermingled with autochthonous components, mainly diatoms and amorphous organic material, but also leaf and wood fragments. The detrital minerals in this sub-layer reach grain sizes of coarse silt and show no significant grading.

The following sub-layer, I-B, consists of quartz and feldspar and, towards the top, also clay. The sub-layer contains only very minor amounts of autochthonous material. No plant fragments are found in this or the following sub-layers. The sub-layer shows distinct normal grading, starting with medium to fine silt, decreasing to clay sized minerals.

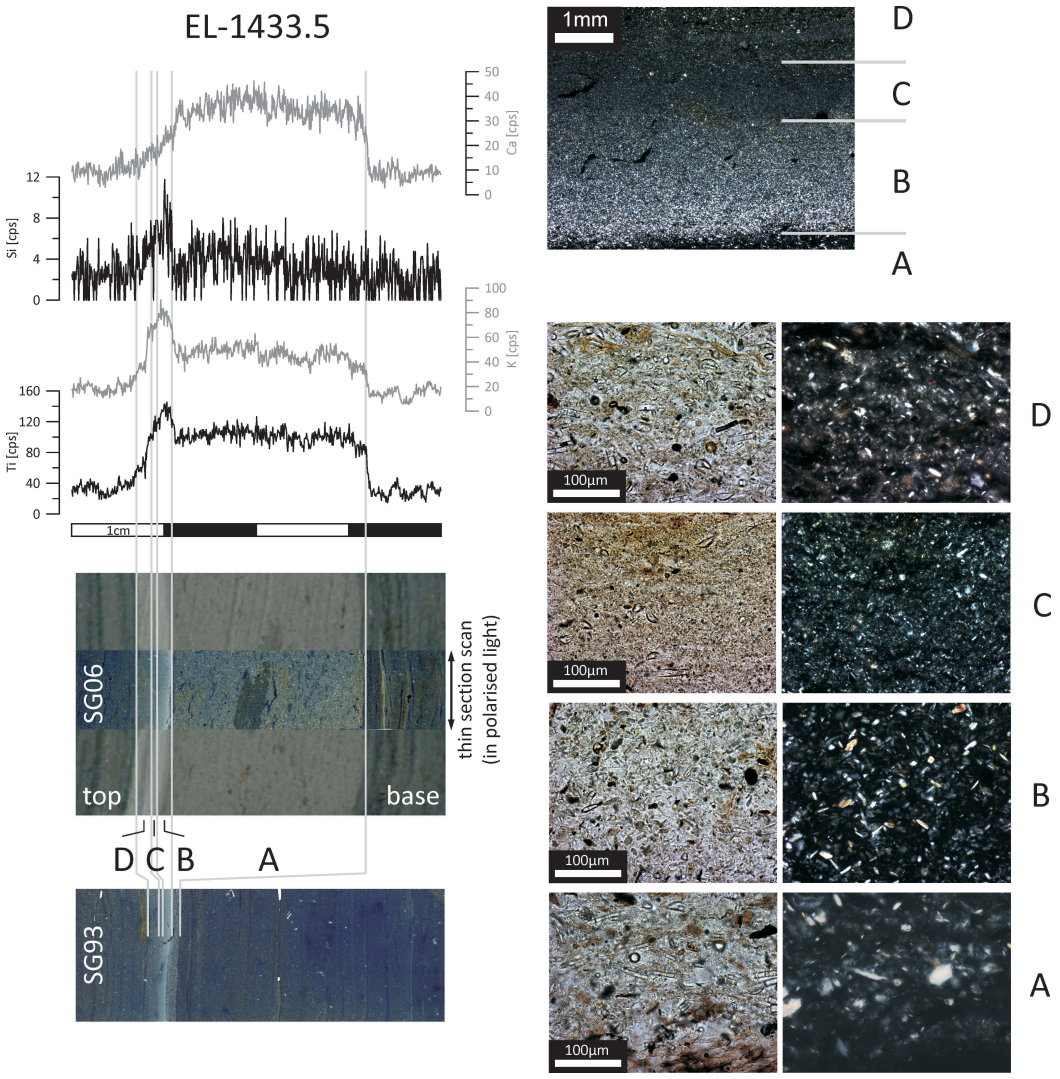

Figure V.2.: Microfacies of event layer type I: left panel shows µXRF scans aligned to the core photo, overlain by a thin section scan in polarised light and below the thin section scan from SG93 containing the same event layer. In the upper right a microscope photo shows the detailed structure of the 'clay cap'. The lower right panel shows microscope photos of the different sub-layers in plain (left) and polarised (right) light.

Above follows a sub-layer (I-C) of homogenous, clay sized detrital material, with an increased proportion of clay minerals. Otherwise, mineral grains are usually too small to reliably identify the mineral type by light microscopy. Autochthonous material is usually absent.

The top sub-layer (I-D) is a mixture of detrital material and the sediment matrix. It is highly variable in the proportion of these two components, the grain size of the detrital minerals, as well as in its thickness. Often the upper boundary of this sub-layer is indistinct and it gradually fades into the sediment matrix.

In the µXRF signal (Fig. V.2) the I-A sub-layer is characterised by increased Ti, K and Ca values. At the base of I-B, Ti and K increase further and then decrease towards the top of the event layer. Ca starts to decrease from the base of I-B. Si shows a distinct peak in the I-B layer. The boundary between I-C and I-D cannot be identified reliably in the µXRF signal.

In the core photos (Fig. V.2) sub-layer I-A can be distinguished by its greyish colour, while the three upper sub-layers show no clear boundaries between themselves and appear as one 'clay cap' of light grey colour.

In most cases the I-A sub-layer is absent and only the characteristic clay top is found. Only in 12 out of 279 type I event layers was a I-A sub-layer present (considering only those type I layers that were in the microscopically analysed interval, as only microscopic analysis ensures reliable identification of thin I-A sub-layers). That there is a high lateral thickness variability of the I-A sub-layers is shown in Fig. V.2, where the same event layer was identified in an SG06 and an 'SG93' thin section. SG93 was a predecessor project of SG06 (Kitagawa and van der Plicht, 2000; Staff et al., 2013b) but thin sections from SG93 were only available for a part of the Last Glacial-Interglacial Transition (LGIT, also Last Termination or Late Glacial) and contained only one event layer with a clear I-A sub-layer. In this event layer (EL-1431.2) the I-A sub-layer has a thickness of ≈20 mm in SG06, but only ≈1 mm in SG93.

Type I event layers occur repeatedly above siderite layers and layers of amorphous organic material (LAO layers). Both layers have been identified as seasonal layers and relate to autumn and summer respectively (Schlolaut et al., 2012), placing the type I event layers into autumn. That a seasonal layer does not occur below every type I event layer is simply due to the fact that not every year seasonal layers formed. The relationship between the event and seasonal layers is best observed in the LGIT, where the frequency of the seasonal layers is much higher than in the Glacial. In the Glacial a reliable season placement is not possible.

Event layer type II

Only two layers of type II occur in the analysed interval (EL-2244.2, EL-3107). They appear to be rather similar to type I layers in the core photos, consisting of a coarse base and a clay top, but micro-facies and μXRF analyses show significant differences (Fig. V.3). Most notably, type II event layers consist of 5 rather than 4 sub-layers and contain much larger plant fragments and siderite. Furthermore, Ti and K values tend to decrease rather than increase. The coarse base of type II event layers consists of 4 sub-layers, whereas with type I layers it is a single sub-layer (I-A). The bottom sub-layer of type II event layers (II-A) is similar to the I-A sub-layer, but reaches larger grain sizes (coarse silt to fine sand). In the II-B sub-layer siderite occurs and plant fragments are much larger than in type I event layers (up to 1 mm). In the case of EL-2244.2 the sub-layer is also enriched in amorphous organic material, which is a component of the sediment matrix. In the next two sub-layers grain sizes, size and number of plant fragments and the siderite concentration decrease with a well defined drop at the boundary between II-C and II-D. Furthermore, the amorphous organic material increases in II-C in EL-2244.2. The top sub-layer (II-E) is characterised by a clearly graded silt/clay layer, intercalated with siderite layers, which are rather massive in EL-3107.

In the μXRF data (Fig. V.3) the layer type is characterised by high Fe and Mn values, increasing from the base of the II-B sub-layer to the lower part of II-C, then decreasing again to the normal background values in II-D. In the II-E sub-layer clear peaks occur at the positions of the siderite layers. The other elements (Ti, K, Ca, Si) do not give as clear a type-specific signal, with the signal to noise ratio being clearly lower than in type I event layers. The four elements differ slightly between the two type II event layers. However, K shows a clear, Ti and Si a slight tendency to lower values in II-B and II-C, while Ca values tend to be elevated from II-A to II-D.

Event layer type III

The 5 event layers of type III are matrix supported layers, characterised by a distinctly homogenous structure and a high proportion of material from the sediment matrix. For this reason event layers of type III are much more difficult to distinguish in the core photographs than the other two types. Hence, identification in the upper core interval,

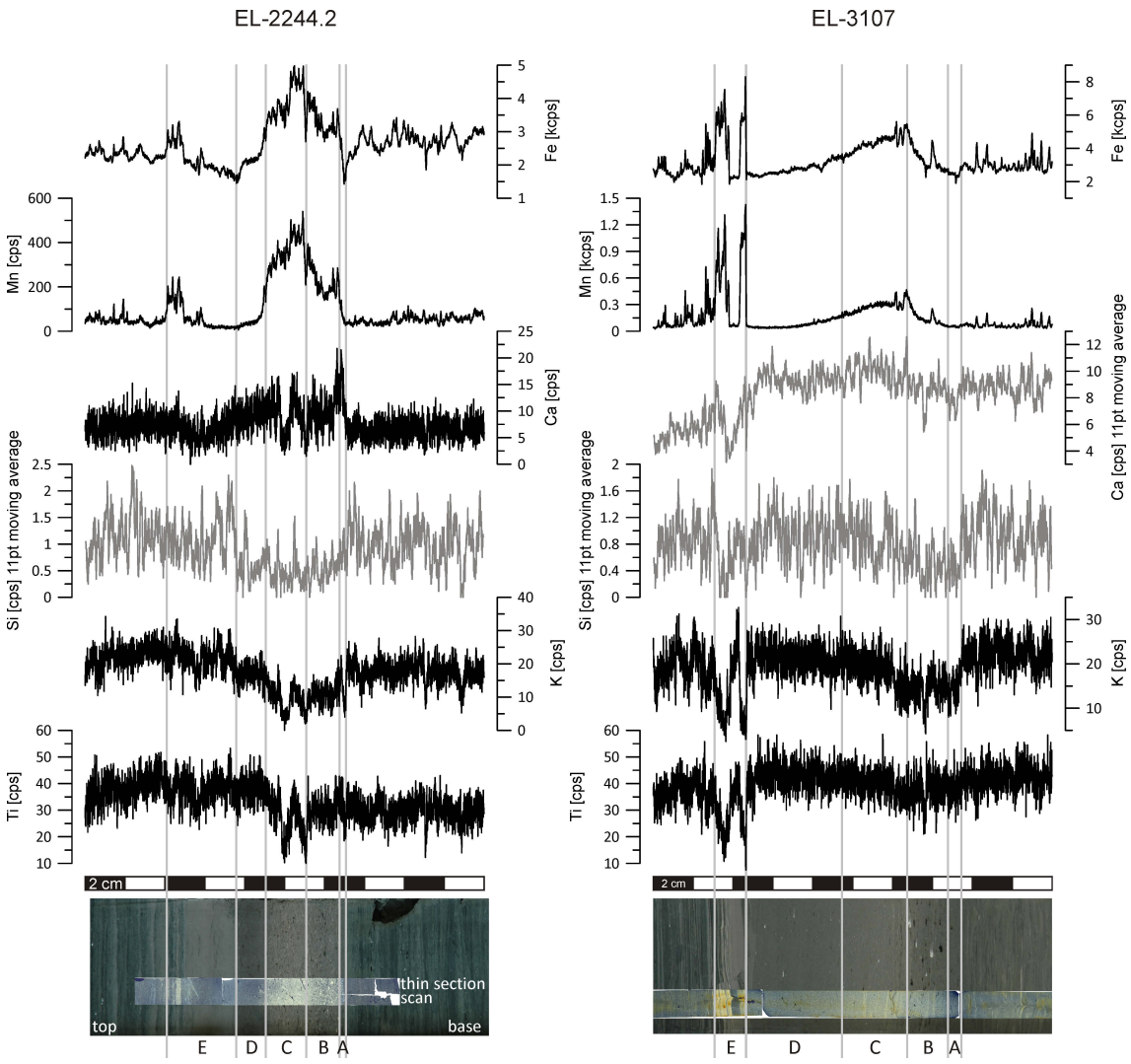

Figure V.3.: Microfacies of event layer type II: µXRF scans aligned with core photos, overlain by thin section scans in polarised light. The left panel shows EL-2244.2, the right panel EL-3107. Grey µXRF curves show the 11pt moving average.

above 1288 cm cd (where identification is based solely on core photographs), is less reliable for this layer type. Only 1 of the 5 identified layers lies in the upper part (EL-91). From the 4 event layers that can be characterised by microscopy 3 differ from the surrounding sediment matrix by containing an increased number of larger mineral grains (about 3 to 7 times larger, reaching fine to medium sand). At the top of these 3 layers a cap of large lenses of aggregated siderite occurs. The 4th event layer (EL-1731.8) exhibits only the homogenous structure. The layers show no common signature in the µXRF signal. Two are indistinct (EL-1731.8, EL-1979.2), EL-1632.6 shows clearly increased values of Ti, K and Ca, and EL-2464.5 shows a weak increase in Ca and K and a distinct increase in Fe and Mn. The siderite caps are enriched in Mn.

V.3.3. Event layer type I frequency

The type I event layer frequency shows a high variability over the past ≈40 kyr, reaching from 0 up to 22 event layers per 1000 years (Fig. V.4). Based on the mean frequency the curve can be divided into 5 zones (FLZ - flood layer zone, for event layer interpretation see section V.4.1).

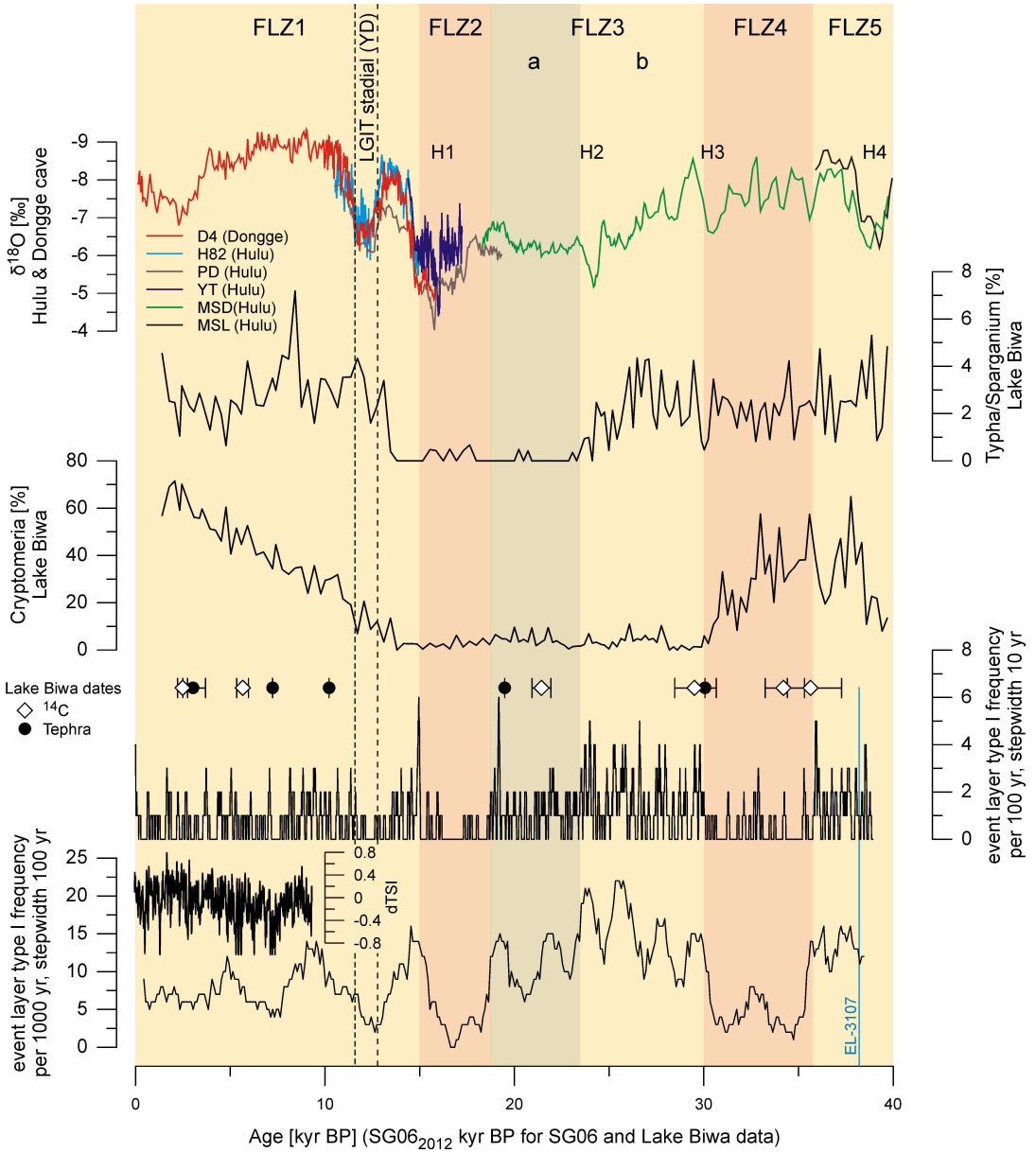

Figure V.4.: From base to top: SG06 flood layer frequency per 1000 yr; difference of total solar irradiance from the value of the PMOD composite during the solar cycle minimum of the year AD 1986 (1365.57 W/m^2) (Steinhilber et al., 2009); SG06 flood layer frequency per 100 yr; position and type of Lake Biwa dates (Hayahsi et al., 2010); pollen curves from Lake Biwa (Hayahsi et al., 2010) (For better comparison of the SG06 and Lake Biwa data the age model of (Hayahsi et al., 2010) was transferred to the SG06$_{2012}$ yr BP age scale, using tephras as isochrons and modelling the ^{14}C dates on to the SG06$_{2012}$ yr BP age scale. A discrepancy can be observed at the onset of the LGIT, which is considerably younger in the Lake Biwa data. This we relate to the fact that it falls into a 10 kyr long interval, which is only constrained by two tephras, the U-Oki (10,217 ± 40 SG06$_{2012}$ yr BP; Staff et al. 2013a; Smith et al. 2013) and the Sakata tephra (19,487 ± 112 SG06$_{2012}$ yr BP; Smith et al. 2013). Some major climate changes fall into this time frame, so that the assumption of a near linear mean sedimentation rate between these two points in Lake Biwa might be invalid. Nevertheless, the pollen data can still be used to characterise the general climate conditions in central Japan over the last 40 kyr.); U-Th dated Chinese speleothem records of δ^{18}O from Hulu and Dongge cave (Wang et al., 2001; Yuan et al., 2004), Heinrich Events are labelled H1 to H4. Flood layer zones (FLZ) are labelled at the top.

The lowermost zone, FLZ5, reaches to about 35,750 $SG06_{2012}$ yr BP (rounded to half a century) and is characterised by about 13 flood layers per 1000 yr.

The following zone, FLZ4, shows about 3 flood layers per 1000 yr, but reaches a maximum of 8 layers per 1000 yr in a well defined peak at around 33,900 $SG06_{2012}$ yr BP. The boundary between this and the next zone coincides with the AT tephra (30,009 189 $SG06_{2012}$ yr BP (Smith et al., 2013)).

Zone FLZ3 has the highest mean value of 13 layers per 1000 yr and also reaches the highest maximum value of 22 layers per 1000 yr. It also exhibits a strong cyclicity with T≈2000 yr. Based on the per 100 yr plot, FLZ3 can be divided into two sub-zones: FLZ3a (upper) and FLZ3b (lower). The lower subzone shows a higher frequency of flood layers (3-4 per 100 yr) than the upper zone (2 per 100 yr). The boundary between the two sub-zones lies at about 23,450 $SG06_{2012}$ yr BP and the upper boundary of FLZ3 at 18,500 $SG06_{2012}$ yr BP. The timing of FLZ3 is approximately contemporaneous with the global sea level minimum of the last Glacial (30 to 19 kyr BP, Lambeck et al. 2000).

The next zone, FLZ2, shows the lowest values from all zones, with between 0 and 4 layers per 1000 yr. It ends at about 15,000 $SG06_{2012}$ yr BP, which coincides with the onset of the LGIT. Therefore, FLZ2 is approximately synchronous with Heinrich Event 1 (H1, 19 to 15 kyr BP, Stanford et al. 2011).

The top-most zone, FLZ1, comprises the Holocene and the LGIT and reaches to the top of the core. The flood layer frequency is generally as low as 6 per 1000 yr, but shows three distinct peaks at ≈15,000 $SG06_{2012}$ yr BP, ≈9,500 $SG06_{2012}$ yr BP and ≈5,000 $SG06_{2012}$ yr BP, where values reach between 12 and 18 layers per 1000 yr. A distinct minimum occurs during the LGIT stadial (climatic equivalent of the European Younger Dryas pollen zone (Jessen, 1935; Mangerud et al., 1974))

Frequency analysis of the per 100 yr data (Fig. V.5) using REDFIT software (Schulz and Stattegger, 1997; Schulz and Manfred, 2002) suggests cycles at T≈220 yr, T≈450 yr and T≈5000 yr, while the per 1000 yr data suggest T≈2000 yr and T≈5000 yr. Wavelet analysis (Torrence and Compo, 1998) of the per 100 yr data (Fig. V.5e) also clearly shows bands around T≈2000 yr and T≈5000 yr, while the bands at smaller periodicities are less well defined.

V.3.4. XRF analysis of catchment samples

A central finding from the analysis of the catchment samples (Fig. V.6) is a strong anti-correlation between Ti and K ($R=-0.72$). K is enriched (defined as greater than the mean value of all samples) in samples that are influenced by the granite pluton to the East, while the highest Ti values are found in the distal watershed of the Hasu River in the South and at the Northeast coast of the lake. The data also show that Ca is generally low. The highest values are found in the tributary streams of the Hasu River, especially in the southernmost samples. Only 2 out of 10 samples in which Ca values were greater than the mean were found directly at the lake, both from the Northeastern shore.

V.4. Discussion

V.4.1. Interpretation of event layers

Event layers of type I and II show some similarities, as they consist of coarse detrital material mixed with plant fragments and autochthonous material, overlain by graded silt/clay (Fig. V.2 and V.3). Such sequences are typical of erosional hyperpycnal turbidity flows (Mulder and Alexander, 2001; Mangili et al., 2005; Gilli et al., 2013) and may be the result of flood events or landslides (possibly triggered by earthquakes) (Swierczynski et al., 2012; Gilli et al., 2013).

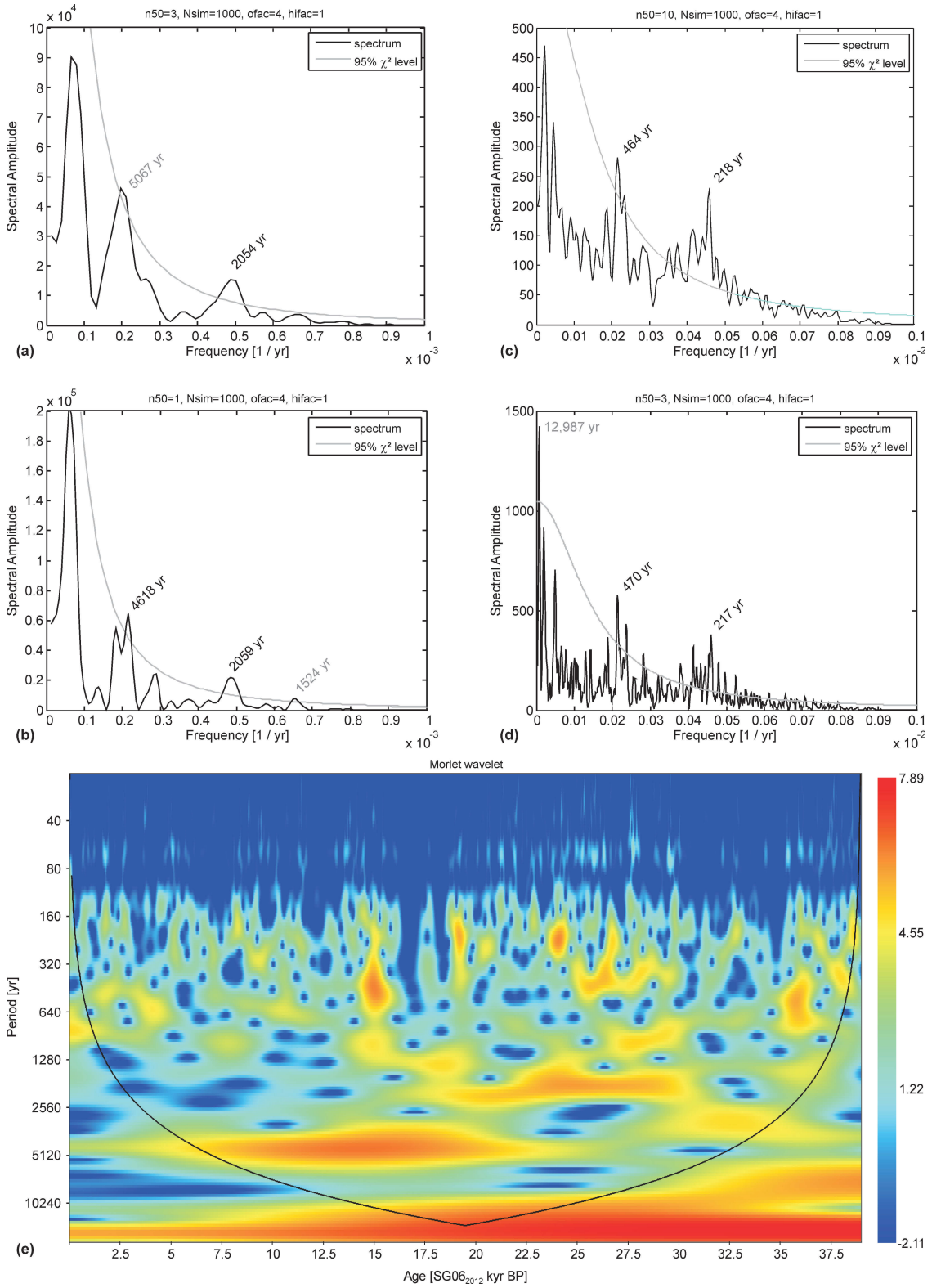

Figure V.5.: Periodograms from flood layer frequency data per 1000 yr with (a) n50=3 and (b) n50=1 and from data per 100 yr with (c) n50=10 and (d) n50=3; n50 gives the number of segments with 50% overlap, ofac is the oversampling factor, hifac is the factor for highest frequency (see Schulz and Stattegger (1997) for details). Cycles marked in light grey are considered problematic as they are very close to the 95% χ^2 level or too large considering the length of the dataset. (e) Wavelet analysis of the per 100 yr data using a Morlet wavelet.

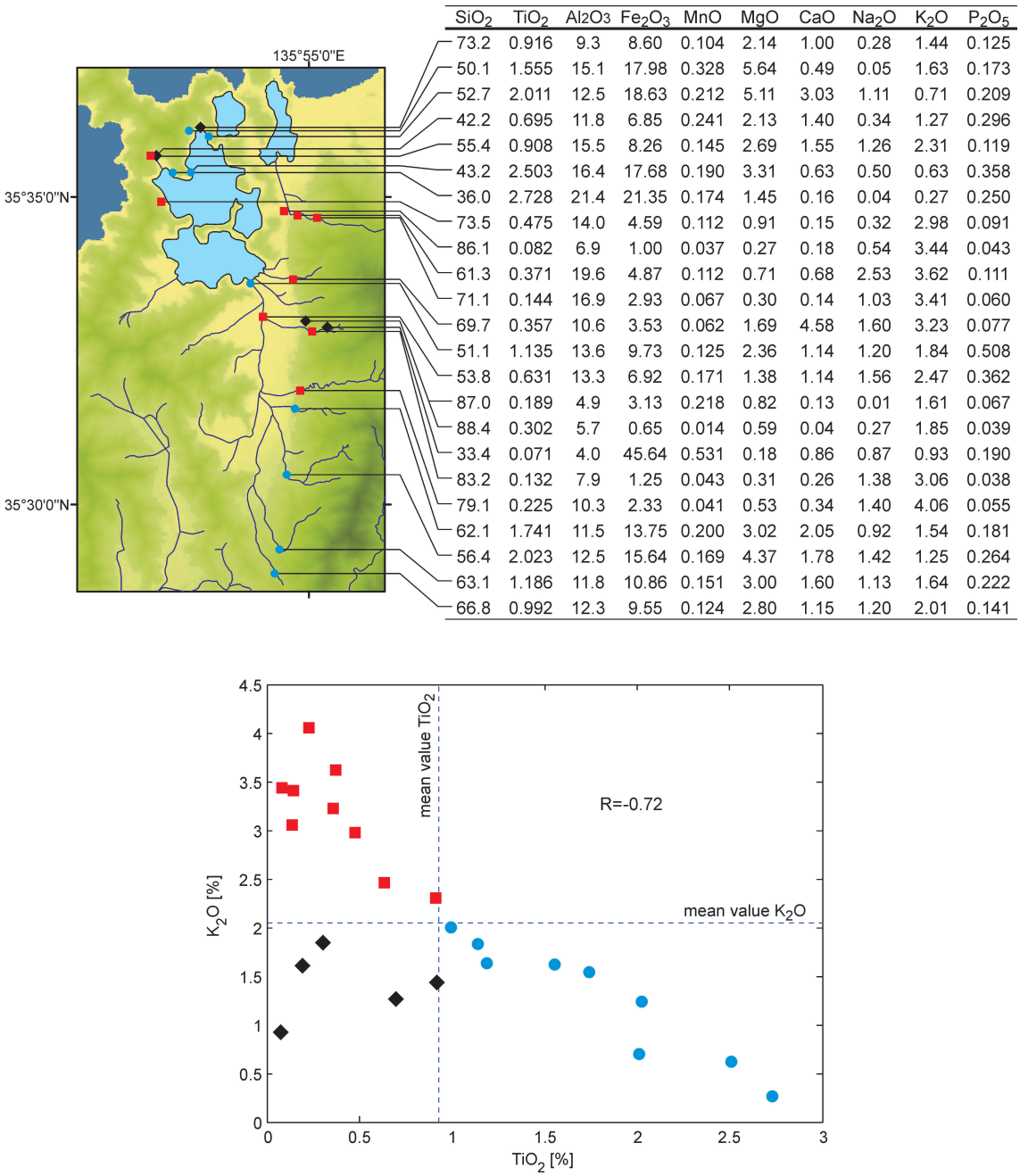

Figure V.6.: Locations of catchment samples and XRF composition values [%]; scatter plot shows the anticorrelation between Ti and K

Considering the seasonality (occurrence often above siderite or LAO layers in the LGIT) and the high frequency of type I event layers, it is likely that type I layers are related to flood events. In contrast, type II event layers are likely to be related to landslides. This is, for instance, indicated by the µXRF data. In type I event layers Ti and K are enriched and correlate well (e.g. $R_{EL-1298.3}$=0.858, $R_{EL-1442.5}$=0.857), which means that the source area of the material includes the Ti rich (in the South) and the K rich (East) regions. In contrast, K and Ti correlate less well in type II events. The layers are clearly depleted in K and only slightly depleted in Ti ($R_{EL2244.2}$=0.687, $R_{EL-3107}$=0.581), meaning that the source area was local, excluding stream and soil material influenced by the pluton, possibly deriving directly from the Northeastern shore area.

This interpretation is further supported by the microfacies data, which show larger plant fragments and larger mineral grains in type II layers, as well as a more erosive character

(higher proportion of material from the sediment matrix in EL-2244.2), which suggests a higher energy flow, which could be the result of a shorter distance between source and lake (Swierczynski et al., 2012). Whether or not EL-3107 is enriched in material from the sediment matrix too is not clear since the layer lies in the detrital rich facies, the redeposited material would be enriched in detrital mineral grains, which are not distinguishable from the detrital minerals of the event layer itself.

Event layers of type III are likely to be the result of subaqueous slope failures. The high proportion of autochthonous components argues against an origin from outside the lake and the large detrital grains (3 to 7 times larger than in the surrounding sediment) indicate a source closer to the lake shore (i.e. away from the lake centre). The fact that the event layers have no common μXRF signature indicates that they originate from different parts of the lake, influenced by different surrounding lithologies. Similar to type II events, earthquakes represent the likeliest trigger for these event layers (Wilhelm et al., 2012). This is further supported by the fact that according to the SG06 age model, EL-91 occurred around AD 1660 and is therefore most likely related to the AD 1662 earthquake.

V.4.2. Facies change at EL-3107 (38,213 $SG06_{2012}$ yr BP)

As stated earlier, the change from a clastic rich to a clastic poor facies occurs very suddenly and is marked by the event layer EL-3107 (type II, Fig. V.3). Therefore, it appears likely that event sedimentation and facies change are related.

The high content of clastic material below event layer EL-3107 suggests that Lake Mikata did not act as a filter for the detrital material. Probably the Hasu River did not discharge into Lake Mikata at the time, but into Lake Suga, which has a much wider and sloping connection to Lake Suigetsu and therefore a lesser filtering effect on the detrital material. The East coast of Lake Suga shows a possible inflow point for the Hasu River, characterised by a rather flat morphology (Fig. V.1). If this were indeed the case, a mechanism is needed that shifted the Hasu River estuary from Lake Suga to Lake Mikata, 'turning the filter on'. An earthquake blocking/moving the old riverbed, analogous to the AD 1662 displacement of the lake system outlet (see section V.1.1), is the most likely explanation. It would not only explain the very sudden facies change, but also EL-3107 marking the transition, with the event layer having been triggered by the earthquake (in concordance with the interpretation of type II event layers).

An effect on the flood layer frequency by this change in the hydrology is not evident. However, since this change is close to the base of the analysed interval (Fig. V.4), the data available from below the event layer are limited.

V.4.3. Comparison with earlier findings from Lake Suigetsu

Compared to the study of Katsuta et al. (2007), we have identified a considerably higher number of event layers (about 3 times as many in the common interval of the two studies), which we relate to a higher sensitivity of the multi-proxy identification approach applied here. Furthermore, Katsuta et al. (2007) assumed that turbidites are generally the results of earthquakes and clay layers the result of floods. Our data suggest that clay layers represent the clay cap of (type I) turbidites and represent cases in which the coarsest material did not reach the drilling location (i.e. the I-A sub-layer did not form at the drilling location). Hence, we propose that most turbidites (type I) relate to floods and only a minor number to earthquakes (type II). Event layer types II and III have not been described before and are reported here for the first time, both likely to be related to earthquakes.

V.4.4. Flood layer frequency

Detrital layer frequency and flood frequency are related but not identical and, unless there is other evidence, it must be assumed that not all floods are represented by detrital flood layers in the sediment record (Kämpf et al., 2012). Thresholds to when a flood produces an associated layer depend on variables such as flow speed, entry point into the lake, morphology of the lake site and weathering rates (Sturm and Matter, 1978; Czymzik et al., 2010; Gilli et al., 2013). A special form of weathering in tectonically active regions like Japan are earthquakes. Hovius et al. (2011) showed that the amount of eroded material can significantly increase when a heavy earthquake occurred (up to a couple of years) prior to a precipitation event, making the formation of a flood layer more likely. Another influence on the sedimentary flood record is the flood layer geometry. Flood layers usually do not form homogeneously over the lake floor, so that the coring position relative to the entry point of the floods influences the number of layers found in the core. In distal positions flood layers may not be present when the energy of the turbidity current was rather low (Kämpf et al., 2012), in proximal positions older flood layers can be eroded by later turbidity currents (Sturm and Matter, 1978).

The flood layer frequency (i.e. event layer type I frequency) values reported here are much smaller than in comparable studies from other sites (e.g. Czymzik et al., 2010; Swierczynski et al., 2012). The reason for this is that in the study presented here only macroscopic event layers ($\geq$1 mm) were considered. This aims to single out high magnitude floods. Even though flood layer thickness and flood magnitude are not directly proportional to one another, there is a general trend that larger floods produce thicker detrital layers (Kämpf et al., 2012). A possible threshold system for the formation of macroscopic flood layers can be deduced when comparing the thickness of the I-A sub-layer in EL-1433.5 between SG06 and SG93 (the only flood layer with a distinct I-A sub-layer for which thin sections from both campaigns are available). Figure V.2 shows that the I-A sub-layer is much thinner in the Southern core (SG93), and therefore it appears unlikely that the turbidity current propagated from the South (i.e. from the Hasu River via Lake Mikata). We assume that for smaller floods Lake Mikata still acted as a filter for most of the detrital material and that the macroscopic flood layers derive from floods, which flooded the whole area and entered Lake Suigetsu through Lake Suga, which has a much deeper and wider connection to Lake Suigetsu and therefore does not act as a barrier.

As stated earlier, the flood layer frequency (Fig. V.4) shows a high variability and the boundaries of two flood layer zones coincide with major climatic changes: FLZ2 occurred at about the same time as H1 and FLZ3 coincides with the glacial sea level lowstand (Lambeck et al., 2000). The onset of FLZ3 also correlates with the onset of colder and drier climate conditions in central Japan, indicated by a decrease in *Cryptomeria japonica* and an increase in *Pinus*, *Tsuga* and *Picea* trees in the Lake Biwa pollen assemblage (Hayahsi et al., 2010) (Fig. V.4). Lake Biwa pollen data are used here for comparison since pollen data from Lake Suigetsu are not yet finalised for the analysed section. Lake Biwa is located about 20 km Southeast of Lake Suigetsu and is thus expected to reflect the same regional climate signal. The pollen record of Lake Biwa also shows high values of upland herb taxa during FLZ3, which suggest moderately open or discontinuous forests. However, an influence on erosion rates and subsequently the flood layer frequency is not apparent. For instance, the flood layer frequency decreases in FLZ2 despite there still being high non-arboreal pollen. Furthermore, the strong 2000 yr cyclicity in the flood layer frequency observed in FLZ3 is not present in the pollen data. We also exclude an increase in heavy precipitation events related to the monsoon front as a possible explanation for the high flood layer frequency in FLZ3 since at that time the front was weaker and most likely located further to the South, which caused the colder and drier climatic conditions in Japan. An increase in snowfall and subsequently in the magnitude of snow melts can be ruled out too since at the time the warm Tsushima current did not enter the

Sea of Japan due to lower eustatic sea levels (Ono et al., 2005). Therefore, during the winter monsoon season less moisture was taken up and precipitation is likely to have been decreased. This leaves an increase in the summer typhoon frequency in the region as the most likely explanation for the increase in flood layers. This interpretation is in line with coupled ocean-atmosphere model simulations for the LGM, which have revealed an increased potential for tropical cyclone genesis in the central and western North Pacific, despite the generally colder conditions (Korty et al., 2012). An increase in typhoons does not contradict drier climate conditions (Hayahsi et al., 2010) or generally reduced erosion rates (Oguchi et al., 2001) in Japan, since the flood layer record only shows relatively infrequent, extreme events.

The apparent cyclicity of T≈2000 yr during FLZ3 could be related to solar variation, namely the Hallstatt Cycle. Alternatively, it could also be indicative of an influence of the El Niño Southern Oscillation (ENSO). Today, during central Pacific El Niño years typhoons are more likely to make landfall over Japan (Woodruff et al., 2009; Zhang et al., 2012) and Moy et al. (2002) showed that ENSO exhibited a ≈2000 yr cyclicity over the Holocene. It is quite possible that a similar mode was also operating during FLZ3.

The boundary of the subdivision of FLZ3 coincides with H2, after which δ^{18}O values in the Hulu Cave (Eastern China) speleothems stabilised (Wang et al., 2001). Even though H2 itself did not leave an imprint on the flood layer record, the climatic change following led to a decrease in the flood layer frequency. Possibly the stabilisation of the monsoon system reduced the typhoons affecting central Japan.

While no significant changes in the flood layer frequency can be observed contemporaneous with H2 and H3, the frequency is strongly reduced during H1, reaching the lowest overall values down to 0 per 1000 yr. Also, the Hulu Cave δ^{18}O speleothem record reaches its absolute minimum in the last 40 kyr in this time frame (Fig. V.4). Apparently, the further decreased temperatures greatly reduced the number of typhoons affecting central Japan, leaving no persistent mechanism to cause major flood events.

The following zone FLZ1 is characterised by the three maxima in the flood layer frequency, separated by minima relating to the LGIT stadial and the middle Holocene. This pattern is also mainly responsible for the 5000 yr cyclicity evident in the spectral analysis (Fig. V.5). However, this might be a pseudo-cyclicity with the three maxima having independent causes. In particular, the earliest maximum is set apart from the other two. The sudden increase in flood layers coincides precisely with the onset of the LGIT, suggesting some relationship with the sudden warming. Alternatively, the maximum could be related to an increase in erosion rates after an earthquake (Hovius et al., 2011), which is indicated by a type III event layer (EL-1731.8) marking the boundary between the Glacial and the LGIT. Furthermore, if the shape in the frequency curve, a sudden increase followed by a slightly slower decrease, is representative of enhanced erosion following earthquakes, then the last peak in FLZ3 at 19,200 $SG06_{2012}$ yr BP might also relate to an earthquake, although there is no earthquake related layer (type II or III) at the base of this maximum. The low number of earthquake related layers (7) over the last 40 kyr in such a tectonically active area clearly shows that not every earthquake produces an associated event layer. Therefore, the absence of an earthquake-related layer does not exclude the occurrence of an earthquake.

The early Holocene is characterised by increased flood frequency values compared to the LGIT, which persist until ≈8,000 $SG06_{2012}$ yr BP. The remainder of the Holocene shows generally lower values than during the early Holocene, with a weak minimum in the middle Holocene between ≈8,000 and ≈5,000 $SG06_{2012}$ yr BP. The trend towards lower values in the middle and late Holocene can be attributed to a decrease in summer insolation (associated with an increase in winter insolation), weakening the monsoon system (Zhao et al., 2009). The minimum in the mid Holocene could be the result of lower solar activity at the time (Fig. V.4) (Solanki et al., 2004; Steinhilber et al., 2009). The reduction in the

flood layer frequency at 8,000 $SG06_{2012}$ yr BP is also interesting with respect to winter precipitation, since the Tsushima current entered the Sea of Japan again at the time (Takei et al., 2002). But rather than an increase in flood layers due to additional snow melt-triggered layers, the flood layer frequency declines, which suggests that snow melts had only a minor impact on the flood layer frequency.

A solar influence on the flood layer frequency is not only suggested by the minimum in the middle Holocene, but also by the spectral analysis, with the 2000 yr cycle possibly relating to the Hallstatt Cycle (see above) and the 220 yr cycle probably reflecting the de Vries (Suess) Cycle.

Lastly, the pattern of FLZ5 and FLZ4 is difficult to interpret since the character of FLZ5 beyond 40 kyr BP is unknown. Furthermore, the pattern is not mirrored in other key records from the region, which might indicate a local change. This illustrates that floods are short-term meteorological events and that a straightforward relationship with climate patterns is not a matter of course.

V.5. Conclusions

The flood layer frequency in Lake Suigetsu shows a complex progression. Prior to about 30 kyr BP it appears to reflect local changes, later it is clearly influenced by northern hemispheric climate patterns. But even after 30 kyr BP non-climatic mechanisms influenced the flood layer record. Earthquakes appear to have had an impact on the flood frequency on two occasions, increasing the amount of erodible material and subsequently increasing the number of flood layers formed. This means that flood layer records are not straightforward proxies for climate change *per se* and that the influence of processes in the catchment must be carefully ascertained. Despite these additional influences, clear climate driven changes in the flood layer frequency are evident. In this respect it is most surprising that between 30 and 18.5 $SG06_{2012}$ kyr BP the flood layer frequency reaches its highest mean and absolute values, although this was an episode of cold and dry climate in Japan. Other cold episodes such as H1 and the LGIT stadial show clearly reduced flood layer frequency values, in the case of H1 even the lowest overall values. The warm and wet Holocene shows intermediate values between the two extremes. These differences between wet and dry episodes show that short term extreme precipitation was decoupled from the centennial to millennial average precipitation. Furthermore, the large scale changes in the flood layer frequency appear to have been modulated by solar activity. Changes in typhoon genesis and/or typhoon tracks appear to be the likeliest explanation for the variability of the flood layer frequency during the Glacial. In the Holocene it is unclear whether extreme precipitation events were related to typhoons or rather to the monsoon front. But it could be shown that snow melts had only a minor impact on the record.

In summary, the data illustrate that the microfacies analysis of event layers in lacustrine sediments provides highly valuable proxy data for improving our understanding of (palaeo-)environmental mechanisms in the East Asian realm. In the future, detailed comparison with high-resolution pollen (and other proxy) data directly from Lake Suigetsu offers the potential to gain a further improved understanding of the site specific climatic and hydrological changes and to separate their individual impacts on the flood layer record.

Acknowledgements

We thank the German Research Foundation (DFG grants TA-540/3-1, BR 2208/7-1), the UK Natural Environment Research Council (NERC grants NE/D000289/1, NE/F003048/1, SM/1219.0407/001), the KAKENHI project of Japan (grant 211001002) and INTIMATE EU cost for funding. Furthermore, we thank Prof. K. Takemura for providing map material of the Lake Suigetsu region and Dr. R. Hayashi for providing the raw Lake Biwa pollen data. We also thank H. Kitagawa and J. van der Plicht for inspiration for the project.

VI. Synthesis

VI.1. Summary

Within the PhD project two central goals were pursued: (i) Establishment of a varve chronology for the 'Suigetsu Varves 2006' (SG06) sediment core and (ii) Reconstruction of palaeo-environmental changes by microfacies analysis. The varve chronology was not only to serve as age control for the various proxies analysed within the SG06 project but also as calendar age scale for an atmospheric radiocarbon calibration dataset beyond the tree-ring limit of the current IntCal calibration curve.

For varve counting two independent approaches were applied: counting by thin section microscopy and counting by μXRF. The latter method was carried out by Dr. Michael Marshall in cooperation with the PhD candidate. A total of 19 m of the SG06 composite profile were counted by thin section microscopy, covering the time window from c. 10 to 40 kyr BP. Microscopic analysis revealed seven main seasonal layers, from which siderite layers are the most frequently and consistently occurring seasonal layer type. Hence, both counting methods relied on these. Siderite is easily distinguished under the microscope in polarised light and also produces distinct peaks in Fe and Mn in the μXRF signal (Mn easily substitutes for Fe in the mineral lattice). But results from the two methods differed significantly. The μXRF count distinguished a much higher number of seasonal element signals than the thin section count distinguished seasonal siderite layers (+88% in the LGIT). This is in part due to low quality seasonal element signals included in the μXRF count. It is likely that an unknown proportion of the low quality signals represent noise. But even when excluding the lowest quality counts (Qlt4), the μXRF count was still much higher than the microscopic count (+45% in the LGIT). This means that not all the difference can be attributed to noise and hence, that some of the seasonal element signals have no visual counterpart. Reason for that could be that the siderite concentration in the sediment is at times too low to form a visible layer and/or that oxides rather than carbonates formed, with the former not being distinguishable under the microscope.

During counting a second problem became apparent, which is that both counts are undercounts, i.e. they underestimate the time that passed during sediment formation. Apparently, siderite layers did not form every year or were not preserved. Incomplete varve formation/preservation is common problem in varve counting and is usually solved by interpolation.

For varve interpolation a novel, automated method was developed by the PhD candidate. Basis for interpolation is the knowledge of the mean sedimentation rate (SR) (length of compromised interval divided by the mean SR gives the number of years that passed). For deriving the SR estimate the program uses the distances (in [mm]) between the counted, seasonal layers, by statistically analysing the frequency distribution of those distance values. This means that the new interpolation program derives the SR estimate from the compromised interval itself. This is a clear improvement compared to traditional, manual varve interpolation, where the SR is usually derived from neighbouring, well varved intervals, in which the SR might differ from that in the compromised interval. Another advantage of the interpolation program over manual interpolation is that since the program is automated it generally avoids subjectivity and ensures reproducibility. Furthermore, it provides objective interpolation errors.

Some prerequisites for interpolation should be fulfilled, which are: low annual sediment accumulation variability, low mean SR variability, random (non-)formation of seasonal

layers (i.e. formation does not depend on other variables like the SR) and seasonal layers which are one year apart dominate the count. Even though these requirements are generally met in the SG06 sediment, potentially problematic intervals can occur and must be identified. To aid the identification, quality selective count datasets were created as addition to the raw counts from the two counting methods, by excluding single counts, which were based on low quality layers/seasonal μXRF signals. Ideally the interpolation of the quality selective and raw counts should yield similar results since the counts derive from the same sediment. Differences between the interpolation results point towards problems in at least one of the datasets. Manual re-evaluation of count distance frequency plots and comparison of count distance frequency plots from the different count datasets were used to identify the cause of different interpolation results and to discard erroneous results in the respective intervals.

Despite the very different count results from the two counting methods, the interpolation results show a high degree of similarity. Comparison with the ^{14}C chronology (calibrated with IntCal09 dataset back to the tree-ring limit, to which it is considered reliable) also showed that the interpolation results are accurate within the 68.2% error range of the ^{14}C chronology. Both observations show that the novel interpolation program produces realistic and reliable results. Combination of the results from the two counting methods, by using the mean of the two most similar results from either method centimetre wise, produced a final varve model with further improved accuracy, underlining the value of the dual-method counting approach.

The varve chronology was then combined with the SG06 ^{14}C chronology in order to create a purely atmospheric ^{14}C calibration dataset. Since the cumulative error estimate of the varve chronology became unsuitably large towards the older parts, the dataset was constrained by U-Th dated speleothem data, using the low frequency signal of the SG06 and the speleothem ^{14}C data as link. The resulting dataset does provide an improved calibration dataset but also an improved age scale for the palaeo-environmental proxies analysed within the SG06 project.

As part of the proxy study event layers were analysed within the PhD project. An earlier study from Lake Suigetsu (Katsuta et al., 2007) identified two types of event layers by Scanning X-ray Analytical Microscope (SXAM): (i) relatively thin, clay-rich laminae which they related to floods and (ii) graded quartz/feldspar layers (turbidites) which they related to earthquakes. The microscopic analysis presented here revealed a more diverse event layer micro-facies. Three types of event layers were distinguished: two different kinds of turbidites (event layer type I and II) and matrix supported layers (event layer type III). Type I turbidites were related to flood events and it was shown that the clay-rich layers from Katsuta et al. (2007) represent the clay top of these turbidites. A total of 362 out of 369 identified event layers relate to these flood events. The type II turbidites, from which only two occurred, were related to landslides (probably triggered by earthquakes) and the five matrix supported layers were related to subaqueous slope failures (probably triggered by earthquakes, too). The latter two event layer types are described here for the first time for the Lake Suigetsu sediment.

The flood layer frequency over the last 40 kyr shows a pronounced variability, with the highest values occurring during the global sea level low-stand of the last Glacial, while the lowest values are related to the Heinrich 1 Event. It is suggested here, that the high frequency during the sea level low-stand was related to an increase in the number of typhoons affecting the region. Spectral analysis revealed various cycles modulating the frequency curve, most pronounced at T=2000 yr, T= 470 yr and T= 220 yr. Especially the first and the third cycle could be related to solar variations, i.e. the Hallstatt cycle and the de Vries (Suess) cycle.

The data also suggest non-climatic influences on the flood layer formation. Earthquakes appear to have had an impact on two occasions, by increasing the amount of erodible

material, which made the formation of flood layers at the drilling location more likely. This led to an increased number of flood layers formed after the earthquake.

VI.2. Conclusions and Outlook

The aims of PhD project within the SG06 project, creating a varve chronology for the SG06 core and palaeo-environmental reconstruction by micro-facies analysis, were met. Varve analysis using thin section analysis drew a far more detailed picture of the seasonal layers occurring in the sediment than earlier studies did. The dual method varve counting approach was successfully implemented and produced a more accurate and precise chronology than either method could have alone and, in combination with the novel interpolation approach, overcame the problems of the SG93 project. The produced ^{14}C calibration dataset is the first derived from lake sediments to achieve a sufficient accuracy to be included into the next IntCal dataset.

The analysis of the event layers in the Suigetsu sediment revised an earlier interpretation of the origin of the event layers types and identified new types. The results enabled the construction of the first quantitative flood chronology for Japan back to about 40 kyr BP, which shows that the flood frequency was higher during the global sea level minimum than during the Holocene despite colder and generally drier conditions. Variations in the flood occurrence were mainly, but not only, due to climate phenomena like typhoons and the EAM system. Indirect influences by earthquakes were suggested by the data, too.

In the following subsections the results will be discussed in more detail with special focus on possible further improvements. The last subsection gives a brief overview of hitherto unpublished methods and results, their potential value but also yet unresolved questions.

VI.2.1. Varve Counting and Varve Interpolation

The novel varve counting approach by μXRF showed its high potential. While it was initially assumed that μXRF and microscopic counting would produce comparable results, μXRF distinguished a much higher amount of seasonal element-signals. However, this does not mean that μXRF counting is a superior method and it should not be considered a stand-alone replacement for conventional, microscopic varve counting. For instance, it cannot distinguish organic or diatom layers, which often represent an important part of the varve structure with respect to counting and interpretation. Furthermore, the distinction between actual seasonal signals and noise can be problematic. There is also a methodological limit to which distance of successive seasonal layers, these layers can be distinguished separately (with the settings used in this study about 0.4 mm). However, together with conventional varve counting it can produce clearly improved results.

The approach selected here, to carry the counting methods out independently, aimed to identify problematic intervals, i.e. intervals in which the counting results from the two methods disagreed. But differences were high throughout the analysed core section due to very different sensitivities of the two counting techniques. Therefore, problematic intervals could not be distinguished this way and for future applications it would probably be more advantageous to use both approaches alongside rather than independently. This would produce a true 'maximum count', combining the advantages of the two methods directly. To compare method-specific results, method selective counts could still be produced, analogous to quality selective counts.

As stated above, the varve interpolation algorithm produced reliable results. It provides a novel approach to deal with incompletely varved sediment profiles and produced much better results than initial attempts of manual varve interpolation for the SG06 core. Three main advantages should be highlighted, which are reproducibility, the opportunity to in-

terpolate cores which do not contain well varved intervals and objective interpolation error estimates.

However, further improvements are possible and intended. For example, the implementation of age control points. In studies where the varve and the ^{14}C chronology do not need to be kept fully independent, the ^{14}C dates can be used as such points. In case of SG06, independently dated tephras or OSL dates could be used as age control points once available (Staff et al., 2013a). As described in chapter II, overlapping sub-sections or alternating settings in the iteration of settings produce a range of possible age models, from which currently the one with the highest probability is used as resulting age model. With the age control points the most likely model which also passes through the control point could be selected. Analogous, the interpolation error estimates would be reduced as well.

Furthermore, the empirical determination of the bin size and the peakvalue can be regarded as a weakness in an algorithm which otherwise can be run fully automated. For the future an optimisation process, going from large bin sizes (low accuracy, low noise) to small bin sizes (high accuracy, high noise) and subsequent synthesis could allow to automate the process, too. Simillarily peak values could be run from large to low values with subsequent result synthesis.

Lastly, probability distribution fitting onto the count distance frequency plots could potentially be used to further improve the interpolation program.

VI.2.2. Radiocarbon Calibration

Nearly Fifteen years after the first publication describing the potential of the Lake Suigetsu sediments to create an (reliable) atmospheric radiocarbon calibration dataset, this goal has finally been achieved. Furthermore, the SG06 dataset is the first such derived from lake sediments to be included into the (next) IntCal dataset. This success is on the one hand due to the nature of the Lake Suigetsu sediment itself, namely the uninterrupted, continuous sedimentation and the persistent occurrence of seasonal (though often not annual) laminations from 10 kyr BP back to the limit of the ^{14}C dating method. On the other hand, the novel interpolation program together with the dual-method counting approach were able to overcome the common problem of incomplete varve formation with sufficient accuracy for the first time. Despite this rather remarkable success, it must be pointed out that the data are not without weaknesses. The original aim, to construct a completely independent calibration curve could (yet) not be achieved, mainly due to poor varve preservation and the subsequent large absolute errors towards the older part of the varve chronology. Therefore, constraining the dataset by linking with speleothem data was necessary. But there are also some uncertainties related to ^{14}C dating itself, deriving from the plant macrofossils used. The fossils are small and fragile, limiting the opportunities for repeat measurements and making the sensitivity to contamination relatively high. Compared to, for instance, wood samples this increases the number of (potential) outliers. Since only clear outliers have been rejected here, this leads to an increase the noise in the data, especially towards the limit of the ^{14}C method.

Further improvements on the calibration dataset are mainly possible through improvements of the varve chronology (see above). The modelling could be improved by age control points, in which case it would be necessary to test whether these points should rather be integrated into the interpolation or the ^{14}C modelling.

VI.2.3. Event Layer Analysis

The event layer analysis produced the first long-term, quantitative (with respect to recurrence) and well dated flood chronology from Japan. In comparison to comparable studies from European sites (Czymzik et al., 2013; Swierczynski et al., 2012) the data presented

here lacks a 'calibration' of the event layers, i.e. it was generally not possible to relate historic floods and earthquakes to event layers in the Lake Suigetsu sediment (except for one type III layer). This is mainly due to the fact that the top 20 cm of sediment (the recent history) were not recovered. However, also the availability of instrumental meteorological and run-off data directly from the site is limited. Furthermore, since the lake is brackish since the mid 17^{th} century, the behaviour of density currents might have changed due to the change in water density, leading to different kinds of event layers. Lastly, event layers of type II are extremely rare in the sediment (2 layers) and therefore these layers might not have formed in historic times.

Another possibility to improve the understanding of the event layers would be additional sediment cores from different locations within the lake, which would allow the 3-dimensional reconstruction of the event layer geometry. This would improve our understanding of how the turbidity currents propagated through the lake and enable a more precise determination of the event layer origins. This in turn could improve the understanding of the site specific, morphological influences on the event layer formation. Short cores from the lake shore could be used to investigate how the different surrounding geologies influenced the chemical signature of the event layers, especially with respect to types II and III. In this context also XRD analysis of lake sediment and field samples would be suggested (currently only XRF measurements available).

With respect to the climatological and non-climatological influences on the flood layer formation, the subsequent release of other proxy data from Lake Suigetsu should enable us to further improve the understanding of these controls.

VI.2.4. Unpublished Methods and Preliminary Results

During the PhD project more data was produced than published. Therefore, further publications are either in preparation or intended.

Probably of most interest is the work related to the microfacies analysis of the whole sediment (rather than just the event layers). Frequency curves of seasonal layers are used as representatives of microfacies changes, most suitable are LAO, siderite and the different seasonal detrital layers. A very minor portion of these data were published in Kossler et al. (2011), giving a first impression of the value these data can have for palaeo-environmental research. Another, yet unpublished, example is the frequency of spring related Qz-Fsp layers, which is indicative of dust transport from the Asian continent to Japan, as comparison with unpublished dust data revealed (cf. Nagashima and Tada, 2012). The frequency of these layers shows an increased dust transport during the LGIT stadial and also a well developed internal structure of the stadial with cyclic in- and decreases, which in turn are related to changes in the westerly jet position.

Also the frequency of siderite layers as well as the ratio between high and low quality siderite layers contain interesting palaeo-environmental information. And since siderite layers are the only consistently occurring seasonal layer type, information (other than absence) is available for the whole studied interval. However, the controls on the siderite layer formation are yet not fully understood. With the model for siderite formation proposed in chapter II, the stratification and mixing of the lake are certainly controlling factors. However, Fe, Mn and CO_3^{2-} fugacity could play a role as well. Therefore, stable Fe isotope measurements of sediment and field samples are currently being carried out (following a pilot study by Maekeler (2012)). These measurements can reveal information on the redox pathways of the Fe. The study is lead by R. Maekeler and Dr. J. Schüssler (GFZ Potsdam, Section 3.4). Furthermore, $\delta^{18}O$ and $\delta^{13}C$ measurements of siderite samples from the LGIT section of SG06 were carried out (by the PhD candidate). These showed no relation with climate changes, but seem to be dependent on the siderite concentration. How this can be interpreted with respect to siderite formation is currently discussed.

Also more publications related to μXRF analysis are indented. For example, the potential of the SG06 μXRF data as palaeo-environmental proxy has so far not been addressed. The data are an ideal complement to the above mentioned microfacies data, adding semi-quantitative concentration information on the sediment matrix. Furthermore, μXRF measurements have also been made on the impregnated samples from thin section preparation for selected intervals. In difference to the published ITRAX measurements, the same plane is measured which is visible in the thin-section (Brauer et al., 2009) and spot measurements were made rather than using a measuring window. Both approaches to μXRF measuring have advantages and a publication addressing the differences is intended.

In summary, the potential of the SG06 core for palaeo-environmental research has so far only been hinted. The data collected by the PhD candidate and other SG06 members (such as pollen, diatom, geochemistry data etc.) in combination with the now available $SG06_{2012}$ age model are promising to improve our understanding of the East Asian climate system and make Lake Suigetsu one of the key sites in the East Asian realm.

Bibliography

Adkins, J., 2001. Dating - Vive la Différence. Science 294, 1844 – 1845.

Alley, R.B., Meese, D.A., Shuman, C.A., Gow, A.J., Taylor, K.C., Grootes, P.M., White, J.W.C., Ram, M., Waddington, E.D., Mayewski, P.A., Zielinski, G.A., 1993. Abrupt increase in Greenland snow accumulation at the end of the Younger Dryas event. Nature 362, 527 – 529.

Andersen, K.K., Svensson, A., Johnsen, S.J., Rasmussen, S.O., Röthlisberger, M.B.R., Ruth, U., Siggaard-Andersen, M.L., Steffensen, J.P., Dahl-Jensen, D., Vinther, B.M., Clausen, H.B., 2006. The Greenland Ice Core Chronology 2005, 15-42 ka. Part 1: constructing the time scale. Quaternary Science Reviews 25, 3246 – 3257.

Anderson, E.C., Libby, W.F., 1951. World-Wide Distribution of Natural Radiocarbon. Physical Review 81, 64 – 69.

Anderson, E.C., Libby, W.F., Weinhouse, S., Reid, A.F., Kirshenbaum, A.D., Grosse, A.V., 1947. Radiocarbon from Cosmic Radiation. Science 105, 576 – 577.

Arnaud, F., Lignier, V., Revel, M., Desmet, M., Beck, C., Pourchet, M., Charlet, F., Trentesaux, A., Tribovillard, N., 2002. Flood and earthquake disturbance of ^{210}Pb geochronology (Lake Anterne, NW Alps). Terra Nova 14, 225 – 232.

Bahrig, B., 1988. Palaeo-environment information from deep water siderite (Lake of Laach, West Germany). Geological Society, London, Special Publications 40, 153 – 158.

Bard, E., Rostek, F., Ménot-Combes, G., 2004. Radiocarbon calibration beyond 20,000 ^{14}C yr B.P. by means of planktonic foraminifera of the Iberian Margin. Quaternary Research 61, 204 – 214.

Beck, C., 2009. Late Quaternary lacustrine paleo-seismic archives in north-western Alps: Examples of earthquake-origin assessment of sedimentary disturbances. Earth-Science Reviews 96, 327 – 344.

Beck, J.W., Richards, D.A., Edwards, R.L., Silverman, B.W., Smart, P., Donahue, D.J., Hererra-Osterheld, S., Burr, G.S., Calsoyas, L., Timothy, A.J., Biddulph, J.D., 2001. Extremely Large Variations of Atmospheric ^{14}C Concentration During the Last Glacial Period. Science 292, 2453 – 2458.

Björck, S., Walker, M.J.C., Cwynar, L.C., Johnsen, S., Kundsen, K.L., Lowe, J.J., Wohlfarth, B., Members, I., 1998. An event stratigraphy for the Last Termination in the North Atlantic region based on the Greenland ice-core record: a proposal by the INTIMATE group. Journal of Quaternary Science 13, 283 – 292.

Blockley, S.P.E., Lane, C.S., Hardiman, M., Rasmussen, S., Seierstad, I., Turney, C.S., Bronk Ramsey, C., 2012. Synchronisation of palaeoenvironmental records over the last 60,000 years, and an extended INTIMATE event stratigraphy to 48,000 b2k. Quaternary Science Reviews 36, 2 – 10.

Blunier, T., Brook, E., 2001. Timing of Millennial-Scale Climate Change in Antarctica and Greenland During the Last Glacial Period. Science 291, 109 – 112.

Blunier, T., Chappellaz, J., Schwander, J., Dallenbach, A., Stauffer, B., Stocker, T.F., Raynaud, D., Jouzel, J., Clausen, H.B., Hammer, C.U., Johnsen, S.J., 1998. Asynchrony of Antarctic and Greenland climate change during the last glacial period. Nature 394, 739 – 743.

Brauer, A., 2003. Varve chronology. ESF HOLIVAR-Workshop "Holocene dating, chronologies and age modelling", Utrecht, The Netherlands 24.-27.04.2003, 97 – 101.

Brauer, A., 2004. Annually laminated lake sediments and their palaeoclimatic relevance, in: Fischer, H., Kumke, T., Lohmann, G., Floser, G., Miller, H., von Storch, H., NEGENDANK, J.F.W. (Eds.), The Climate in Historical Times. Towards a Synthesis of Holocene Proxy Data and Climate Models. Springer Verlag, pp. 109 – 127.

Brauer, A., Casanova, J., 2001. Chronology and depositional processes of the laminated sediment record from Lac d'Annecy, French Alps. Journal of Paleolimnology 25, 163 – 177.

Brauer, A., Dulski, P., Mangili, C., Mingram, J., Liu, J., 2009. The potential of varves in high-resolution paleolimnological studies. PAGES news 17, 96 – 98.

Brauer, A., Endres, C., , Negendank, J.F.W., 1999. Lateglacial calendar year chronology based on annually laminated sediments from Lake Meerfelder Maar, Germany. Quaternary International 61, 17 – 25.

Brauer, A., Mangili, C., Moscariello, A., Witt, A., 2008. Palaeoclimatic implications from micro-facies data of a 5900 varve time series from the Piànico interglacial sediment record, southern Alps. Palaeogeography, Palaeoclimatology, Palaeoecology 259, 121 – 135.

Bronk Ramsey, C., 2008. Deposition models for chronological records. Quaternary Science Reviews 27, 42 – 60.

Bronk Ramsey, C., Staff, R.A., Bryant, C.L., Brock, F., Kitagawa, H., van der Plicht, J., Schlolaut, G., Marshall, M.H., Brauer, A., Lamb, H.F., Payne, R.L., Tarasov, P.E., Haraguchi, T., Gotanda, K., Yonenobu, H., Yokoyama, Y., Tada, R., Nakagawa, T., 2012. A Complete Terrestrial Radiocarbon Record for 11.2 to 52.8 kyr B.P. Science 338, 370 – 374.

Bryan, S.P., Marchitto, T.M., Lehman, S.J., 2010. The release of ^{14}C-depleted carbon from the deep ocean during the last deglaciation: Evidence from the Arabian Sea. Earth and Planetary Science Letters 298, 244 – 254.

Cockburn, J.M.H., Lamoreux, S.F., 2007. Century-scale variability in late-summer rainfall events recorded over seven centuries in subannually laminated lacustrine sediments, White Pass, British Columbia. Quaternary Research 67, 193 – 203.

Cooper, M.C., 1993. The use of digital image analysis in the study of laminated sediments. Journal of Paleolimnology 19, 218 – 220.

Craig, H., 1953. The geochemistry of the stable carbon isotopes. Geochimica et Cosmochimica Acta 3, 53 – 92.

Craig, H., 1957. The Natural Distribution of Radiocarbon and the Exchange Time of Carbon Dioxide Between Atmosphere and Sea. Tellus 9, 1 – 17.

Croudace, I.W., Rindby, A., Rothwell, R., 2006. ITRAX: description and evaluation of a new X-ray core scanner, in: Rothwell, R.G. (Ed.), New ways of looking at sediment cores and core data. Geological Society Special Publication. volume 267, pp. 51 – 63.

Czymzik, M., Brauer, A., Dulski, P., Plessen, B., Naumann, R., von Grafenstein, U., Scheffler, R., 2013. Orbital and solar forcing of shifts in Mid- to Late Holocene flood intensity from varved sediments of pre-alpine Lake Ammersee (southern Germany). Quaternary Science Reviews 61, 96 – 110.

Czymzik, M., Dulski, P., Plessen, B., von Grafenstein, U., Naumann, R., Brauer, A., 2010. A 450 year record of spring-summer flood layers in annually laminated sediments from Lake Ammersee (southern Germany). Water Resources Research 46.

Dansgaard, W., Johnsen, S.J., Clausen, H.B., Dahl-Jensen, D., Gundestrup, N.S., Hammer, C.U., Hvidberg, C.S., Steffensen, J.P., 1993. Evidence for general instability of past climate from a 250-kyr ice core record. Nature 364, 218 – 220.

Dean, W.E., 1993. Physical properties, mineralogy, and geochemistry of Holocene varved sediments from Elk Lake, Minnesota, in: Bradbury, J., Dean, W. (Eds.), Elk Lake, Minnesota: Evidence for rapid climate change in the north-central United States. Geological Society of America Special Paper. volume 276, pp. 135 – 158.

EPICA community members, 2005. One-to-one coupling of glacial climate variability in Greenland and Antarctica. Nature 444, 195 – 198.

Fairbanks, R.G., Mortlock, R.A., T.-C. Chiu, Cao, L., Kaplan, A., Guilderson, T.P., Fairbanks, T.W., Bloom, A.L., Grootes, P.M., Nadeau, M.J., 2005. Radiocarbon calibration curve spanning 10,000 to 50,000 years BP based on paired $^{230}Th/^{234}U/^{238}U$ and ^{14}C dates on pristine corals. Quaternary Science Reviews 24, 1781 – 1796.

Francus, P., Lamb, H., Nakagawa, T., Marshall, M., Brown, E., project members, S.., 2009. The potential of high-resolution X-ray fluorescence core scanning: Applications in paleolimnology. PAGES news 17, 93 – 95.

Fukutome, S., Frei, C., Schär, C., 2003. Interannual Covariance between Japan Summer Precipitation and Western North Pacific SST. Journal of the Meteorological Society of Japan 81, 1435 – 1456.

Gibson, C., Anderson, J., Haworth, E., 2003. Aulacoseira subarctica: taxonomy, physiology, ecology and palaeoecology. European Journal of Phycology 38, 83 – 101.

Gilli, A., Anselmetti, F.S., Glur, L., Wirth, S.B., 2013. Lake Sediments as Archives of Recurrence Rates and Intensities of Past Flood Events, in: Schneuwly-Bollschweiler, M., Stoffel, M., Rudolf-Miklau, F. (Eds.), Dating Torrential Processes on Fans and Cones - Methods and Their Application for Hazard and Risk Assessment. volume 47 of *Advances in Global Change Research*, pp. 225 – 242.

Godwin, H., 1962. Radiocarbone Dating: Fifth International Conference. Nature 195, 943 – 944.

Goslar, T., Arnold, M., Bard, E., Kuc, T., Pazdur, M.F., Ralska-Jasiewiczowa, M., Różański, K., Tisnerat, Walanus, A., Wicik, B., Więckowski, 1995. High concentration of atmospheric ^{14}C during the Younger Dryas cold episode. Nature 377, 414 – 417.

Goslar, T., Arnold, M., Tisnerat-Laborde, N., Hatté, C., Paterne, M., Ralska-Jasiewiczowa, M., 2000. Radiocarbon Calibration by Means of Varves Versus ^{14}C Ages of Terrestrial Macrofossils from Lake Gościaż and Lake Peresplino, Poland. Radiocarbon 42, 335 – 348.

Gotanda, K., Nakagawa, T., Tarasov, P.E., Kitagawa, J., Inoue, Y., Yasuda, Y., 2002. Biome classification from Japanese pollen data: application to modern-day and late quaternary samples. Quaternary Science Reviews 21, 647 – 657.

Gotanda, K., Yasuda, Y., 2008. Spatial biome changes in southwestern Japan since the Last Glacial Maximum. Quaternary International 184, 84 – 93.

Grossman, M.J., 2001. Large floods and climatic change during the Holocene on the Ara River, Central Japan. Geomorphology 39, 21 – 37.

Hajdas, I., Bonani, G., Zolitschka, B., 2000. Radiocarbon dating of varve chronologies; Soppensee and Holzmaar lakes after ten years. Radiocarbon 42, 349 – 353.

Hajdas, I., Ivy, S.D., Beer, J., Bonani, G., Imboden, D., Lotted, A.F., Sturm, M., Suter, M., 1993. AMS radiocarbon dating and varve chronology of Lake Soppensee: 6000 to 12000 ^{14}C years BP. Climate Dynamics 9, 107 – 116.

Haltia-Hovi, E., Timo, S., Maaret, K., 2007. A 2000-year record of solar forcing on varved lake sediment in eastern Finland. Quaternary Science Reviews 26, 678 – 689.

Hayahsi, R., Takahara, H., Hayashida, A., Takemura, K., 2010. Millennial-scale vegetation changes during the last 40,000 yr based on a pollen record from Lake Biwa, Japan. Quaternary Research 74, 91 – 99.

Hoffmann, D.L., Beck, J.W., Richards, D.A., Smart, P.L., Singarayer, J.S., Ketchmark, T., Hawkesworth, C.J., 2010. Towards radiocarbon calibration beyond 28 ka using speleothems from the Bahamas. Earth and Planetary Science Letters 289, 1 – 10.

Hovius, N., Meunier, P., Lin, C.W., Chen, H., Chen, Y.G., Dadson, S., Horng, M.J., Lines, M., 2011. Prolonged seismically induced erosion and the mass balance of a large earthquake. Earth and Planetary Science Letters 304, 347 – 355.

Hua, Q., Berbetti, M., Fink, D., Kaiser, K.F., Friedrich, M., Kromer, B., Levchenko, V.A., Zoppig, U., Smith, A.M., Bertuch, F., 2009. Atmospheric ^{14}C variations derived from tree rings during the early Younger Dryas. Quaternary Science Reviews 28, 2982 – 2990.

Hughen, K., Southon, J., Lehman, S., Bertrand, C., Turnbull, J., 2006. Marine-derived ^{14}C calibration and activity record for the past 50,000 years updated from the Cariaco Basin. Quaternary Science Reviews 25, 3216 – 3227.

Hughen, K.A., Overpeck, J.T., Jehman, S.J., Kashgarian, M., Southon, J., Peterson, L.C., Alley, R., Sigman, D.M., 1998. Deglacial changes in ocean circulation from an extended radiocarbon calibration. Nature 391, 65 – 68.

Hughen, K.A., Overpeck, J.T., Peterson, L.C., Trumbore, S., 1996. Rapid climate changes in the tropical Atlantic region during the last deglaciation. Nature 380, 51 – 54.

Hughen, K.A., Southon, J.R., Lehman, S.J., Overpeck, J.T., 2000. Synchronous Radiocarbon and Climate Shifts During the Last Deglaciation. Science 290, 1951 – 1954.

Hughen, K.A., Southton, J.R., Bertrand, C.J.H., Frantz, B., Zermeño, P., 2004. Cariaco basin calibration update: Revisions to calendar and ^{14}C chronologies for core PL07-58PC. Radiocarbon 46, 1161 – 1187.

Imbrie, J., Hays, J.D., Martinson, D.G., McIntyre, A., Mix, A.C., Morley, J.J., Pisias, N.G., Prell, W.L., Shackleton, N.F., 1984. The orbital theory of Pleistocene climate: Support from a revised chronology of the marine δ^{18}O record, in: Berger, A., Imbrie, J., Hays, J., Kukla, G., Saltzman, B. (Eds.), Milankovitch and Climate. Reidel Publishing, pp. 269 – 305.

Japan Meteorological Agency, 1998a. Daily and every 3-hours meteorological data at the ground surface (1971-1990). Japan Meteorological Agency, CD-ROM.

Japan Meteorological Agency, 1998b. Daily and every 3-hours meteorological data at the ground surface (1961-1970). Japan Meteorological Agency, CD-ROM.

Jessen, K., 1935. Archaelogical dating in the history of North Jutland's vegetation. Acta Archaeologica 5, 185 – 214.

Kaiser, K.F., Friedrich, M., Miramont, C., Kromer, B., Sgier, M., Schaub, M., Boeren, I., Remmele, S., Talamo, S., Guibal, F., Sivan, O., 2012. Challenging process to make the Lateglacial tree-ring chronologies from Europe absolute an inventory. Quaternary Science Reviews 36, 78 – 90.

Kämpf, L., Brauer, A., Dulski, P., Lami, A., Marchetto, A., Gerli, S., Ambrosetti, W., Guilizzoni, P., 2012. Detrital layers marking flood events in recent sediments of Lago Maggiore (N. Italy) and their comparison with instrumental data. Freshwater Biology 57, 2076 – 2090.

Katsuta, N., Takano, M., Kawakami, S.I., Togami, S., Fukusawa, H., Kumazawa, M., Yasuda, Y., 2006. Climate system transition from glacial to interglacial state around the beginning of the last termination: Evidence from a centennial- to millennial-scale climate rhythm. Geochemistry Geophysics Geosystems 7.

Katsuta, N., Takano, M., Kawakami, S.I., Togami, S., Fukusawa, H., Kumazawa, M., Yasuda, Y., 2007. Advanced Micro-XRF Method to Separate Sedimentary Rhythms and Event Layers in Sediments: Its Application to Lacustrine Sediment from Lake Suigetsu, Japan. Journal of Paleolimnology 37, 259 – 271.

Kawakami, S.I., Fukusawa, H., Kanaori, Y., 1996. A new opportunity to detect paleo-earthquake events dating back to the past 10 millennia: a record from lacustrine sediment. Engineering Geology 43, 177 – 188.

Kido, Y., Koshikawa, T., Tada, R., 2006. Rapid and quantitative major element analysis method for wet fine-grained sediments using an XRF microscanner. Marine Geology 229, 209 – 225.

Kim, J.H., Ho, C.H., Sui, C.H., 2005. Circulation features associated with the record-breaking typhoon landfall on Japan in 2004. Geophysical Research Letters 32.

Kitagawa, H., Fukuzawa, H., Nakamura, T., Okumura, M., Takemura, K., Hayashida, A., Yasuda, Y., 1995. AMS ^{14}C dating of varved sediments from Lake Suigetsu, Central Japan and atmospheric ^{14}C change during the Late Pleistocene. Radiocarbon 37, 371 – 378.

Kitagawa, H., van der Plicht, J., 1998a. Atmospheric Radiocarbon Calibration to 45,000 yr B.P.: Late Glacial Fluctuations and Cosmogenic Isotope Production. Science 279, 1187 – 1190.

Kitagawa, H., van der Plicht, J., 1998b. A 40,000-year varve chronology from Lake Suigetsu, Japan: Extension of the ^{14}C calibration curve. Radiocarbon 40, 505 – 515.

Kitagawa, H., van der Plicht, J., 2000. Atmospheric radiocarbon calibration beyond 11,900 cal BP from Lake Suigetsu laminated sediments. Radiocarbon 42, 369 – 380.

Kondo, R., Nakagawa, A., Mochizuki, L., Osawa, K., Fujioka, Y., Butani, J., 2009. Dominant bacterioplankton populations in the meromictic Lake Suigetsu as determined by denaturing gradient gel electrophoresis of 16S rRNA gene fragments. Limnology 10, 63 – 69.

Korty, R.L., Camargo, S.J., Galewsky, J., 2012. Tropical Cyclone Genesis Factors in Simulations of the Last Glacial Maximum. Journal of Climate 25, 4348 – 4365.

Kossler, A., Tarasov, P., Schlolaut, G., Nakagawa, T., Marshall, M., Brauer, A., Staff, R., Bronk Ramsey, C., Bryant, C., Lamb, H., Demske, D., Gotanda, K., Haraguchi, T., Yokoyama, Y., Yonenobu, H., Tada, R., 2011. Onset and termination of the late-glacial climate reversal in the high-resolution diatom and sedimentary records from the annually laminated SG06 core from Lake Suigetsu, Japan. Palaeogeography, Palaeoclimatology, Palaeoecology 306, 103 – 115.

Kromer, B., Becker, B., 1993. German oak and pine ^{14}C calibration, 7200-9439 BC. Radiocarbon 35, 125 – 135.

Kromer, B., Friedrich, M., Hughen, K.A., Kaiser, F., Remmele, S., Schaub, M., Talamo, S., 2004. Late glacial ^{14}C ages from a floating, 1382-ring pine chronology. Radiocarbon 46, 1203 – 1209.

Lambeck, K., Yokoyama, Y., Purcell, T., 2000. Into and out of the Last Glacial Maximum: sea-level change during Oxygen Isotope Stages 3 and 2. Quaternary Science Reviews 21, 343 – 360.

Lamoureux, S.F., 2001. Varve chronology techniques, in: Last, W.M., Smol, J.P. (Eds.), Developments in Paleoenvironmental Research (DPER), Vol. 2 - Tracking Environmental Change Using Lake Sediments: Physical and Chemical Techniques. Kluwer Academic Publishers, pp. 247 – 260.

Lamourex, S., 2000. Five centuries of interannual sediment yield and rainfall-induced erosion in the Canadian High Arctic recorded in lacustrine varves. Water Resources Research 36, 309 – 318.

Lane, C.S., Blockley, S.P.E., Bronk Ramsey, C., Lotter, A.F., 2011. Tephrochronology and absolute centennial scale synchronisation of European and Greenland records for the last glacial to interglacial transition: A case study of Soppensee and NGRIP. Quaternary International 246, 145 – 156.

Lauterbach, S., Chapron, E., Brauer, A., Hüls, M., Gilli, A., Arnaud, F., Piccin, A., Nomade, J., Desmet, M., von Grafenstein, U., DecLakes Participants, 2012. A sedimentary record of Holocene surface runoff events and earthquake activity from Lake Iseo (Southern Alps, Italy). The Holocene 22, 749 – 760.

Libby, W.F., 1946. Atmospheric Helium Three and Radiocarbon from Cosmic Radiation. Physical Review 69, 671 – 672.

Libby, W.F., 1949. Atmospheric Helium Three and Radiocarbon from Cosmic Radiation. Science 109, 227 – 228.

Lowe, J.J., Rasmussen, S.O., Björck, S., Hoek, W.Z., Yu, Z.C., INTIMATE members, 2008. Synchronisation of palaeoenvironmental events in the North Atlantic region during the Last Termination: a revised protocol recommended by the INTIMATE group. Quaternary Science Reviews 27, 6 – 17.

Machida, H., Arai, F., 2003. Atlas of Tephra in and around Japan - 2nd ed. Univ. of Tokyo press.

Maekeler, R., 2012. Stabile Eisenisotope an laminierten Sedimenten des Lake Suigetsu. diploma thesis (in German). Leibnizuniversität Hannover.

Mangerud, J., Andersen, S.T., Berglund, B.E., Donner, J.J., 1974. Quaternary stratigraphy of Norden, a proposal for terminology and classification. Boreas 3, 109 – 126.

Mangili, C., Brauer, A., Moscariello, A., Naumann, R., 2005. Microfacies of detrital event layers deposited in Quaternary varved lake sediments of the Piànico-Sèllere Basin (northern Italy). Sedimentology 52, 927 – 943.

Marshall, M., Schlolaut, G., Brauer, A., Nakagawa, T., Staff, R.A., Bronk Ramsey, C., Lamb, H., Gotanda, K., Haraguchi, T., Yokoyama, Y., Yonenobu, H., Tada, R., SG06 project members, 2012. A novel approach to varve counting using μXRF and X-radiography in combination with thin-section microscopy, applied to the Late Glacial chronology from Lake Suigetsu, Japan. Quaternary Geochronology 13, 70 – 80.

Masuzawa, T., Kitano, Y., 1982. Sulfate reduction and sulfur fixation in sediment of a historically meromictic lake, Lake Suigetsu, Japan. Journal of Oceanography 38, 21 – 27.

Matsumoto, A., 1996. K-Ar age determinations of young volcanic rocks - correlation for initial $^{40}Ar/^{39}Ar$ ratios and its application. Chishitsu News 501, 12 – 17. In Japanese.

Matsumoto, A., Ui, T., 1997. K-Ar Age of Ata Pyroclastic Flow Deposit, Southern Kyusyu, Japan. Kazan (Volcano) 42, 223 – 225. In Japanese with English summary.

Matsuyama, M., Saijo, Y., 1971. Studies on Biological Metabolism in a Meromictic Lake Suigetsu. Journal of the Oceanographical Society of Japan 27, 197 – 206.

McHargue, L.R., Damon, P.E., Donahue, D.J., 1995. Enhanced cosmic-ray production of 10Be coincident with the Mono Lake and Laschamp Geomagnetic Excursions. Geophysical Research Letters 22, 659 – 662.

Mingram, J., Negendank, J.F.W., Brauer, A., Berger, D., Hendrich, A., Köhler, M., Usinger, H., 2006. Long cores from small lakes-recovering up to 100 m-long lake sediment sequences with a high-precision rod-operated piston corer (Usinger-corer). Journal of Paleolimnology 37, 517 – 528.

Miyairi, Y., Yoshida, K., Miyazaki, Y., Matsuzaki, H., Kaneoka, I., 2004. Improved ^{14}C dating of a tephra layer (AT tephra, Japan) using AMS on selected organic fractions. Nuclear Instruments and Methods in Physics Research Section B 223-224, 555 – 559.

Moreno, A., Valero-Garcés, B.L., González-Sampériz, P., Rico, M., 2008. Flood response to rainfall variability during the last 2000 years inferred from the Taravilla Lake record (Central Iberian Range, Spain). Journal of Paleolimnology 40, 943 – 961.

Moy, C.M., Seltzer, G.O., Rodbell, D.T., Anderson, D.M., 2002. Variability of El Niño/Southern Oscillation activity at millennial timescales during the Holocene epoch. Sedimentology 420, 162 – 165.

Mulder, T., Alexander, J., 2001. The physical character of subaqueous sedimentary density flows and their deposits. Sedimentology 48, 269 – 299.

Muscheler, R., Beer, J., Kubik, P.W., Synal, H.A., 2005. Geomagnetic field intensity during the last 60,000 years based on ^{10}Be and ^{36}Cl from the Summit ice cores and ^{14}C. Quaternary Science Reviews 24, 1849 – 1860.

Muscheler, R., Kromer, B., Björck, S., Svensson, A., Friedrich, M., Kaiser, K.F., Southon, J., 2008. Tree rings and ice cores reveal ^{14}C calibration uncertainties during the Younger Dryas. Nature Geoscience 1, 263 – 267.

Nagashima, K., Tada, R., 2012. Teleconnection mechanism between millennial-scale Asian Monsoon dynamics and North Atlantic climate. PAGES news 20, 64 – 65.

Nakagawa, T., 2007. Double-L channel: an amazingly non-destructive method of continuous sub-sampling from sediment cores. Quaternary International Supplement 167-168, 298.

Nakagawa, T., Gotanda, K., Haraguchi, T., Danhara, T., Yonenobu, H., Brauer, A., Yokoyama, Y., Tada, R., Takemura, K., Staff, R.A., Payne, R., Bronk Ramsey, C., Bryant, C., Brock, F., Schlolaut, G., Marshall, M., Tarasov, P., Lamb, H., 2012. SG06, a fully continuous and varved sediment core from Lake Suigetsu, Japan: stratigraphy and potential for improving the radiocarbon calibration model and understanding of late Quaternary climate changes. Quaternary Science Reviews 36, 164 – 176.

Nakagawa, T., Kitagawa, H., Yasuda, Y., Tarasov, P.E., , Nishida, K., Gotanda, K., Sawai, Y., 2003. Asynchronous Climate Changes in the North Atlantic and Japan During the Last Termination. Science 299, 688 – 691.

Nakagawa, T., Kitagawa, H., Yasuda, Y., Tarasov, P.E., Gotanda, K., Sawai, Y., 2005. Pollen/event stratigraphy of the varved sediment of Lake Suigetsu, central Japan from 15,701 to 10,217 SG vyr BP (Suigetsu varve years before present): Description, interpretation, and correlation with other regions. Quaternary Science Reviews 24, 1691 – 1701.

Nakagawa, T., Okuda, M., Yonenobu, H., Miyoshi, N., Fujiki, T., Gotanda, K., Tarasov, P.E., 2008. Regulation of the monsoon climate by two different orbital rhythms and forcing mechanisms. Geology 36, 491 – 494.

Nakagawa, T., Tarasov, P.E., Kitagawa, H., Yasuda, Y., Gotanda, K., 2006. Seasonally specific responses of the East Asian monsoon to deglacial climate changes. Geology 34, 521 – 524.

Nakagawa, T., Tarasov, P.E., Nishida, K., Gotanda, K., Yasuda, Y., 2002. Quantitative pollen-based climate reconstruction in central Japan: application to surface and Late Quaternary spectra. Quaternary Science Reviews 21, 2099 – 2113.

Neugebauer, I., Brauer, A., Dräger, N., Dulski, P., Wulff, S., Plessen, B., Mingram, J., Herzschuh, U., Brande, A., 2012. A Younger Dryas varve chronology from the Rehwiese palaeolake record in NE-Germany. Quaternary Science Reviews 36, 91 – 102.

Oguchi, T., Saito, K., Kadomura, H., Grossman, M., 2001. Fluvial geomorphology and paleohydrology in Japan. Geomorphology 39, 3 – 19.

Ojala, A.E.K., Francus, P., 2002. Comparing X-ray densitometry and BSE-image analysis of thin section in varved sediments. Boreas 31, 57 – 64.

Ojala, A.E.K., Francus, P., Zolitschka, B., Besonen, M., Lamoureux, S.F., 2012. Characteristics of sedimentary varve chronologies - A review. Quaternary Science Reviews 43, 45 – 60.

Ojala, A.E.K., Tiljander, M., 2003. Testing the fidelity of sediment chronology: comparing varve and paleomagnetic results from Holocene lake sediments from central Finland. Quaternary Science Reviews 22, 1787 – 1803.

Oldfield, F., Wake, R., Boyle, J., Jones, R., Nolan, S., Gibbs, Z., Appleby, P., Fisher, E., Wolff, G., 2003. The late-Holocene history of Gormire Lake (NE England) and its catchment: a multiproxy reconstruction of past human impact. The Holocene 13, 677 – 690.

Olsson, I.U., 2009. Radiocarbon dating history : Early days, questions, and problems met. Radiocarbon 51, 1 – 43.

Olsson, I.U., Osadebe, F.A.N., 1974. Carbon isotope variations and fractionation corrections in ^{14}C dating. Boreas 3, 139 – 146.

Ono, Y., Aoki, T., Hasegawa, H., Dali, L., 2005. Mountain glaciation in Japan and Taiwan at the global Last Glacial Maximum. Quaternary International 138-139, 79 – 92.

Petterson, G., Odgaard, B., Renberg, I., 1999. Image analysis as a method to quantify sediment components. Journal of Paleolimnology 22, 443 – 455.

van der Plicht, J., Beck, J.W., Bard, E., Guilderson, T.P., Hughen, K.A., Kromer, B., McCormac, F.G., Bronk Ramsey, C., Reimer, P.J., Reimer, R.W., Remmele, S., Richards, D.A., Southon, J.R., Stuiver, M., Weyhenmeyer, C.E., 2004. NotCal04 - Comparison/calibration ^{14}C records 26-50 cal kyr BP. Radiocarbon 46, 1225 – 1238.

Porter, S.C., An, Z.S., 1995. Correlation between climate events in the North Atlantic and China during the last glaciation. Nature 375, 305 – 308.

Prasad, S., Negendank, J.F.W., Stein, M., 2009. Varve counting reveals high resolution radiocarbon reservoir age variations in palaeolake Lisan. Journal of Quaternary Science 24, 690 – 696.

Rasmussen, S.O., Selerstad, I.K., Andersen, K.K., Bigler, M., Dahl-Jensen, D., Johnsen, S.J., 2008. Synchronization of the NGRIP, GRIP, and GISP2 ice cores across MIS 2 and palaeoclimatic implications. Quaternary Science Reviews 27, 18 – 28.

Reimer, P.J., 2012. Refining the Radiocarbon Time Scale. Science 338, 337 – 338.

Reimer, P.J., Baillie, M.G.L., Bard, E., Bayliss, A., Beck, J.W., Bertrand, C.J.H., Blackwell, P.G., Buck, C.E., Burr, G.S., Cutler, K.B., Damon, P.E., Edwards, R.L., Fairbanks, R.G., Friedrich, M., Guilderson, T.P., Hogg, A., Hughen, K., Kromer, B., McCormac, G., Manning, S., Ramsey, C.B., Reimer, R.W., Remmele, S., Southon, J., Stuiver, M., Talamo, S., Taylor, F.W., van der Plicht, J., Weyhenmeyer, C.E., 2004. IntCal04 terrestrial radiocarbon age calibration, 0-26 cal kyr BP. Radiocarbon 46, 1029 – 1058.

Reimer, P.J., Baillie, M.G.L., Bard, E., Bayliss, A., Beck, J.W., Blackwell, P.G., Bronk Ramsey, C., Buck, C.E., Burr, G.S., Edwards, R.L., Friedrich, M., Grootes, P.M., Guilderson, T.P., Hajdas, I., Heaton, T.J., Hogg, A.J., Hughen, K.A., Kaiser, K.F., Kromer, B., McCormac, F.G., Manning, S.W., Reimer, R.W., Richards, D.A., Southon, J.R., Talamo, S., Turney, C.S.M., van der Plicht, J., Weyhenmeyer, C.E., 2009. IntCal09 and Marine09 radiocarbon age calibration curves, 0-50,000 years cal BP. Radiocarbon 51, 1111 – 1150.

Rioual, P., Andrieu-Ponel, V., de Beaulieu, J.L., Reille, M., Svobodova, H., Battarbee, R.W., 2007. Diatom responses to limnological and climatic changes at Ribains Maar (French Massif Central) during the Eemian and Early Würm. Quaternary Science Reviews 26, 1557 – 1609.

Ripepe, M., Roberts, L.T., Fischer, A.G., 1991. Enso and sunspot cycles in varved Eocene oil shales from image analysis. Journal of Sedimentary Petrology 61, 1155 – 1163.

Rose, K.A., Silkes, E.L., Guilderson, T.P., Shane, P., Hill, T.M., Zahn, R., Spero, H.J., 2010. Upper-ocean-to-atmosphere radiocarbon offsets imply fast deglacial carbon dioxide release. Nature 466, 1093 – 1097.

Saarinen, T., Petterson, G., 2001. Image analysis techniques, in: Last, W.M., Smol, J.P. (Eds.), Tracking Environmental Change Using Lake Sediments, Vol. 2: Physical and Geochemical methods. Kluwer Academic Publishers, pp. 23 – 40.

Schlolaut, G., Brauer, A., Marshall, M.H., Nakagawa, T., Staff, R.A., Bronk Ramsey, C., Lamb, H.F., Bryant, C.L., Naumann, R., Dulski, P., Brock, F., Yokoyama, Y., Tada, R., Haraguchi, T., Suigetsu 2006 project members, submitted. Event layers in the Japanese Lake Suigetsu 'SG06' sediment core: description, interpretation and climatic implications. Quaternary Science Reviews .

Schlolaut, G., Marshall, M.H., Brauer, A., Nakagawa, T., Lamb, H.F., Staff, R.A., Bronk Ramsey, C., Bryant, C.L., Brock, F., Kossler, A., Tarasov, P.E., Yokoyama, Y., Tada, R., Haraguchi, T., Suigetsu 2006 project members, 2012. An automated method for varve interpolation and its application to the Late Glacial chronology from Lake Suigetsu, Japan. Quaternary Geochronology 13, 52 – 69.

Schramm, A., Stein, M., Goldstein, S.L., 2000. Calibration of the ^{14}C time scale to >40 ka by ^{234}U-^{230}Th dating of Lake Lisan sediments (last glacial Dead Sea). Earth and Planetary Science Letters 175, 27 – 40.

Schulz, M., Manfred, M., 2002. REDFIT: estimating red-noise spectra directly from unevenly spaced paleoclimatic time series. Computers & Geosciences 28, 421 – 426.

Schulz, M., Stattegger, K., 1997. SPECTRUM: Spectral analysis of unevenly spaced paleoclimatic time series. Computers & Geosciences 23, 929 – 945.

Shen, C.C., Kano, A., Hori, M., Lin, K., Chiu, T.C., Burr, G.S., 2010. East Asian monsoon evolution and reconciliation of climate records from Japan and Greenland during the last deglaciation. Quaternary Science Reviews 29, 3327 – 3335.

Shigematsu, T., Tabushi, M., Nishikawa, Y., Muroga, T., Matsunaga, Y., 2010. Geochemical Study on Lakes Mikata. Bulletin of the Institute for Chemical Research, Kyoto University 39, 43 – 56.

Shotton, F.W., 1972. An Example of Hard-Water error in Radiocarbon Dating of Vegetable Matter. Nature 240, 461 – 462.

Smith, V.C., Mark, D.F., Staff, R.A., Blockley, S.P.E., Bronk Ramsey, C., Bryant, C.L., Nakagawa, T., Han, K.K., Weh, A., Takemura, K., Danhara, T., 2011. Toward establishing precise ^{40}Ar/^{39}Ar chronologies for Late Pleistocene palaeoclimate archives: an example from Suigetsu SG06, Japan. Quaternary Science Reviews 30, 2845 – 2850.

Smith, V.C., Staff, R.A., Blockley, S.P.E., Bronk Ramsey, C., Nakagawa, T., Mark, D.F., Takemura, K., Danhara, T., Suigetsu 2006 Project Members, 2013. Identification and correlation of visible tephras in the Lake Suigetsu SG06 sedimentary archive, Japan: chronostratigraphic markers for synchronising of east Asian/west Pacific palaeoclimatic records across the last 150 ka. Quaternary Science Reviews 67, 121 – 137.

Snowball, I., Sandgren, P., Petterson, G., 1999. The mineral magnetic properties of an annually laminated Holocene lake-sediment sequence in Northern Sweden. The Holocene 9, 353 – 362.

Solanki, S.K., Usoskin, I.G., Kromer, B., Schüssler, M., Beer, J., 2004. Unusual activity of the Sun during recent decades compared to the previous 11,000 years. Nature 431, 1084 – 1087.

Southon, J., Noronha, A.L., Cheng, H., Edwards, R.L., Wang, Y., 2012. A high-resolution record of atmospheric ^{14}C based on Hulu Cave speleothem H82. Quaternary Science Reviews 33, 32 – 41.

Staff, R.A., Bronk Ramsey, C., Bryant, C.L., Brock, F., Payne, R.L., Schlolaut, G., Marshall, M.H., Brauer, A., Lamb, H.F., Tarasov, P., Yokoyama, Y., Haraguchi, T., Gotanda, K., Yonenobuk, H., Nakagawa, T., Suigetsu 2006 project members, 2011. New ^{14}C Determinations from Lake Suigetsu, Japan: 12,000 to 0 cal BP. Radiocarbon 53, 511 – 528.

Staff, R.A., Bronk Ramsey, C., Nakagawa, T., Suigetsu 2006 project members, 2010. A re-analysis of the Lake Suigetsu terrestrial radiocarbon calibration dataset. Nuclear Instruments and Methods in Physics Research Section B: Beam Interactions with Materials and Atoms 268, 960 – 965.

Staff, R.A., Nakagawa, T., Schlolaut, G., Marshall, M.H., Brauer, A., Lamb, H., Bronk Ramsey, C., Bryant, C.L., Brock, F., Kitagawa, H., van der Plicht, J., Payne, R.L., Smith, V.C., Mark, D.F., MacLeod, A., Blockley, S.P.E., Schwenninger, J.L., Tarasov, P., Haraguchi, T., Gotanda, K., Yonenobu, H., Yokoyama, Y., Suigetsu 2006 project members, 2013a. The Multiple Chronological Techniques Applied to the Lake Suigetsu (SG06) Sediment Core. Boreas 42, 259 – 266.

Staff, R.A., Schlolaut, G., Bronk Ramsey, C., Brock, F., Bryant, C.L., Kitagawa, H., van der Plicht, J., Marshall, M.H., Brauer, A., Lamb, H., Payne, R.L., Tarasov, P., Haraguchi, T., Gotanda, K., Yonenobu, H., Yokoyama, Y., Nakagawa, T., Suigetsu 2006 project members, 2013b. Integration of the Old and New Lake Suigetsu (Japan) Terrestrial Radiocarbon Calibration Data Sets. Radiocarbon 55, in press.

Stanford, J.D., Rohling, E.J., Bacon, S., Roberts, A.P., Grousset, F., Bolshaw, M., 2011. A new concept for the paleoceanographic evolution of Heinrich event 1 in the North Atlantic. Quaternary Science Reviews 30, 1047 – 1066.

Steinhilber, F., Beer, J., Fröhlich, C., 2009. Total solar irradiance during the Holocene. Geophysical Research Letters 36.

Stuiver, M., Braziunas, T.F., Becker, B., Kromer, B., 1991. Climatic, solar, oceanic, and geomagnetic influences on late-glacial and holocene atmospheric $^{14}C^{12}C$ change. Quaternary Research 35, 1 – 24.

Stuiver, M., Pearson, G.W., Braziunas, T., 1976. Radiocarbon Age Calibration of Marine Samples Back to 9000 cal yr BP. Radiocarbon 28, 980 – 1021.

Stuiver, M., Polach, H.A., 1977. Discussion: Reporting of ^{14}C Data. Radiocarbon 19, 355 – 363.

Stuiver, M., Reimer, P.J., Bard, E., Beck, J.W., Burr, G.S., Hughen, K.A., Kromer, B., McCormac, G., van der Plicht, J., Spurk, M., 1998. INTCAL98 radiocarbon age calibration, 24,000-0 cal BP. Radiocarbon 40, 1041 – 1083.

Sturm, M., Matter, A., 1978. Turbidites and Varves in Lake Brienz (Switzerland): Deposition of Clastic Detritus by Density Currents. Special Publications of the International Association of Sedimentologists 2, 147 – 168.

Svensson, A., Andersen, K.K., Bigler, M., Clausen, H.B., Dahl-Jensen, D., Davies, S.M., Johnsen, S.J., Muscheler, R., Parrenin, F., Rasmussen, S.O., Röthlisberger, R., Seierstad, I., Steffensen, J.P., , Vinther, B.M., 2008. A 60 000 year Greenland stratigraphic ice core chronology. Climate of the Past 4, 47 – 57.

Svensson, A., Andersen, K.K., Bigler, M., Clausen, H.B., Dahl-Jensen, D., Davies, S.M., Johnsen, S.J., Muscheler, R., Rasmussen, S.O., Röthlisberger, R., Steffensen, J.P., Vinther, B., 2006. The Greenland Ice Core Chronology 2005, 15-42 ka. Part 2: comparison to other records. Quaternary Science Reviews 25, 3258 – 3267.

Swierczynski, T., Brauer, A., Lauterbach, S., Martín-Puertas, C., Dulski, P., von Grafenstein, U., Rohr, C., 2012. A 1600 yr seasonally resolved record of decadal-scale flood variability from the Austrian Pre-Alps. Geology 40, 1047 – 1050.

Tada, R., Irino, T., Koizumi, I., 1999. Land-ocean linkages over orbital and millennial timescales recorded in Late Quaternary sediments of the Japan Sea. Paleoceanography 14, 236 – 247.

Takano, Y., Tachibana, Y., Iwamoto, K., 2008. Influences of Large-scale Atmospheric Circulation and Local Sea Surface Temperature on Convective Activity over the Sea of Japan in December. Sola 4, 113 – 116.

Takei, T., Minoura, K., Tsukawaki, S., Nakamura, T., 2002. Intrusion of a branch of the Oyashio Current into the Japan Sea during the Holocene. Paleoceanography 17, 11–1–11–10.

Takemura, K., Kitagawa, H., Hayashida, A., Yasuda, Y., 1994. Sedimentary Facies and chronology of Core Samples from Lake Mikata, Lake Suigetsu and Kurota Lowland, Central Japan - Sedimentary environment in Mikata Lowland since the last interglacial time. Journal of Geography 103, 233 – 242.

Tian, J., Brown, T.A., Hul, F.S., 2005. Comparison of varve and ^{14}C chronologies from Steel Lake, Minnesota, USA. The Holocene 15, 510 – 517.

Torrence, C., Compo, G.P., 1998. A Practical Guide to Wavelet Analysis. Bulletin of the American Meteorological Society 79, 61 – 78.

Tyler, J., Kashiyama, Y., Ohkouchi, N., Ogawa, N., Yokoyama, Y., Chikaraishi, Y., Staff, R.A., Ikehara, M., Bronk Ramsey, C., Bryant, C., Brock, F., Gotanda, K., Haraguchi, T., Yonenobu, H., Nakagawa, T., 2010. Tracking aquatic change using chlorine-specific carbon and nitrogen isotopes: The last glacial-interglacial transition at Lake Suigetsu, Japan. Geochemistry Geophysics Geosystems 11.

Vasskog, K., Nesje, A., Støren, E.N., Waldmann, N., Chapron, E., Ariztegui, D., 2011. A Holocene record of snow-avalanche and flood activity reconstructed from a lacustrine sedimentary sequence in Oldevatnet, western Norway. The Holocene 21, 597 – 614.

Wang, Y.J., Cheng, H., Edwards, R.L., An, Z.S., Wu, J.Y., Shen, C.C., Dorale, J.A., 2001. A High-Resolution Absolute-Dated Late Pleistocene Monsoon Record from Hulu Cave, China. Science 294, 2345 – 2348.

Ward, G.K., Wilson, S.R., 1978. Procedure for comparing and combining radiocarbon age determinations: A critique. Archaeometry 20, 19 – 31.

Weber, M.E., Reichelt, L., Kuhn, G., Pfeiffer, M., Korff, B., Thurow, J.W., Ricken, W., 2010. BMPix and PEAK tools: New methods for automated laminae recognition and counting - Application to glacial varves from Antarctic marine sediment. Geochemistry, Geophysics, Geosystems 11.

Weltje, G.J., Tjallingii, R., 2008. Calibration of XRF core scanners for quantitative geochemical logging of sediment cores: Theory and application. Earth and Planetary Science Letters 274, 423 – 438.

Wilhelm, B., Arnaud, F., Enters, D., Allignol, F., Legaz, A., Magand, O., Revillon, S., Ciguet-Covex, C., Malet, E., 2012. Does global warming favour the occurrence of extreme floods in European Alps? First evidence from a NW Alps proglacial lake sediment record. Climatic Change 113, 563 – 581.

Wohlfarth, B., 2000. AMS Radiocarbon Measurements from the Swedish Varved Clays. Radiocarbon 42, 323 – 333.

Woodruff, J.D., Donnelly, J.P., Okusu, A., 2009. Exploring typhoon variability over the mid-to-late Holocene: evidence of extreme coastal flooding from Kamikoshiki, Japan. Quaternary Science Reviews 28, 1774 – 1785.

Yamada, K., Fukusawa, H., 1999. Paleointensity of the Asian Winter Monsoon and the Westerlies Since the Last Glacial Period, Reconstructed by Eolian Dust Flux in Lacustrine Sediments of Lake Biwa and Lake Suigetsu, central Japan. Geographical Reports of Tokyo Metropolitan University 34, 39 – 57.

Yamaura, T., Tomita, T., 2011. Spatiotemporal differences in the interannual variability of Baiu frontal activity in June. International Journal of Climatology 31, 57 – 71.

Yarincik, K.M., Murray, R.W., 2000. Climatically sensitive eolian and hemipelagic deposition in the Cariaco Basin, Venezuela, over the past 578,000 years: Results from Al/Ti and K/Al. Paleoceanography 15, 210 – 228.

Yasuda, Y., Yamaguchi, K., Nakagawa, T., Fukusawa, H., Kitagawa, J., Okamura, M., 2004. Environmental variability and human adaptation during the Lateglacial/Holocene transition in Japan with reference to pollen analysis of the SG4 core from Lake Suigetsu. Quaternary International 123-125, 11 – 19.

Yuan, D., Cheng, H., Edwards, R.L., Dykoski, C.A., Kelly, M.J., Zhang, M., Qing, J., Lin, Y., Wang, Y., Wu, J., Dorale, J.A., An, Z., Cai, Y., 2004. Timing, Duration, and Transitions of the Last Interglacial Asian Monsoon. Science 304, 575 – 578.

Zhang, W., Graf, H.-F., Leung, Y., Herzog, M., 2012. Different El Niño Types and Tropical Landfall in East Asia. Journal of Climate 25, 6510 – 6523.

Zhao, Y., Yu, Z., Chen, F., 2009. Spatial and temporal patterns of Holocene vegetation and climate changes in arid and semi-arid China. Quaternary International 194, 6 – 18.

Zolitschka, B., 1991. Absolute dating of late Quaternary lacustrine sediments by high resolution varve chronology. Hydrobiologia 214, 59 – 61.

Zolitschka, B., 2003. Dating based on freshwater and marine laminated sediments, in: Mackay, A., Battarbee, R.W., Birks, H.J.B., Oldfield, F. (Eds.), Global Change in the Holocene. Edward Arnold Publishers, pp. 92 – 106.

Zolitschka, B., 2006. Varved lake sediments, in: Elias, S. (Ed.), Encyclopaedia of Quaternary Science. Elsevier, pp. 3105 – 3114.

Zolitschka, B., Brauer, A., Negendank, J.F.W., Stockhausen, H., Lang, A., 2000. Annually dated late Weichselian continental paleoclimate record from the Eifel, Germany. Geology 28, 783 – 786.

Appendix

A. Main Matlab commands for VIP (Chapter II)

The varve interpolation program (VIP) has been written in Matlab. The following commands are required to conduct the interpolation.
The generation of the Settings Matrix is performed by `genart`:

- `genart(div_bs, pv, sil, sir, mode, remove, mvws, runs);`

  `div_bs:` divisor for bin size (dividend is sr)

  `pv:` peak value

  `sil:` left sided σ=μ/sil

  `sir:` right sided σ=μ/sir

  `mode:` μ

  `remove:` percentage of to be removed counts [start stepsize end]

  `mvws:` mode variance window size [start stepsize end]

  `runs:` number of runs with same settings

The interpolation of a count is performed by `efint`:

- `[ADM,IM]=interpvarve(Count, EventList);`

  `ADM:` interpolated age-depth model

  `IM:` Interpolation Matrix

  `Count:` count for interpolation [compositeDepth measuredDepth varveYears]

  `EventList:` events in composite depth for creation of event-free depth [top base]

When different Settings Matrices are applied to the same count the resulting Interpolation Matrices are combined by `combIntMat`, which also produces the resulting age model:

- `[ADM,CIM]=combIntMat(Eventlist, IM1, IM2, IM3, ...);`

  `CIM:` combined interpolation matrix

  `IM:` interpolation matrix (for combination)

Different age-depth models (e.g. from different quality selective counts) from the same core are combined by `combADM`:

- `[CADM]=combADM(Anchorpoint, forcemodels, ADM1, ADM2, ADM3, ...);`

  `CADM:` combined age depth model

  `forcemodels:` allows the user to force a model into combination, vector whose length equals the number of models, at the position of the forced model the value is 1 and 0 otherwise, for example when 3 models are to be combined and the second model is always to be included in the combination, forcemodels is [0 1 0]

  `ADM:` age depth models for combination

B. Supporting (online) material (SOM) to chapter IV

B.1. Materials and Methods

B.1.1. Radiocarbon dating methodology

The AMS dating methodology for the extended (earlier) time period, as with that of the Holocene samples, consisted of cleaning in ultrapure water, storage in 0.2 M HCl, standard acid-base-acid (ABA) pre-treatment, and AMS measurement at the Oxford Radiocarbon Accelerator Unit (OxA) and the NERC Radiocarbon Facility at East Kilbride (SUERC), with sample-size dependent background correction (Staff et al., 2011). Dates from SG93 (Kitagawa and van der Plicht, 1998a) were measured at the Groningen Centre for Isotope Research (GrA). Outliers (single measurements in poor agreement with their neighbors) have been identified and removed from the analysis (Table B.2).

B.1.2. Varve counting

Varve counting of SG06 was performed using a combination of high-resolution micro-XRF (Marshall et al., 2012) and microscopic sedimentary analysis (Schlolaut et al., 2012), and covers the range 12.88-31.67 m composite depth (CD), (ca. 10.2-40.0 kyr BP). These complementary methods have been combined, with indistinguishable varves interpolated using a numerical algorithm (Schlolaut et al., 2012). The varve chronology for Suigetsu is tied to a marker layer at composite depth 1397.4 cm, with an age of 11241±17 cal BP obtained (Staff et al., 2011) by fitting the radiocarbon data to the tree-ring-derived portion of IntCal09 (Reimer et al., 2009).

The methodologies for varve counting by micro-XRF (Marshall et al., 2012) and microscopic sedimentary analysis (Schlolaut et al., 2012) are already published, as well as the approach to combination (Marshall et al., 2012). However, the varve chronology presented here is extended further back in time and in two places the combination does not follow the reasoning given in (Marshall et al., 2012). Between 2375 and 2413 cm CD the mean sedimentation rate is below 0.4 mm/yr, which is below the resolution of the μXRF scan, and hence the model uses only the microscopic age model in this interval. Furthermore, the μXRF count appears to pick up double the annual sediment accumulation between 2550 and 2690 cm CD, and hence this interval is also based solely on the microscopic age model. The microscopic age model is built in accordance with the discussion given in (Schlolaut et al., 2012).

This varve-based chronology for Suigetsu (given in $SG06_{2012}$ vyr BP, before 1950) is tied to a marker layer at 1397.4 cm CD, with an age of 11241±17 yr cal BP (1σ error, or a 68.2% highest probability density (hpd) range of 11255-11222 cal BP).

B.1.3. Compilation of the radiocarbon dataset

All of the radiocarbon dates are placed onto the $SG06_{2012}$ varve chronology. Beyond the varve chronology (>3167.6 cm CD), linear extrapolation by event-free depth (EFD) is used to put the radiocarbon data onto a preliminary age scale. We start with 856 measurements from the complete Suigetsu record; this includes all of the measurements from SG06 and the measurements from the varved portion of SG93 (Kitagawa and van der Plicht, 1998a,b,

2000). Ages are converted to inferred Δ^{14}C values and compared to their neighbors to check for outliers. Outliers were identified on the basis of three main criteria:

- duplicate samples from the same level that fail a χ^2 test at 5% (Ward and Wilson, 1978); there were 13 such samples.
- samples which imply a $\geq$400‰ shift in Δ^{14}C unsupported by adjacent measurements; there were 12 such samples.
- samples which imply a Δ^{14}C which is $\geq 4\sigma$ outside the value implied by the average of adjacent measurements; there were 23 such samples.

In total, 808 samples were retained in the dataset (Table B.1) and 48 rejected (Table B.2). There was a higher proportion of rejected samples amongst some of the very small samples dated for SG06 (Fig. B.1; Nb. sample size information only available for SG06 samples), but otherwise there was no pattern with radiocarbon laboratory or with age.

B.1.4. Modeling of speleothem datasets onto the SG06 varve chronology

A five-point moving average of the inferred Δ^{14}C values (using a 0.1, 0.2, 0.4, 0.2, 0.1 weighting) was used to generate a 'comparison curve', which summarizes the data and removes some of the noise associated with individual measurements. Data from H82 (Southon et al., 2012) and GB-89-25-3 (Hoffmann et al., 2010) were then fitted to this comparison curve. The Poisson process algorithm used is identical to that for calibration of sedimentary sequences (Bronk Ramsey, 2008), with the Suigetsu comparison curve used in place of a calibration curve, and U-Th age from the speleothems entered as a proxy for depth. To be conservative, we assume that the variability in the DCF of these records might be double that estimated from Late Glacial control data (that is, 140 for H82 and 540 for GB-89-25-3, each at 1σ), because of the long time scales involved, and the changes in the climate system (including lower CO_2 levels and increased ^{14}C production in the Last Glacial). To account for this, we added extra uncertainty (in quadrature) to the speleothem radiocarbon dates.

A single model was used to fit both speleothem records onto the $SG06_{2012}$ varve chronology on the basis that the U-Th time scale for both speleothems should be congruent. In the Poisson process model, it is necessary to define the model rigidity (k-parameter). A range of different rigidities was tested to see how sensitive the model was, and to determine the most appropriate value. Table B.3 shows the effective varve count uncertainty implied by these values. Thus, for example, given a known duration core section and k=0.2 the uncertainty is equivalent to 10 for interpolation from each end, giving a combined uncertainty of 7.1%. To put this in context, the average estimated varve counting uncertainty is 6.2% making k=0.2 a conservative assumption.

We chose a uniform prior for the average reservoir offsets to each speleothem to allow the model to determine these independently. In order to achieve reasonable model start-up and convergence, it was necessary to limit the ranges over which reservoirs were considered; these limits were chosen to cover the range of values seen in the tested models. For GB-89-25-3 we considered values between 2100 and 2800, with a prior ~U(2100,2800). Extending this wider yielded similar posterior estimates, but with poorer convergence. For H82, the range 350-500 was explored with a prior ~U(350,500).

The models provide two main outputs:

- $SG06_{2012}$ varve age estimate for all of the U-Th dated samples from the speleothems, with an associated uncertainty; $SG06_{2012}$ varve ages are also generated for samples with all intervening U-Th ages (at 100 year intervals). These estimates can be used to map the $SG06_{2012}$ time scale onto the U-Th time scale, removing the long-term drift due to varve uncertainty and correcting sections that are clearly at variance

with the U-Th data. The resulting age-depth models and inferred deposition rates are shown in Fig. B.2.

- Posterior estimates for the average reservoir offsets of the two spelothems; the posterior estimates for different k-values are shown in Fig. B.3. This estimate for H82 is insensitive to choice of k. For GB-89-25-3 there is some sensitivity and this is related to the average offset in the period 28-32 $SG06_{2012}$ kyr BP; with lower k values the Suigetsu curve is effectively forced to fit the speleothem data, even though this requires large deviations from the varve model.

The rigidity of the Poisson process model essentially defines the weight given to the varve and speleothem-based chronologies. If the rigidity is set very high, the varve chronology is used rigidly to interpolate points and only the overall slope is determined by the fit to the speleothem data. At very low rigidity, the varve chronology is essentially ignored and the Suigetsu data are simply fitted onto the speleothem data. Clearly, there needs to be a compromise between these two extremes. Fig. B.2 and Fig. B.3 show the sensitivity of the different aspects of the model to the rigidity; in practice, there is very little sensitivity for much of the chronology. The age-depth models are only sensitive to k in the region around 30 kyr BP, where the fit between the Suigetsu data and those from GB-89-25-3 is not consistently good (Fig. B.4).

There is also some sensitivity in the extrapolated section beyond 43 kyr BP (Fig. B.5), but this is within error limits of the age estimates in that region.

It is clear from the deposition rate estimates that at low values of k (k=0.1 and even more so at k=0.05) the deposition rate is forced to deviate very widely from the varve estimates. These deviations reduce, but then become fairly stable from k=0.2 onwards. On the other hand, it is clear that by the time we reach k=0.3 the model is struggling to fit the speleothems with constant reservoir offsets for each speleothem. The k=0.3 model failed to converge satisfactorily, but all of the other models show a clear local maximum in the predicted value for the DCF; this does not mean that there would not be other possible fits to the data with radically different DCFs, but within the ranges considered the best fit is clear. We chose 0.2 as the most appropriate value for k; this value is equivalent to assuming a varve counting uncertainty of 10 on a 500 year section of core (see above).

The k=0.2 model gives an age for the marker layer at 1397.4 cm CD of 11179±64 yr BP, which agrees with the independent IntCal09 derived value of 11241±17 cal BP (χ^2 test: df=1 T=0.9 (5% 3.8)).

For our final model, we chose k=0.2 and fixed the age of the marker layer to the IntCal09 derived value. This gives us an age-depth model for SG06 (below 1397.4 cm CD) that is based on four sets of information:

- The IntCal09 derived tie point (1397.4 cm CD)
- The varve count (1397.4-3167.6 cm CD)
- The U-Th time scale of H82 (11241-26850 yr BP)
- The U-Th time scale of GB-89-25-3 (28005-43853 yr BP)

Extrapolation beyond 43.8 kyr BP assumes a constant deposition rate (in EFD). Above 1397.4 cm CD, the fit to IntCal09 can be used.

Table B.1 gives the complete radiocarbon record of our modeled chronology and, for completeness, includes the data from the Holocene section (Staff et al., 2011). There are 808 radiocarbon dates in this series covering the time range 182-52824 $SG06_{2012}$ yr BP. Fig. B.6 shows all of the data (including the outliers given in Table B.2). The overall age model is referred to as $SG06_{2012}$, with ages expressed in yr BP (before 1950).

Fig. B.7 shows the inferred deposition rate for the final model in comparison to the varve-only estimate. Fig. B.8 shows the inferred mean reservoirs for GB-89-25-3 and H82.

B.1.5. Using the SG06 dataset in comparison to other records

Using the Suigetsu radiocarbon dataset and $SG06_{2012}$ modeled age profile, we can define a comparison curve that can be used to examine other records. To do this, we use a five-point moving average (as above) to create a comparison curve (shown in gray in Fig. B.6). This can be used to place radiocarbon data onto the $SG06_{2012}$ time scale in the same way as a calibration curve is used to put radiocarbon data onto the calibrated (IntCal) age scale.

Terrestrial data (Soppensee)

For Soppensee (Switzerland), we used the existing dataset (Hajdas et al., 1993) and the recently published model (Lane et al., 2011), but without any constraints on the absolute ages of the Vedde and Laacher See tephras (since we do not know these on the $SG06_{2012}$ time scale). This model allows us to estimate the timing of environmental changes in the European lake in relation to similar changes in Suigetsu (Japan). This ability to compare climate records between different continents is one of the important outcomes of the high-density Suigetsu radiocarbon dataset. It also allows us to place chrono-stratigraphic markers (such as tephra) from other locations onto the $SG06_{2012}$ time scale. In this particular case we can thereby check the $SG06_{2012}$ time scale against the independent varve chronology from Meerfelder Maar, Germany (Brauer et al., 1999).

Marine data (Cariaco Basin and Iberian Margin)

The datasets for the Cariaco Basin (Hughen et al., 2006) and Iberian Margin (Bard et al., 2004) are on climate-derived time scales, which assume synchrony between climate signals in Hulu Cave speleothems and changes in the Atlantic. The assumptions are based on different mechanisms and therefore it is reasonable to test these against the $SG06_{2012}$ time scale. To do this, we have estimated the chronology for these records on the basis of the radiocarbon data. Suigetsu is a terrestrial record and so we need to make some assumptions about what the offset (R) is between the atmosphere and the local ocean for both the Cariaco Basin and Iberian Margin (the same assumptions that we need to make if we use these for atmospheric calibration, as applied in IntCal09 (Reimer et al., 2009)). We use a Poisson process model (Bronk Ramsey, 2008), with the existing U-Th chronology as a proxy for depth. We choose k=0.1, because we must expect some variability in both the $SG06_{2012}$ time scale and that of the other records.

For Cariaco, we explored two models: in the first we conservatively assumed that R can vary anywhere between 0 and 800 yrs, which gives a prior for R~U(0,800); in the second model we assumed that R is approximately 400 yrs (the value assumed in IntCal09 is 430 yrs (Reimer et al., 2009)), but with double the uncertainty than currently assumed in IntCal09, which gives a prior R~N(400,200). Fig. B.9 shows the inferred difference between the current Cariaco cal time scale and that of $SG06_{2012}$; these time scales agree at the younger end.

For the Iberian Margin data (Bard et al., 2004) we applied four models. As for Cariaco, we used an unbiased estimate for R but, because the reservoir is higher here, we took a prior of R~U(0,1000). For a more constrained model, we tried a prior of R~N(500,200). Because these models were suggesting a significant offset at the younger end, we also applied models where we assumed that the age models were congruent at the $SG06_{2012}$ IntCal09 tie point. Fig. B.10 shows the results of these four models.

The conclusions seem to be fairly model-independent. We see only minor offsets with respect to the Iberian Margin chronology - but substantially larger offsets with respect to the Cariaco time scale for the older half of the considered period. Fig. IV.1C of the main paper shows the Cariaco model based on a prior for R~U(0,800) and for the Iberian Margin with a prior R~U(0,1000) and with the tie point. Having assessed the differences

between the time scales for these two records, we can then look at the residual variation in R inferred from the modeled sequences. For the Iberian Margin, we do this for all four models tried. For the Cariaco Basin, given the large offsets seen against the time scale, we also tried the same exercise but just using the depth of the samples in the original Cariaco core as our starting point (as we would if we had no time scale to work from), and so there are also four models in this case. Figure B.11 shows the inferred R for Cariaco and the Iberian Margin under all of the different model assumptions, showing that most of the signal we see here is fairly insensitive. Fig. IV.4 of the main paper shows data for the same model assumptions as Fig. IV.1C (see above).

Coral data

Marine coral data can generally be compared directly with the Suigetsu data since they are both linked to a U-Th chronology. Fig. B.12 shows all of the coral data used in IntCal09 (Reimer et al., 2009) against the Suigetsu radiocarbon dataset. Here we can see that some of the older corals (Fairbanks et al., 2005) appear consistently younger than the atmospheric data of Suigetsu. The younger corals seem consistent, but can be used to infer changes in R over time in different regions. See main paper for discussion.

B.2. Figures

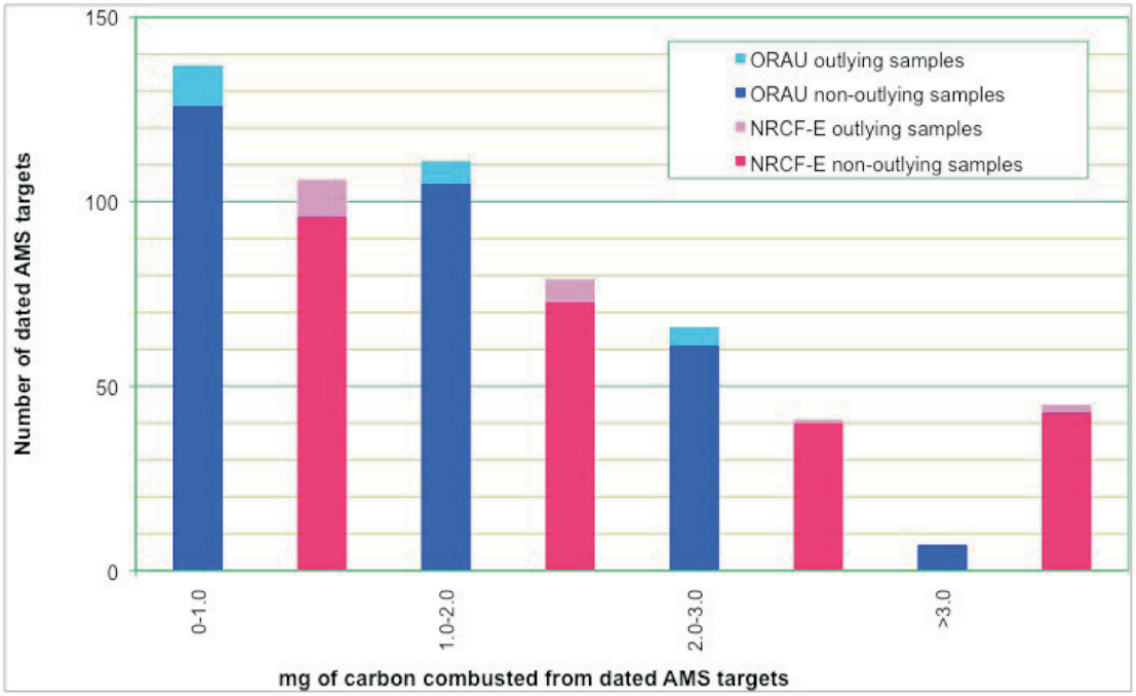

Figure B.1.: The proportion of outlying and non-outlying samples measured at SUERC (NRCF-E: red/pink) and ORAU (blue/light blue) by sample size. The highest proportion of outliers (8.6%) is where the carbon content drops below 1 mg.

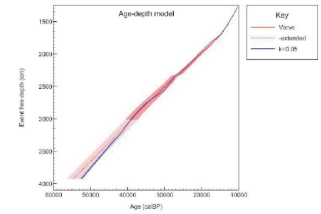

k=0.05

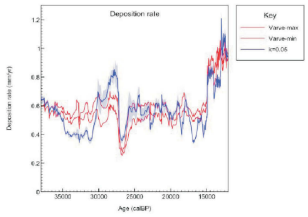

k=0.05

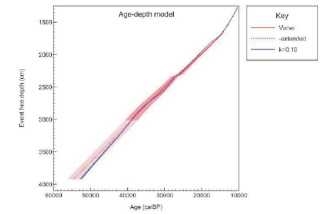

k=0.10

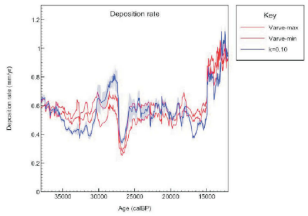

k=0.10

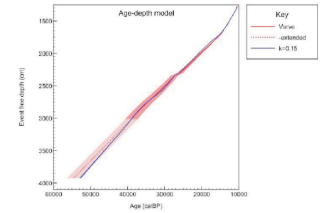

k=0.15

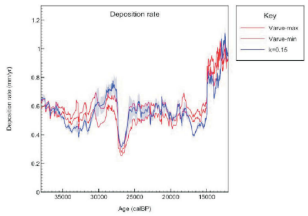

k=0.15

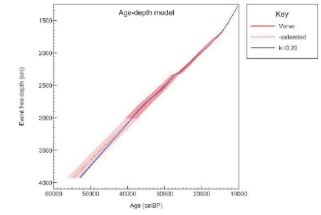

k=0.20

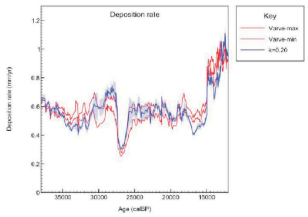

k=0.20

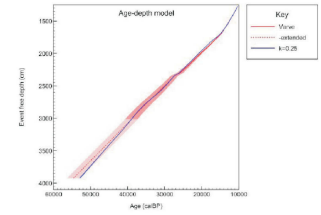

k=0.25

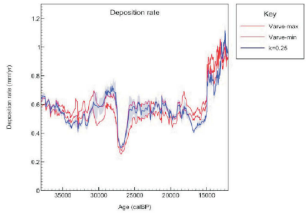

k=0.25

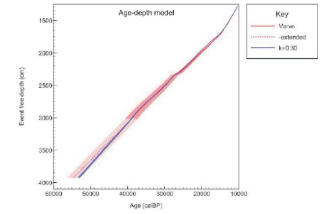

k=0.30

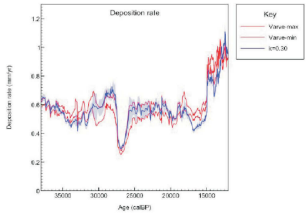

k=0.30

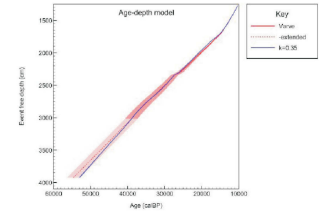

k=0.35

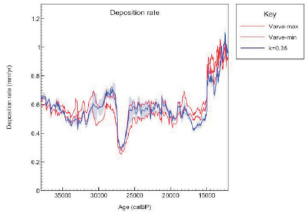

k=0.35

Figure B.2.: Sensitivity of age-depth model and deposition rate to k parameter.

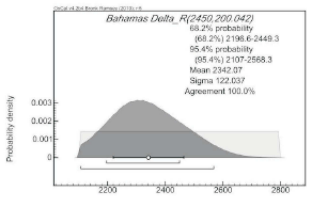

k=0.05

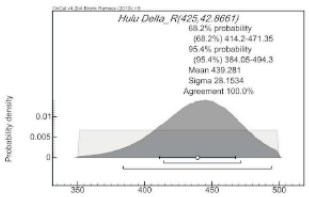

k=0.05

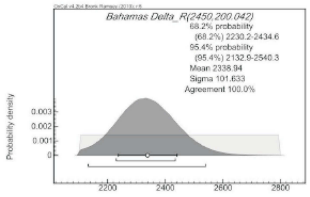

k=0.10

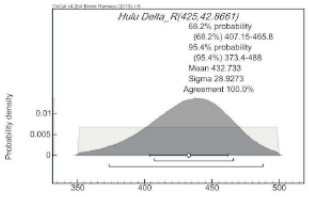

k=0.10

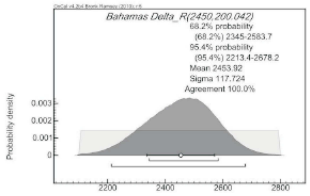

k=0.15

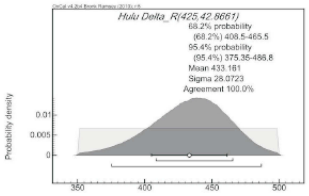

k=0.15

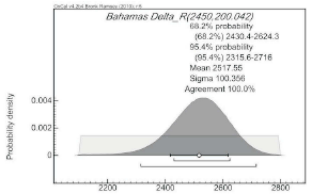

k=0.20

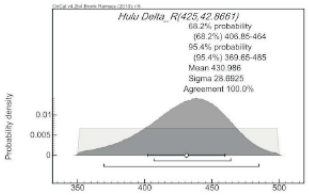

k=0.20

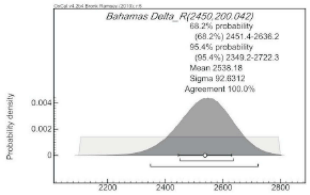

k=0.25

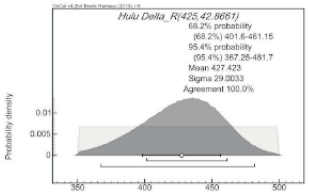

k=0.25

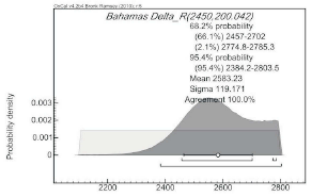

k=0.30

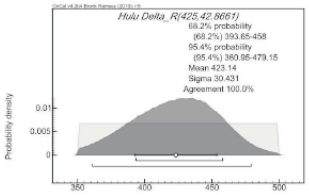

k=0.30

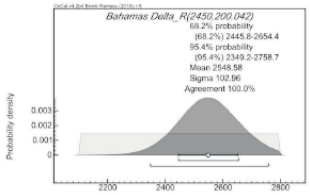

k=0.35

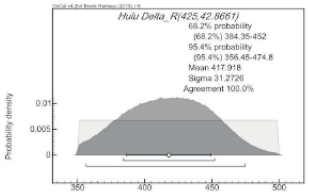

k=0.35

Figure B.3.: Sensitivity of DCF estimates for speleothems to k parameter.

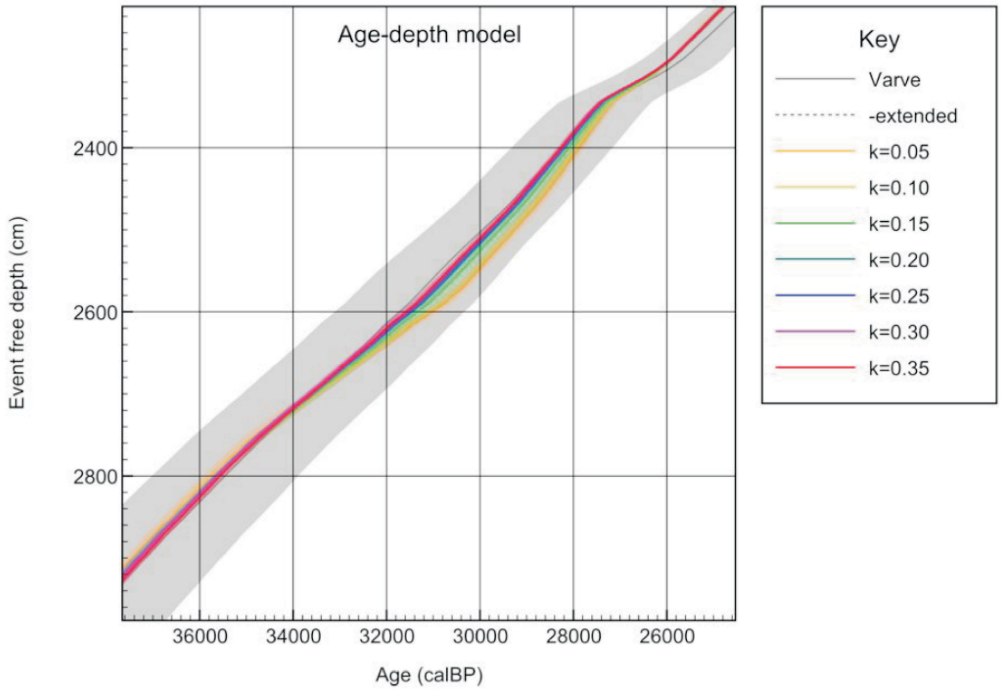

Figure B.4.: Model sensitivity to k in the region around 30 kyr BP; models are coded by color; if low k values are chosen, the data fit those from GB-89-25-3 better, but only by introducing a kink in the deposition model, which is significantly at variance with the varve model.

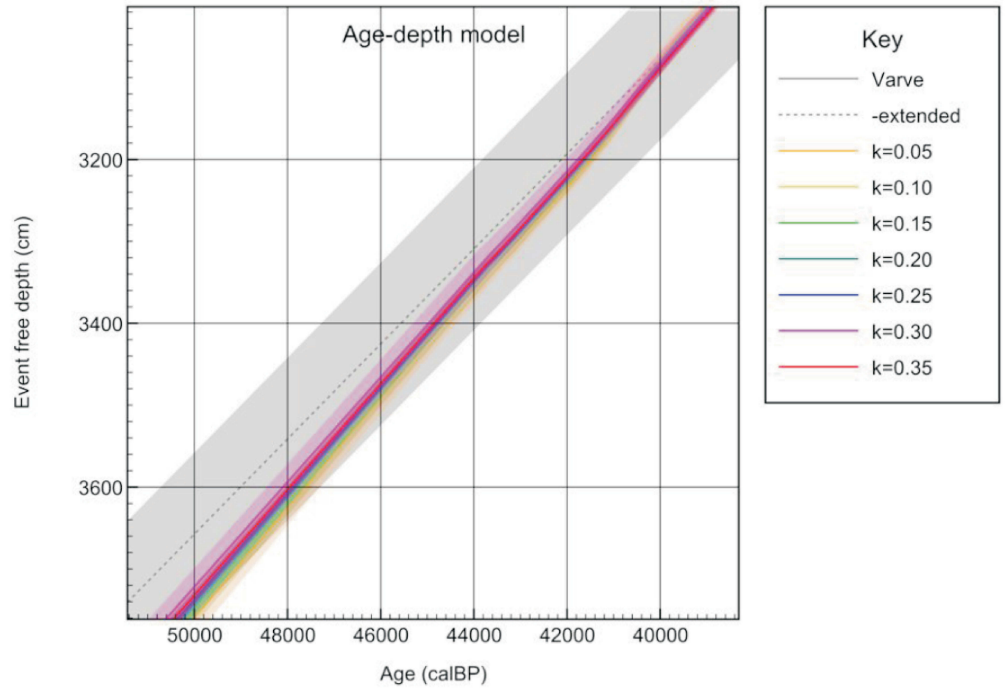

Figure B.5.: The model sensitivity to k in the region where the varve chronology is only interpolated; models are coded by color with a semi-transparent band showing the uncertainty; beyond 44 kyr BP, the whole model is dependent only on extrapolation by EFD and has greater uncertainty; the chosen model (k=0.2) is a compromise solution and the other solutions are, within errors, compatible with this.

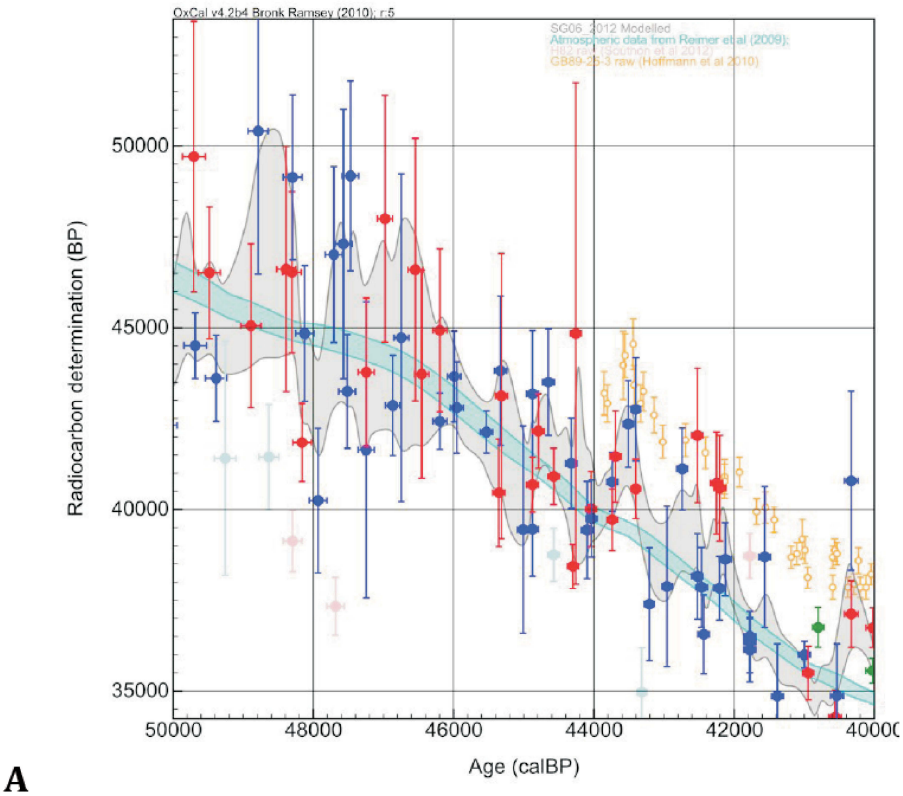

A

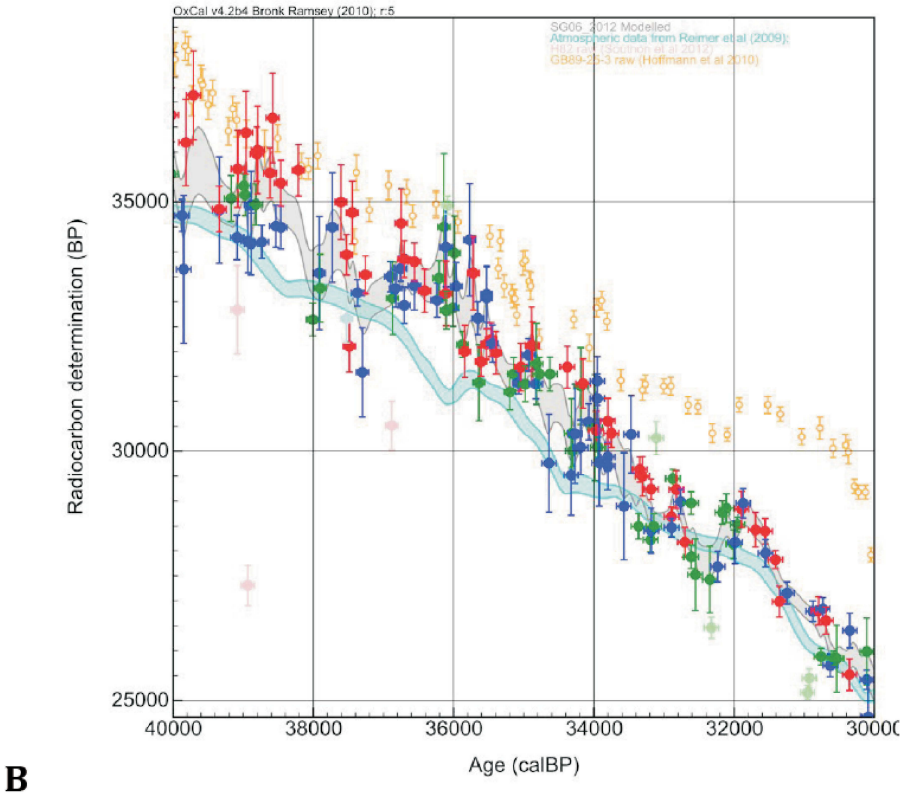

B

Figure B.6.: Full Suigetsu dataset shown in comparison to IntCal09 (Reimer et al. 2009; light blue curve), GB-89-25-3 (Hoffmann et al. 2010; orange, open circles) and H82 (Southon et al. 2012; pink, open circles); speleothem data are uncorrected for DCF; Suigetsu data are shown in solid circles for SG06 (OxA, blue; SUERC, red) and SG93 (GrA; green); identified outliers are shown (light blue, pink and light green, respectively); the 5-point Suigetsu weighted mean is also shown (gray). (Figure continued on next pages)

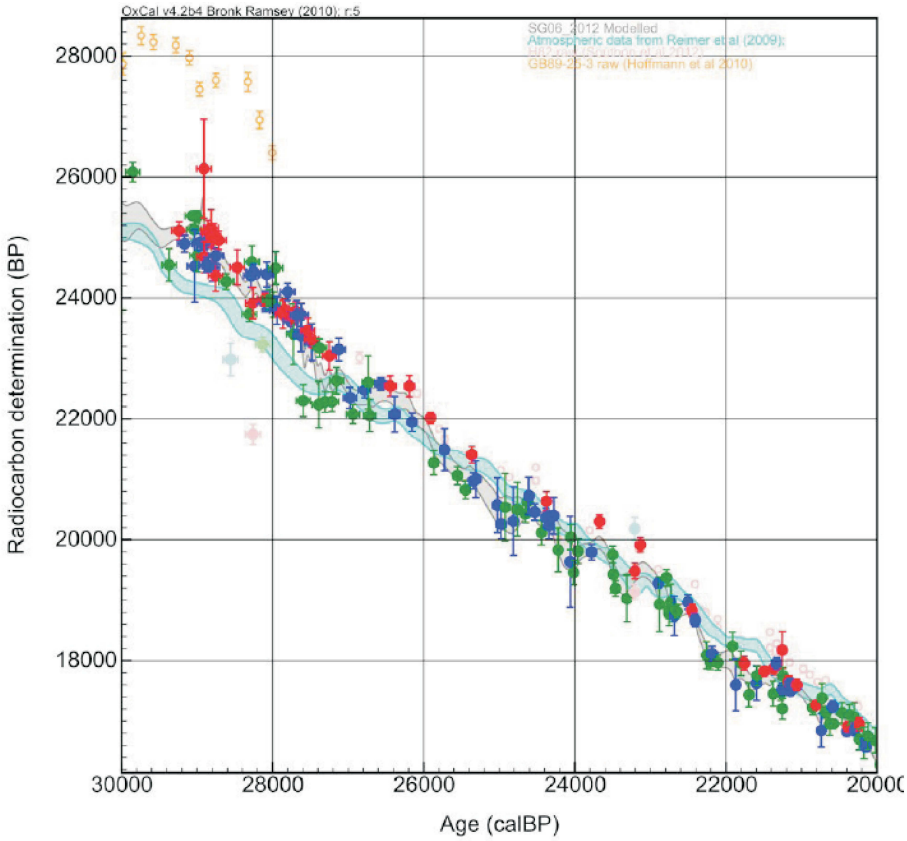
OxCal v4.2b4 Bronk Ramsey (2010); r:5
SG06_2012 Modelled
Atmospheric data from Reimer et al (2009);
GB89-25-3 raw (Hoffmann et al 2010)
Radiocarbon determination (BP)
28000
26000
24000
22000
20000
18000
30000
28000
26000
24000
22000
20000
Age (calBP)

C

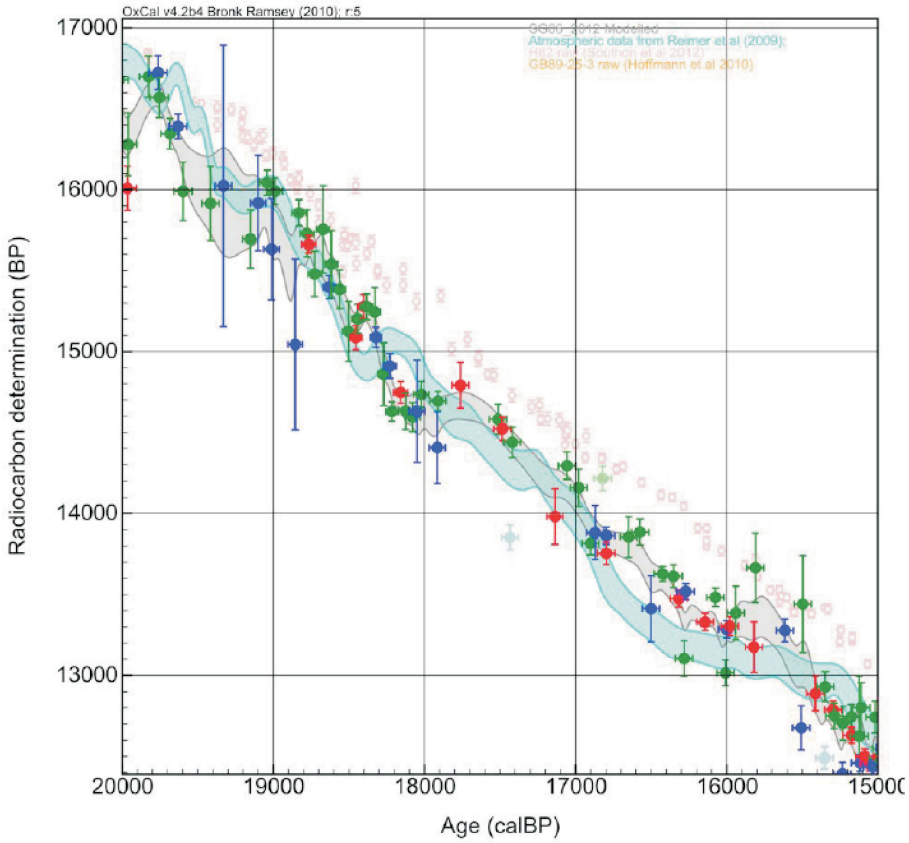
OxCal v4.2b4 Bronk Ramsey (2010); r:5
SG06_2012 Modelled
Atmospheric data from Reimer et al (2009);
GB89-25-3 raw (Hoffmann et al 2010)
Radiocarbon determination (BP)
17000
16000
15000
14000
13000
20000
19000
18000
17000
16000
15000
Age (calBP)

D

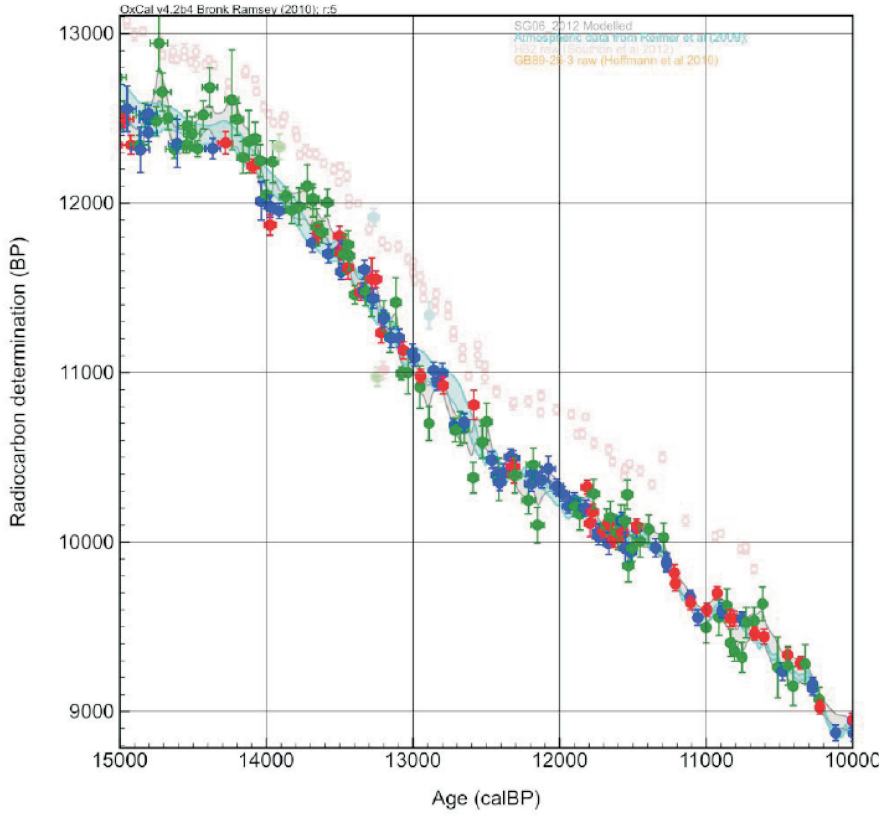
OxCal v4.2b4 Bronk Ramsey (2010); r:5
SG06_2012 Modelled
Atmospheric data from Reimer et al (2009);
GB89-25-3 raw (Hoffmann et al 2010)
Radiocarbon determination (BP)
13000
12000
11000
10000
9000
15000
14000
13000
12000
11000
10000
Age (calBP)

E

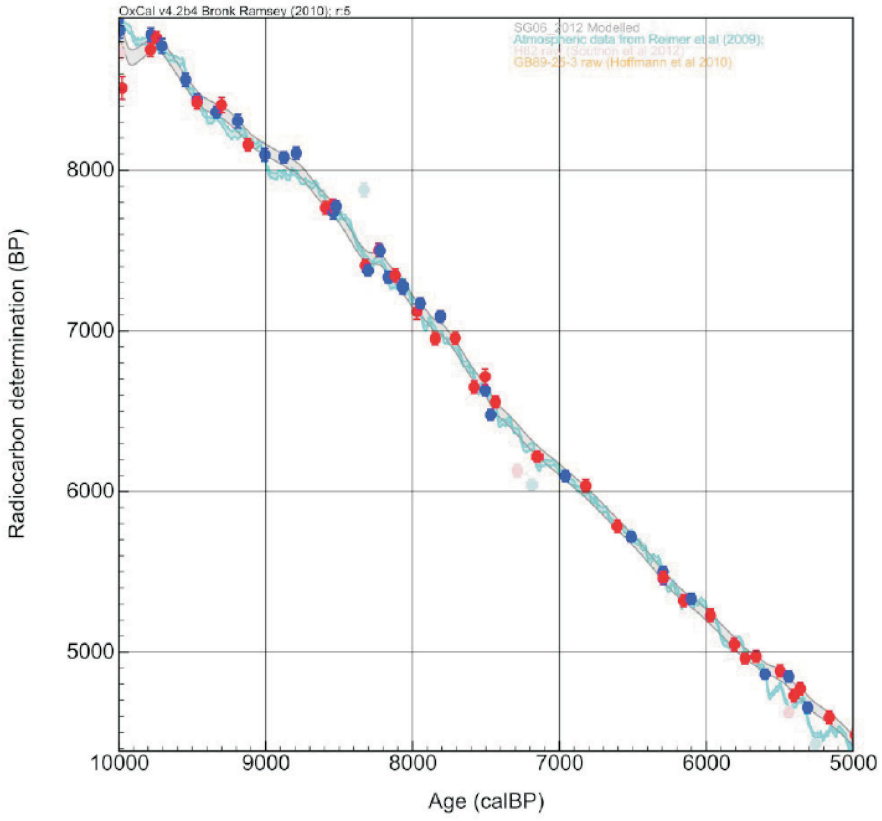
OxCal v4.2b4 Bronk Ramsey (2010); r:5
SG06_2012 Modelled
Atmospheric data from Reimer et al (2009);
GB89-25-3 raw (Hoffmann et al 2010)
Radiocarbon determination (BP)
8000
7000
6000
5000
10000
9000
8000
7000
6000
5000
Age (calBP)

F

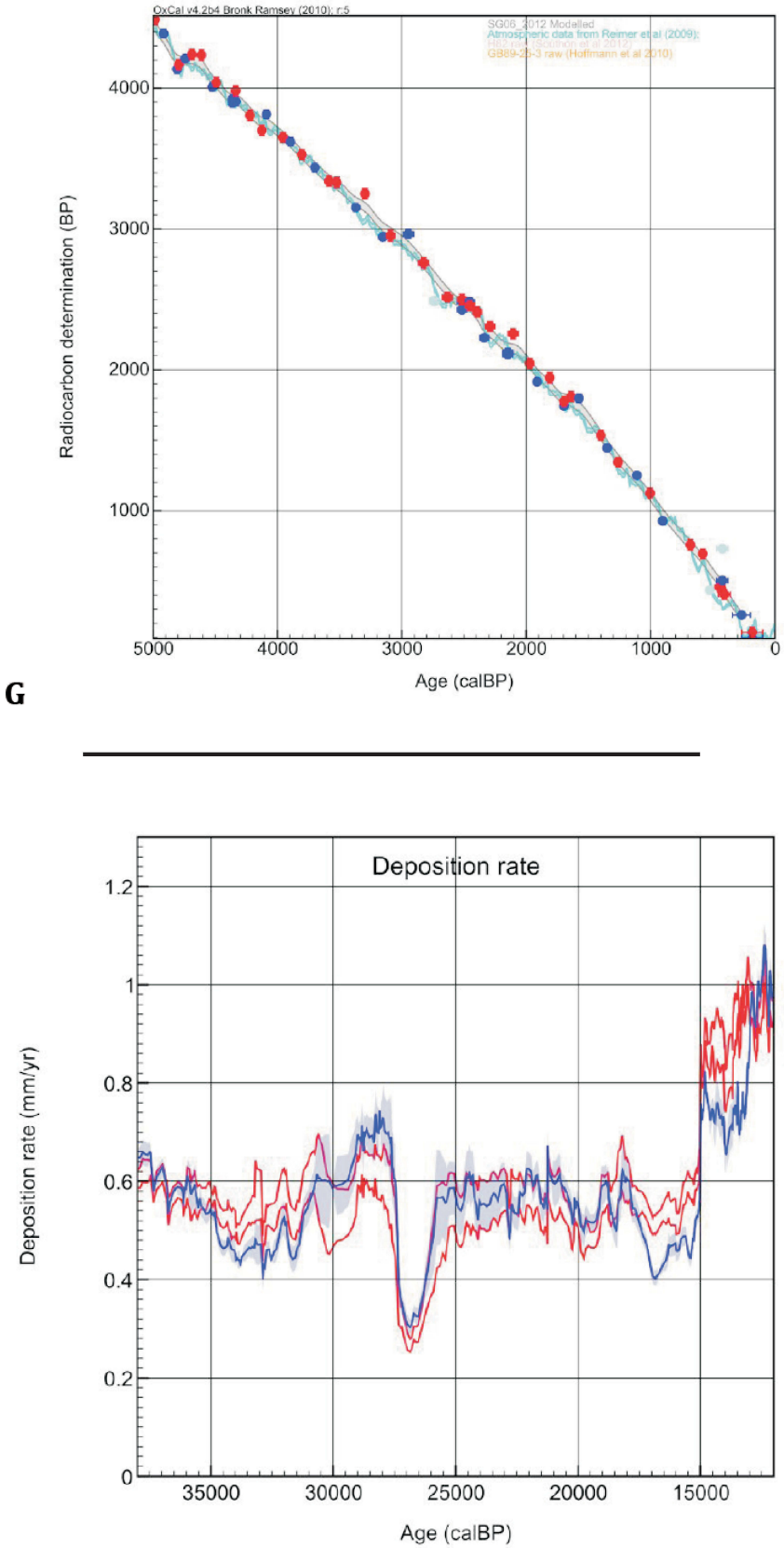

Figure B.7.: The inferred deposition rate for SG06 from our combined age model (blue), compared to the varve-estimated range (68.2% range; red); the most significant deviations are around 15 kyr BP where there is a significant change in deposition rate; note that there is also a low deposition rate at around 27 kyr BP.

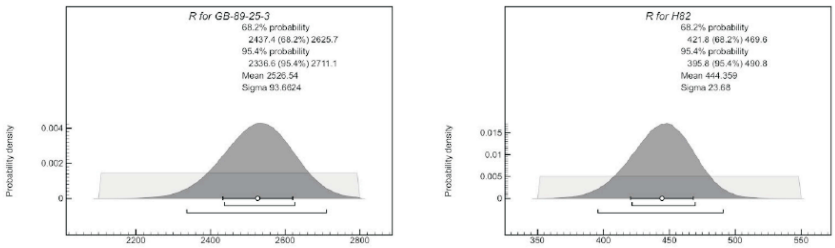

Figure B.8.: The inferred mean reservoir (R) values for the two speleothems when fitted to the Suigetsu data; the values are 2500±90 for GB89-25-3 and 440±25 for H82, which are in good agreement with estimates (Hoffmann et al., 2010; Southon et al., 2012).

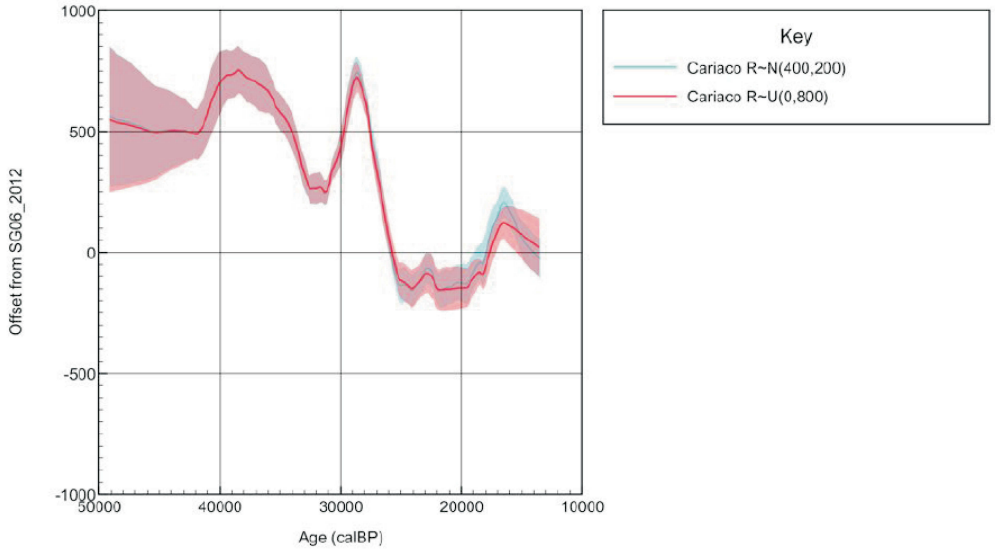

Figure B.9.: The inferred offsets between the $SG06_{2012}$ modeled chronology and that of the Cariaco Basin (Hughen et al., 2006) under the different model assumptions.

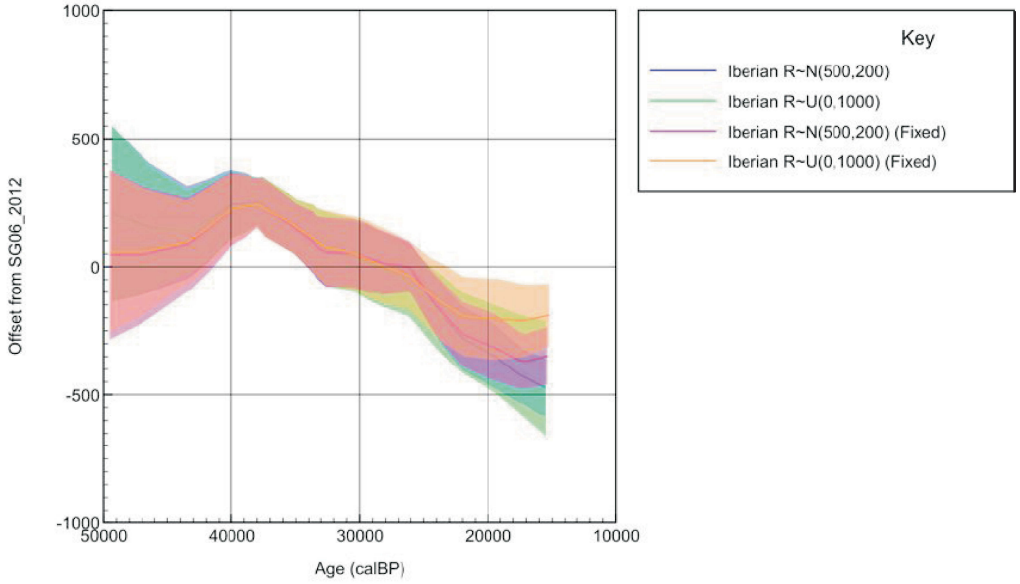

Figure B.10.: The inferred offsets between the $SG06_{2012}$ modeled chronology and that of the Iberian Margin (Bard et al., 2004) under the four different model assumptions.

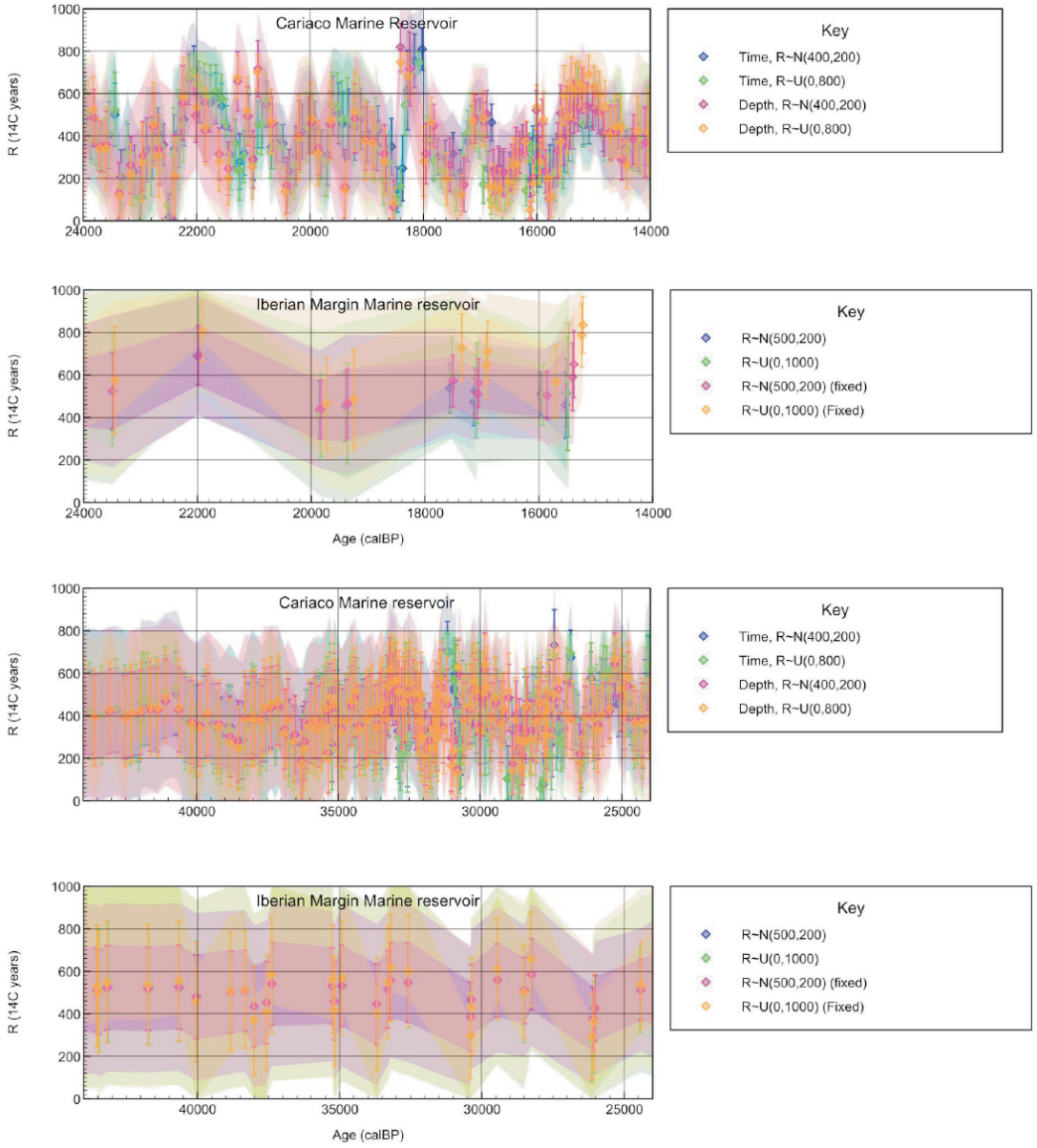

Figure B.11.: The inferred marine reservoirs for the Cariaco Basin and Iberian Margin under different model assumptions; all models are overlain so that the consistency of the conclusions can be assessed; 1σ error bars are shown and 68.2% and 95.4% hpd ranges shown in transparent colors.

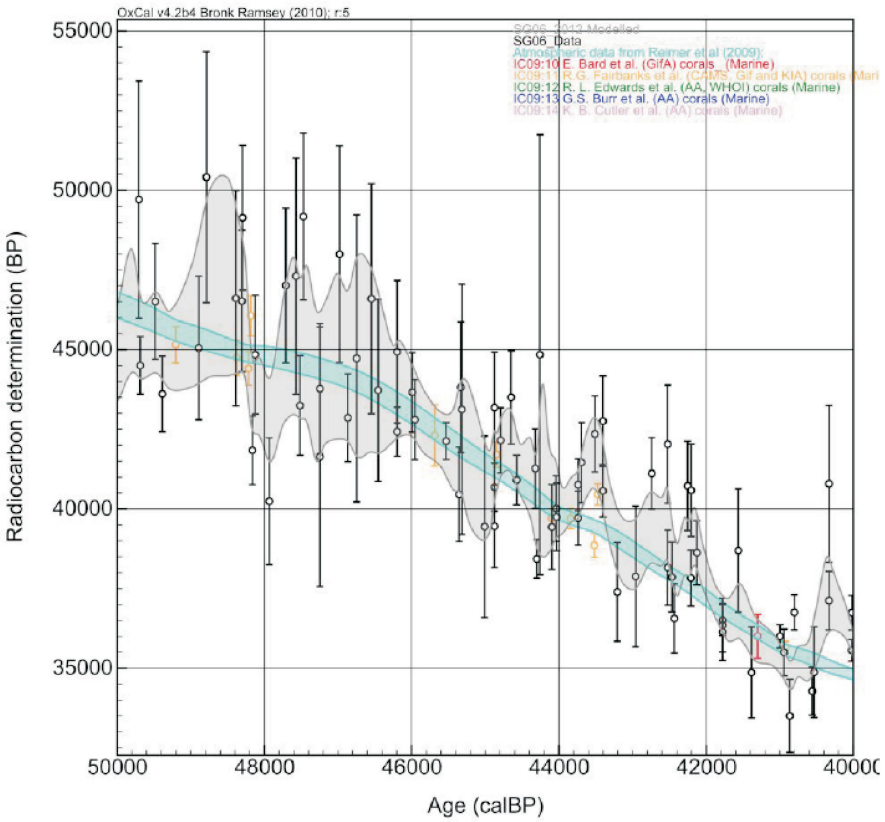

A

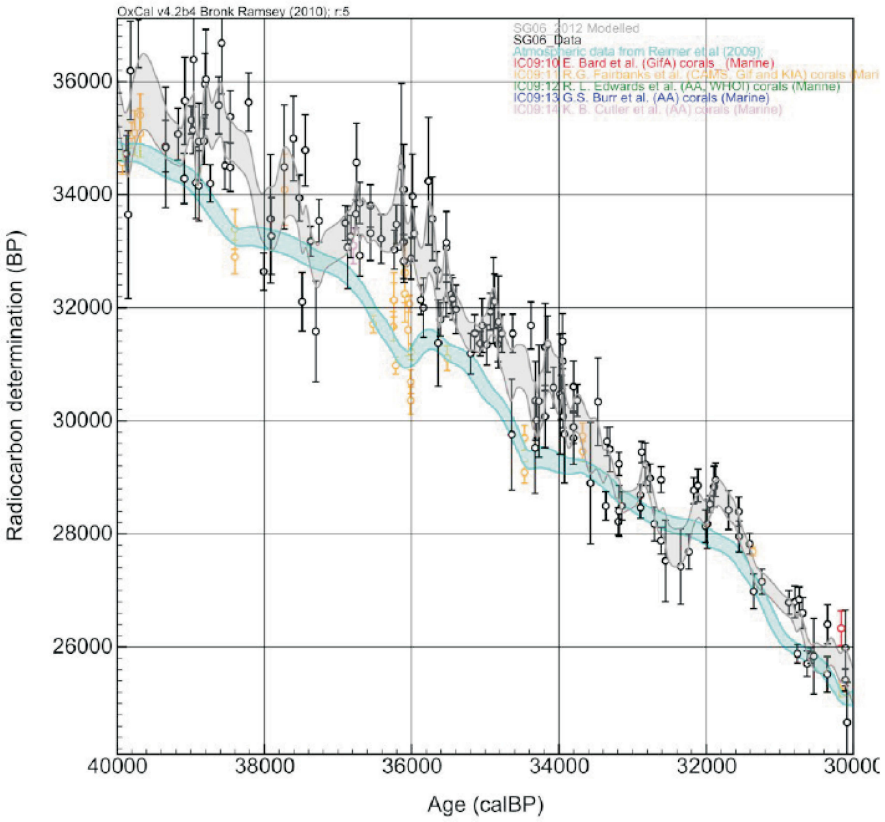

B

Figure B.12.: The Suigetsu data (black) and five-point moving average (gray) as compared to the coral datasets (uncorrected) from IntCal09 (Reimer et al. 2009; light blue). (Figure continued on next page

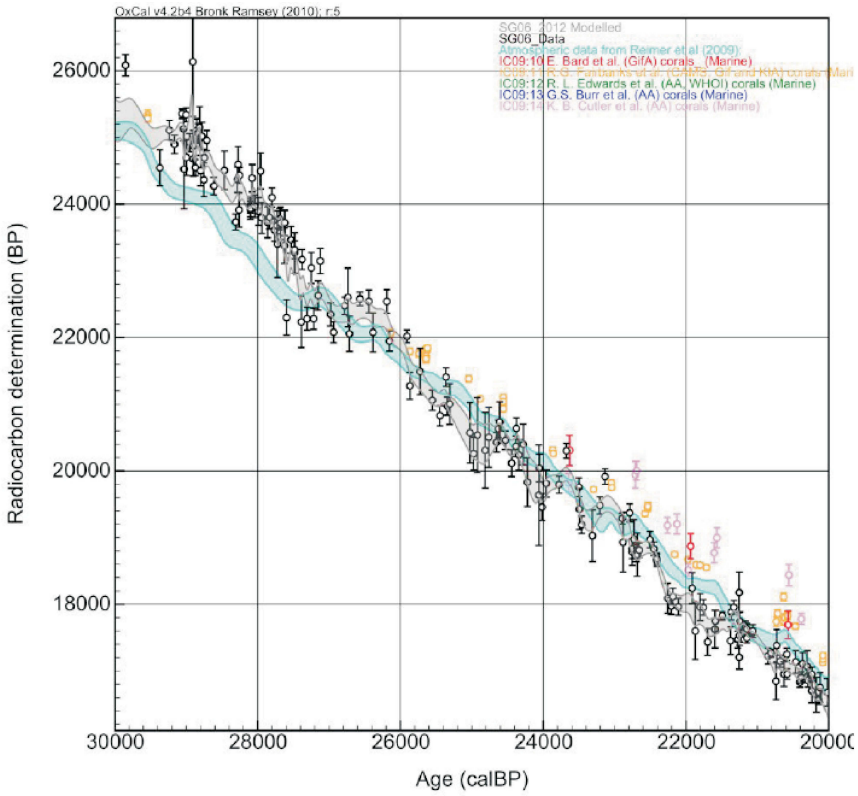
OxCal v4.2b4 Bronk Ramsey (2010); r:5
SG06_2012 Modelled
SG06_Data
Atmospheric data from Reimer et al (2009);
IC09:10 E. Bard et al. (GifA) corals...(Marine)
IC09:12 R. L. Edwards et al. (AA, WHOI) corals (Marine)
IC09:13 G.S. Burr et al. (AA) corals (Marine)
IC09:14 K. B. Cutler et al. (AA) corals (Marine)
Radiocarbon determination (BP)
26000
24000
22000
20000
18000
30000
28000
26000
24000
22000
Age (calBP)

C

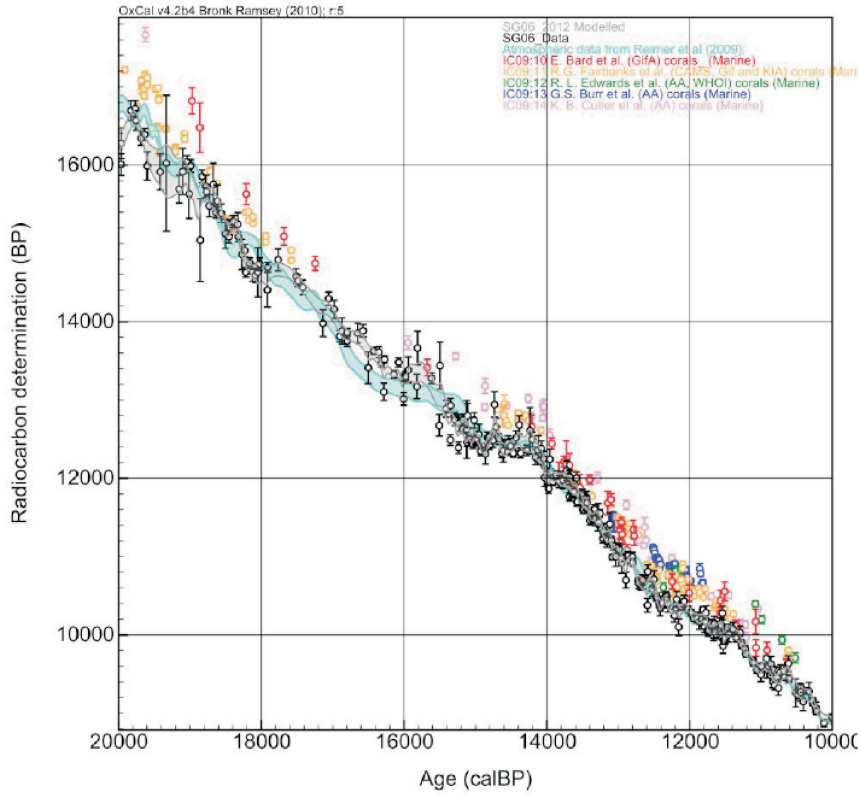
OxCal v4.2b4 Bronk Ramsey (2010); r:5
SG06_2012 Modelled
SG06_Data
Atmospheric data from Reimer et al (2009);
IC09:10 E. Bard et al. (GifA) corals...(Marine)
IC09:12 R. L. Edwards et al. (AA, WHOI) corals (Marine)
IC09:13 G.S. Burr et al. (AA) corals (Marine)
IC09:14 K. B. Cutler et al. (AA) corals (Marine)
Radiocarbon determination (BP)
16000
14000
12000
10000
20000
18000
16000
14000
12000
Age (calBP)

D

B.3. Tables

- **Table B1**: Radiocarbon dataset from cores SG06 and SG93 cores on the $SG06_{2012}$ varve and modeled time scales; CD and EFD depth scales are from the SG06 core. (also included on data CD)
- **Table B2**: Samples identified as outliers
- **Table B3**: The equivalent uncertainties (1σ; as a percentage of 500 years) for the midpoint of a 1000 year core section, interpolated using different k values (see equation A17 in (Bronk Ramsey, 2008)).

Table B1

AMS Labcode(s)	^{14}C Date BP	±1σ	CD cm	EFD cm	$SG06_{2012}$ modelled yr BP	±1σ	$SG06_{2012}$ varve yyr BP	±1σ
OxA-24466	37395	1550	3455.0	3299.3	43207	72	43829	1708
OxA-24472	37681	2208	3439.3	3283.6	42958	76	43559	1708
OxA-24256	41116	1126	3425.5	3269.8	42739	79	43321	1708
OxA-24219	38158	1179	3411.9	3256.2	42524	82	43087	1708
SUERC-20500	42034	1852	3411.9	3256.2	42524	82	43087	1708
OxA-24465	37859	1096	3408.2	3252.5	42465	83	43023	1708
OxA-24443	36563	1091	3406.2	3250.5	42434	83	42989	1708
SUERC-29626	40723	1401	3394.7	3239.0	42251	85	42791	1708
OxA-24396	37831	878	3391.9	3236.2	42207	84	42742	1708
SUERC-17124	40584	1455	3391.7	3236.0	42204	84	42739	1708
OxA-24289	38628	1007	3386.0	3231.1	42126	85	42654	1707
OxA-24437	36569	485	3360.9	3208.7	41776	83	42269	1707
OxA-24452	36349	845	3360.9	3208.7	41776	83	42269	1707
OxA-24453	36142	892	3360.9	3208.7	41776	83	42269	1707
OxA-24198	38694	1937	3347.1	3194.9	41565	82	42031	1707
OxA-24464	34867	1431	3335.1	3182.9	41384	81	41824	1707
OxA-24229	36001	367	3309.0	3156.8	40998	82	41374	1707
SUERC-27778	35497	732	3305.1	3152.9	40943	81	41307	1707
OxA-24451	33503	1144	3299.4	3147.2	40865	82	41209	1707
GrA-4517	36755	550	3294.7	3142.5	40801	83	41128	1707
SUERC-27777	34283	752	3277.1	3124.9	40560	90	40825	1707
OxA-24402	34876	1425	3275.3	3123.1	40535	91	40794	1707
OxA-24185	40788	2464	3258.3	3108.4	40330	97	40540	1707
SUERC-23652	37121	917	3258.3	3108.4	40330	97	40540	1707
GrA-4515/GrA-4516	35560	340	3236.9	3087.0	40026	99	40172	1707
SUERC-29625	35744	542	3236.7	3086.8	40023	99	40168	1707
OxA-24228	34728	320	3236.6	3076.7	39873	101	39994	1707
OxA-24471	33648	1481	3224.9	3075.0	39846	102	39965	1707
SUERC-28277	35154	670	3212.8	3062.9	39817	102	39929	1707
OxA-24450	34740	892	3211.6	3061.7	39799	101	39909	1707
OxA-24356	34838	1068	3191.0	3041.1	39340	101	39381	1707
GrA-5623	35070	460	3180.0	3030.1	39171	98	39191	1707
OxA-24436	34287	446	3174.5	3024.6	39087	94	39097	1707
SUERC-28690	35660	772	3174.0	3024.1	39079	94	39088	1707
GrA-10434	35322	249	3168.1	3018.2	38991	94	38986	1706
GrA-5632	35140	415	3166.8	3016.9	38972	94	38964	1707
SUERC-29650	36389	631	3165.7	3015.8	38961	94	38951	1706
OxA-24218	34213	635	3163.4	3013.5	38934	95	38921	1705
OxA-24341	34138	620	3159.3	3009.4	38888	96	38869	1704
OxA-24342	34940	678	3159.3	3009.4	38888	96	38869	1703
GrA-5631	34950	415	3153.8	3003.9	38820	95	38793	1700
SUERC-29646	35957	545	3152.5	3002.6	38805	95	38776	1699
SUERC-29664	36043	880	3151.4	3002.0	38793	95	38762	1699
OxA-24327	34199	332	3146.3	2996.9	38733	95	38695	1696
SUERC-29645	35580	507	3136.8	2987.4	38619	92	38565	1686
SUERC-20501	36684	902	3133.6	2984.2	38580	92	38521	1681
OxA-24435	34514	422	3130.3	2980.9	38535	91	38470	1678
OxA-24434	34485	427	3125.2	2975.8	38464	91	38389	1674
SUERC-29644	35378	458	3125.2	2975.8	38464	91	38389	1674
SUERC-29643	35636	517	3105.5	2957.6	38213	85	38107	1660
GrA-5627	32640	330	3082.4	2944.1	38006	86	37887	1654
OxA-24484	33573	1139	3076.6	2938.3	37915	85	37788	1651
GrA-5626	33270	680	3075.9	2937.6	37904	86	37776	1651
OxA-24441	34490	1099	3064.3	2926.0	37729	84	37591	1644
SUERC-17129	34995	748	3056.2	2917.9	37606	84	37462	1639
SUERC-29624	33941	405	3051.1	2912.8	37526	83	37378	1636
SUERC-18132	32106	518	3048.3	2910.2	37487	83	37336	1634
SUERC-29623	34787	631	3043.6	2907.3	37445	83	37292	1633
OxA-24326	33176	264	3040.9	2902.6	37371	87	37216	1632
OxA-24463	31582	696	3036.5	2898.7	37300	87	37145	1630
SUERC-29622	33538	379	3033.7	2896.4	37257	86	37101	1628
OxA-24382	33501	307	3011.2	2873.9	36900	88	36740	1617
GrA-5619	33070	730	3009.4	2872.1	36870	88	36710	1616
OxA-24316	33262	374	3006.7	2869.4	36827	87	36665	1615
SUERC-24040	32660	631	3001.5	2865.2	36755	88	36592	1612
OxA-24441	32669	537	3001.1	2864.8	36747	88	36584	1612
OxA-24430	32925	364	2999.0	2862.5	36704	88	36540	1610
SUERC-29621	32854	366	2994.3	2858.0	36658	89	36492	1608
OxA-24395	33319	486	2991.6	2854.3	36558	89	36392	1605
SUERC-29620	33803	375	2991.6	2854.3	36558	89	36392	1605
SUERC-28689	33219	432	2983.1	2845.8	36413	88	36245	1601
OxA-24217	33028	343	2972.7	2835.4	36235	88	36065	1595
GrA-5620	33475	345	2970.9	2833.6	36206	87	36036	1595
OxA-10430	34497	1472	2829.6	2829.6	36137	86	35966	1593
OxA-24361	34093	798	2965.3	2828.0	36109	86	35937	1592
SUERC-28216	33163	648	2828.0	2828.0	36109	86	35937	1592
GrA-5622	32825	380	2965.1	2827.8	36105	86	35933	1592

AMS Labcode(s)	^{14}C Date BP	±1σ	CD cm	EFD cm	$SG06_{2012}$ modelled yr BP	±1σ	$SG06_{2012}$ varve yyr BP	±1σ
OxA-24428	48783	2383	4097.7	3924.8	52824	229	54606	1720
OxA-24283	48042	1636	4095.5	3922.6	52790	228	54568	1720
OxA-24318	46459	2431	4085.8	3912.9	52642	225	54401	1719
OxA-24263	> 52900		4080.8	3907.9	52566	223	54315	1719
SUERC-26010	49140	2015	4075.2	3902.3	52480	222	54219	1719
SUERC-23745	> 37700		4066.0	3893.1	52339	218	54060	1719
OxA-24282	49055	1278	4064.5	3891.6	52316	218	54034	1719
SUERC-28902	50261	2264	4064.5	3891.6	52316	218	54034	1719
OxA-24254	> 40200		4060.3	3887.4	52252	217	53962	1719
OxA-24275	49089	1930	4047.8	3874.9	52061	212	53746	1718
SUERC-26378	48816	4811	4042.1	3869.2	51973	210	53648	1718
SUERC-26009	49300	1023	4031.0	3858.1	51803	207	53457	1718
OxA-24384	47086	1618	4026.4	3853.5	51733	205	53378	1718
SUERC-27522	48713	2066	4026.4	3853.5	51733	205	53378	1718
SUERC-27521	46352	1704	4023.4	3850.5	51687	204	53326	1718
SUERC-28226	45646	1367	4016.5	3843.6	51582	202	53207	1718
OxA-24358	44138	3006	4016.3	3843.4	51579	202	53204	1718
SUERC-27520	49280	4663	4016.3	3843.4	51579	202	53204	1718
OxA-24397	45178	2227	4011.8	3838.9	51510	200	53126	1717
SUERC-17128	48868	3663	4011.6	3838.7	51507	200	53123	1717
OxA-24346	50129	3856	4004.3	3831.4	51395	198	52997	1717
SUERC-28223	> 42700		3988.6	3815.7	51155	193	52726	1717
OxA-24326	50191	2528	3981.5	3808.6	51046	190	52604	1717
SUERC-27787	47785	1762	3977.9	3805.0	50991	189	52542	1717
SUERC-27786	47677	2031	3940.6	3767.7	50420	177	51899	1716
OxA-24395	43127	1223	3934.3	3761.4	50324	175	51791	1716
SUERC-27785	49375	3931	3915.7	3742.8	50132	172	51643	1715
OxA-24357	46216	1718	3910.5	3737.6	50113	170	51593	1715
SUERC-23901	47411	3221	3893.7	3720.8	49834	162	51071	1715
OxA-24346	44707	1803	3882.5	3709.6	49684	161	50843	1714
SUERC-27784	46513	1814	3877.2	3704.4	49482	155	50734	1714
OxA-24317	43609	1187	3870.2	3700.1	49286	150	50738	1714
SUERC-28222	45054	2252	3835.6	3667.7	48896	145	50177	1713
OxA-24333	50412	3938	3828.8	3660.9	48786	143	50059	1713
SUERC-20900	46612	3376	3802.8	3634.9	48388	135	49611	1713
SUERC-28221	46526	2220	3797.3	3629.4	48304	134	49517	1713
OxA-24106	49142	2270	3796.7	3628.8	48295	134	49506	1713
SUERC-28699	41842	1075	3787.9	3620.0	48160	131	49355	1713
OxA-24390	44844	1867	3785.4	3617.5	48122	130	49312	1713
OxA-24444	40244	1992	3773.0	3605.1	47932	127	49098	1712
OxA-24264	47015	2421	3758.3	3590.4	47707	123	48845	1712
OxA-24365	47306	3708	3749.4	3581.5	47571	120	48691	1712
OxA-24389	43247	1564	3745.9	3578.0	47517	119	48631	1712
OxA-24258	49178	2614	3742.8	3574.9	47470	118	48578	1712
OxA-24364	41639	4074	3728.1	3560.2	47245	115	48324	1711
SUERC-28697	43775	2045	3728.1	3560.2	47245	115	48324	1711
SUERC-20943	48000	3399	3707.4	3542.8	46979	110	48025	1711
OxA-24427	42863	1378	3700.1	3535.5	46867	108	47899	1711
OxA-24199	44726	4507	3692.1	3527.5	46745	106	47761	1711
SUERC-28696	46597	3613	3679.1	3514.5	46546	103	47537	1711
SUERC-20942	43724	2863	3673.2	3508.6	46455	102	47435	1711
OxA-24241	42425	773	3656.2	3491.6	46195	98	47143	1710
SUERC-27781	44930	2239	3656.2	3491.6	46195	98	47143	1710
OxA-24387	43660	1249	3638.1	3478.4	45993	95	46915	1710
OxA-24343	42803	1258	3635.6	3475.9	45955	95	46872	1710
OxA-24221	42131	583	3608.0	3448.3	45533	90	46397	1710
SUERC-20220	40459	1483	3596.4	3436.7	45355	88	46197	1710
OxA-24257	43817	2053	3594.8	3435.1	45331	87	46169	1710
SUERC-23742	43123	3927	3593.9	3434.2	45317	87	46154	1710
OxA-24403	39445	2849	3572.7	3414.0	45008	84	45806	1709
OxA-24362	39455	1296	3562.5	3405.3	44875	83	45656	1709
OxA-24363	43181	1743	3562.5	3405.3	44875	83	45656	1709
SUERC-28219	40682	757	3562.5	3405.3	44875	83	45656	1709
SUERC-28692	42155	1024	3557.0	3399.8	44791	83	45561	1709
OxA-24253	43501	1462	3546.7	3390.5	44648	82	45401	1709
SUERC-28218	40909	777	3541.8	3385.6	44573	81	45316	1709
OxA-24290	41268	1243	3525.3	3369.1	44321	80	45032	1709
SUERC-28691	38433	606	3523.9	3367.7	44299	80	45008	1709
OxA-24354	44042	6902	3521.1	3364.9	44257	80	44960	1709
SUERC-23741	39433	1336	3510.6	3354.4	44096	79	44779	1709
SUERC-27780	40012	1034	3506.8	3350.6	44038	79	44713	1709
OxA-24205	42155	1061	3506.4	3350.2	44032	79	44706	1709
OxA-24383	40758	813	3486.7	3331.0	43738	79	44376	1708
SUERC-27779	39716	849	3486.7	3331.0	43738	79	44376	1708
SUERC-29656	41455	1259	3484.0	3328.3	43692	78	44329	1708
OxA-24394	42352	1189	3473.4	3317.7	43511	73	44146	1708
OxA-24252	42755	1420	3467.0	3311.3	43403	69	44036	1708
SUERC-29655	40567	821	3467.0	3311.3	43403	69	44036	1708

Table B.1.: Radiocarbon dataset from cores SG06 and SG93 cores on the $SG06_{2012}$ varve and modeled time scales; CD and EFD depth scales are from the SG06 core. (also included on data CD)

Table B1

AMS Labcode(s)	^{14}C Date BP	±1σ	CD cm	EFD cm	$SG06_{2012}$ modelled yr BP	±1σ	$SG06_{2012}$ varve yyr BP	±1σ
GrA-5623	32875	370	2959.4	2822.1	36008	84	35834	1588
GrA-10426	33975	743	2958.3	2821.0	35989	84	35815	1588
OxA-24204	33310	476	2956.8	2819.5	35963	84	35788	1587
GrA-5624	32140	260	2951.3	2814.0	35875	84	35700	1581
SUERC-28888	32002	522	2949.3	2812.0	35840	84	35665	1579
OxA-24400	34240	1128	2945.3	2808.0	35770	84	35595	1574
SUERC-29860	33574	739	2942.3	2805.0	35718	83	35543	1570
OxA-24426	32667	330	2938.5	2801.2	35654	83	35479	1565
GrA-10422	31375	763	2937.6	2800.3	35639	83	35464	1565
SUERC-28887	31795	294	2935.8	2798.5	35609	82	35434	1562
OxA-24349	33072	622	2931.4	2794.1	35530	81	35356	1558
OxA-24350	33150	563	2931.4	2794.1	35530	81	35356	1558
SUERC-27775	32152	310	2931.4	2794.1	35530	81	35356	1558
SUERC-26376	32236	343	2927.9	2790.6	35466	80	35292	1554
OxA-24306	32158	372	2926.7	2789.4	35445	80	35271	1554
SUERC-28213	31973	427	2923.8	2786.5	35396	79	35223	1552
GrA-5625	31190	360	2913.2	2775.9	35198	82	35033	1544
GrA-5614	31547	330	2910.3	2773.0	35143	85	34982	1542
OxA-24227	31367	219	2906.5	2769.2	35071	85	34915	1539
SUERC-26005	31687	479	2904.9	2767.6	35042	86	34888	1539
GrA-5613	31345	355	2901.5	2764.2	34980	90	34829	1538
OxA-24386	31933	325	2898.9	2761.6	34931	91	34782	1536
SUERC-29817	32130	762	2896.6	2759.3	34887	94	34740	1536
SUERC-27774	32112	485	2895.9	2758.6	34874	94	34728	1536
OxA-24381	31351	301	2893.3	2756.0	34826	95	34682	1534
GrA-10419	31751	813	2893.0	2755.7	34820	95	34677	1534
GrA-5615	31545	335	2890.5	2753.2	34773	99	34634	1533
OxA-24482	29759	982	2884.1	2746.8	34640	100	34514	1529
GrA-5616	31545	340	2883.5	2746.2	34626	100	34502	1528
SUERC-29842	31687	417	2872.0	2734.7	34379	102	34280	1520
OxA-24481	29521	806	2869.5	2732.2	34324	102	34232	1519
GrA-10417	30356	698	2869.2	2731.9	34319	102	34227	1519
GrA-5617	30010	310	2868.4	2731.1	34302	102	34212	1519
OxA-24480	30348	994	2866.8	2729.5	34269	101	34182	1517
OxA-24462	30077	551	2862.9	2725.6	34187	103	34108	1514
GrA-10416	31307	772	2862.8	2725.5	34185	103	34106	1514
SUERC-27771	31358	496	2861.4	2724.1	34154	103	34078	1512
OxA-24355	30589	362	2857.7	2720.4	34074	105	34007	1508
GrA-10415	30471	1062	2853.6	2716.3	33985	105	33927	1504
SUERC-27770	30415	388	2852.7	2715.4	33965	105	33909	1503
OxA-24376	31056	491	2852.1	2714.8	33951	104	33897	1503
OxA-24377	31407	488	2852.1	2714.8	33951	104	33897	1503
GrA-5618	30080	200	2851.7	2714.4	33942	104	33889	1503
OxA-24469	29768	867	2850.9	2713.6	33924	104	33873	1502
OxA-24394	29697	469	2845.5	2708.2	33801	103	33763	1497
OxA-24429	29887	286	2845.5	2708.2	33801	103	33763	1497
SUERC-23351	30604	458	2845.5	2708.2	33801	103	33763	1497
SUERC-28238	30360	282	2842.5	2706.0	33750	103	33717	1495
OxA-24479	28897	1073	2834.5	2698.0	33572	104	33560	1489
OxA-24399	30337	775	2829.7	2693.2	33469	104	33470	1486
GrA-6167	28495	255	2824.8	2688.3	33363	103	33376	1483
SUERC-29841	29634	252	2824.0	2687.5	33346	103	33362	1482
SUERC-17127	29496	394	2822.2	2685.7	33308	102	33327	1480
GrA-6170	28220	245	2816.7	2680.2	33190	104	33226	1475
SUERC-29840	29239	203	2816.4	2679.9	33183	104	33220	1475
OxA-24360	28405	452	2816.3	2679.8	33181	104	33218	1475
GrA-6174	28495	250	2814.5	2678.0	33144	104	33186	1471
SUERC-29836	28685	193	2800.9	2666.3	32894	104	32971	1453
OxA-24325	28466	187	2800.8	2666.2	32892	104	32969	1453
GrA-10391	29449	186	2799.9	2665.3	32874	104	32954	1452
SUERC-28237	29232	379	2797.6	2663.5	32824	103	32910	1450
OxA-24315	28985	250	2794.7	2660.6	32761	103	32856	1447
SUERC-29835	28175	302	2792.1	2658.0	32702	103	32805	1446
GrA-6169	27880	235	2787.9	2653.8	32613	103	32728	1443
GrA-10389	28959	229	2787.9	2653.8	32613	103	32728	1443
GrA-10388	27524	719	2785.2	2651.1	32553	104	32676	1440
GrA-10395	27424	667	2775.6	2642.0	32346	103	32495	1430
OxA-24216	27684	308	2770.1	2636.5	32234	103	32397	1425
GrA-10376	28769	233	2767.0	2633.4	32168	103	32339	1423
GrA-10380	28857	290	2764.2	2630.6	32113	104	32291	1420
GrA-10378	28136	287	2758.7	2625.1	32010	103	32200	1414
OxA-24354	28174	428	2757.5	2623.9	31986	103	32179	1413
GrA-10381	28528	146	2755.7	2622.1	31951	103	32148	1410
SUERC-23348	28838	359	2752.8	2619.2	31894	102	32098	1408
OxA-24251	28957	297	2751.6	2618.0	31872	102	32078	1407
SUERC-20940	28423	345	2743.4	2609.8	31695	103	31921	1399
SUERC-28210	28396	256	2737.7	2604.1	31558	103	31800	1391
OxA-24305	27953	275	2737.5	2603.9	31553	103	31796	1391

AMS Labcode(s)	^{14}C Date BP	±1σ	CD cm	EFD cm	$SG06_{2012}$ modelled yr BP	±1σ	$SG06_{2012}$ varve yyr BP	±1σ
SUERC-26004	27825	181	2730.8	2597.2	31411	103	31668	1384
SUERC-28915	26984	309	2728.2	2594.6	31354	101	31616	1381
OxA-24340	27154	221	2723.0	2589.4	31244	101	31514	1375
OxA-24385	26789	207	2702.5	2568.9	30877	102	31168	1353
SUERC-20947	26800	282	2697.8	2564.2	30795	101	31090	1348
GrA-15727	25880	165	2695.7	2562.1	30761	98	31056	1346
OxA-24234	26839	225	2694.1	2560.5	30733	98	31028	1344
SUERC-20939	26602	271	2691.5	2557.9	30690	99	30984	1341
OxA-24296	25703	225	2687.8	2554.2	30629	101	30923	1334
GrA-15722	25850	140	2684.5	2550.9	30577	99	30870	1325
GrA-6172	25840	670	2682.4	2548.8	30539	99	30831	1320
SUERC-20504	25518	316	2671.2	2537.6	30355	98	30636	1291
OxA-24359	26402	347	2670.9	2537.3	30351	98	30632	1291
OxA-24304	25416	196	2656.0	2522.9	30110	91	30375	1250
GrA-6173	25980	670	2656.0	2522.9	30110	91	30375	1250
OxA-24409	24665	712	2654.6	2521.5	30088	91	30351	1246
GrA-15729	26080	160	2605.7	2507.7	29851	92	30090	1215
GrA-6176	24545	270	2569.1	2479.1	29369	94	29555	1167
SUERC-27769	25110	147	2560.9	2470.9	29237	95	29408	1153
OxA-24314	24895	139	2556.4	2466.4	29165	95	29328	1148
GrA-15718	25355	70	2548.5	2459.4	29060	96	29210	1136
GrA-6177	25130	185	2547.1	2458.0	29039	96	29187	1134
OxA-24418	24525	597	2546.7	2457.6	29032	96	29179	1133
GrA-15723	25340	100	2544.7	2455.6	29004	96	29148	1132
GrA-6178	24700	270	2544.4	2455.3	28999	96	29143	1131
OxA-24274	24924	136	2541.2	2452.1	28953	96	29091	1129
SUERC-16528	26135	620	2538.2	2449.1	28909	96	29042	1127
OxA-24353	24875	230	2537.7	2448.6	28902	95	29034	1126
SUERC-28236	24678	258	2537.7	2448.6	28902	95	29034	1126
OxA-24281	24548	121	2535.7	2446.6	28872	96	29001	1124
SUERC-28209	25109	171	2533.8	2445.3	28853	96	28980	1123
SUERC-27768	25063	144	2532.5	2444.0	28834	96	28959	1121
SUERC-28912	25152	306	2531.0	2442.5	28813	96	28934	1120
OxA-24339	24501	228	2529.9	2441.4	28799	96	28919	1119
SUERC-28911	25020	206	2528.7	2440.2	28780	96	28898	1117
SUERC-23345	24364	252	2526.9	2438.4	28753	96	28868	1114
OxA-24248	24695	126	2526.5	2438.0	28747	96	28862	1114
SUERC-29857	24954	150	2523.9	2435.4	28711	96	28821	1113
GrA-15731	24270	130	2516.4	2428.7	28613	96	28711	1106
SUERC-28233	24506	290	2505.9	2418.2	28467	96	28546	1099
GrA-15728	23730	120	2492.4	2407.5	28307	96	28365	1087
OxA-24333	24367	191	2490.9	2406.0	28285	96	28341	1086
GrA-6179	24595	265	2490.0	2405.1	28274	96	28328	1085
SUERC-28910	23912	260	2488.9	2404.0	28259	96	28311	1084
OxA-24270	24432	120	2488.4	2403.5	28252	96	28303	1084
OxA-24422	23938	169	2477.9	2393.0	28101	95	28132	1071
OxA-24423	23923	115	2477.9	2393.0	28101	95	28132	1071
SUERC-27516	23970	104	2477.9	2393.0	28101	95	28132	1071
OxA-24332	24389	205	2476.2	2391.3	28078	95	28106	1068
GrA-6180	23970	170	2473.5	2388.6	28039	95	28062	1066
GrA-6181	23890	210	2470.1	2385.2	27991	95	28007	1062
GrA-6182	24495	270	2467.7	2382.8	27960	95	27971	1060
OxA-24378	23794	232	2466.5	2381.6	27943	95	27952	1058
SUERC-27515	23727	232	2449.5	2375.7	27861	95	27858	1048
SUERC-28231	23800	175	2447.8	2374.0	27835	95	27830	1045
OxA-24263	24099	143	2445.4	2371.6	27800	94	27790	1042
OxA-24344	23611	169	2442.6	2368.8	27762	94	27746	1037
SUERC-28909	23677	124	2440.5	2366.7	27730	94	27711	1034
GrA-6183	23400	500	2440.0	2366.2	27723	94	27702	1033
SUERC-27790	23774	159	2437.7	2363.9	27691	93	27666	1028
OxA-24348	23714	243	2434.0	2363.1	27678	93	27651	1027
OxA-24438	23377	266	2428.9	2359.3	27623	93	27589	1019
OxA-24375	23717	190	2427.0	2359.1	27620	93	27585	1019
GrA-10375	22298	264	2425.3	2357.4	27595	93	27558	1015
SUERC-23350	23464	200	2421.6	2353.7	27534	93	27488	1007
OxA-24345	23269	303	2418.4	2350.5	27482	92	27428	1000
SUERC-27514	23315	134	2418.4	2350.5	27482	92	27428	1000
GrA-10373	22233	386	2412.8	2344.9	27388	91	27323	987
GrA-6184	23170	150	2412.3	2344.4	27377	91	27310	985
GrA-10372	22280	171	2409.5	2341.6	27308	90	27231	973
SUERC-20938	23042	233	2407.3	2339.4	27248	90	27163	969
GrA-10371	22281	159	2406.1	2338.2	27214	90	27124	966
GrA-6185	22630	220	2403.9	2336.0	27152	89	27054	961
OxA-24261	23147	188	2402.9	2335.0	27123	89	27021	959
OxA-24352	22346	172	2397.4	2330.3	26978	87	26856	948
GrA-10370	22078	157	2396.2	2329.1	26937	87	26810	945
OxA-24370	22475	130	2391.6	2324.5	26782	84	26633	935
GrA-6186	22600	440	2390.0	2322.9	26734	83	26579	935

Table B1

AMS Labcode(s)	^{14}C Date BP	±1σ	CD cm	EFD cm	SG06$_{2012}$ modelled yr BP	±1σ	SG06$_{2012}$ varve vyr BP	±1σ
GrA-10369	22055	264	2389.3	2322.2	26714	83	26555	935
OxA-24189	22578	103	2384.5	2317.4	26567	79	26389	923
SUERC-23349	22541	170	2380.5	2313.4	26442	76	26246	917
OxA-24483	22076	293	2378.6	2311.5	26384	74	26181	913
SUERC-27789	22540	176	2370.5	2304.0	26189	67	25960	896
OxA-24313	21946	151	2368.9	2302.4	26153	65	25919	893
SUERC-26375	22017	95	2358.2	2291.7	25909	60	25646	859
GrA-10404	21274	201	2355.9	2289.4	25867	59	25599	849
OxA-24478	21489	346	2347.9	2281.4	25724	58	25440	817
GrA-10368	21059	151	2335.2	2271.6	25554	60	25258	792
GrA-10360	20826	151	2329.2	2265.6	25447	61	25142	772
SUERC-20937	21406	137	2324.5	2260.9	25363	62	25053	761
OxA-24459	20971	136	2323.4	2259.8	25342	62	25030	758
OxA-24477	21001	304	2321.5	2257.9	25309	63	24994	754
OxA-24407	20571	454	2303.8	2241.2	25027	64	24691	727
OxA-24458	20258	249	2300.9	2238.3	24975	63	24636	722
GrA-10367	20537	562	2297.8	2235.2	24922	63	24577	716
OxA-24405	20307	567	2292.0	2229.4	24813	62	24458	705
GrA-10362	20503	446	2289.2	2226.6	24761	61	24401	699
GrA-10361	20428	147	2283.2	2220.6	24652	59	24281	688
GrA-6187	20630	130	2281.8	2219.2	24628	59	24255	686
OxA-24467	20728	305	2280.7	2218.1	24609	59	24235	684
OxA-24215	20458	139	2276.1	2213.5	24530	57	24148	676
GrA-19401	20115	201	2270.5	2207.9	24442	53	24048	668
OxA-24457	20367	154	2266.9	2204.3	24382	51	23979	661
SUERC-23344	20636	157	2266.5	2203.9	24376	51	23972	660
OxA-24456	20238	231	2264.5	2201.9	24342	50	23934	657
OxA-24476	20396	305	2260.6	2198.0	24278	48	23861	651
GrA-6188	19830	365	2254.8	2194.4	24220	49	23796	646
OxA-24417	19636	753	2246.4	2186.0	24061	53	23634	631
GrA-10266	20041	207	2246.0	2185.6	24054	53	23627	630
GrA-10265	19457	201	2236.3	2183.8	24017	53	23589	627
GrA-10264	19810	203	2232.7	2180.3	23959	53	23530	622
OxA-24293	19792	129	2222.8	2170.4	23778	53	23346	605
SUERC-27513	20299	112	2217.2	2164.8	23674	53	23238	595
GrA-10261	19755	139	2207.5	2155.1	23500	53	23059	580
GrA-6189	19425	305	2207.0	2154.6	23493	53	23051	579
GrA-10263	19191	131	2205.1	2152.7	23462	53	23020	577
GrA-10262	19027	388	2196.6	2144.2	23311	50	22863	564
SUERC-27788	19481	130	2190.6	2138.2	23206	49	22755	556
SUERC-20936	19915	117	2186.7	2134.3	23134	47	22681	549
OxA-24226	19285	82	2172.0	2119.6	22894	43	22434	531
GrA-10258	18931	453	2171.3	2118.9	22881	43	22421	531
GrA-6190	19370	135	2166.7	2114.3	22787	42	22333	527
GrA-10256	18831	146	2160.2	2112.7	22753	42	22301	525
GrA-10383	18781	201	2157.1	2112.7	22753	42	22300	525
GrA-6191	18975	290	2155.4	2111.3	22727	42	22276	524
GrA-10255	18769	132	2153.4	2109.3	22691	41	22242	522
OxA-24404	18741	322	2152.9	2108.8	22682	41	22234	521
GrA-6192	18810	110	2151.4	2107.3	22654	40	22208	520
OxA-24347	18967	122	2142.7	2099.3	22505	36	22066	511
SUERC-18127	18831	102	2139.8	2096.4	22450	34	22015	508
OxA-24371	18681	89	2137.5	2094.1	22408	31	21975	505
OxA-24373	18652	91	2137.5	2094.1	22408	31	21975	505
GrA-10254	18088	226	2128.6	2085.2	22256	33	21822	495
GrA-10253	17973	126	2125.4	2082.6	22207	35	21769	492
OxA-24398	18112	126	2124.0	2081.2	22182	36	21741	490
GrA-10252	17962	127	2119.4	2076.6	22107	40	21660	486
GrA-10250	18240	228	2107.0	2064.2	21913	46	21448	474
OxA-24416	17598	427	2104.5	2061.7	21870	46	21401	472
GrA-10270	17957	201	2100.5	2057.7	21802	47	21327	467
SUERC-17126	17951	115	2097.7	2054.9	21755	48	21276	465
GrA-10248	17433	201	2094.1	2051.3	21696	49	21211	462
OxA-24406	17626	284	2087.9	2045.1	21596	50	21101	456
GrA-10249	17747	162	2087.6	2044.8	21590	50	21095	456
SUERC-26003	17825	60	2082.0	2039.2	21492	53	20988	450
GrA-10269	17451	208	2075.7	2032.9	21376	53	20863	442
SUERC-27512	17881	115	2075.1	2032.3	21364	53	20850	441
OxA-24260	17954	100	2073.2	2030.4	21330	54	20813	439
GrA-10247	17469	128	2069.9	2027.1	21273	53	20752	436
GrA-10246	17203	177	2067.3	2026.1	21254	53	20731	434
SUERC-23740	18174	304	2066.1	2026.1	21254	53	20731	434
OxA-24393	17531	98	2064.9	2026.0	21253	53	20730	434
GrA-6193	17745	140	2064.3	2025.4	21244	53	20720	434
SUERC-20495	17653	93	2059.6	2020.7	21168	53	20638	428
OxA-24303	17630	80	2058.3	2019.4	21147	53	20615	427
OxA-24368	17493	72	2058.3	2019.4	21147	53	20615	427
OxA-24380	17572	73	2053.5	2014.6	21068	53	20531	421

AMS Labcode(s)	^{14}C Date BP	±1σ	CD cm	EFD cm	SG06$_{2012}$ modelled yr BP	±1σ	SG06$_{2012}$ varve vyr BP	±1σ
SUERC-17125	17597	96	2053.3	2014.4	21065	53	20528	421
GrA-10245	17221	117	2040.7	2001.8	20853	52	20301	403
SUERC-29833	17267	60	2037.1	1998.9	20804	52	20248	398
OxA-24408	16846	275	2033.0	1994.8	20738	53	20177	393
GrA-5660	17380	240	2032.4	1994.2	20728	53	20166	393
GrA-4570/GrA-8187	17145	90	2029.4	1991.2	20679	53	20113	390
GrA-4569	16950	185	2026.4	1988.2	20627	53	20057	387
OxA-24331	17247	92	2024.0	1985.8	20587	53	20013	385
GrA-8155	16952	79	2023.8	1985.6	20583	53	20010	385
GrA-4586	17135	170	2016.8	1978.6	20464	53	19881	380
OxA-24372	16830	76	2013.3	1975.1	20402	53	19815	377
SUERC-26372	16905	84	2012.5	1974.3	20387	54	19800	376
GrA-8127	17106	167	2011.3	1973.1	20367	54	19777	375
GrA-4567	17065	240	2007.7	1969.5	20302	54	19708	372
OxA-24297	16859	102	2007.2	1969.0	20292	55	19698	371
SUERC-27511	16950	105	2004.2	1966.0	20236	55	19638	367
GrA-5668b	16700	178	2004.2	1966.0	20236	55	19638	367
GrA-8115	16640	263	2001.2	1963.0	20175	57	19575	363
OxA-24311	16685	74	1999.4	1961.2	20143	57	19541	362
OxA-24312	16568	71	1999.4	1961.2	20143	57	19541	362
GrA-5669	16750	220	1998.2	1960.0	20122	58	19519	361
GrA-8122	16678	206	1992.7	1954.5	20020	59	19412	356
SUERC-19063	16009	137	1989.5	1951.3	19965	59	19355	354
GrA-4566	16280	195	1989.2	1951.0	19961	59	19350	354
GrA-8123	16698	127	1982.2	1944.0	19825	61	19207	347
OxA-24460	16723	104	1979.2	1941.0	19763	60	19142	342
GrA-8118	16570	125	1978.8	1940.6	19755	60	19133	341
GrA-8124	16346	94	1975.2	1937.0	19684	59	19058	336
OxA-24295	16391	77	1971.8	1934.2	19630	59	19001	333
GrA-4565	15990	180	1970.0	1932.4	19597	59	18966	331
GrA-4564	15915	230	1960.0	1923.1	19416	57	18773	325
OxA-24412	16024	868	1955.6	1918.7	19330	55	18679	323
GrA-4562	15695	180	1940.5	1909.4	19151	52	18487	315
OxA-24415	15918	295	1937.7	1906.6	19100	50	18434	312
GrA-8192	16044	77	1934.1	1903.0	19041	51	18373	307
OxA-24414	15632	313	1932.5	1901.4	19012	51	18344	305
GrA-8186	15991	82	1931.2	1900.1	18989	50	18321	303
OxA-24413	15044	528	1923.1	1892.0	18855	48	18181	295
GrA-8114	15857	81	1921.7	1890.6	18830	48	18156	293
GrA-5668a	15730	145	1918.5	1887.4	18777	46	18102	290
SUERC-28208	15661	53	1917.8	1886.7	18765	46	18089	290
GrA-5658	15480	140	1915.5	1884.4	18727	44	18050	287
GrA-4561	15755	270	1912.5	1881.4	18671	44	17994	283
OxA-24338	15398	72	1910.4	1879.3	18631	41	17955	281
GrA-8112	15540	209	1909.6	1878.5	18616	41	17940	280
GrA-8119	15385	119	1906.6	1875.5	18561	39	17887	276
GrA-4556b	15125	185	1903.6	1872.5	18502	41	17833	273
SUERC-17114	15086	74	1901.2	1870.1	18454	40	17791	270
GrA-8120	15202	90	1900.6	1869.5	18442	39	17780	269
SUERC-27510	15279	74	1898.6	1867.5	18402	39	17745	266
GrA-8111	15277	80	1897.6	1866.5	18382	39	17728	265
GrA-8116	15245	149	1894.5	1863.4	18328	37	17679	261
OxA-24247	15088	63	1894.1	1863.0	18320	37	17672	260
GrA-4559	14860	195	1891.3	1860.2	18270	38	17627	257
OxA-24214	14911	76	1888.9	1857.8	18229	41	17588	253
GrA-4558	14630	60	1888.1	1857.0	18216	42	17576	252
SUERC-26001	14748	67	1884.4	1853.3	18157	46	17520	247
GrA-8113	14631	113	1882.3	1851.2	18123	47	17487	244
GrA-4557	14595	90	1879.6	1848.5	18078	49	17443	241
OxA-24411	14632	316	1877.8	1846.7	18049	50	17414	238
GrA-8193	14736	80	1876.3	1845.2	18022	50	17388	237
OxA-24206	14407	222	1869.7	1838.6	17915	53	17282	229
GrA-4556a	14695	60	1869.5	1838.4	17911	53	17278	228
SUERC-23744	14792	142	1860.7	1829.6	17762	55	17131	220
GrA-8132	14582	93	1847.3	1816.7	17513	57	16891	208
SUERC-27507	14523	74	1845.8	1815.2	17485	57	16866	207
GrA-4555	14440	95	1842.2	1811.6	17419	55	16806	204
SUERC-23752	13981	172	1828.7	1798.1	17136	54	16558	196
GrA-5652	14295	85	1825.2	1794.6	17057	57	16491	193
GrA-8133	14159	116	1822.0	1791.4	16980	56	16429	191
GrA-4554	13815	70	1818.8	1788.2	16901	57	16367	189
OxA-24475	13882	166	1817.6	1787.0	16870	57	16342	188
OxA-24269	13863	54	1814.6	1784.0	16797	57	16285	186
SUERC-17121	13753	69	1814.6	1784.0	16797	57	16285	186
GrA-4553	13855	125	1808.6	1778.0	16649	57	16167	182
GrA-5651	13885	80	1805.4	1774.8	16573	58	16107	180
OxA-24410	13412	204	1802.2	1771.6	16501	57	16049	179
GrA-4552/GrA-8128	13627	46	1798.9	1768.3	16424	57	15987	176

Table B1

AMS Labcode(s)	^{14}C Date BP	±1σ	CD cm	EFD cm	SG06$_{2012}$ modelled yr BP	±1σ	SG06$_{2012}$ varve yyr BP	±1σ
GrA-8134	13612	70	1795.7	1765.1	16351	56	15926	173
SUERC-26371	13474	55	1794.1	1763.5	16317	57	15897	172
GrA-5636	13105	110	1792.5	1761.9	16282	57	15867	170
OxA-24188	13518	49	1792.0	1761.4	16272	57	15859	170
SUERC-26000	13339	52	1786.0	1755.4	16143	56	15744	165
GrA-5650/GrA-8130	13402	57	1782.8	1752.2	16075	57	15682	162
GrA-4551	13015	60	1779.6	1749.0	16008	57	15622	159
SUERC-24335	13304	55	1778.2	1747.6	15979	56	15594	158
SUERC-23907	13384	53	1776.7	1746.1	15950	57	15567	156
GrA-5649	13385	165	1776.3	1745.7	15940	57	15561	156
SUERC-21174	13175	157	1776.5	1745.9	15940	57	15561	156
GrA-4550	13465	215	1771.0	1740.4	15820	57	15453	151
OxA-24330	13278	70	1770.5	1739.9	15810	57	15444	151
OxA-24474	12678	137	1768.7	1738.1	15767	57	15408	149
GrA-5648	13440	300	1755.2	1724.6	15497	57	15180	141
SUERC-16526	12608	107	1751.3	1720.6	15413	58	15117	139
OxA-24392	12490	69	1748.8	1718.2	15352	57	15071	137
GrA-8136	12929	92	1748.6	1718.0	15348	57	15068	137
SUERC-27506	12788	54	1746.1	1715.5	15296	55	15026	135
GrA-8140	12750	78	1745.8	1715.2	15289	55	15020	135
OxA-24213	12391	72	1743.2	1712.6	15235	56	14975	134
GrA-6205	12705	105	1743.0	1712.4	15231	56	14971	133
GrA-4543	12745	75	1740.1	1709.5	15176	57	14923	132
SUERC-26370	12630	50	1740.0	1709.4	15174	57	14921	132
GrA-5646	12625	370	1737.3	1706.7	15123	58	14877	130
OxA-24439	12459	52	1737.0	1706.4	15117	58	14872	130
GrA-10242	12001	154	1736.6	1706.0	15110	58	14865	130
SUERC-20230	12499	48	1735.4	1704.8	15087	59	14845	130
SUERC-25999	12451	43	1733.8	1703.2	15057	60	14819	129
OxA-24450	12435	55	1732.6	1702.0	15035	60	14801	128
GrA-8135	12742	98	1731.7	1701.1	15018	61	14786	127
OxA-24302	12476	56	1729.8	1699.9	14998	61	14768	126
GrA-4542	12490	55	1728.9	1699.0	14997	61	14767	126
GrA-8173	12548	57	1726.5	1697.9	14972	61	14745	126
SUERC-10128	12496	50	1726.3	1697.7	14969	61	14743	126
OxA-24202	12557	134	1725.1	1696.5	14951	61	14727	126
SUERC-17722	12344	55	1723.1	1694.5	14925	61	14704	125
GrA-4541	12345	55	1718.8	1690.2	14865	62	14651	124
OxA-24473	12315	133	1718.3	1689.7	14859	62	14645	124
GrA-5645	12520	70	1715.9	1687.3	14828	62	14616	123
OxA-24294	12528	51	1714.0	1685.4	14805	61	14596	123
OxA-24323	12493	50	1714.0	1685.4	14805	61	14596	123
OxA-24324	12483	87	1709.7	1681.1	14751	60	14547	120
GrA-8159	12943	163	1708.3	1679.7	14732	60	14530	120
GrA-10235	12656	112	1706.6	1678.0	14710	60	14510	119
GrA-8156	12502	70	1703.5	1674.9	14670	60	14475	118
GrA-5644/GrA-6160	12320	55	1700.4	1671.8	14628	59	14438	117
GrA-4540	12352	142	1699.0	1670.4	14609	58	14421	116
OxA-24203	12345	49	1694.4	1665.8	14545	57	14368	114
GrA-5643/GrA-8188	12456	90	1694.2	1665.6	14542	57	14365	114
GrA-10231	12410	100	1691.6	1663.0	14508	56	14337	113
GrA-6204	12322	48	1690.1	1660.1	14469	55	14304	112
GrA-4539/GrA-8185	12521	84	1685.9	1657.3	14431	54	14271	111
GrA-8143	12683	116	1682.8	1654.2	14386	52	14233	106
GrA-8150	12323	61	1681.3	1652.7	14366	52	14216	107
OxA-24212	12357	66	1674.6	1646.0	14279	49	14143	103
SUERC-17116	12610	295	1671.4	1642.8	14236	47	14107	101
GrA-5654	12495	95	1668.9	1640.3	14200	45	14076	99
GrA-8148	12270	95	1665.9	1637.3	14160	42	14042	97
GrA-6202	12363	185	1662.9	1634.3	14120	41	14008	96
GrA-8191	12219	42	1661.0	1632.4	14092	40	13986	94
SUERC-26369	12381	97	1660.0	1631.4	14077	39	13974	94
GrA-8189	12250	95	1657.3	1628.7	14042	37	13944	92
GrA-5642	12012	113	1656.8	1628.2	14035	37	13938	92
OxA-24470	12050	85	1654.5	1625.9	14001	38	13909	90
GrA-4537	11981	64	1652.7	1624.1	13974	39	13886	88
OxA-24211	11870	60	1652.7	1624.1	13974	39	13886	88
SUERC-10126	12245	125	1651.6	1623.0	13957	39	13871	88
GrA-6206	11954	45	1648.8	1620.2	13914	40	13835	86
OxA-24224	12040	55	1645.9	1617.3	13870	40	13798	84
GrA-4536	11958	78	1643.0	1614.4	13829	41	13764	82
GrA-8175	11980	110	1639.3	1610.7	13777	41	13719	79
GrA-5653	12101	126	1635.3	1606.7	13721	42	13672	76
GrA-8194	11766	55	1632.7	1604.1	13685	41	13642	74
OxA-24210	12028	63	1631.5	1604.0	13683	41	13641	74
GrA-4535	12015	96	1627.8	1604.0	13682	41	13640	74
GrA-8151	11838	108	1625.0	1602.0	13656	41	13619	73
GrA-8176	11838	108	1625.0	1602.0	13656	41	13619	73

Table B1

AMS Labcode(s)	^{14}C Date BP	±1σ	CD cm	EFD cm	SG06$_{2012}$ modelled yr BP	±1σ	SG06$_{2012}$ varve vyr BP	±1σ
OxA-24448	10034	50	1451.6	1428.6	11735	41	11769	23
OxA-24449	10056	49	1451.6	1428.6	11735	41	11769	23
SUERC-29832	10065	38	1448.0	1425.0	11699	40	11730	22
GrA-2916	10095	100	1446.1	1423.1	11681	40	11711	22
OxA-24292	9992	64	1444.3	1421.3	11665	40	11695	22
SUERC-29831	10112	40	1444.2	1421.2	11664	40	11693	22
SUERC-29830	10120	39	1443.2	1420.2	11654	40	11682	21
GrA-2917	10145	95	1443.1	1420.1	11653	40	11681	21
SUERC-20491	10014	45	1440.6	1417.6	11632	39	11658	21
GrA-2838	10055	100	1437.5	1414.5	11603	38	11628	21
GrA-2961	10095	125	1434.8	1411.8	11582	38	11604	20
OxA-24196	10124	50	1433.7	1410.7	11573	37	11595	20
SUERC-23746	10054	75	1433.5	1410.5	11571	37	11593	20
GrA-2911	10125	95	1429.7	1409.0	11557	37	11578	20
OxA-24468	9962	93	1429.0	1408.3	11552	38	11572	20
GrA-10233	10280	87	1427.5	1406.8	11539	37	11558	19
GrA-2905	9860	95	1426.7	1406.0	11531	37	11551	19
OxA-24455	9941	56	1424.9	1404.2	11514	36	11533	19
GrA-8182	9963	77	1424.0	1403.3	11506	36	11524	19
OxA-24200	10080	55	1420.7	1400.0	11475	35	11491	18
SUERC-29521	10094	41	1420.7	1400.0	11475	35	11491	18
GrA-2904	10005	95	1418.6	1397.9	11452	33	11467	18
GrA-3086	10075	85	1412.4	1391.7	11392	30	11403	18
OxA-24487	9966	54	1408.0	1387.3	11346	27	11356	17
GrA-10260	10027	84	1403.0	1382.3	11291	21	11299	17
OxA-24446	9884	50	1400.9	1380.2	11271	19	11277	17
OxA-24447	9872	49	1400.9	1380.2	11271	19	11277	17
SUERC-17115	9817	50	1394.9	1374.2	11217	14	11217	17
SUERC-17717	9755	44	1394.3	1373.6	11211	13	11211	17
OxA-24431	9672	40	1383.2	1362.5	11110	15	11110	17
OxA-24432	9678	39	1383.2	1362.5	11110	15	11110	17
SUERC-20490	9642	42	1383.1	1362.4	11108	15	11109	17
OxA-24445	9554	46	1378.4	1357.7	11058	17	11062	18
GrA-2907	9495	90	1372.7	1352.0	11001	20	11004	18
SUERC-29520	9600	38	1372.2	1351.5	10996	20	10999	18
SUERC-29519	9699	38	1365.1	1344.4	10925	18	10928	19
GrA-3083	9555	105	1363.7	1343.0	10913	19	10915	20
OxA-24310	9598	43	1361.4	1340.7	10892	20	10893	20
GrA-2912	9625	100	1357.2	1337.1	10859	21	10859	21
SUERC-17721	9550	50	1354.5	1334.4	10837	21	10832	22
GrA-2913a	9405	80	1354.1	1334.0	10834	21	10828	22
SUERC-20489	9549	43	1351.6	1331.5	10812	21	10802	22
GrA-8183	9356	59	1351.1	1331.0	10808	21	10796	22
OxA-24367	9547	39	1345.1	1325.0	10757	21	10734	23
GrA-2944	9320	90	1345.0	1324.9	10756	21	10733	23
GrA-2847	9525	90	1341.9	1321.8	10728	21	10701	24
GrA-3081	9535	80	1335.9	1315.8	10673	21	10641	25
SUERC-29518	9460	37	1335.6	1315.5	10670	21	10638	25
GrA-2915	9635	100	1330.1	1310.0	10616	20	10586	27
SUERC-17120	9442	45	1329.1	1309.0	10606	20	10578	27
GrA-4585	9260	180	1320.5	1300.4	10513	21	10494	29
OxA-24207	9235	52	1317.4	1297.3	10480	22	10462	30
SUERC-29517	9334	42	1314.0	1293.9	10445	22	10427	31
GrA-2921	9270	115	1314.0	1293.9	10445	22	10427	31
GrA-2845	9150	115	1310.7	1290.6	10408	24	10395	32
SUERC-29516	9286	37	1306.2	1286.1	10357	27	10347	33
GrA-2971	9280	115	1303.4	1283.3	10325	25	10316	34
OxA-24239	9137	40	1299.2	1279.1	10276	22	10271	36
OxA-24187	9161	38	1298.9	1278.8	10273	22	10268	36
GrA-8184	9071	72	1289.6	1275.0	10229	19	10228	37
SUERC-26732	9024	39	1288.8	1274.2	10225	19	10219	38
OxA-24391	8874	46	1274.3	1261.6	10118	24		
OxA-24291	8946	43	1260.8	1248.1	10004	29		
SUERC-29513	8951	38	1260.1	1247.4	9998	29		
OxA-24440	8870	47	1259.6	1246.9	9994	29		
SUERC-16524	8512	71	1257.7	1245.0	9978	29		
SUERC-17118	8751	43	1234.1	1221.4	9784	25		
OxA-24309	8845	41	1233.6	1220.9	9780	25		
SUERC-25995	8825	38	1229.3	1216.6	9744	24		
OxA-24329	8774	46	1225.2	1212.5	9707	23		
OxA-24425	8563	40	1207.9	1195.2	9545	17		
OxA-24420	8439	38	1198.0	1185.3	9468	15		
SUERC-26366	8422	40	1198.0	1185.3	9468	15		
OxA-24192	8362	37	1180.8	1168.1	9336	18		
SUERC-27503	8406	47	1176.2	1163.5	9300	19		
OxA-24280	8306	42	1164.6	1151.9	9190	24		
SUERC-20486	8158	38	1156.9	1144.2	9119	22		
OxA-24249	8096	39	1143.6	1130.9	9006	19		

AMS Labcode(s)	^{14}C Date BP	±1σ	CD cm	EFD cm	SG06$_{2012}$ modelled yr BP	±1σ	SG06$_{2012}$ varve vyr BP	±1σ
OxA-24288	8081	35	1130.3	1117.6	8875	25		
OxA-24259	8107	39	1121.9	1109.2	8791	26		
SUERC-18129	7766	41	1103.6	1090.9	8592	23		
OxA-24424	7739	41	1097.9	1085.2	8540	24		
SUERC-28229	7781	38	1097.9	1085.2	8540	24		
OxA-24366	7775	35	1095.8	1083.1	8520	25		
SUERC-20485	7407	38	1076.6	1063.9	8321	15		
OxA-24246	7375	36	1074.6	1061.9	8303	14		
SUERC-20484	7503	41	1064.6	1051.9	8230	11		
OxA-24287	7500	35	1063.4	1050.7	8221	11		
OxA-24322	7334	37	1056.8	1044.1	8166	15		
SUERC-20482	7345	41	1049.7	1038.4	8117	19		
OxA-24267	7284	37	1043.6	1032.3	8067	20		
OxA-24268	7269	38	1043.6	1032.3	8067	20		
SUERC-23358	7120	48	1032.1	1020.8	7970	21		
OxA-24286	7171	34	1029.2	1017.9	7947	23		
SUERC-17725	6951	39	1019.9	1008.6	7845	29		
OxA-24272	7091	35	1016.2	1004.9	7810	30		
SUERC-25994	6956	40	1007.3	996.0	7709	23		
SUERC-20481	6650	39	998.0	986.7	7581	22		
OxA-24419	6630	34	990.3	979.0	7505	19		
SUERC-28207	6715	47	990.3	979.0	7505	19		
OxA-24245	6477	34	987.3	976.0	7468	21		
SUERC-26365	6558	37	983.8	972.5	7435	22		
SUERC-25993	6216	35	957.1	948.6	7151	37		
OxA-24279	6096	35	939.0	930.5	6959	28		
SUERC-20480	6035	40	925.7	917.2	6820	27		
SUERC-26731	5783	38	906.6	898.1	6605	26		
OxA-24255	5717	31	898.1	889.6	6511	24		
OxA-24181	5500	34	876.9	869.2	6292	14		
OxA-24182	5458	35	876.9	869.2	6292	14		
SUERC-13332	5465	35	876.9	869.2	6292	14		
SUERC-23355	5320	38	861.0	853.3	6153	22		
OxA-24262	5332	33	854.9	847.2	6101	24		
SUERC-26362	5230	38	839.9	832.2	5971	21		
SUERC-28228	5048	38	820.6	812.9	5809	21		
SUERC-20479	4962	35	812.0	804.3	5736	16		
SUERC-25992	4974	35	800.8	793.1	5660	14		
OxA-24220	4862	30	792.7	785.0	5599	10		
SUERC-28206	4883	38	780.0	772.3	5497	11		
OxA-24351	4848	35	773.0	765.3	5438	13		
SUERC-28202	4729	39	768.1	760.4	5402	14		
SUERC-25990	4773	37	761.8	754.1	5359	13		
OxA-24238	4655	34	754.1	746.4	5309	16		
SUERC-23354	4595	38	738.0	730.3	5161	16		
SUERC-25989	4486	35	713.5	707.1	4985	15		
OxA-24285	4388	29	705.8	699.4	4915	17		
OxA-24195	4136	34	693.7	687.3	4806	13		
SUERC-20476	4166	37	691.9	685.5	4793	14		
OxA-24284	4211	28	685.4	679.0	4741	15		
SUERC-26730	4241	37	678.2	671.8	4688	23		
SUERC-26361	4235	37	667.9	661.5	4611	26		
OxA-24271	4009	28	657.6	651.2	4524	25		
SUERC-25988	4041	37	653.4	647.0	4492	26		
OxA-24277	3895	29	635.2	628.8	4362	25		
OxA-24278	3923	30	635.2	628.8	4362	25		
OxA-24237	3906	31	631.6	625.2	4336	24		
SUERC-23353	3982	36	631.6	625.2	4336	24		
SUERC-20475	3806	37	616.0	609.6	4222	23		
SUERC-26360	3700	37	602.1	595.7	4126	24		
OxA-24194	3815	28	596.0	589.6	4088	26		
SUERC-20474	3650	35	579.4	573.0	3956	23		
OxA-24321	3620	30	571.8	565.4	3895	23		
SUERC-25985	3527	37	561.3	554.9	3805	25		
OxA-24300	3436	30	548.9	542.5	3699	22		
SUERC-20473	3340	37	535.0	528.6	3586	22		
SUERC-28201	3331	37	527.5	521.1	3525	23		
OxA-24320	3152	28	508.4	502.0	3369	20		
SUERC-26729	3251	36	500.4	494.0	3297	26		
OxA-24232	2943	27	484.7	478.3	3153	30		
SUERC-28200	2952	38	477.5	471.1	3091	33		
OxA-24308	2964	30	461.6	455.2	2947	40		
SUERC-26359	2760	37	449.4	443.0	2825	38		
SUERC-23360	2514	35	428.4	422.0	2632	40		
OxA-24235	2426	25	413.9	407.5	2516	38		
OxA-24236	2489	26	413.9	407.5	2516	38		
SUERC-20472	2499	37	413.9	407.5	2516	38		
OxA-24183	2483	28	406.3	399.9	2454	37		

Table B1

AMS Labcode(s)	^{14}C Date BP	±1σ	CD cm	EFD cm	SG06$_{2012}$ modelled yr BP	±1σ	SG06$_{2012}$ varve yyr BP	±1σ
SUERC-13335	2456	35	406.3	399.9	2454	37		
SUERC-25984	2411	37	399.0	392.6	2392	34		
OxA-X-2347-43	2227	24	392.9	386.5	2337	36		
SUERC-26338	2308	35	387.3	380.9	2290	39		
OxA-24243	2109	27	369.0	362.6	2148	41		
OxA-24244	2123	27	369.0	362.6	2148	41		
SUERC-25983	2256	37	362.7	356.3	2105	41		
SUERC-26337	2046	35	344.6	338.2	1971	31		
OxA-24245	1915	26	337.0	330.6	1912	29		
SUERC-20499	1744	37	321.7	315.3	1810	29		
OxA-24379	1744	24	307.2	300.8	1697	21		
SUERC-26728	1775	35	302.6	296.2	1687	21		
SUERC-25982	1809	37	296.6	290.2	1639	21		
OxA-24299	1798	29	290.6	284.2	1576	23		
SUERC-26336	1535	35	269.4	263.0	1400	18		
OxA-24266	1445	26	263.4	257.0	1350	17		
SUERC-25981	1344	35	251.8	245.4	1262	21		
OxA-24233	1251	22	233.9	227.5	1109	22		
SUERC-23361	1125	35	222.5	216.1	1004	19		
OxA-24191	927	24	211.8	205.4	903	14		
SUERC-20471	757	37	177.6	176.0	600	15		
SUERC-26355	694	35	152.0	152.0	500	10		
SUERC-26727	457	35	113.8	113.8	442	41		
OxA-24231	505	23	108.4	108.4	423	45		
SUERC-25980	406	35	103.6	103.6	406	48		
OxA-24276	259	24	67.5	67.5	268	72		
OxA-24328	96	27	42.0	42.0	102	85		
SUERC-26724	136	37	42.0	42.0	102	85		

Table B2

AMS Labcode(s)	^{14}C Date BP	±1σ	CD cm	EFD cm	SG06$_{2012}$ modelled yr BP	±1σ	SG06$_{2012}$ varve vyr BP	±1σ
OxA-X-2362-20	42269	2140	4113.0	3958.2	53070	189	54989	1709
SUERC-18131	38448	1247	4103.0	3948.1	52915	189	54813	1709
OxA-X-2360-48	42927	1294	3977.9	3823.0	50991	189	52644	1708
OxA-X-2362-19	41582	2367	3951.3	3796.5	50584	180	52185	1708
OxA-X-2374-18	41404	3221	3861.7	3709.0	49257	152	50667	1707
OxA-X-2340-29	41442	1445	3818.9	3669.1	48634	140	49976	1707
SUERC-13334	39129	844	3796.7	3646.9	48295	134	49591	1707
SUERC-28898	37332	796	3756.7	3606.9	47683	122	48897	1707
OxA-X-2360-43	38751	729	3541.8	3403.7	44573	81	45373	1706
SUERC-26008	32998	764	3467.0	3329.4	43403	69	44085	1705
OxA-X-2362-50	34975	1217	3461.7	3324.1	43316	70	43993	1705
SUERC-29853	38721	617	3360.9	3226.8	41776	83	42306	1705
SUERC-16527	32838	885	3174.3	3042.5	39084	94	39110	1705
SUERC-19064	27308	402	3163.4	3031.6	38934	95	38921	1705
OxA-X-2357-20	32662	487	3051.1	2930.9	37526	83	37378	1636
SUERC-17724	30514	489	3010.1	2890.9	36882	88	36721	1616
GrA-10429	34936	180	2964.0	2844.8	36086	86	35913	1591
GrA-10390	30265	331	2812.6	2695.0	33109	104	33153	1468
SUERC-29834	24023	279	2779.6	2664.1	32432	103	32571	1434
GrA-6168	26460	215	2774.5	2659.0	32324	103	32476	1430
GrA-15732	25160	140	2706.8	2591.3	30954	102	31237	1358
GrA-6171	25445	190	2705.4	2589.8	30929	102	31214	1356
GrA-15725	23780	120	2650.8	2536.1	30070	91	30283	1235
OxA-X-2362-11	22980	268	2512.2	2438.7	28555	96	28643	1103
SUERC-17723	21743	165	2488.9	2417.5	28259	96	28311	1084
GrA-15726	23230	120	2479.9	2408.5	28130	95	28163	1074
SUERC-13333	19137	123	2190.6	2132.8	23206	49	22755	556
OxA-X-2219-17	20181	189	2190.6	2132.8	23206	49	22755	556
SUERC-19062	14409	94	2015.5	1963.7	20441	53	19855	378
OxA-X-2245-19	13852	78	1843.0	1801.4	17434	55	16820	205
GrA-6203/GrA-8142	14217	76	1815.6	1773.9	16821	57	16305	187
OxA-X-2357-16	12490	69	1748.8	1707.2	15352	57	15071	137
GrA-8147	12333	74	1648.8	1608.2	13914	40	13835	86
OxA-X-2297-42	11916	53	1596.4	1561.8	13269	37	13310	62
GrA-4533	10975	55	1594.4	1559.8	13243	36	13289	62
SUERC-17720	11016	49	1591.4	1556.9	13203	36	13257	61
OxA-X-2219-16	11339	80	1565.1	1531.0	12890	30	12987	52
SUERC-19061	6968	94	1408.7	1377.5	11353	27	11364	17
SUERC-28906	8730	45	1259.6	1236.8	9994	29		
OxA-X-2297-53	7878	41	1077.5	1055.3	8330	15		
SUERC-17117	6129	38	969.8	952.0	7286	30		
OxA-X-2339-40	6042	34	960.5	945.5	7187	35		
SUERC-28203	4625	35	773.0	759.0	5438	13		
OxA-X-2360-44	4427	32	748.3	734.8	5256	16		
OxA-X-2297-56	2493	25	439.9	430.9	2738	39		
OxA-X-2303-36	2487	27	439.9	430.9	2738	39		
OxA-X-2270-49	436	25	136.4	135.9	524	27		
OxA-X-2248-48	730	24	108.4	107.9	423	45		

Criteria for rejection:

- Fail χ^2 test against coeval samples
- Imply ≥400‰ shift in Δ14C and ≥4σ from neigboring samples
- Imply ≥400‰ shift in Δ14C
- ≥4σ from neigboring samples

Table B.2.: Samples identified as outliers

k	% error
0.05	14.1
0.10	10.0
0.15	8.2
0.20	7.1
0.25	6.3
0.30	5.8
9.35	5.3

Table B.3.: The equivalent uncertainties (1σ; as a percentage of 500 years) for the mid-point of a 1000 year core section, interpolated using different k values (see equation A17 in (Bronk Ramsey, 2008)).